

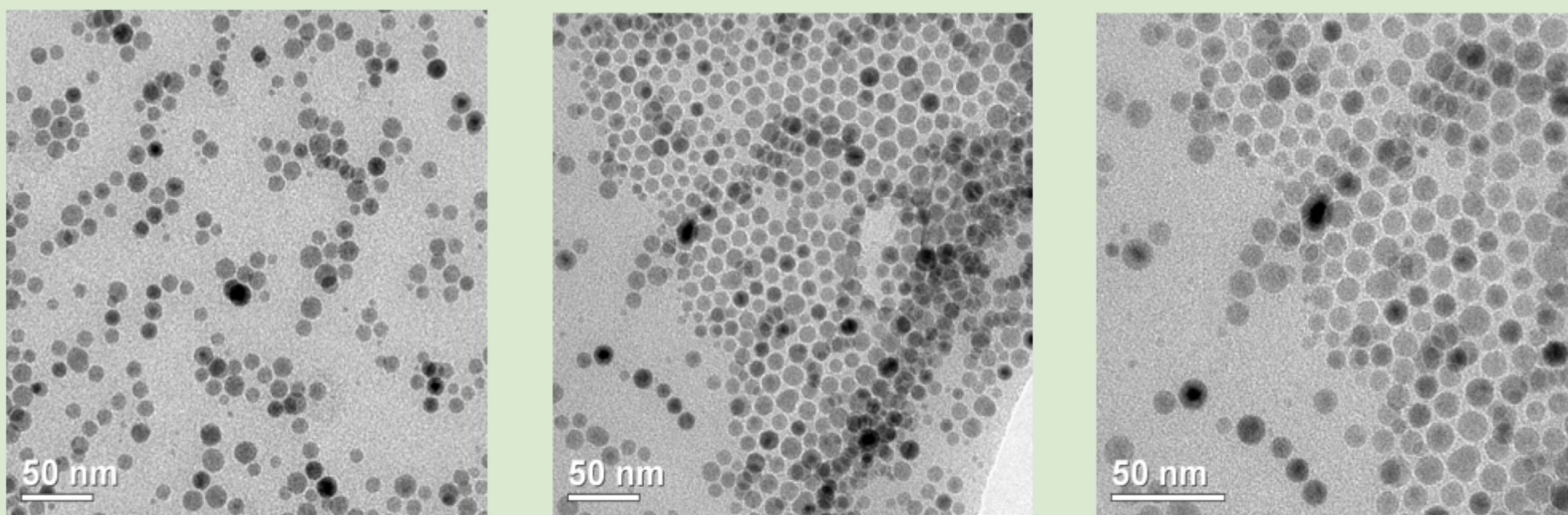
ABSTRACT

SPIONs – Super Paramagnetic Iron Oxide Nanoparticles, are pioneering materials in the field of nanotechnology. These are being used extensively in a wide range of applications such as diagnostics, drug delivery, magnetism and therapeutics¹. A recent study at Imperial, demonstrated that functionalised SPIONs showed fast sorption of uranium from simulated waste solutions with strong selectivity and a high capacity². However, the mechanism is not yet fully understood but is believed to be due to chelation between the phosphate groups and uranyl ions in solution. In addition, the synthesis process to develop these novel nanoparticles is highly complex and lengthy. Furthermore, the particles can only be used in neutral and alkaline environments, which limits their use as acidic conditions are prevalent in untreated nuclear wastes. The current work is focused on overcoming these challenges to demonstrate similar level of performance (even at acidic pH), by synthesising these novel magnetic nanoparticles using a low-cost, greener and simple work-up procedure.

A well-controlled, yet sophisticated & expensive protocol

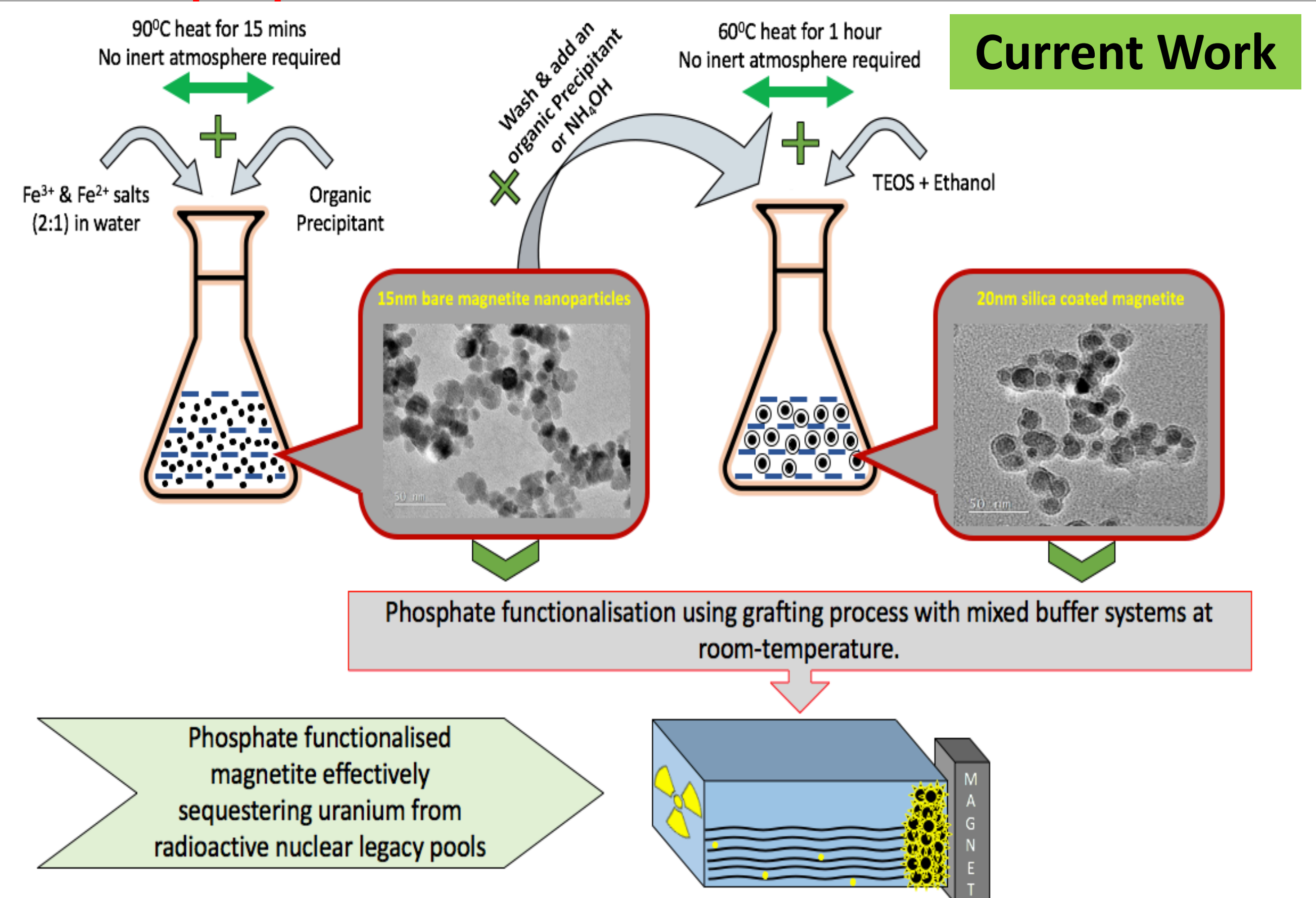
Previous Work

- Fortner's group (ref 1) had reported since 2015 about magnetic nanoparticles of mixed Mn/Fe oxide nanocrystals covered with a bilayered oleyl phosphate to adsorb/exchange uranyl ions in solution.
- Adsorption Capacity reported to be 1667 mg/g of mixed oxide nanocrystals.
- In 2018 Imperial's PhD student (Ref 2) further enhanced the work by using pure magnetite coated with oleic acid (12nm in size).



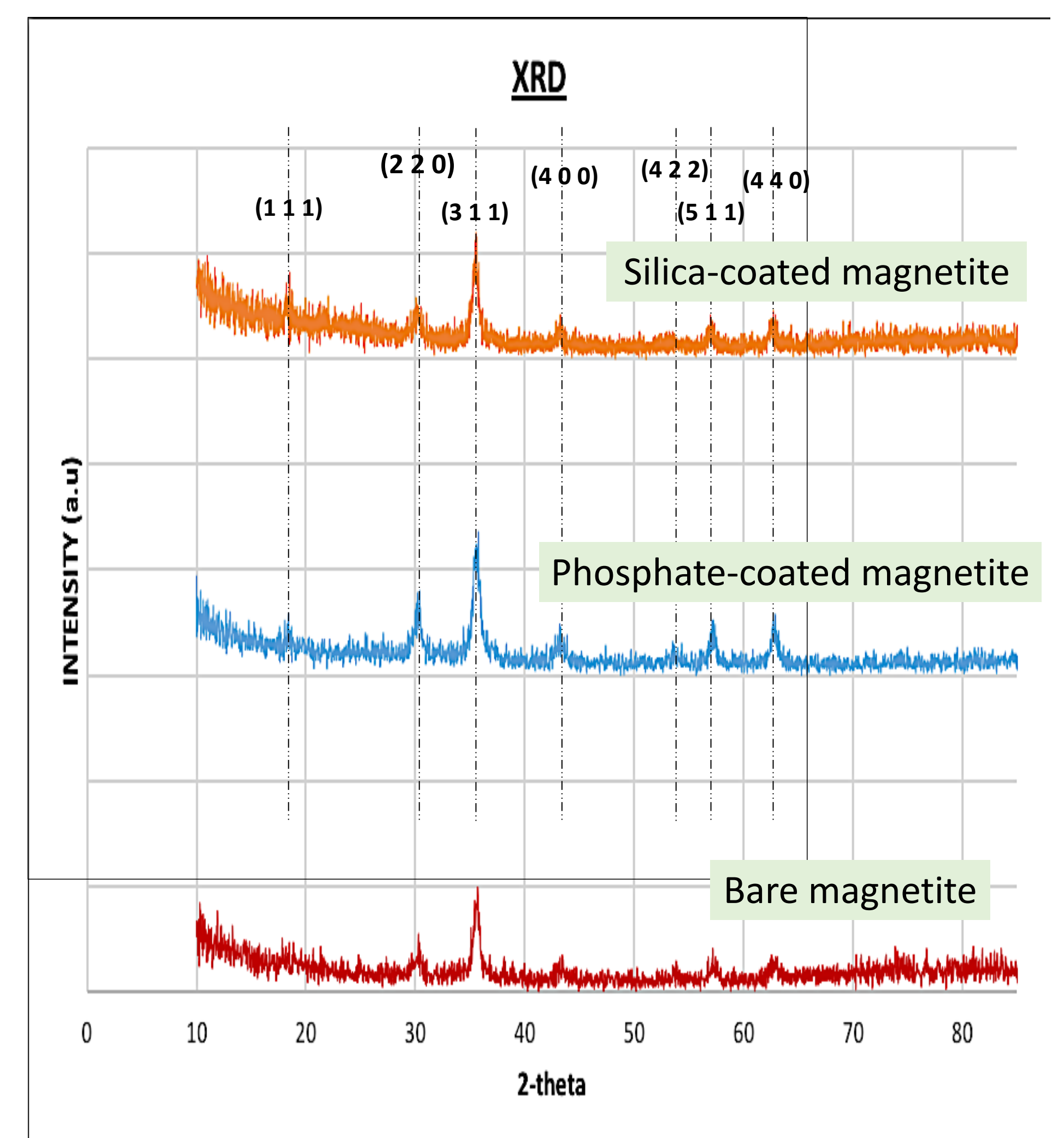
- The nanoparticles were further functionalised with phosphate groups to sequester uranium.
- The reported uptake capacity of Uranyl ions at neutral pH 7 was 1690 mg/g of magnetite in 200ppm U(VI) nitrate solution. This is the highest ever to be reported in the literature.
- Mechanism of uptake unknown.

A quicker, cheaper & greener protocol with good-control



Validation, Advantages & Limitations of Current Approach

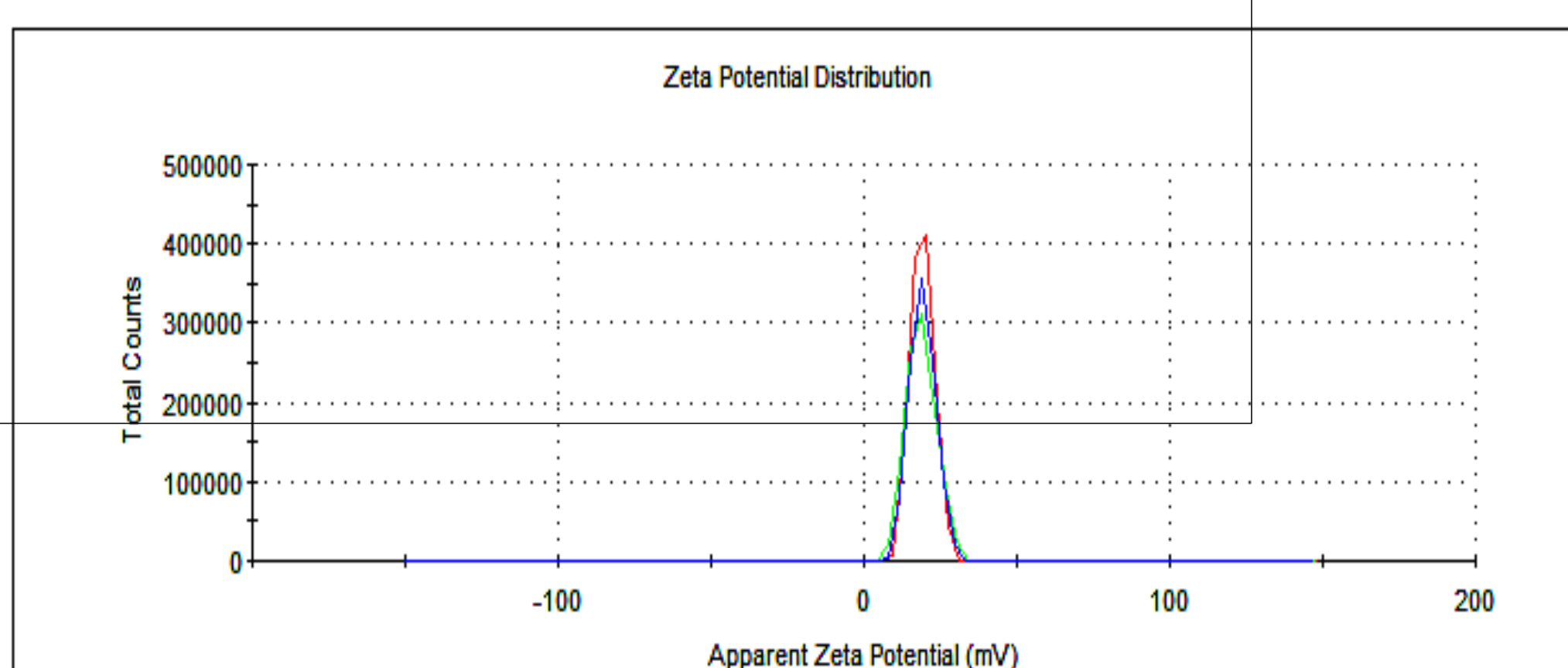
- The current approach synthesises bare-magnetite nanoparticles (~15nm) within 30 minutes and phosphate-coated or silica-coated magnetite nanoparticles within 2 hours.
- The method uses minimum & low-cost chemicals, relatively non-toxic to the environment.
- The degree of control & repeatability is fairly good in terms of size, shape & product yield.
- Aggregation of particles is a substantial issue at hand, that affects overall quality of the coating, leading to multi-cores and flocculation.
- XRD, TEM and Zeta Potential measurements confirm the success of synthesis and functionalised coatings.
- XRD spectrums depict magnetic nanoparticle crystallites with high phase-purity corresponding to magnetite phase only.
- TEM pictures show successful synthesis of nanoparticles with size ~15nm for bare magnetite, and ~20nm for silica coated magnetite.
- Zeta-potential graphs show the surface charge of bare magnetite in water (~pH= 5.3) to be 19.3mV, while that of phosphate-coated & silica-coated nanoparticles are -23.7mV and -34.7mV. It demonstrate increasing stability & better dispersion of the coated nanoparticles.



	Mean (mV)	Area (%)	St Dev (mV)
Zeta Potential (mV): 19.3	Peak 1: 19.3	100.0	4.23
Zeta Deviation (mV): 4.23	Peak 2: 0.00	0.0	0.00
Conductivity (mS/cm): 0.0186	Peak 3: 0.00	0.0	0.00

Result quality : Good

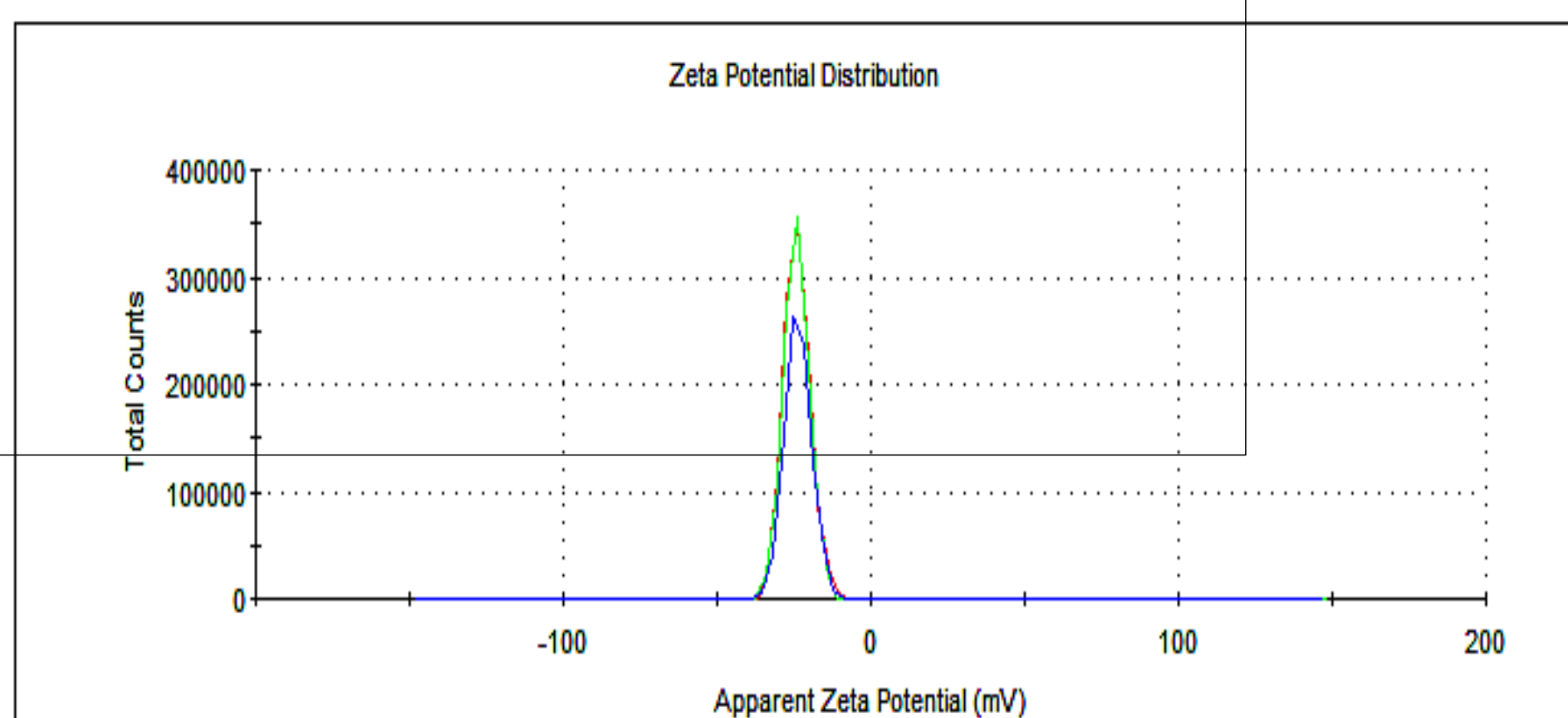
Bare magnetite in water



	Mean (mV)	Area (%)	St Dev (mV)
Zeta Potential (mV): -23.7	Peak 1: -23.7	100.0	4.26
Zeta Deviation (mV): 4.26	Peak 2: 0.00	0.0	0.00
Conductivity (mS/cm): 0.00741	Peak 3: 0.00	0.0	0.00

Result quality : Good

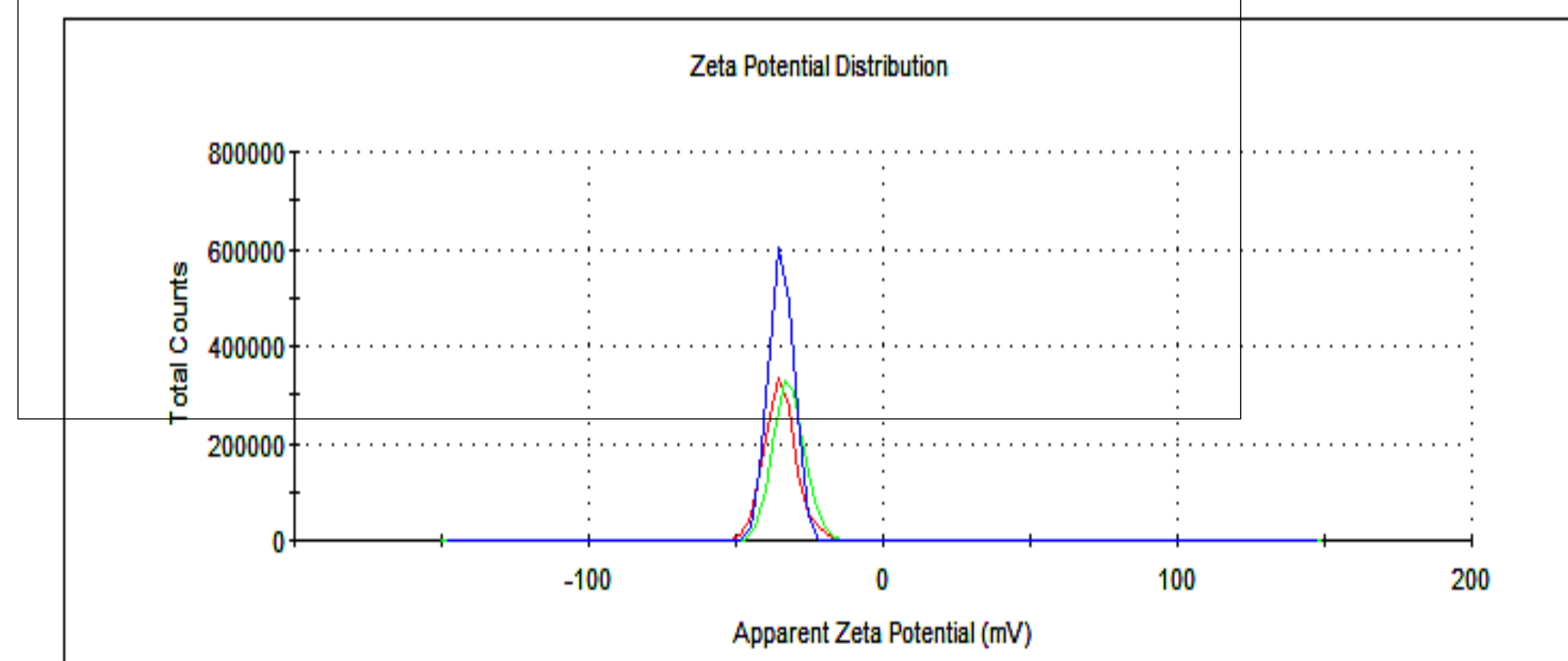
Phosphate-coated magnetite in water



	Mean (mV)	Area (%)	St Dev (mV)
Zeta Potential (mV): -34.7	Peak 1: -34.7	100.0	4.10
Zeta Deviation (mV): 4.10	Peak 2: 0.00	0.0	0.00
Conductivity (mS/cm): 0.0133	Peak 3: 0.00	0.0	0.00

Result quality : Good

Silica-coated magnetite in water

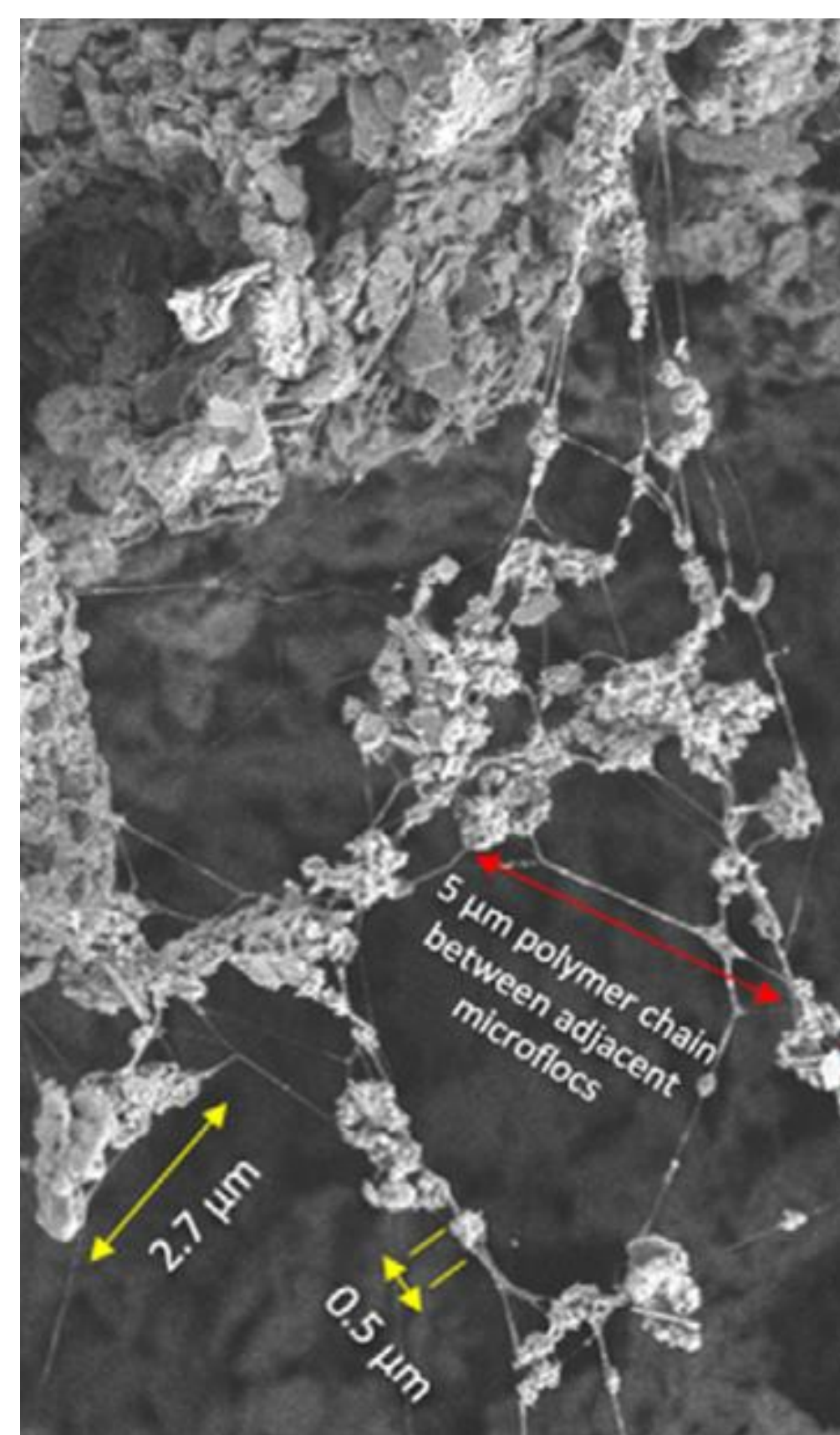


REFERENCE 1 – Fortner et al. (2016) J. Mater. Chem. A, 4(39):15022–15029.

REFERENCE 2 – Cali et al. (2018) J. Mater. Chem. A, 6(10):1039/C7TA09240G.

1. Introduction

- Decontamination of legacy nuclear waste storage ponds and silos is of great importance and stands as a matter of increasing urgency throughout the nuclear industry.
- In facilities around the UK, waste suspension flows transport legacy material from historic ponds to other interim locations where they are safely stored.
- The addition of small amounts of high-molecular-weight polymers to particle-laden flows to separate non-settling fine solids from aqueous suspensions is a promising technique to instigate settling.
- The potential to use polymers in sensitive systems such as nuclear waste processing flows depends upon on the development of a better understanding and demonstrable effectiveness.
- This study aims to elucidate the fundamentals of polymer-particle interaction and adhesion within settling tanks and flow, as well as the way in which chemical or bulk properties affect the dynamics of adhesion, bridging and subsequent flocculation.

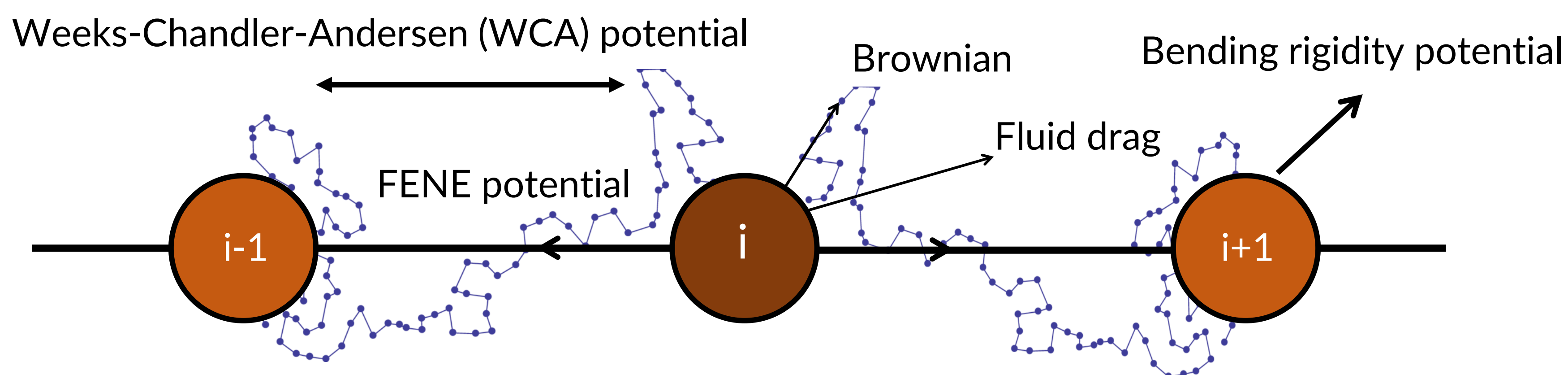


Microstructure of kaolinite flocs as revealed by cryo-SEM
Sharma S., Lin C., Miller J. D., Multi-scale features including water content of polymer-induced kaolinite floc structures, *Minerals Engineering*, 101, 2017, pp. 20-29

2. Polymer-induced flocculation

- Adsorption of polymers onto particle surfaces causes destabilization through bridging or charge neutralization.
-

3. Finitely extensible non-linear elastic (FENE) polymer model



- Langevin dynamics simulation including spherical particles and bead-spring polymers, which are represented as a sequence of beads connected in a chain through FENE bonds.

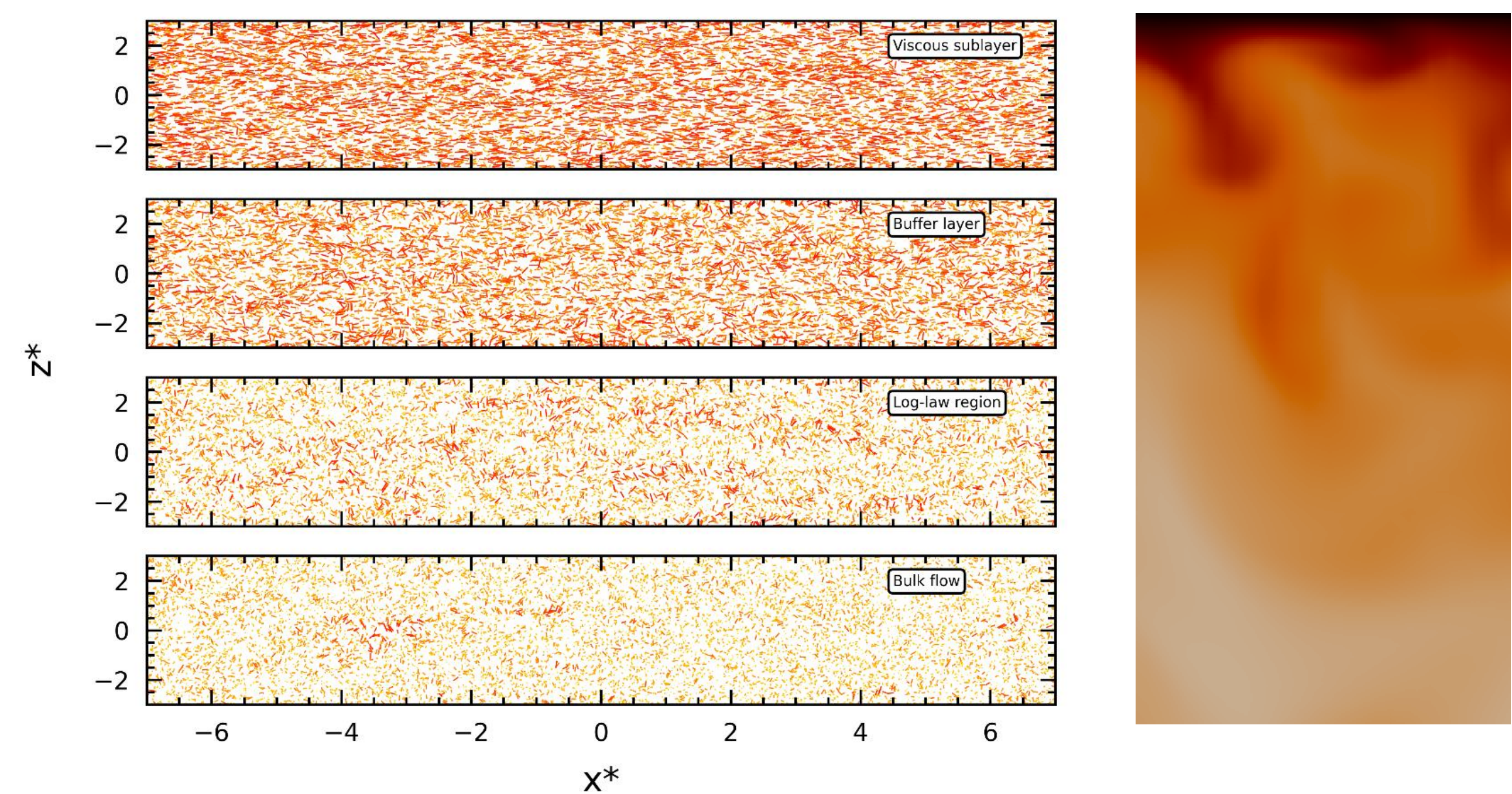
$$\frac{d^2 \mathbf{r}_i^*}{dt^{*2}} = -\nabla V_i^* - \frac{1}{D} \left(\frac{d\mathbf{r}_i^*}{dt^*} - \mathbf{u}_{F,i} \right) + \sqrt{\frac{2}{D}} \boldsymbol{\eta}_i^*(t^*)$$

$$V_{i,WCA}^*(\delta r^*) = 1 + 4 \left[\left(\frac{1}{\delta r^*} \right)^{12} - \left(\frac{1}{\delta r^*} \right)^6 \right]$$

$$V_{i,FENE}^*(\delta r^*) = -\frac{K_F^* R_0^{*2}}{2} \ln \left[1 - \left(\frac{\delta r^*}{R_0^*} \right)^2 \right]$$

$$V_{i,BEND}^*(\theta_i) = K_B^* (1 + \cos(\theta_i))$$

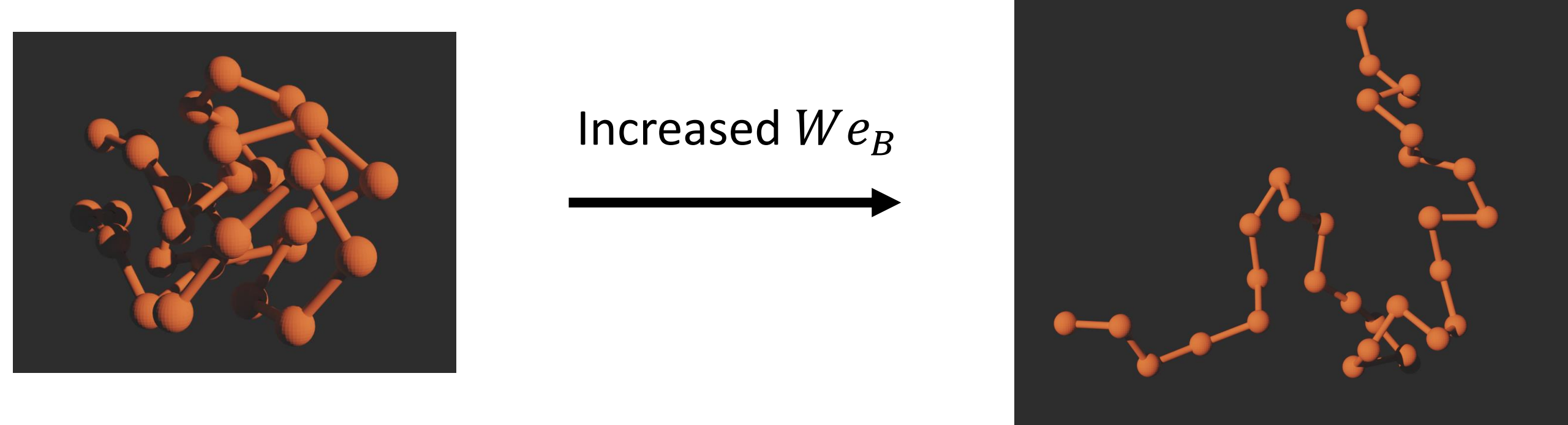
4. Polymer chains in turbulent channel flows



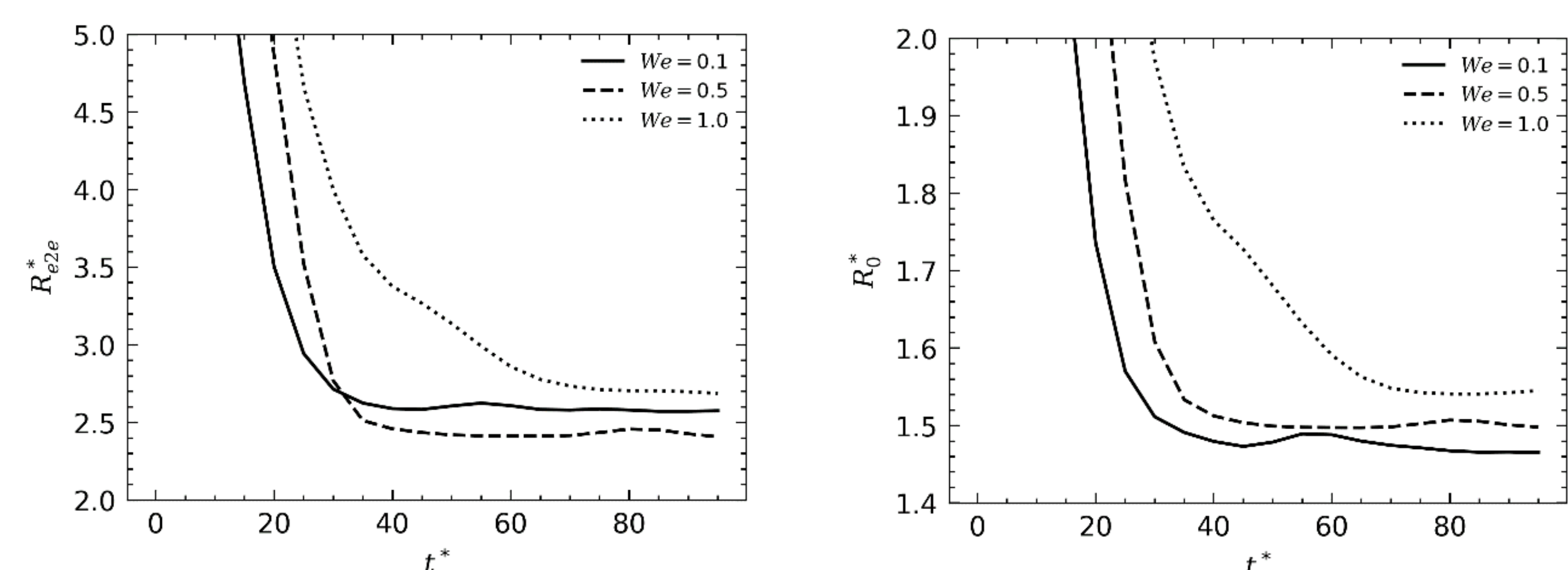
- Conformation is highly shear-dependent, and with polymer-particle interaction shown to depend highly on conformation. Flocculation behaviour will be greatly modified by local shear rate.

5. Polymer conformation under shear

- Increased shear is equivalent to increasing the Weissenberg number. In this study we consider three Weissenberg numbers, 0.1, 0.5 and 1.0.

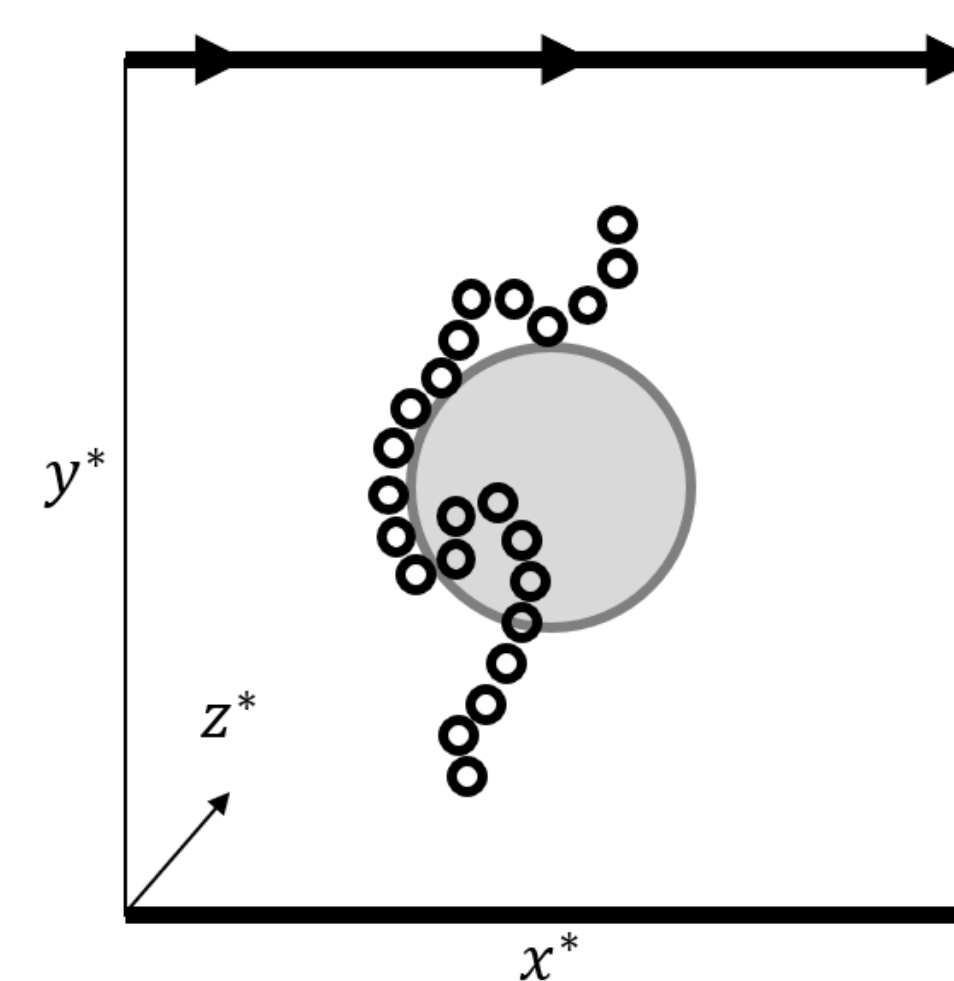


- The temporal evolution of the mean end-to-end distance as a function of We is illustrated in below.
- This property is maximised for the highest shear rate, meaning the velocity gradient across the polymer chain induces stretching.
- Interestingly, for the midrange shear, the end-to-end distance is reduced.
- Tumbling behaviour was also observed, consistent with previous studies.

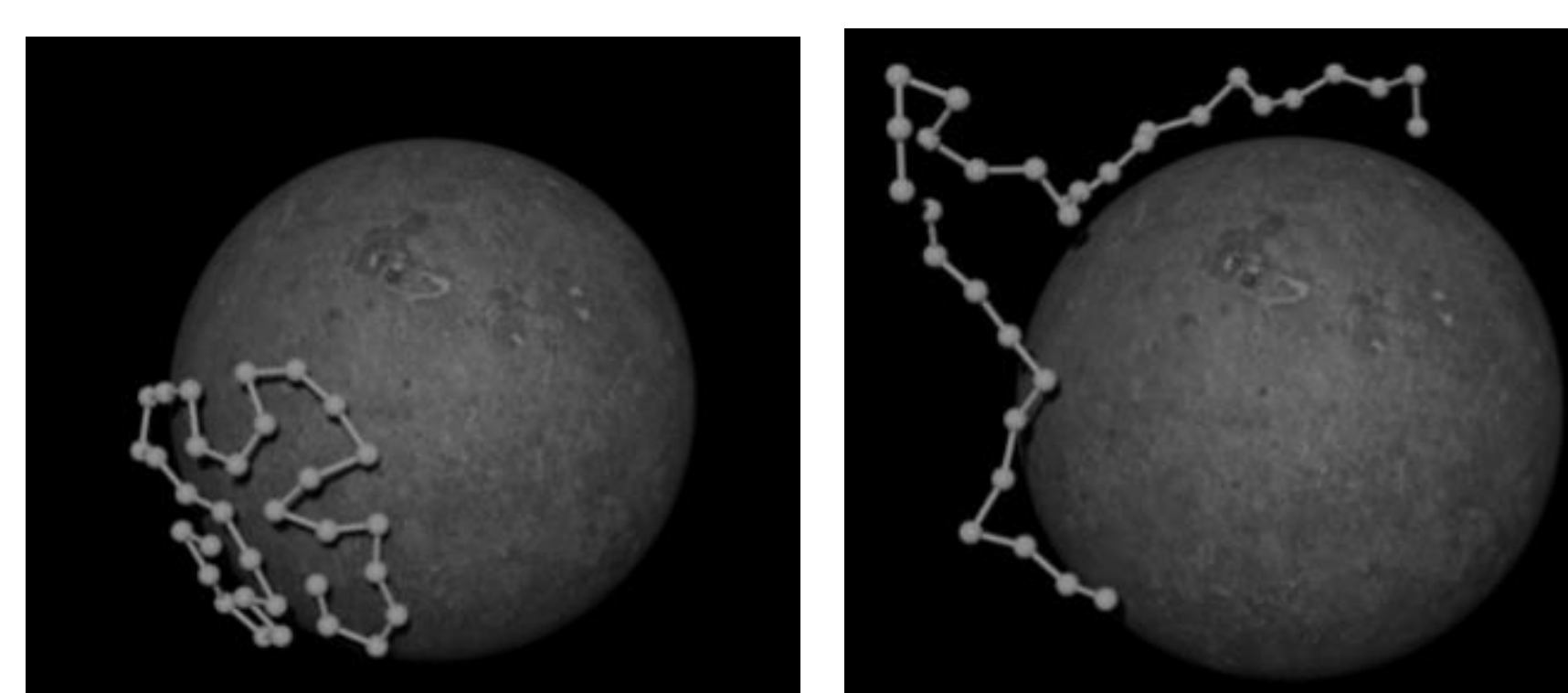


Effect of Weissenberg number, We , on temporal evolution of end-to-end polymer chain distance (left) and radius of gyration (right) under shear flow conditions

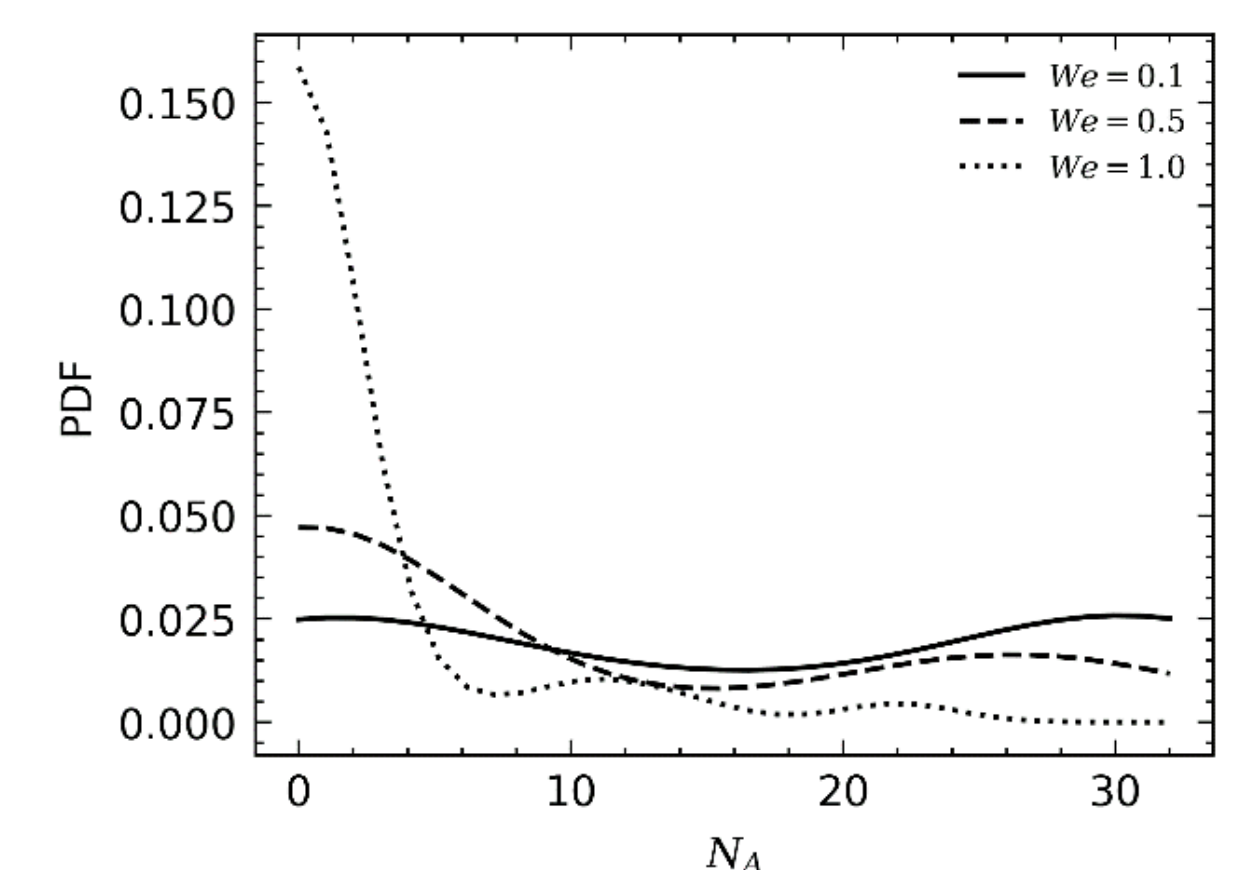
6. Polymer-particle adhesion dynamics under shear



- To elucidate further the dynamics at the point of polymer-particle impact and interaction, the effect of Weissenberg number on the adsorption of polymer chains onto a spherical particle was also studied.
- In these simulations, a single particle was fixed in the centre of the domain, with a polymer chain injected randomly upstream from the particle.
- As the shear rate increases, the number of fully adsorbed chains is reduced and the number of chains in the region where fewer than half of the beads adsorb increases.



Instantaneous snapshots of particle-polymer configuration. $We = 0.1$ (left) and $We = 1.0$ (right).



PDF of the number of adsorbed beads, N_A . Effect of We is illustrated.

6. Conclusions

- A novel potential-based particle-polymer adsorption simulation technique has been developed in order to explore the fundamentals of flocculation and adsorption-surface interaction. Monte-Carlo simulations in shear flows in the presence of a single stationary particle were also performed to determine mechanisms for adsorption.
- Most adsorption took place in the low shear rate system, with beads able to resist the flow and unravelling across the particle surface. For the medium shear rate, some beads were able to adsorb onto the particle, forming tails and trains which increase the effective flocculation radius of the particle. For high shear rate, most beads were unable to adsorb onto the particle, with those successful often being removed later in the simulation.

Introduction:

The ability to predict particle dispersion, particle-particle interaction, deposition and agglomeration effectively within fluid flows can improve nuclear waste management operations, and in particular the retrieval of such waste and post-operational clean-out (POCO) operations. Particle-laden turbulent flow characterisation is being studied using first-principles mathematical modelling. The variation of influential parameters is also being investigated to determine the impact of behavioural modification effects, i.e. studying the impact of key parameters on particle interactions to obtain a desired flow behaviour.

Motivation and Objective:

The overall aim of this study is to address fundamental technical difficulties that are encountered within the nuclear industry. Developing and facilitating approaches for safer, cost-efficient waste management and decommissioning is the focus of the research. Understanding and modelling pond and silo sludge behaviour is essential to the management of radioactive wastes. In legacy ponds and silos, for example at Sellafield, characterising how sludges and slurries containing dense particulates will behave is vital for post-operational clean-out operations. The aim is to establish a predictive tool to support POCO operations through improvements in the flow, mixing and separation of wastes during retrieval and POCO operations. In particular, the impact of behavioural modification on particle agglomeration, and hence the likely deposition of particles during processing.

Methodology:

To solve the descriptive equations in a direct numerical simulation the computational fluid dynamics solver Nek5000 has been used. This solver is based on the spectral element method that is a high-order weighted residual technique. Nek5000 is favourable due to its high accuracy, and low numerical dispersion and dissipation, and is easily and efficiently parallelisable. A Lagrangian particle tracker has been developed to model large quantities of dispersed solids which runs concurrently with Nek5000. And then, a fourth order Runge-Kutta method implemented to solve the particle equation of motion for each particle within every time-step.

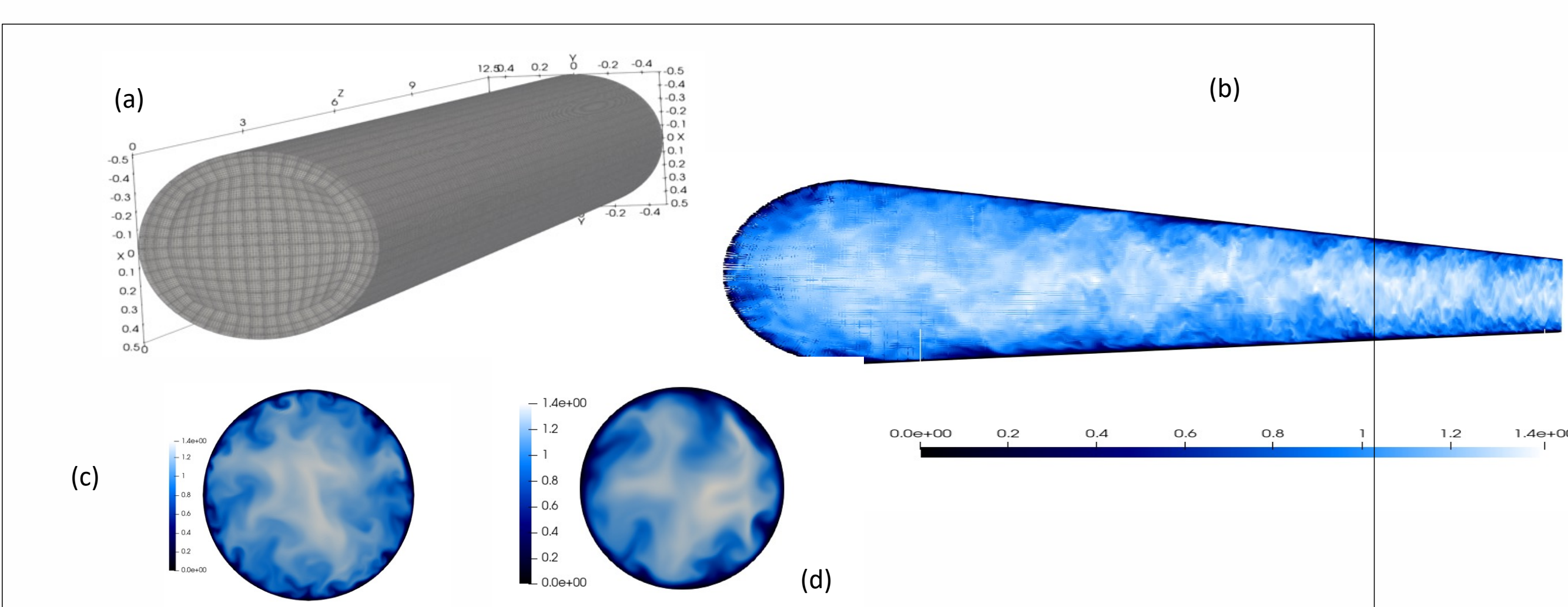


Fig. 1. Computational mesh and pseudo-colour visualisation of the instantaneous axial velocity. Panels: (a) is the computational mesh with Gauss-Lobatto-Legendre quadrature points ($N = 7$) for both simulations at $Re_\tau = 360$ and $Re_\tau = 720$, (b) - clipped at the centreline. (c) & (d) are the instantaneous streamwise velocity normalized by the bulk velocity U_b of simulations at $Re_\tau = 360$ and $Re_\tau = 720$, respectively.

Fluid and Particle Results:

The predictions have been validated and compared with literature simulations and experimental datasets. The outcomes are in good agreement with literature results. Using the fully developed $Re_\tau = 720$ fluid flow computation noted above is being used to simulate one- and four-way coupled flows, and four-way coupled flows with agglomeration, at high concentration with a volume fraction of 10^{-3} . Such a high concentration is required to encourage particle collisions and ensure sufficient agglomeration of particles. Fig.2 to Fig. 4 are the results obtained using 150,000 randomly injected particles initially assigned the local fluid velocity. 100 μm particles with a density ratio (with the fluid) of 2.71 are being used for all the high concentration simulations. The effect of particle Stokes number on particle deposition within a wall-bounded turbulent flow also investigated - Fig.5.

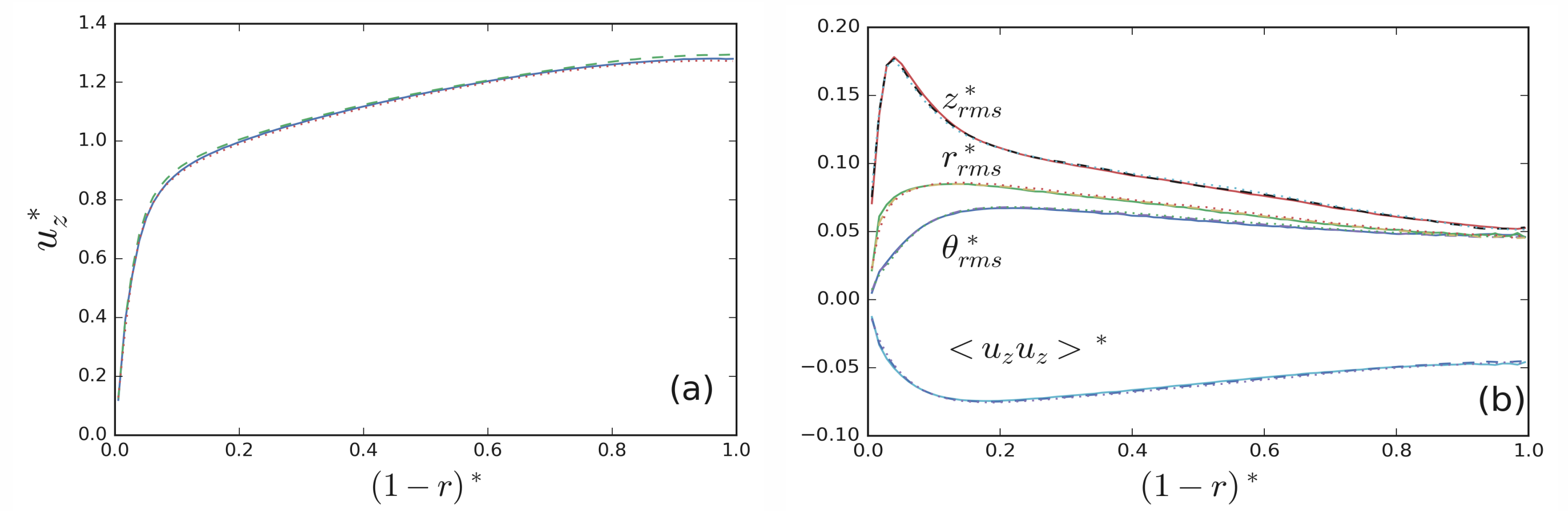


Fig. 2: (a) The Particle mean axial velocity profiles, (b) normal and shear stress profiles (axial, z_{rms}^* , radial, r_{rms}^* , azimuthal, θ_{rms}^* , and Reynolds shear stress, $\langle u_z u_r \rangle^*$ as a function of $(1-r)^*$ — solid lines are one-way coupling, - -dashed lines are four-way coupling and ... dotted lines are four-way coupling with agglomeration.

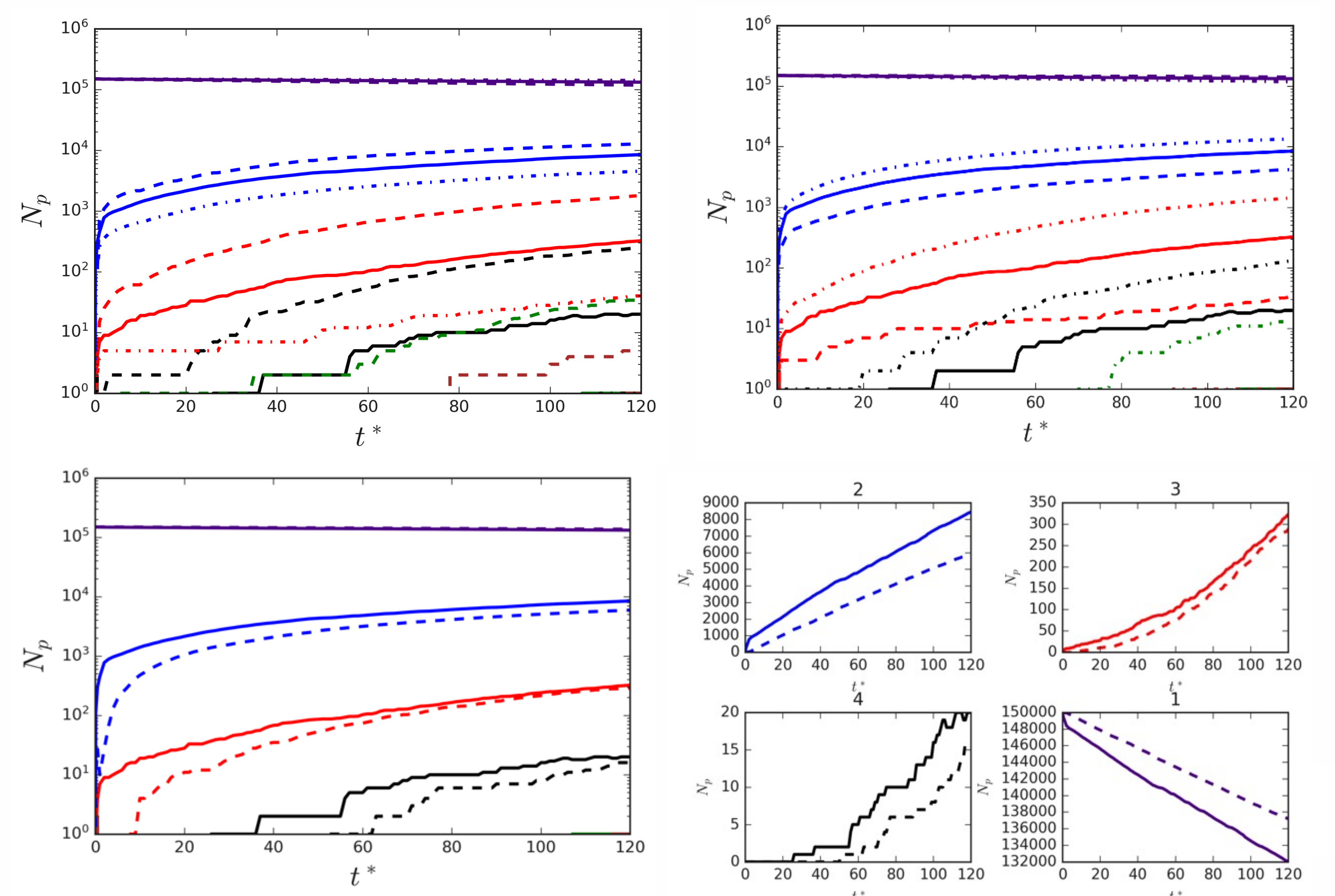


Fig. 3: Influence of the normal restitution coefficient - top left, Hamaker constant - top right, Reynolds number (Re) - lower left and linear plots for Re - lower right. The total number of agglomerates of size N as function of t^* . Indigo: $N =$ singlets; blue: $N =$ doublets; red: triplets; black: $N =$ quadruplet; green: $N =$ quintuplet and brown: $N =$ sextuplets.

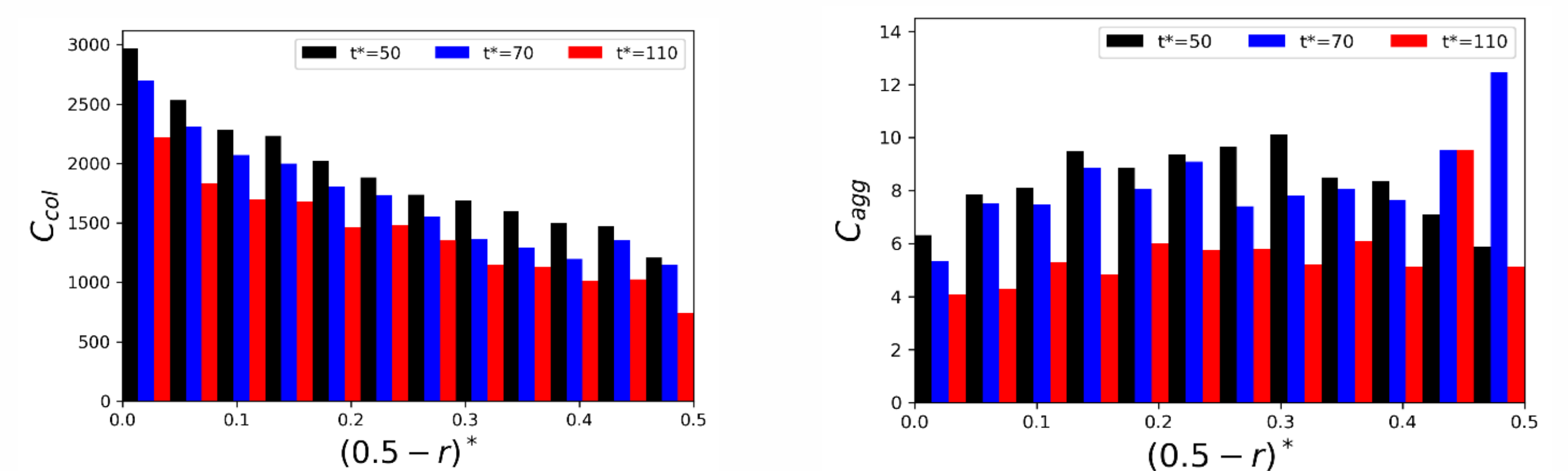


Fig. 4: Distribution of the total number of particle-particle collision and agglomeration events for Calcite.

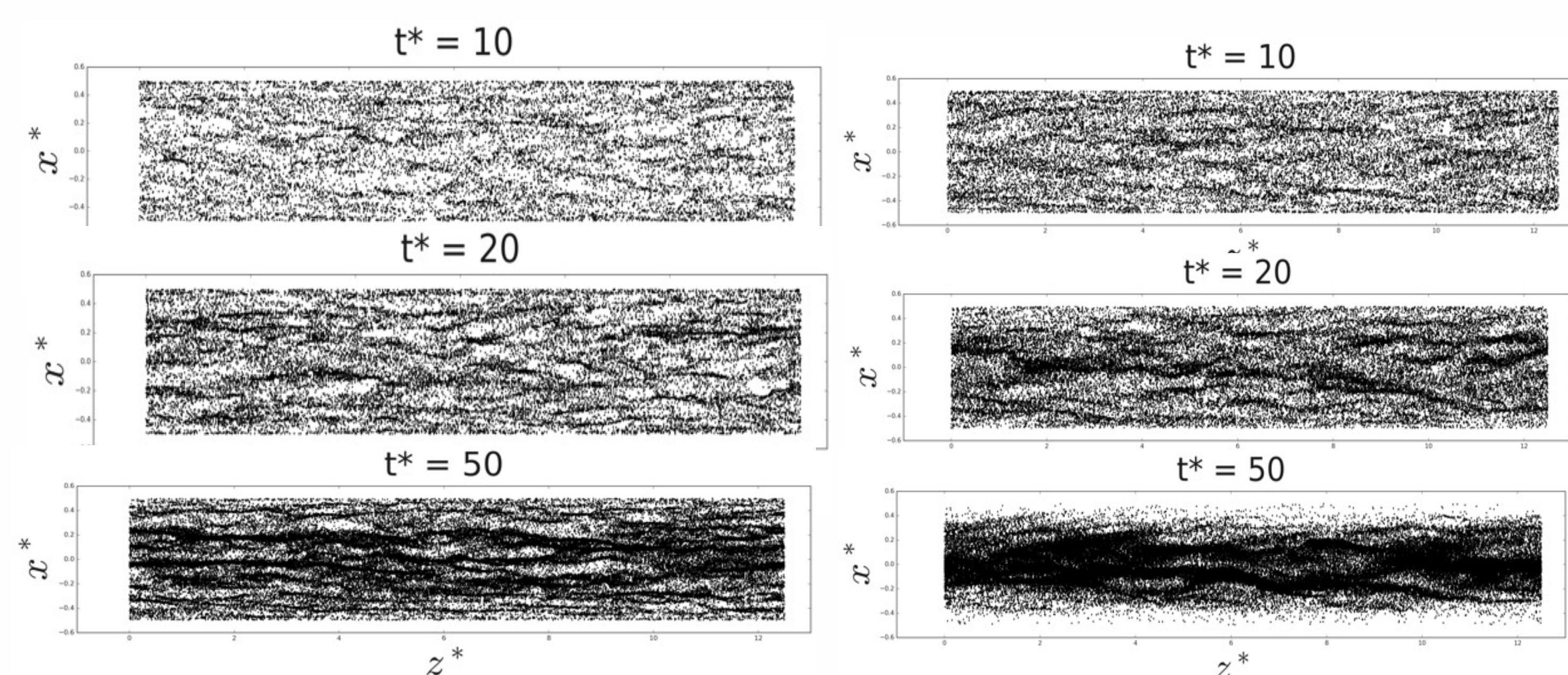


Fig. 5: Instantaneous plots of particle position in the near-wall region of the lower half of the pipe for $St^+ \cong 5.5$ (left) and $St^+ \cong 16.78$ (right.)

Planned work:

- Finalising the behavioural modification techniques using first principles which has been used to examine effects of flow and solid property changes on particle-laden flow characteristics.

Acknowledgments and references:

- <https://ukinventory.nda.gov.uk/about-radioactive-waste/how-do-we-manage-radioactive-waste>
- TRANSCEND proposal



What happens when a NP is subjected to irradiation?

- Irradiated NPs can cause a number of chemical changes in the surrounding media [1]
- Forming a range of chemical species: e.g. H₂, •OH and low energy e^s

Why are NPs relevant to healthcare?

- NPs can be used as radiosensitisers in radiotherapy [2]
- Due to their ability to produce low energy e^s and •OH that are known to cause damage to tumour cell DNA [3]

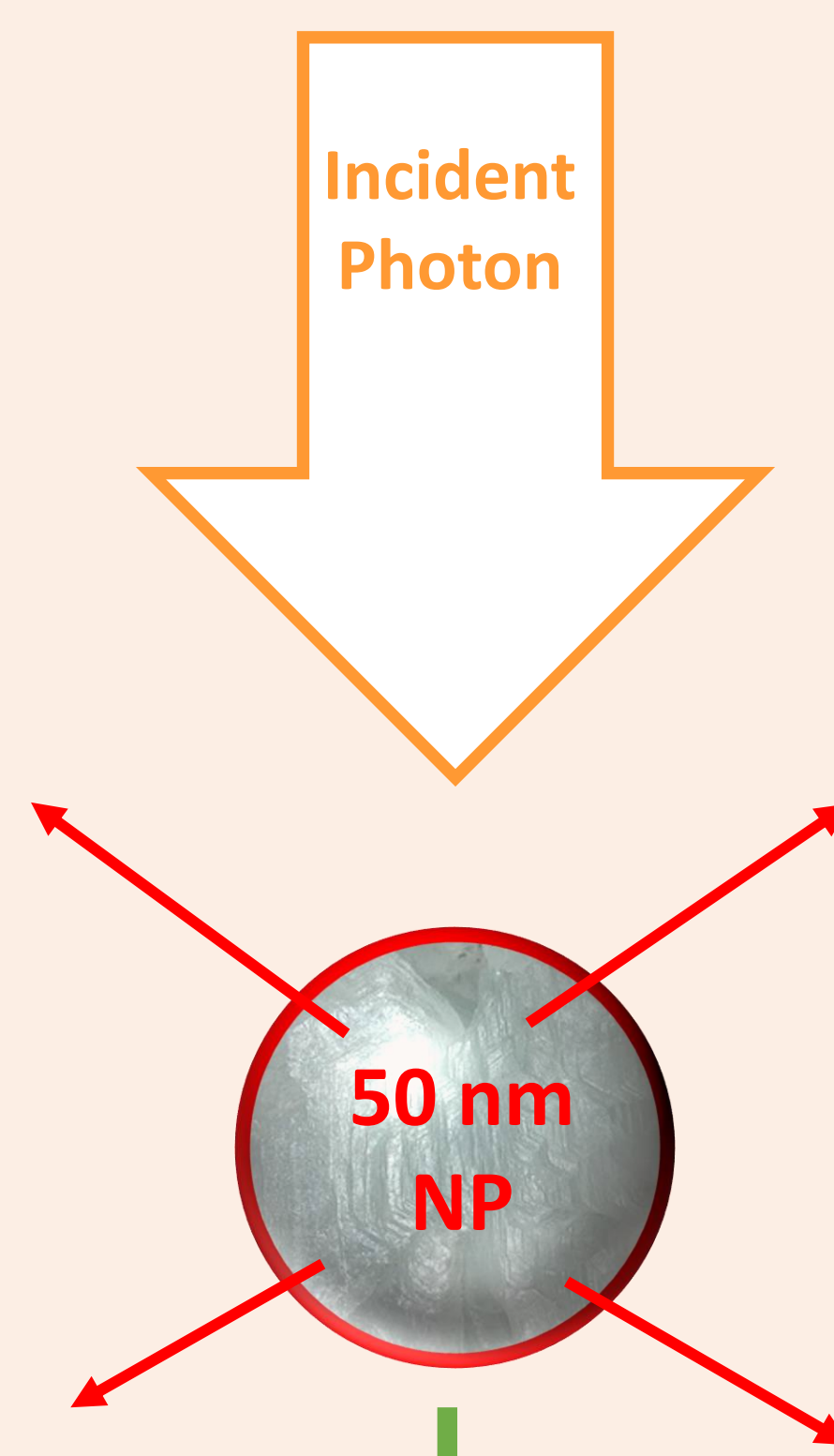
Why are irradiated nanoparticles (NPs) relevant to nuclear waste?

- Light metal oxide/hydroxides are present in nuclear waste storage ponds
- Due to corrosion of the nuclear fuel rod cladding whilst in the legacy ponds
- In the UK a major component of the nuclear waste is Mg(OH)₂, with minor quantities of Al [4]



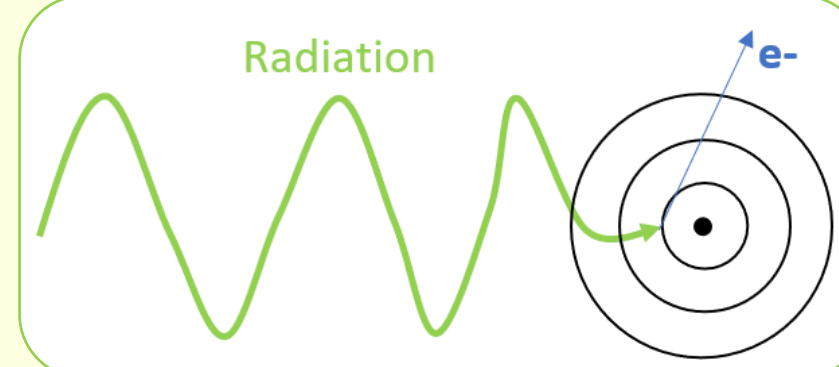
Model

- The simulations were originally performed with Mg(OH)₂ and Al₂O₃, to represent UK nuclear waste sludge
- It is now being applied to a wide range of NPs relevant to both healthcare and nuclear waste industries
- The simulations were built using the TOol for PArticle Simulation (TOPAS) [5]
- The model consists of a 50 nm NP irradiated by a photon beam
- The position, energy and momentum of all secondary particles generated, i.e. the particles that can escape the NP
- The phase space file is then 'released' into a 1500 nm radius water sphere and the results are calculated as below

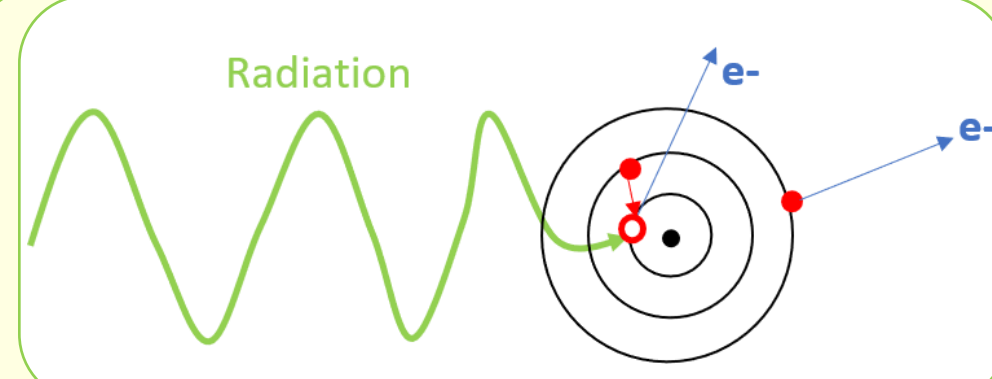


Which energy phenomena occur when a NP is subjected to irradiation?

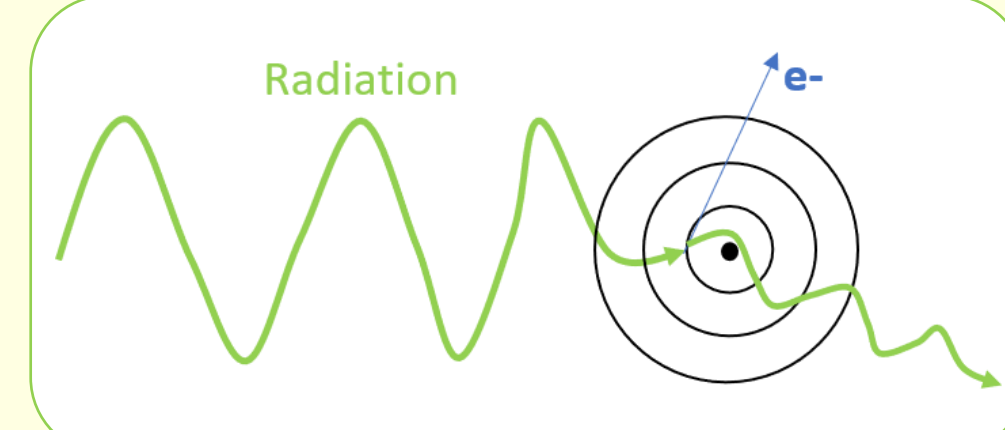
a) Photoelectric Effect



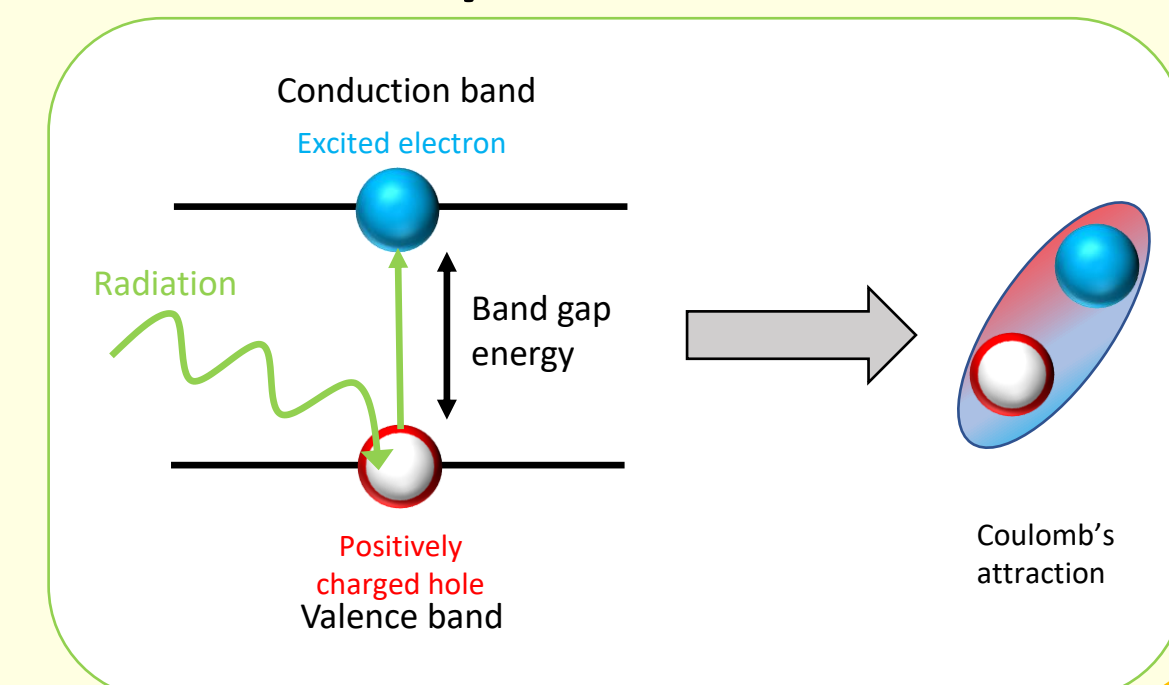
b) Auger Effect



c) Compton Effect

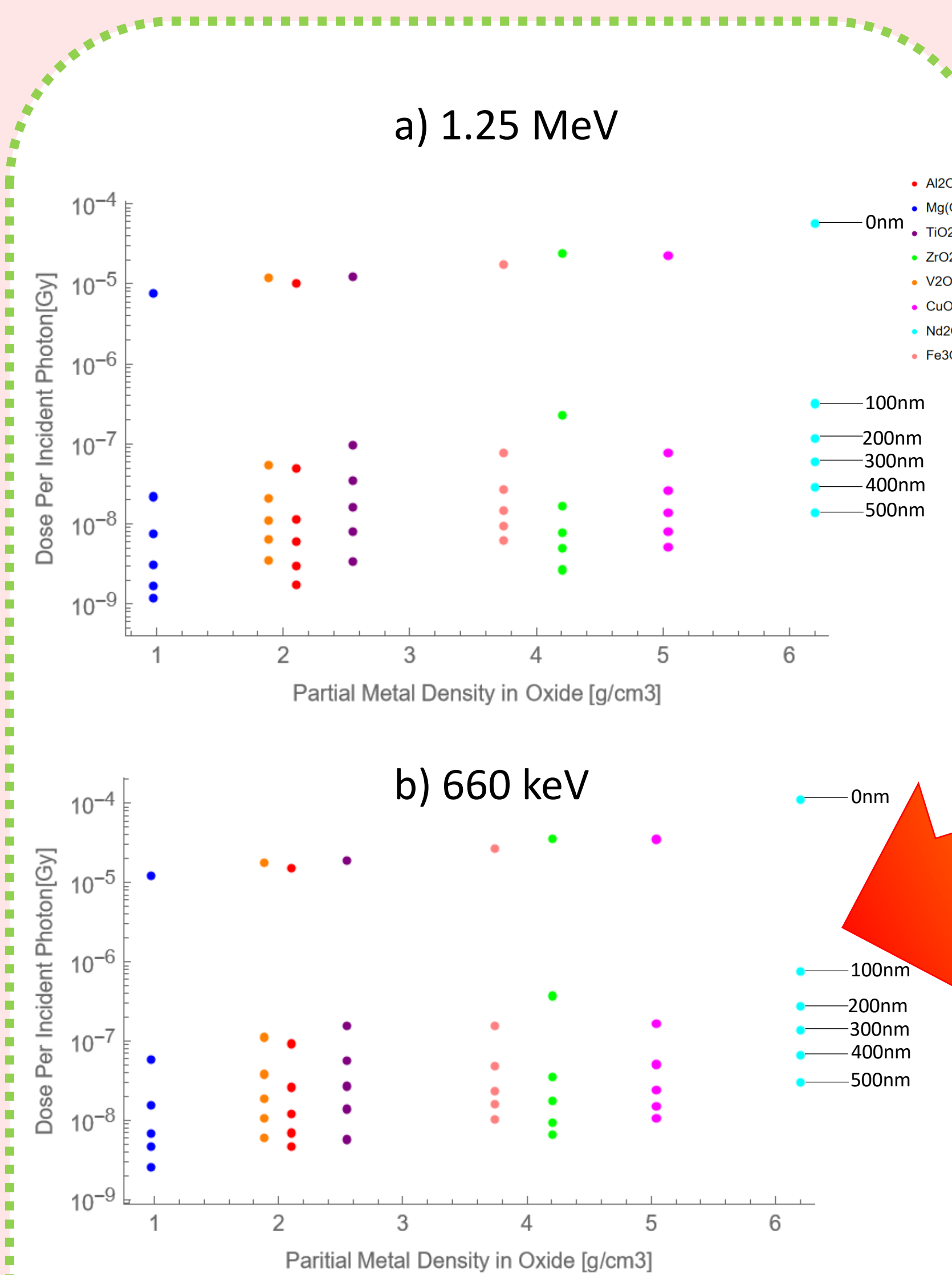


d) Exciton Generation



Dose Distributions

- RDDs (Radial Dose Distributions)
- Dose is measured in 1 nm sections from the NP surface to the edge of the water sphere



Graphs showing the dose distributions for 0 – 500 nm against the metal density of Al₂O₃, Mg(OH)₂, TiO₂, ZrO₂, V₂O₅, CuO, Nd₂O₃ and Fe₃O₄ NPs irradiated by a) 1.25 MeV and b) 660 keV photon beams

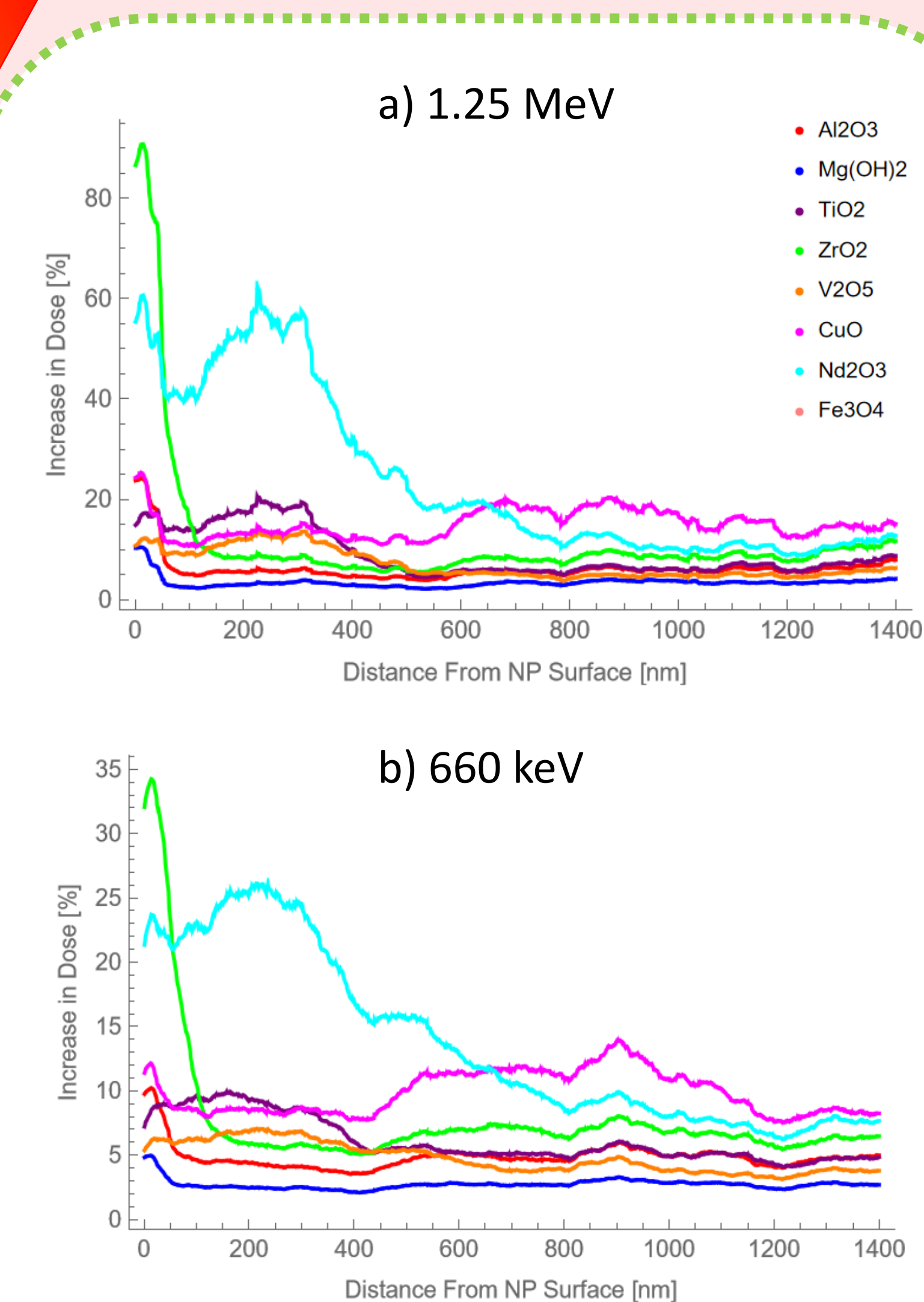
- The higher doses have been attributed to the higher fractional percentage of metal in the oxide NPs
- This results in increased frequency of successful collisions and a higher generation rate of electrons
- Nd₂O₃ is of special note: the increase in dose is due to additional electrons generated by photoelectric (Auger) effects, that are not seen in the other oxides – most likely due to the high atomic number of Nd

Conclusions

- Unique insight into the fundamental processes occurring on the nano-scale in irradiated NP aqueous systems
- A successful model has been built that allows systematic surveys of NPs to be performed
- The higher doses have been attributed to the higher fractional percentage of metal in the oxide NPs
- This results in increased frequency of successful collisions and a higher generation rate of electrons
- Very high atomic numbers also have photoelectric processes occurring which also increase dose

Process RDDs

- Specific versions of the RDDs were run where the particles escaping the NP were filtered by the generation process
- At higher energies ~100+ keV photoelectric (Auger) processes do not occur unless the atomic number is very high
- The graphs shown below are using Compton processes only and are shown as a ratio of NP dose to water alone



Graphs showing the RDDs per incident photon for Al₂O₃, Mg(OH)₂, TiO₂, ZrO₂, V₂O₅, CuO, Nd₂O₃ and Fe₃O₄ NPs : Water NP irradiated by a) 1.25 MeV and b) 660 keV photon beam

- ZrO₂ exhibits a high dose in the first 150 nm – this is believed to be due to a combination of the high atomic number and the high percentage of metal in the oxide

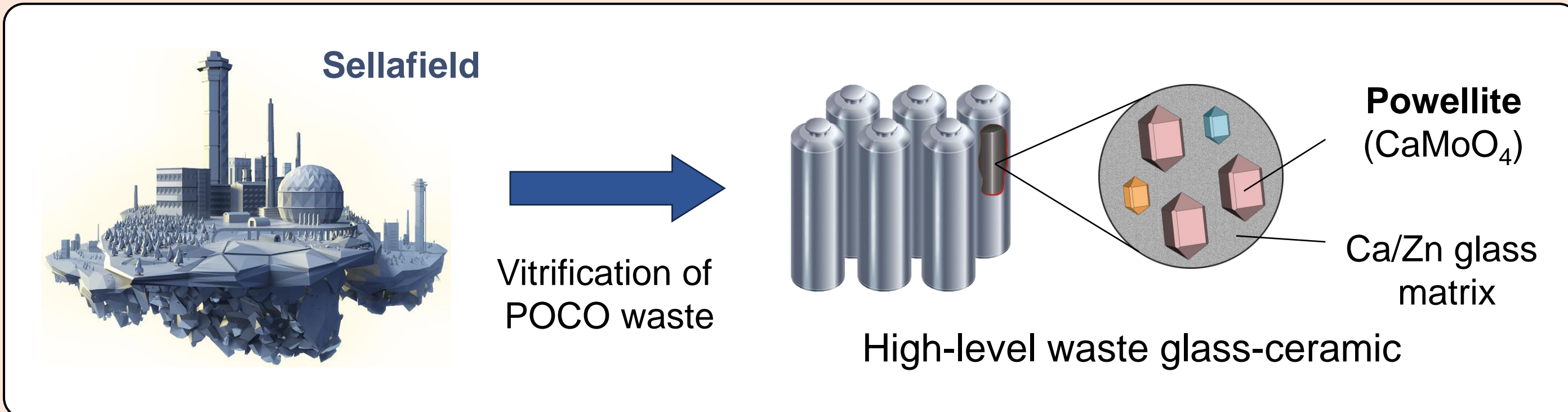
References

- S. Le Caer, *Water*, **2011**, 3, 235-253.
- A. Guerreiro et al., *Cancer Nanotech.*, **2019**, 10, 1-20.
- A. Chatterjee, J. L. Magee, *Rad. Prot. Dosimetry*, **1985**, 13, 137-140.
- J. S. Jackson et al., *Hazard. Mater.* **2014**, 94, 254-259.
- Perl et al *Med. Phys.*, **2012**, 39, 6818-6837.



1. Introduction

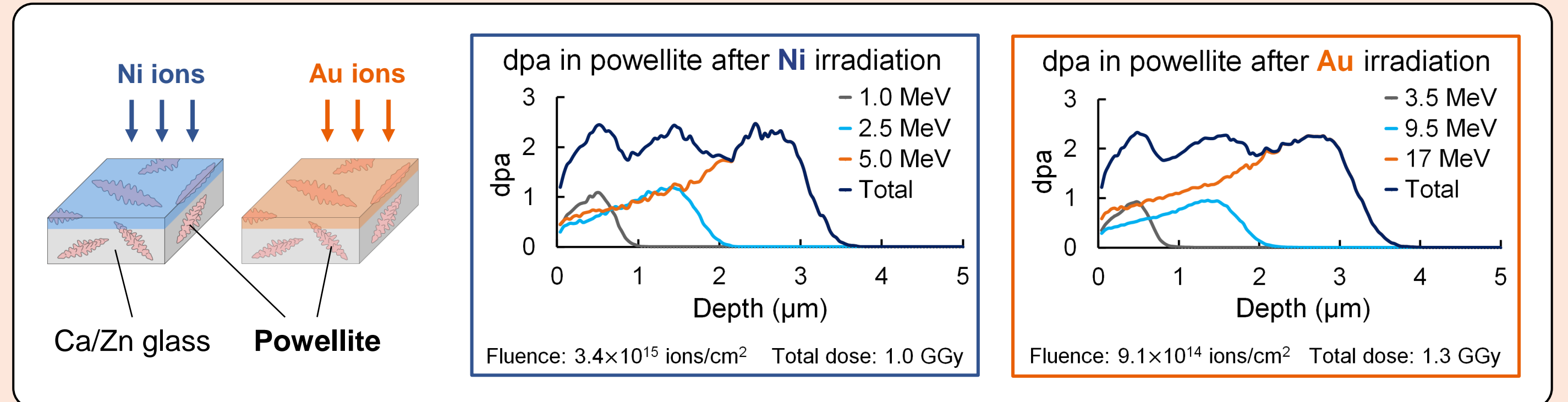
The washout of the Highly Active Storage Tanks at Sellafield during the post-operational clean out (POCO) will generate a radioactive waste stream rich in Mo-containing solids [1]. This waste will be converted into a solid and durable form for long-term disposal. The final waste form is a Ca/Zn borosilicate glass-ceramic containing powellite (CaMoO_4) crystals.



Goal of research: Characterise Mo-rich nuclear waste simulant glass-ceramics and evaluate their long-term radiation tolerance by performing heavy ion irradiation experiments.

2. Materials & Methods

- Mo-rich non-active waste simulant glass-ceramics were produced by National Nuclear Laboratory in the Vitrification Test Rig (VTR).
- Nickel and gold ion irradiation experiments were performed to induce changes similar to alpha recoil nuclei. The average total dose was ~ 2 displacements per atom (dpa), equivalent to 1.0 - 1.3 GGy dose.



- X-ray diffraction (XRD), scanning electron microscopy (SEM), electron backscatter diffraction (EBSD), and transmission electron microscopy (TEM) (with *in situ* Ar & Xe irradiation) were used for characterisation.

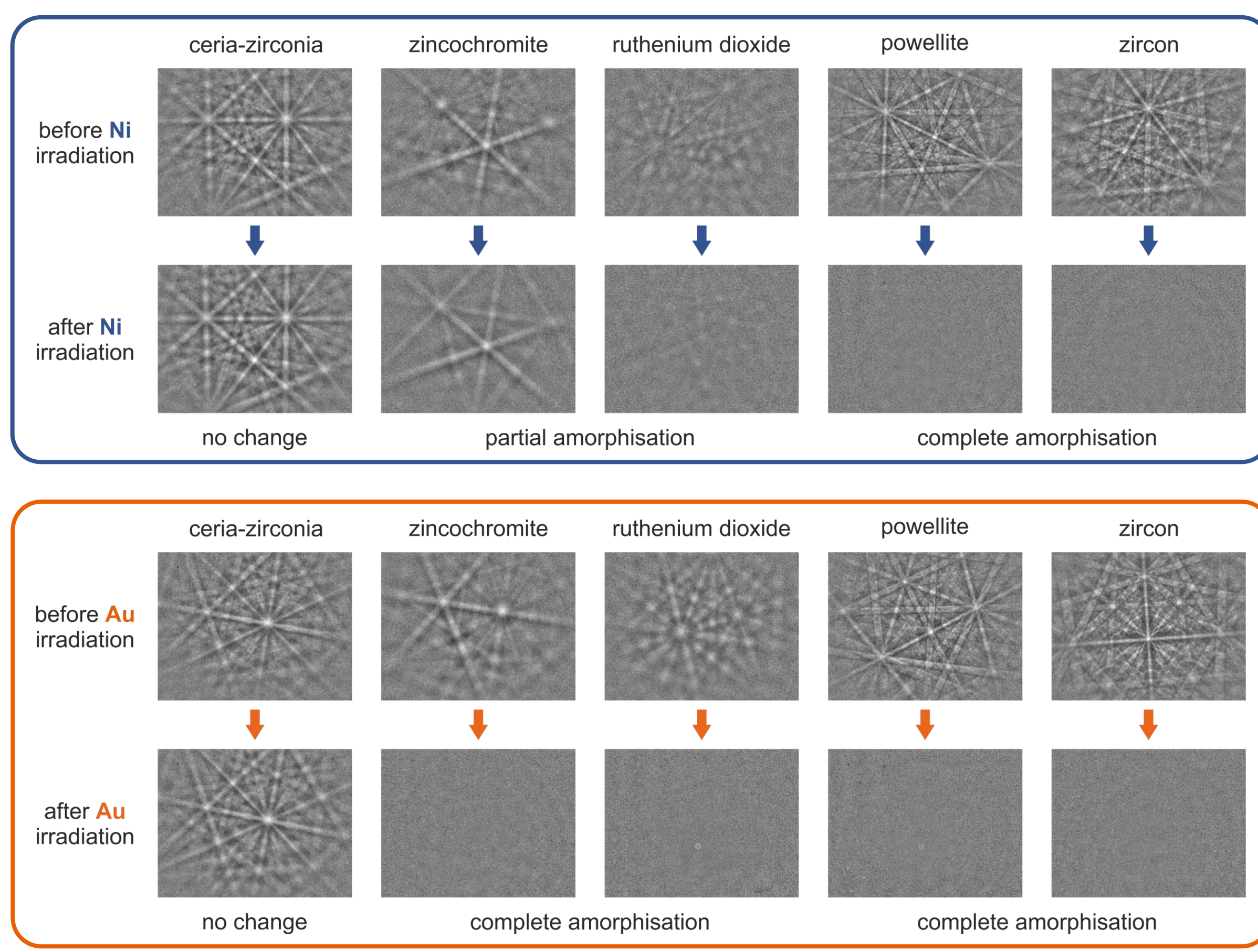
3. Radiation tolerance of glass-ceramics

The main crystal phases in the waste simulant samples were powellite, zircon, ceria-zirconia, zincochromite and ruthenium dioxide. Microcracks formed around large powellite and zircon crystals, presumably due to a thermal expansion mismatch between the glass and these phases.



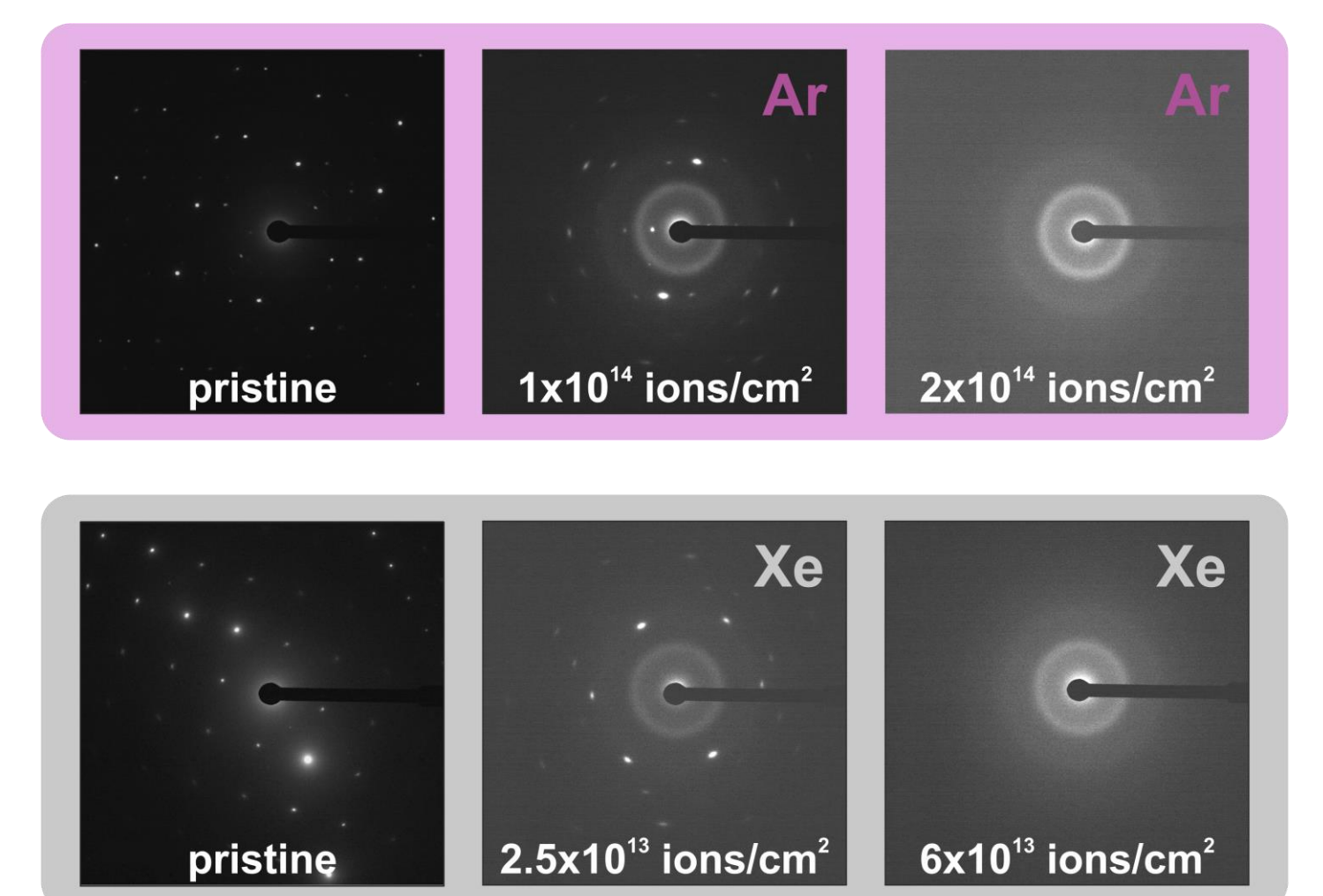
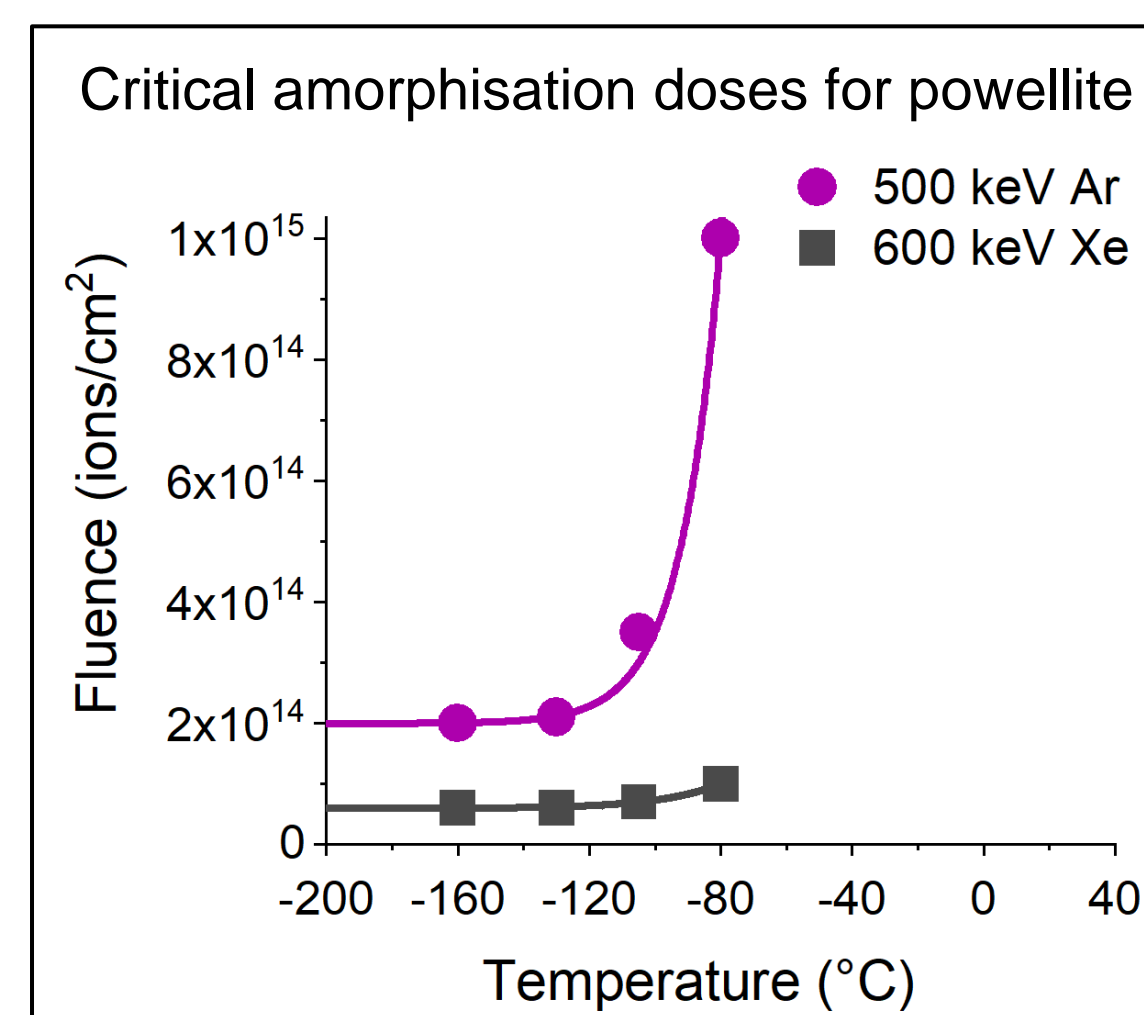
Powellite and zircon swelled considerably after Ni and Au irradiation. The radiation damage was greater in the Au irradiated sample.

EBSD analysis shows the relative radiation tolerance of phases.



4. TEM with *in situ* Ar and Xe ion irradiation on powellite

- Ar irradiation data published in the literature suggests that powellite is highly radiation-tolerant as it remains crystalline at high fluences [2].
- However, our *in situ* Ar and Xe ion irradiation experiments show that amorphisation could occur depending on the temperature and ion type.



TEM analysis above -80 °C was not possible because of the electron beam induced recrystallisation.

A diffraction pattern with bright spots represents crystalline structure, diffuse rings correspond to amorphous material.

5. Conclusions

- Ni and Au irradiation reveal insights into the relative radiation tolerance of crystals (ceria-zirconia > zincochromite \approx ruthenium dioxide > powellite \approx zircon). The amorphised crystals swelled considerably.
- Amorphisation of powellite has been observed for the first time.
- In situ* Ar and Xe ion irradiation experiments proved that powellite is much less radiation tolerant than previously thought [2] [3]. Ions with heavy mass (and with a high nuclear to electronic energy loss ratio) like recoiling radioactive actinides could cause amorphisation.
- The amorphisation of powellite in nuclear wastes might lead to a higher radionuclide leaching rate to the environment. Future research should consider performing leaching tests on amorphous powellite.

6. Acknowledgements

Special thanks to Anamul Haq Mir for the TEM measurements, Chetna Tyagi for the XRD measurements, and Györgyi Glodán for the SEM training. I am also grateful to Samir de Moraes Shubeita and the DCF ion beam accelerator team for the nickel and gold irradiation experiments.

7. References

- [1] M. T. Harrison, 2017, Vitrogeowastes, Chapter 3, pp. 33-76.
 - [2] X. Wang et al. 2014, Journal of Raman Spectroscopy, vol. 45, pp. 383-391.
 - [3] K. B. Patel et al. 2020. Phys. Chem. Chem. Phys., vol. 22, pp. 15616-15631.
- Image of Sellafield Ltd - <https://careers.sellafieldsite.co.uk>

Development of sustainable substitutes for Pulverised Fly Ash in Cement and Concrete

Andrea Kozlowski, Joanna Renshaw, Katherine Dobson

INTRODUCTION

- Cement and concrete industry produces ~10% of the global CO₂ emissions [1] → need to substitute cement clinker [2]
- Substituting cement clinker, such as Pulverised Fly Ash (PFA), also improves physico-chemical properties and performance
- Future trend of PFA in the UK include: Increased costs for climate policy decisions, decrease in security of supply, and reliance on overseas supply

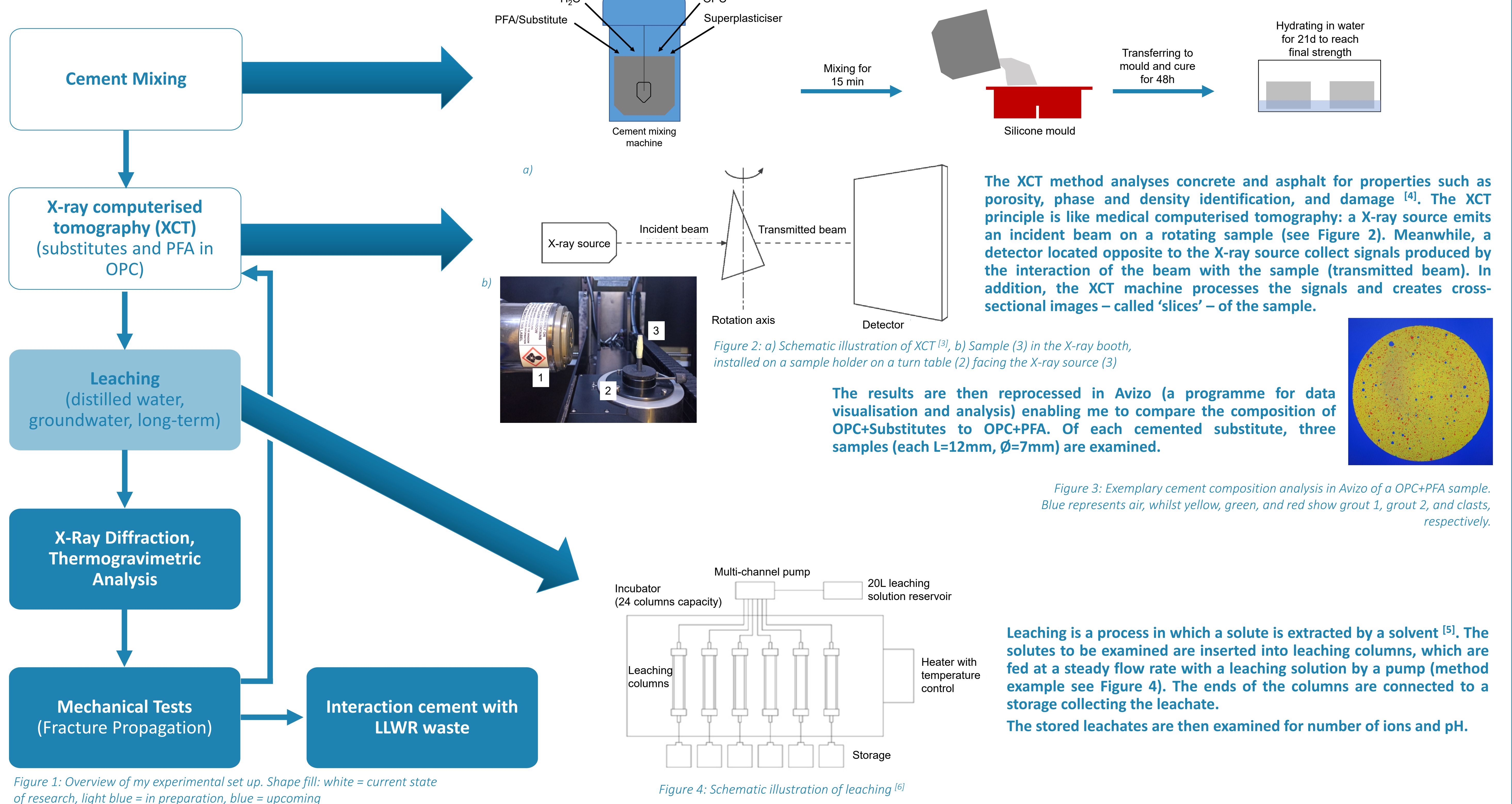
RESEARCH AIM

- Identify sustainable, cost-effective substitutes for PFA, for use in blended cements, such as Ordinary Portland Cement (OPC)
- Study alternative, sustainable materials to replace PFA
- Investigating physical, chemical and mechanical properties of the blended cements
- Assessing performance and suitability of blended cements for industrial use (Low-Level Waste Repository Ltd. (LLWR))

INVESTIGATED PFA SUBSTITUTES

- Beneficiated PFA (BPFA)
- Volcanic ash (Tra)
- Olivine (Oli, Van)
- Calcined clay/Metakaolin (Arg)
- Biomass ash

METHODOLOGY



RESULTS AND DISCUSSION

- Postprocessing of OPC+PFA and OPC+Substitute* in Avizo shows that the samples comprise air, grout**, and clasts
- Most investigated Substitutes (except Oli) show more entrapped air than PFA (range between 2.34% BPFA and 4.10% Tra, 1.05% Oli, 1.55% PFA) → It can be assumed that with a high air entrapment the strength will be lower. Mechanical tests will provide information.
- BPFA and Tra have a similar amount of clasts as PFA, 5.34%, 5.48%, and 6.57% respectively
- Oli and Van have about double the amount of clasts (14.42% and 11.39%) → I need to investigate if clasts provide specific properties to the cement.
- All Substitutes have a share of more than 84.53% in grout, Oli with 84% the lowest to BPFA with 92.32% the highest (PFA 91.88%)

* Results of the Arg samples still need to be acquired

** Darker and lighter grout can be identified; the cause of the differences still needs to be investigated

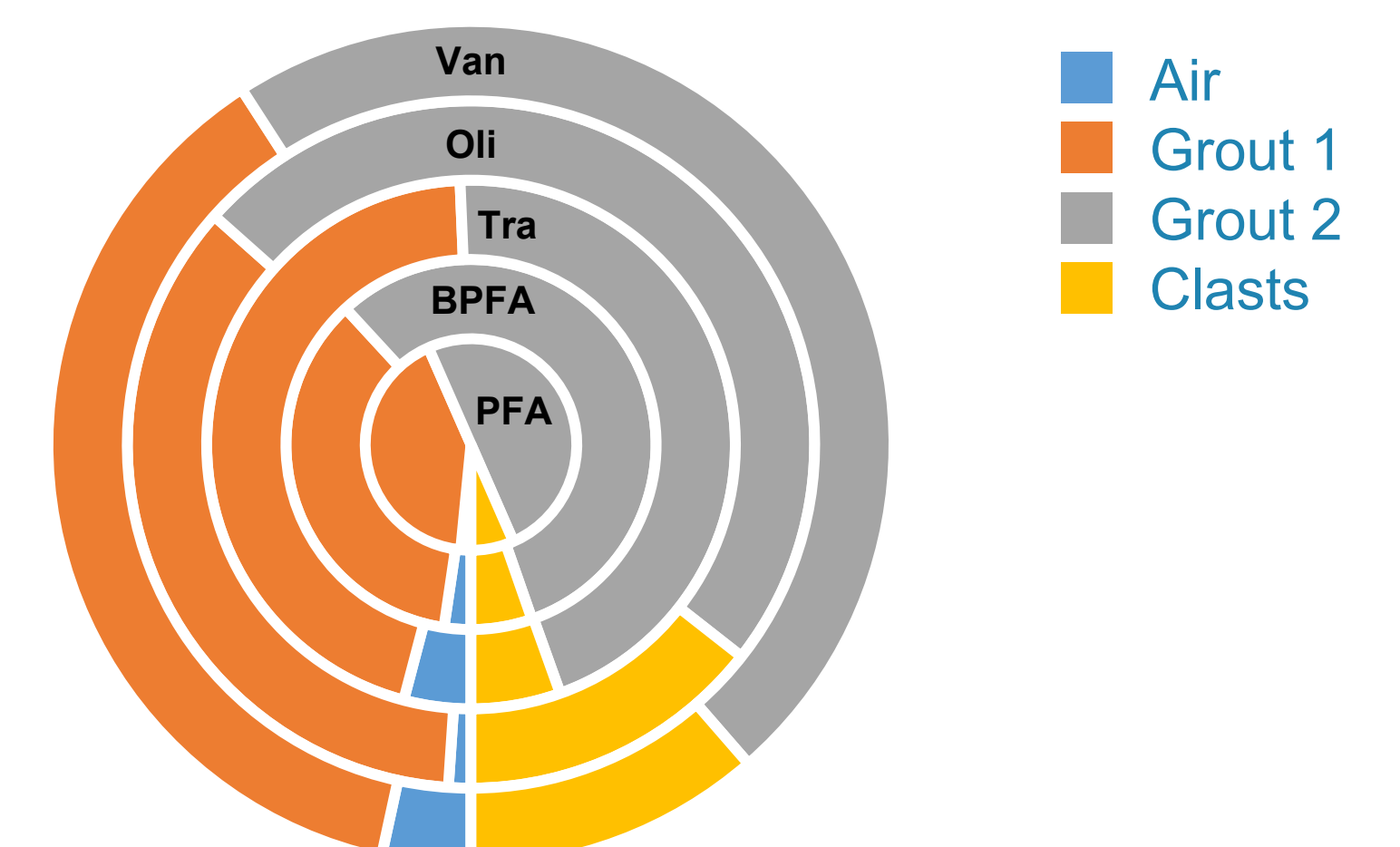


Figure 5: Overview of the cement compositions of OPC+PFA and OPC+Substitutes.

ACKNOWLEDGEMENT

Thanks to the LLWR and the Scottish Research Partnership in engineering for funding and collaboration.

SOURCES

- [1] Lehne, J., Preston, F. (2018): Making Concrete Change Innovation in Low-carbon Cement and Concrete, Chatham House for the Royal Institute of International Affairs, London, UK, ISBN 978-1-78413-272-9.
- [2] World Business Council for Sustainable Development (2002): The Cement Sustainability Initiative: Our agenda for action, Energy Environm. Sci. 7 (1), p.30-189.
- [3] Badel, P. & Maire, E. (2011): X-ray tomography analysis of the mechanical behaviour of reinforcements in composites. In: Boisse, P. (ed.) Composite Reinforcements for Optimum Performance (Second Edition). Woodhead Publishing, doi: /10.1016/B978-0-12-819005-0.00018-6.
- [4] du Plessis, A. & Boshoff, W. P. (2019): A review of X-ray computed tomography of concrete and asphalt construction materials, Con. Build. Mat. 199, p.637-651, doi: /10.1016/j.conbuildmat.2018.12.049,
- [5] Richardson, J. F. et al. (2002): Leaching. In: Chemical Engineering (Fifth Edition), Butterworth-Heinemann, doi: /10.1016/B978-0-08-049064-9.50021-7.
- [6] Lin, Q., et al. (2016): Multi-scale quantification of leaching performance using X-ray tomography. Hydrometallurgy, 164, p.265-277, doi: /10.1016/j.hydromet.2016.06.020, .

INTRODUCTION Thermal treatment has been suggested as an alternative treatment technique for Intermediate Level Waste (ILW). Thermal treatment offers advantages in increased volume reduction and reduced waste reactivity. Studies and industry trials are required to identify the most suited thermal technology and glass formulation for each ILW type. The geomelt technology as been suggested for a range of waste types including 2 waste types from the Hanford site in the USA and 2 waste types from water treatment at the Fukushima Daichi plant in Japan. Veolia Nuclear Federal Services (VNFS) carried out a series of industrial scale trials on behalf of Hanford and the Japanese government at there Rapid Horn Test Facility in the USA. The geomelt technology uses an electrical current generated between two electrodes to resistively melt the waste and glass additive to form a glass waste form. The technology can be used insitu to treat contaminated land (In-Situ) or waste and additive can be added to a suitable container (In-Can) vitrification [1].

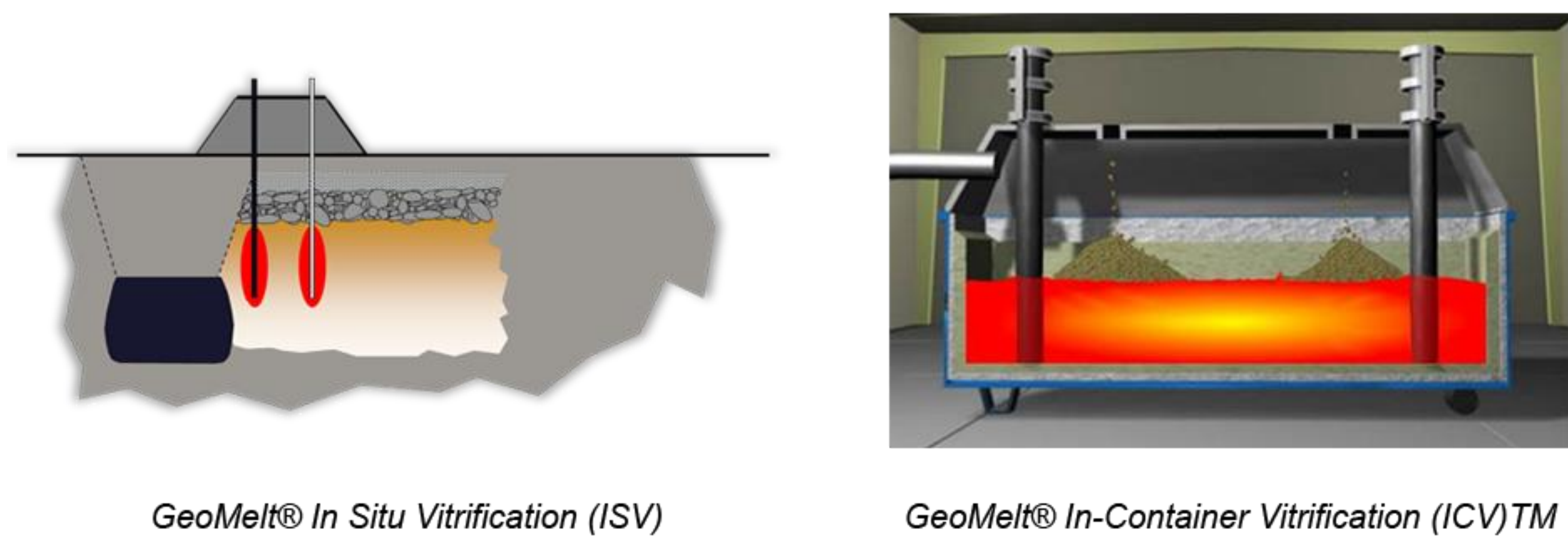


Figure 1 The concept of In Situ Vitrification (ISV) and In-Container Vitrification (ICV).

FUKUSHIMA DAICHI SAMPLES MRI4 [2] Veolia Nuclear Solutions carried out simulant vitrification test for the Japanese Government looking at vitrifying Fukushima water treatment waste. KUR-EH (zeolite-based ion exchange material), KUR-EH (Titanate absorbant) glass additives (B_2O_3 , Li_2CO_3 , ZrO_2 ...etc) and non-radioactive Cs and Sr simulants.

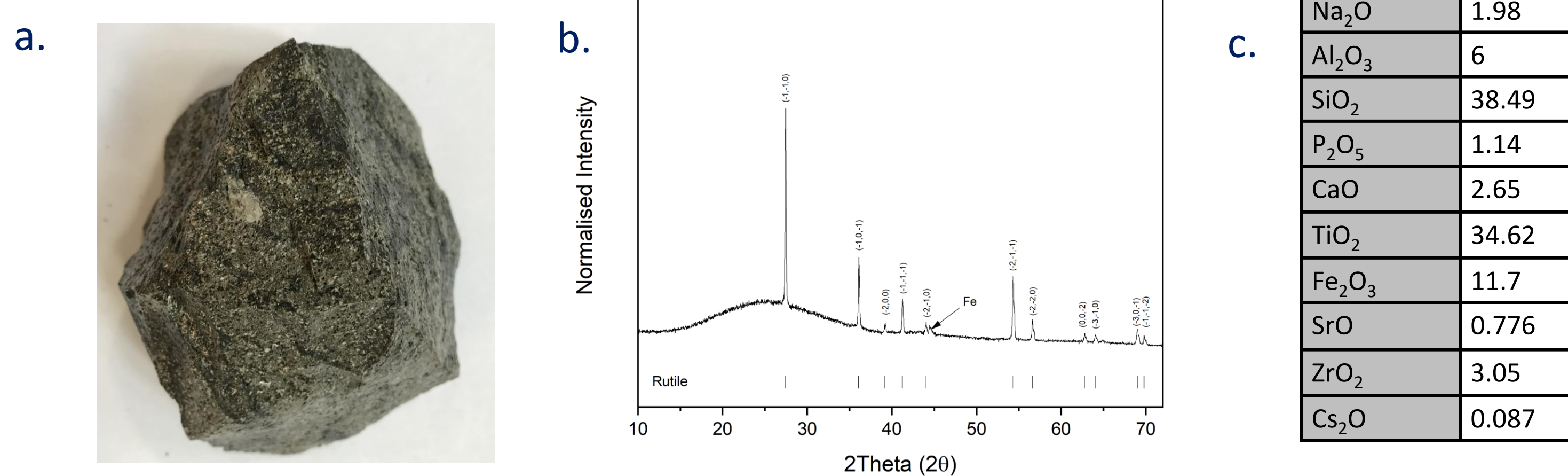


Figure 2a MRI 4 sample photo **1b** XRD graph of MRI 4 **1c** XRF composition of MRI 4 **1d** SEM photo and EDS maps of MRI 4.

MRI 7 [2] Veolia Nuclear Solutions carried out simulant vitrification test for the Japanese Government looking at vitrifying Fukushima water treatment waste. KUR-EH (zeolite-based ion exchange material), simulated barium sulfate/iron ferrocyanide (AREVA) sludge, glass additives (B_2O_3 , Li_2CO_3 , ZrO_2 ...etc) and non-radioactive Cs and Sr simulants.

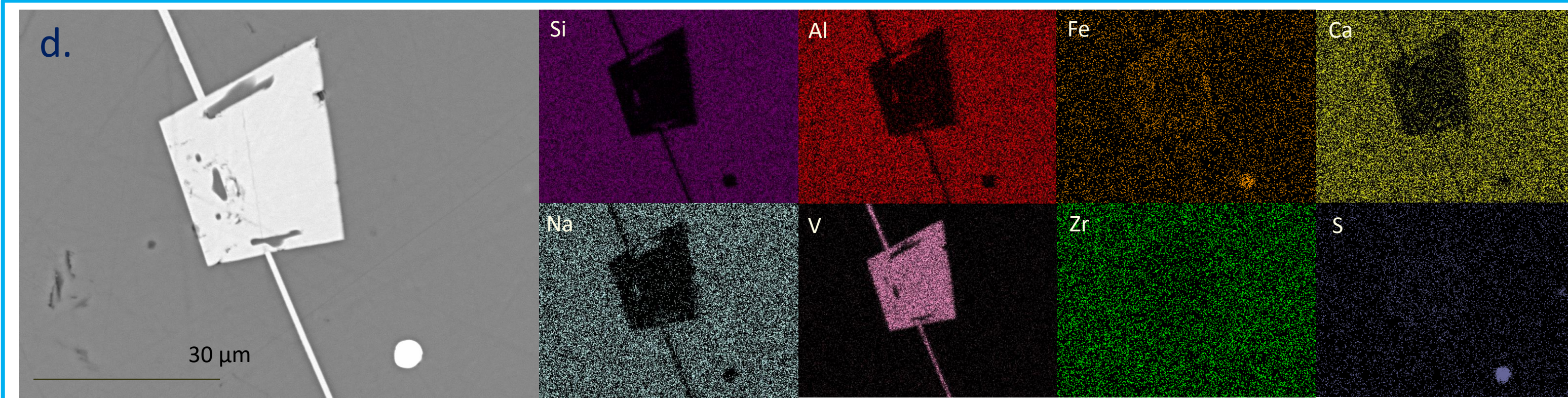
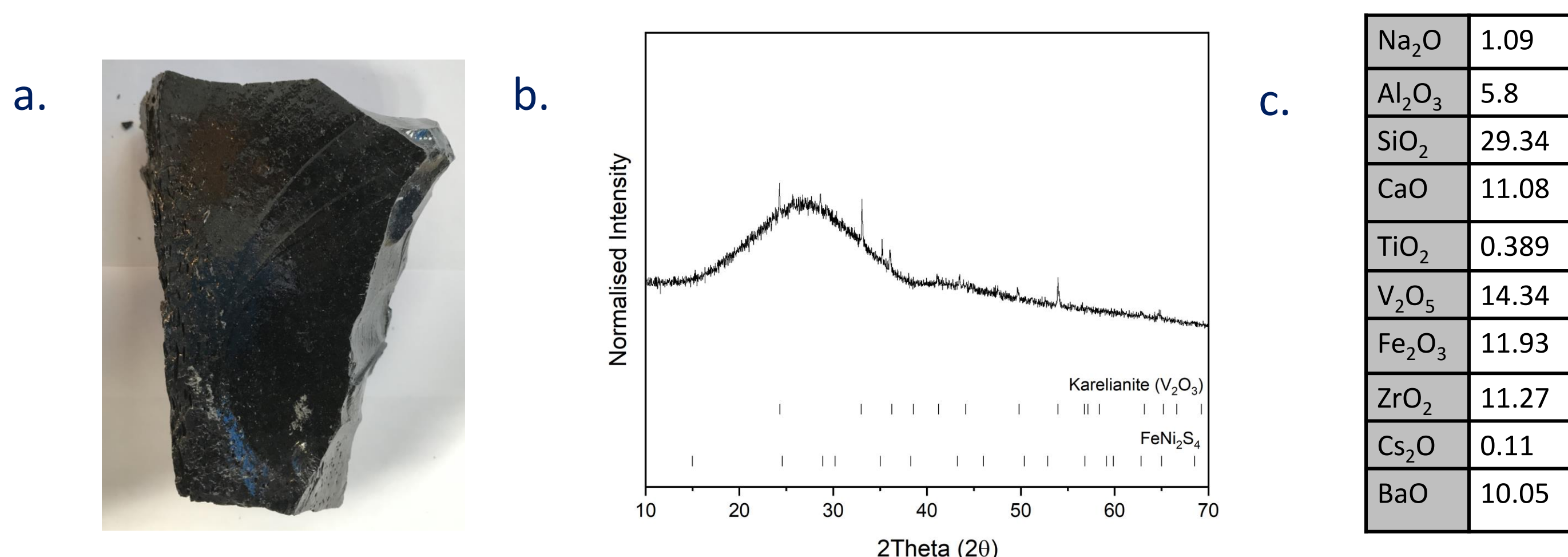


Figure 3a MRI 7 sample photo **1b** XRD graph of MRI 7 **1c** XRF composition of MRI 7 **1d** SEM photo and EDS maps of MRI 7.

HANFORD SAMPLES K Basin [3] Hanford's K west reactor. The K basin was a concrete basin used to store fuel rods. In 2019 degraded sludge was removed from the basin for interim storage. AMEC in 2003 tested ICV as a potential treatment method for this sludge. 40wt% K Basin simulant sludge, local soil and misch metal and Zr used as a simulant for U and fuel cladding were vitrified during the simulant tests.

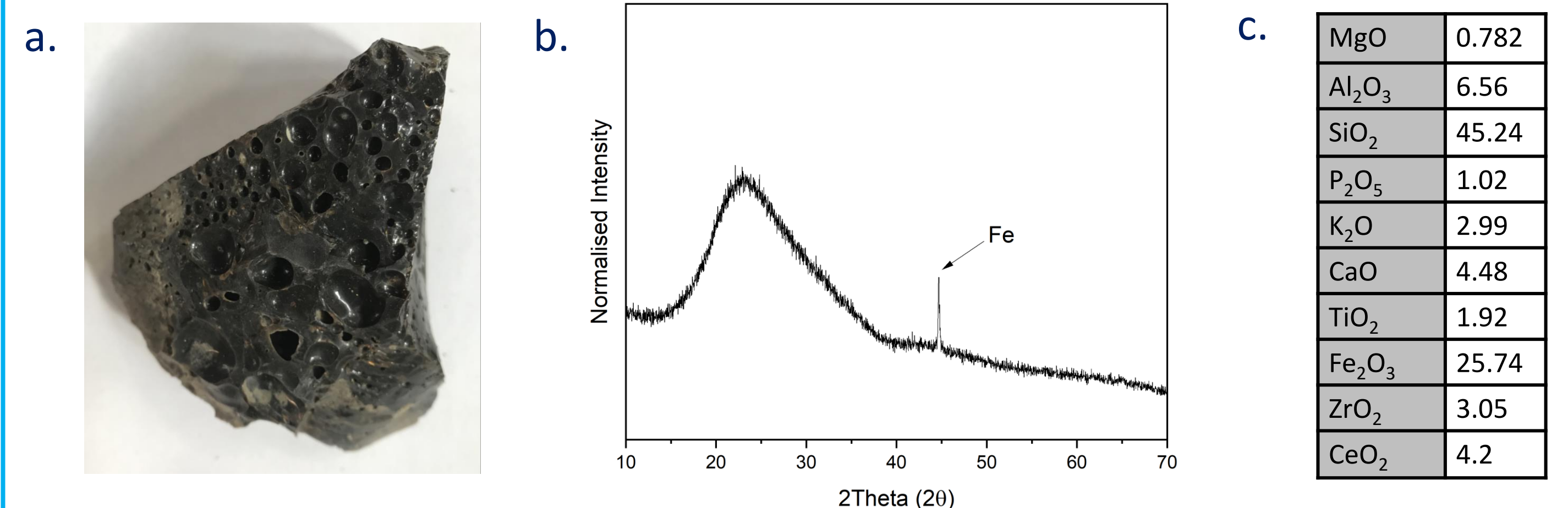


Figure 4a K Basin sample photo **1b** XRD graph of K Basin **1c** XRF composition of K Basin **1d** SEM photo and EDS maps of K Basin.

DBVS [4] The Demonstration Bulk Vitrification Project. AMEC in 2006 carried out tests looking potential to bulk vitrify Hanford Tank 241-S-109 waste (a mixed salt cake-sludge). Re (for Tc) and Cs added to the waste simulant along with local glass forming soil. Specifically the tests aimed to iteratively reduce soluble Tc in the castable refractory block (CRB).

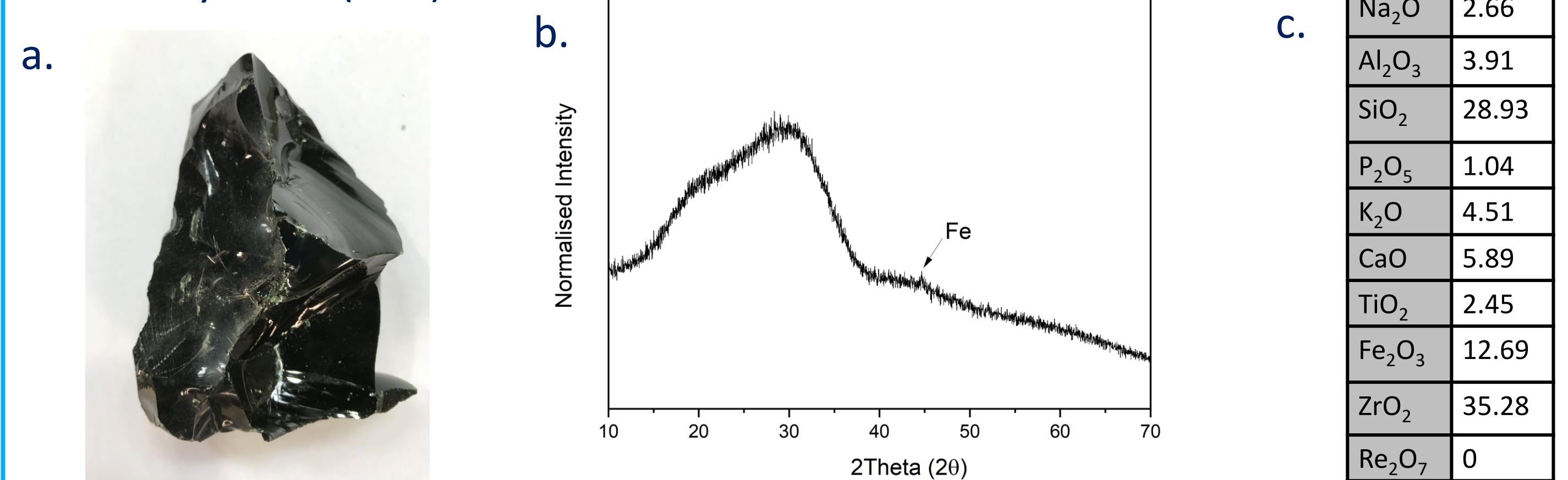


Figure 5a DBVS sample photo **1b** XRD graph of DBVS **1c** XRF composition of DBVS **1d** SEM photo and EDS maps of DBVS.

CONCLUSIONS and FUTURE WORK Characterisation has shown that the geomelt process has successfully created a series of glass/crystalline waste products. The next step is to investigate the distribution of the radionuclide surrogates and the durability of the waste forms using micro-focus XRF, PCT and MCC-1 tests.

References

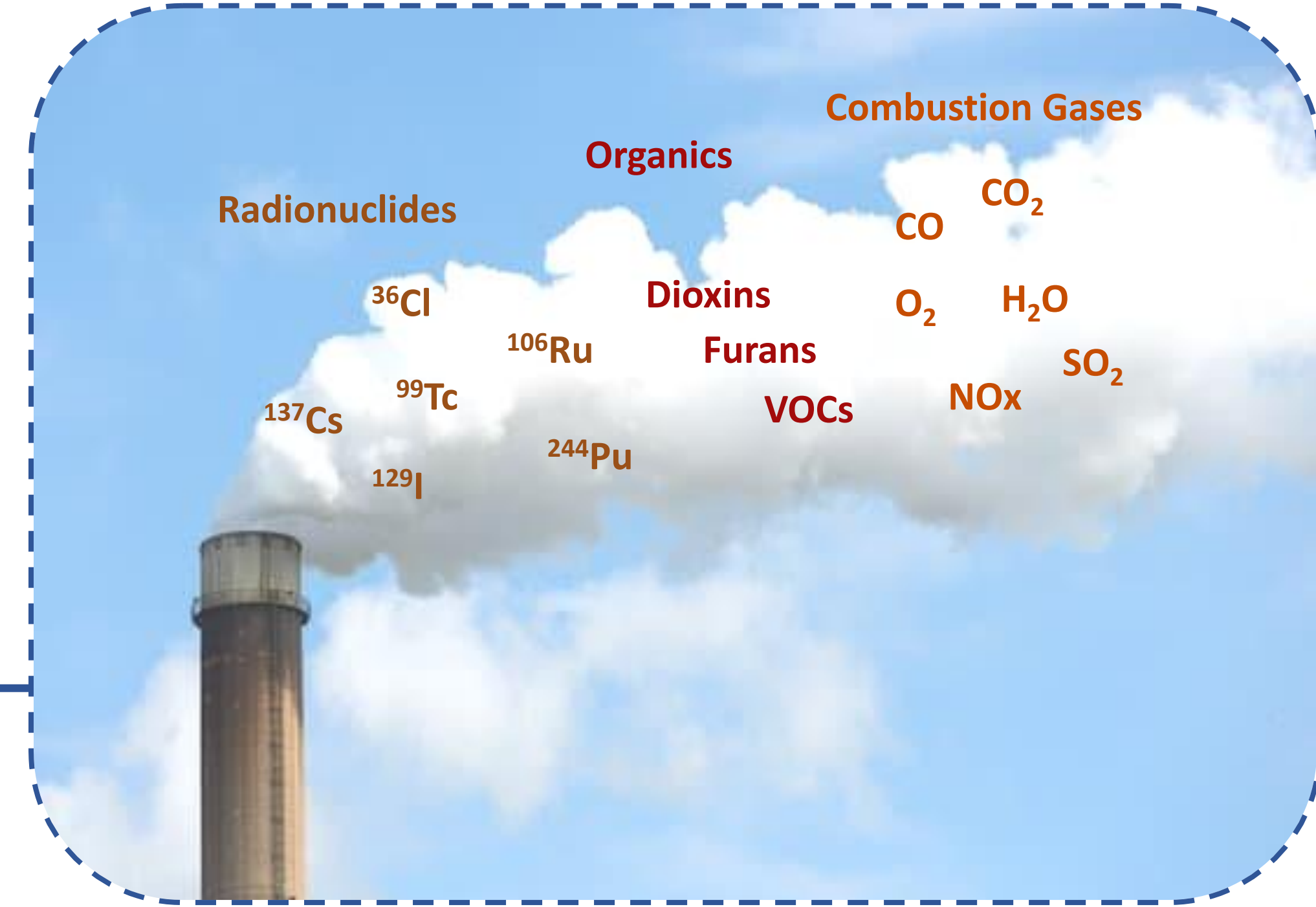
- <https://www.nuclearsolutions.veolia.com/en/our-expertise/technologies/our-geomelt-vitrification-technologies-stabilize-waste>
- Finucane et al 2021 The Development of GeoMelt In-Container Vitrification (ICV) for Fukushima Daiichi Water Treatment Secondary Wastes – 21347. WM2021
- Bagaasen.M.L et al 2008 Method to Reduce Salt Penetration into Bulk Vitrification Refractory Materials – 8275. WM 2008.
- AMEC 2003 Bulk Vitrification Treatment of K Basin Sludge Simulant Final Report.

Acknowledgements

- This research utilised the HADES/MIDAS and PLEIADES national nuclear user facilities at the University of Sheffield, established with financial support from EPSRC and BEIS, under grant numbers EP/T011424/1 and EP/V035215/1.
- This research was made possible by collaboration with Veolia Nuclear Solutions (VNSF) and by VNSF supplying industrial samples from there trials.

Aims

- Develop and demonstrate a system for real time gas analysis applicable for use in the vitrification of intermediate level waste (ILW)
- Understand, constrain and otherwise control the emissions of target pollutants from the vitrification of intermediate level waste (ILW)



The Problem

ILW is one of the largest contributors to the radioactive waste stockpile and can contain a wide range of contaminated materials from cement and steel to sludge and sand. Vitrification is being considered for the treatment of these wastes which requires heating at high temperatures normally exceeding 1000°C. A variety of emissions could arise from these materials upon heat treatment so understanding these is of importance when trying to passivate radionuclides to achieve full accountability.

Radionuclides when exposed to the environment have the potential to cause harm to biological systems and may have repercussions by contaminated crops and groundwater. Other toxic and/or harmful gases are also of concern such as active and non active halide (X) derived gases such as HX, X₂ which can result from decomposition of plastics and from the decay of radionuclides. Monitoring methods for these pollutants is currently based off filter capture methods which will only capture solid phase, can be expensive and is not in real time. Because of this there is a need to improve the current method for off-gas analysis and to understand the emissions from these systems.



Glass Technology

The goal of heat treatment is generally to form a surrogate for the waste that is chemically stable and not susceptible to leaching, reducing the volume in the process. Candidate matrixes applicable to this study are glassy non-water-soluble materials. The focus for these studies will be glass matrixes based on mixture Windscale (MW) and calcium zinc (Ca/Zn) compositions.

These were loaded with two common ILWs Sand/Clinoptilolite and Magnox sludge from 0 – 80% the most successful of which was selected for extension to the off-gas experimentation. These were melted both from batch and fritted glass but for the fritted glass particle size needed to be below 500 micron to achieve waste loading into some glasses. New glasses that required a lower unknown melting temperature were melted over a range to determine correct frit melting temperature.



	Mass Loss (%)	
	MW	CaZn
Total Mass Loss	23	25
% of Cs Loss	2.50	1.83

Oxide in Glass	Composition (wt%)	
	MW	CaZn
SiO ₂	61.74	47.6
Na ₂ O	11.05	8.6
B ₂ O ₃	21.88	23.4
Li ₂ O	5.33	4.2
Al ₂ O ₃	-	4.2
ZnO	-	6.0
CaO	-	6.0

Glass Composition	Melting Temperature (°C) (2hr hold)			
	700	800	900	950
MW 0wt% SiO ₂	x	✓	✓	✓
CaZn 0wt% SiO ₂	x	x (partially glassy)	✓	✓
MW 30wt% SiO ₂	x	x	x (partially glassy)	✓
CaZn 30wt% SiO ₂	x	x	x (partially glassy)	✓

Off-Gas Experimentation

A system to evaluate the emission properties of waste loaded glasses has been developed and is in its final trial stages producing results for both caesium and total chlorides. The diagram to the left shows the basic setup with gas condensation occurring in the impinger solutions with the gas being drawn through by pump. Calculating the uncertainty has been a priority beginning with water evaporation experiments to complete total mass capture which has resulted in an average of 93% mass capture indicating a low leak rate. Using this system, we have found that MW and CaZn have similar mass losses despite variations in composition however with respect to caesium loss there is more volatilisation in the MW glass. This is most likely due to the zinc content in CaZn glass inhibiting caesium loss from the melt. Given this CaZn has been selected as the glass host for all following trials including waste loading (below) and additives.

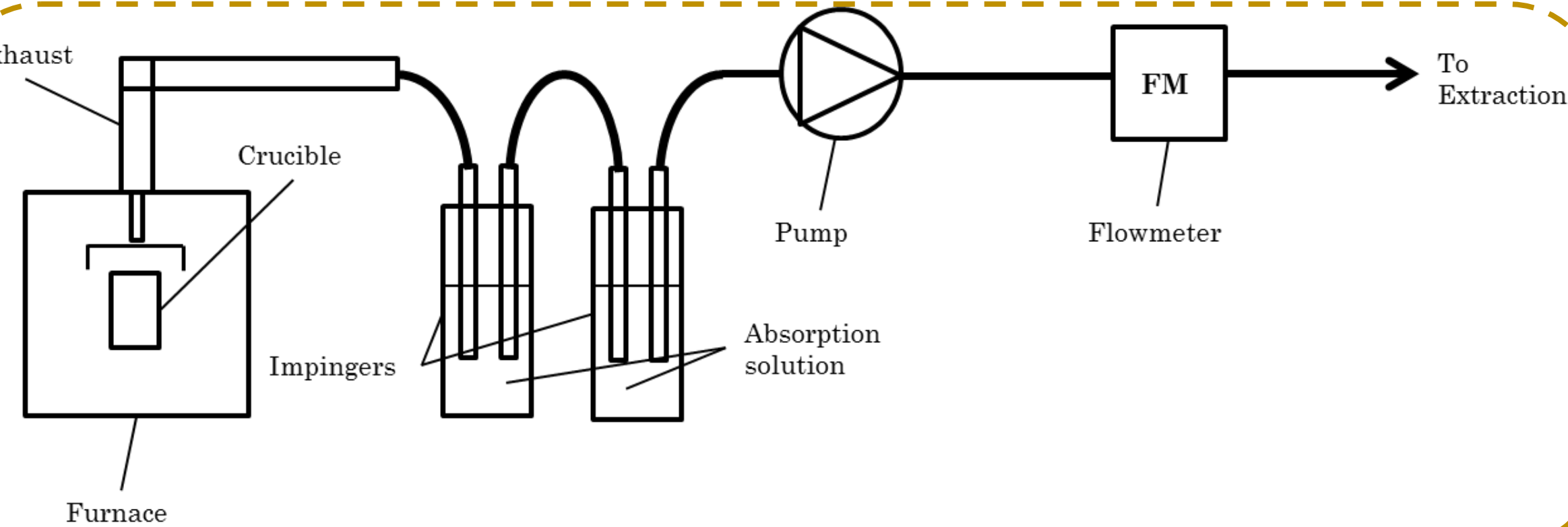


We have recently had a proposal accepted by NNUF to work at the EXACT Southampton facility which has access to a pyrolyser unit. Using this we can conduct active and inactive trials on iodine, caesium and chlorine to determine volatilisation in an even more realistic environment.



	wt%	Dopant wt%	¹³⁷ Cs	^{137m} Cs
Base Glass (With Dopants)	1	1	2	5
Clinoptilolite 10-50wt%	1	1	2	5
Corroded Magnox sludge 10-50wt%	1	1	2	5
Xanthan Gum Additive	2	2	4	5
Graphite Additive	2	2	4	5
Reduced Boron Frit	3	3	4	5

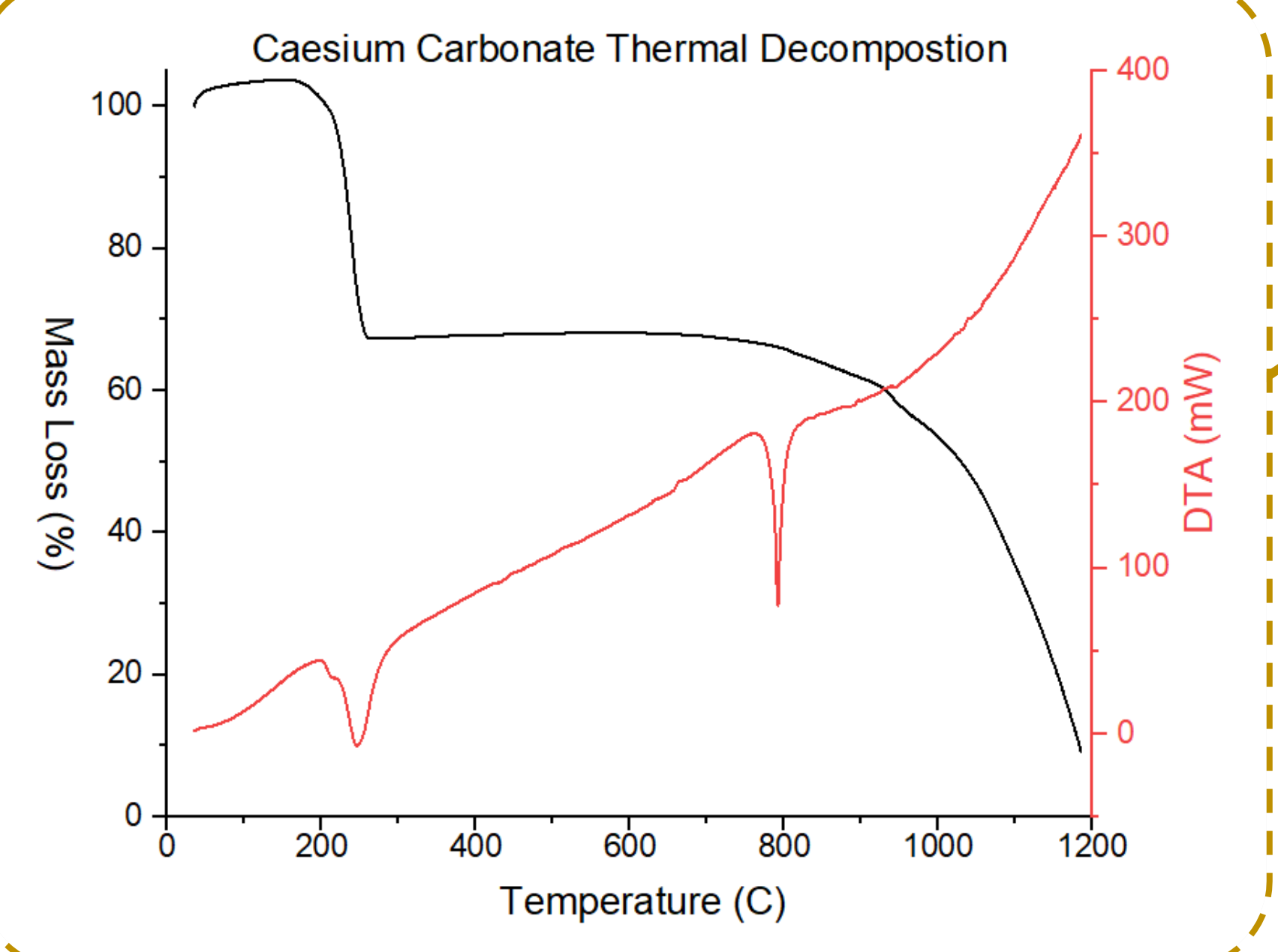
Experimental plan with priority order for work commencing in Southampton



The Future

Experiments are being focused on using waste loaded glasses coped with halides and/or caesium to see the effect of certain ILWs on the emission properties. In addition, additives and compositions will be implemented to try to control the chemistry of the melt environment to reduce emissions from the waste melts. The system should also be developed to accept a wider range of analytes and monitor the effect of any alteration on those.

Real time analysis can be implemented by use of a Raman gas spectrometer which has shown promise in previous studies for the compounds of interest in this project, FTIR is also a promising technique. Future work will include adding graphite, xanthan gum, ZnO and other additives and glass formulations to reduce emissivity. In addition, extra work will be conducted on active reagents at the EXACT facility in Southampton.



References:

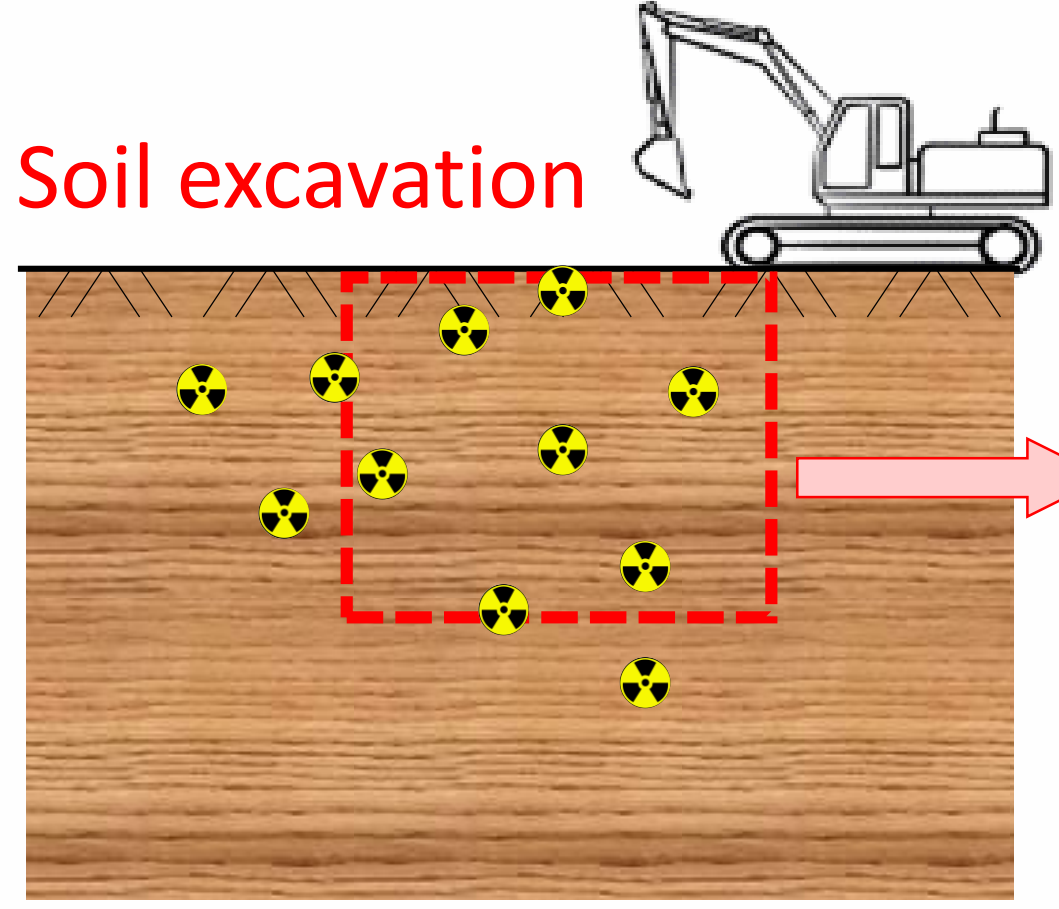
- Langowski, M. H., Darab, J. G., & Smith, P. A. (1996). Air quality - Stationary source emissions - Determination of the total emission of As, Cd, Cr, Co, Cu, Mn, Ni, Pb, Sb, Tl and V. SFS-EN 14385. (Vol. 3). Vol. 3.
- Shelby, J. (2005). *Introduction to glass science and technology* (2nd ed.). Cambridge: Royal Society of Chemistry.
- Nuclear Decommissioning Authority (2019). Annual Report and Accounts 2018/19. In: of Commons. Cumbria: House of Commons, p.15.

Ex-situ vitrification of radioactively contaminated soils

Vitrification of hazardous soils is a thermal treatment that converts contaminated soil masses into glassy and/or crystalline solid matrices. The final product is chemically inert, leaching resistant and durable.

The main advantages of soil vitrification include:

- o Excellent stability and durability of the wasteform
- o Significant volume reduction (up to 96% compared to other stabilisation strategies)
- o Savings from storage costs, resulting from long-term durability and volume reduction of the wasteform

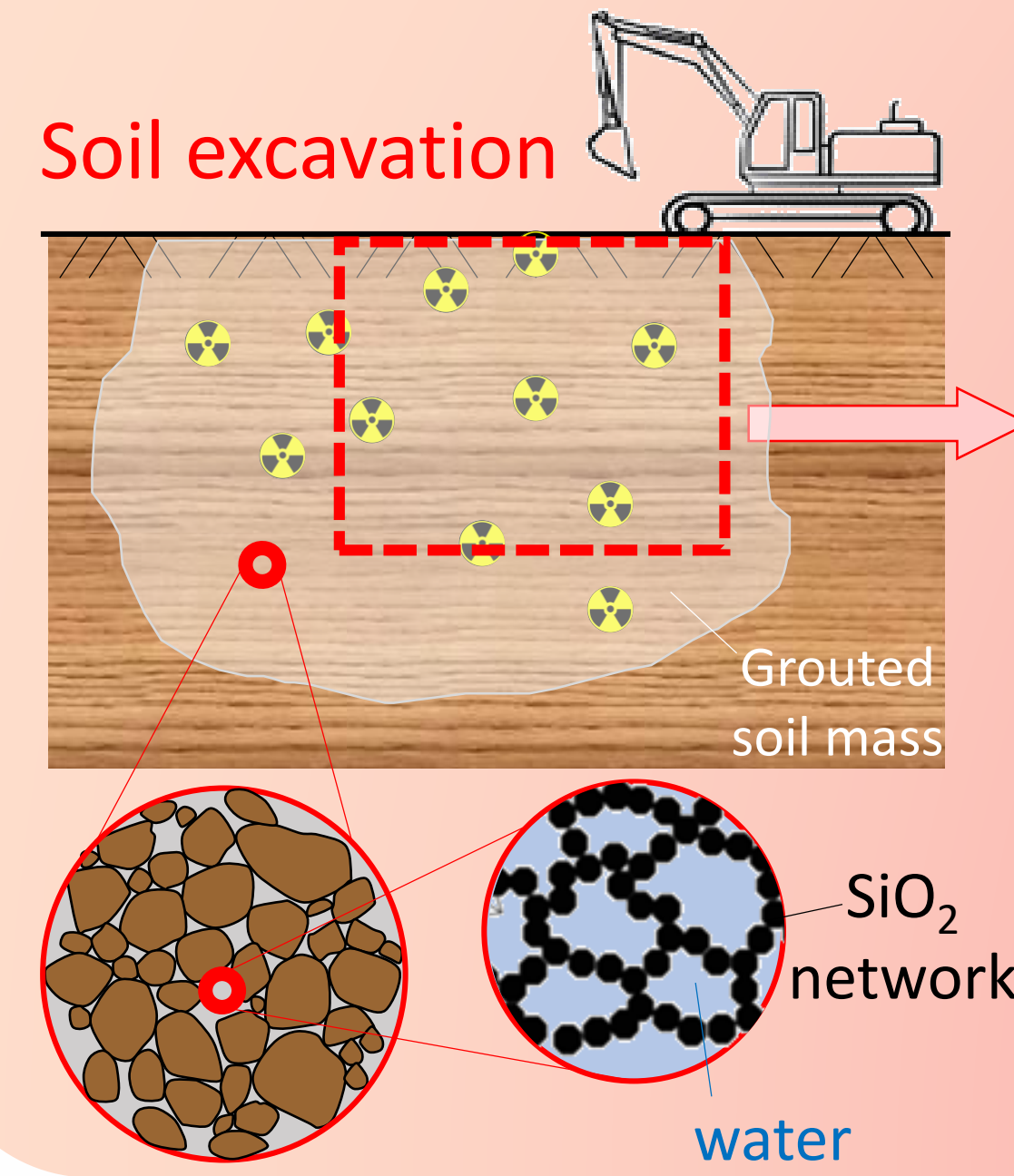


To melting chamber (furnace, in-can system, etc)

Ex-situ vitrification of radioactively contaminated soils requires the excavation and transport of contaminated soil masses to a melting system. These operations may pose serious risks to the population and the environment, in terms of radiation exposure from fugitive hazardous gases and dust emissions.

COLLOIDAL SILICA GROUT TREATMENT:

Colloidal silica is an aqueous suspension of silica nano-particles (SiO_2). The creation of siloxane bonds (Si-O-Si), triggered by the addition of an electrolyte accelerator, leads to the formation of a network of silica nanoparticles in the form of a hydrogel.

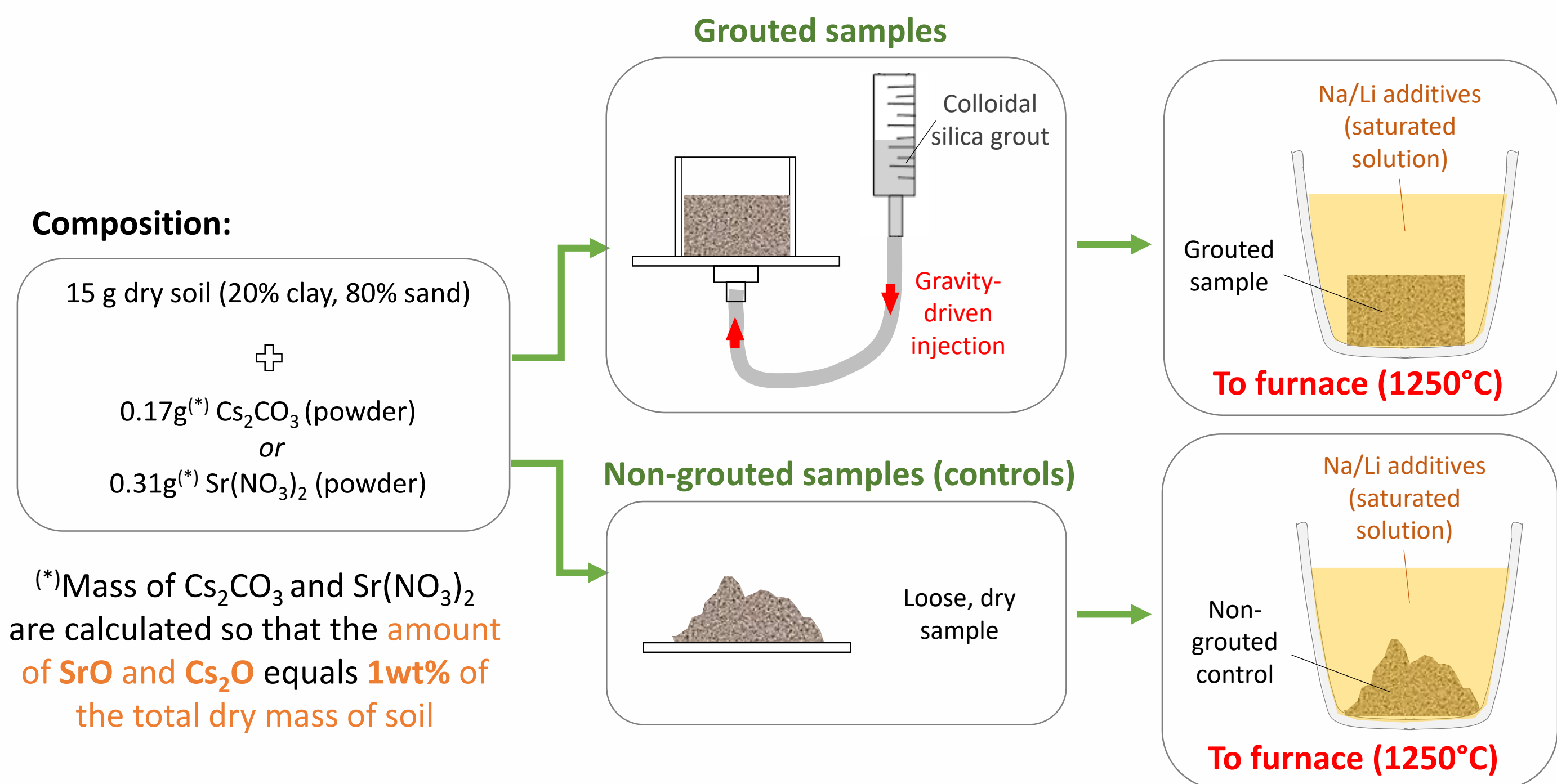


Colloidal silica grouting of contaminated soils prior to ex-situ vitrification would reduce radiation exposure by:

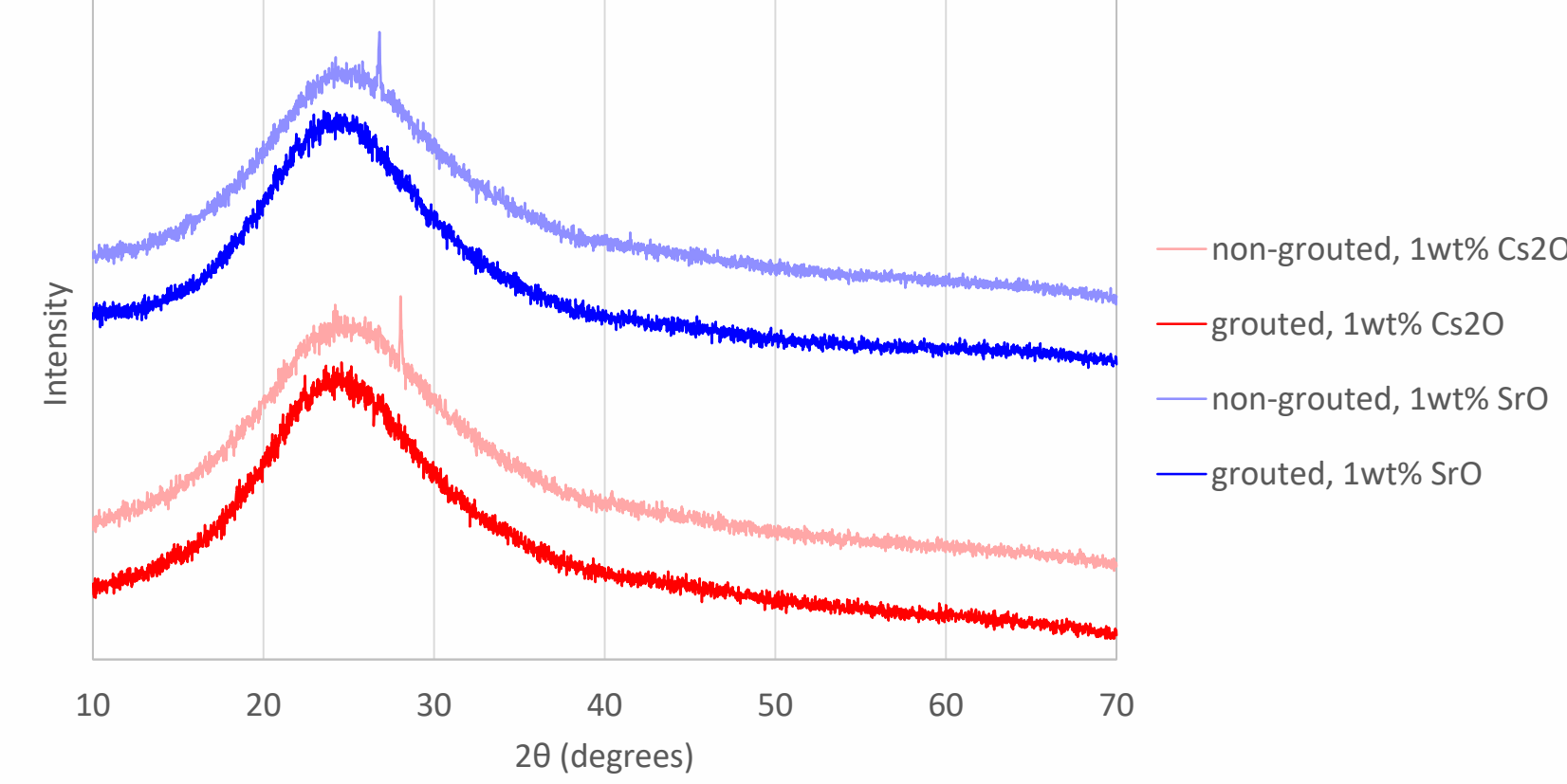
- o Reducing/inhibiting the creation of particulates upon soil excavation and transport
- o Potentially increasing the retention of contaminants (e.g. radionuclides) upon glass formation

In-container vitrification of Sr- and Cs-contaminated soils at different concentrations

1. High Sr/Cs concentration (added dry)



XRD patterns of crushed-up and sieved glasses:

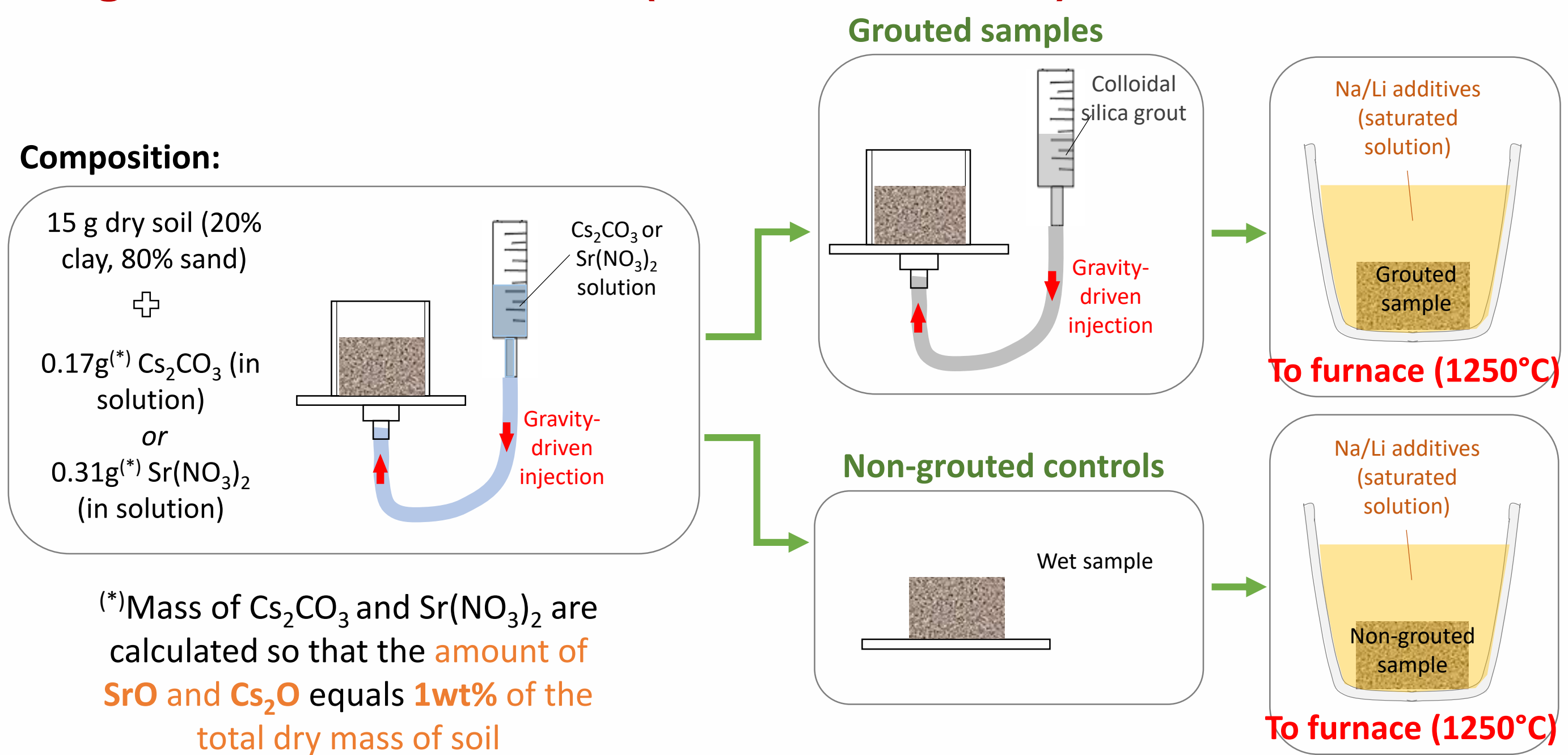


Dry clay/sand was mixed with either Cs_2CO_3 or $\text{Sr}(\text{NO}_3)_2$ powder at high concentrations (1wt% Cs_2O or SrO of the dry soil mass). Upon melting:

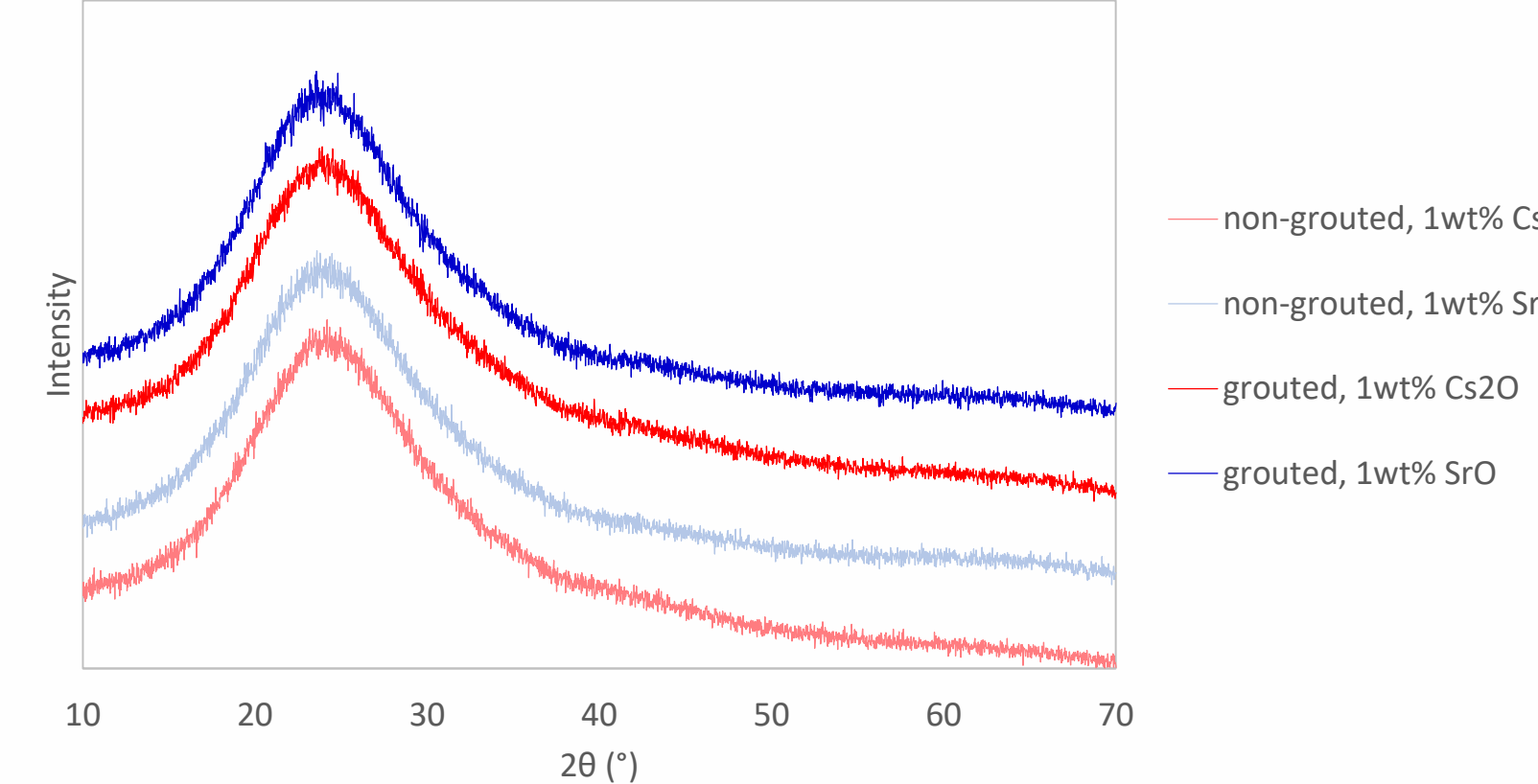
- o Cs-contaminated samples exhibited a higher radionuclide retention when grouted with colloidal silica, compared to non-grouted controls
- o Sr-contaminated samples exhibited similar radionuclide retention when grouted with colloidal silica, compared to non-grouted controls

Radionuclide retention rates (from XRF analyses):

2. High Sr/Cs concentration (added in solution)



XRD patterns of crushed-up and sieved glasses:

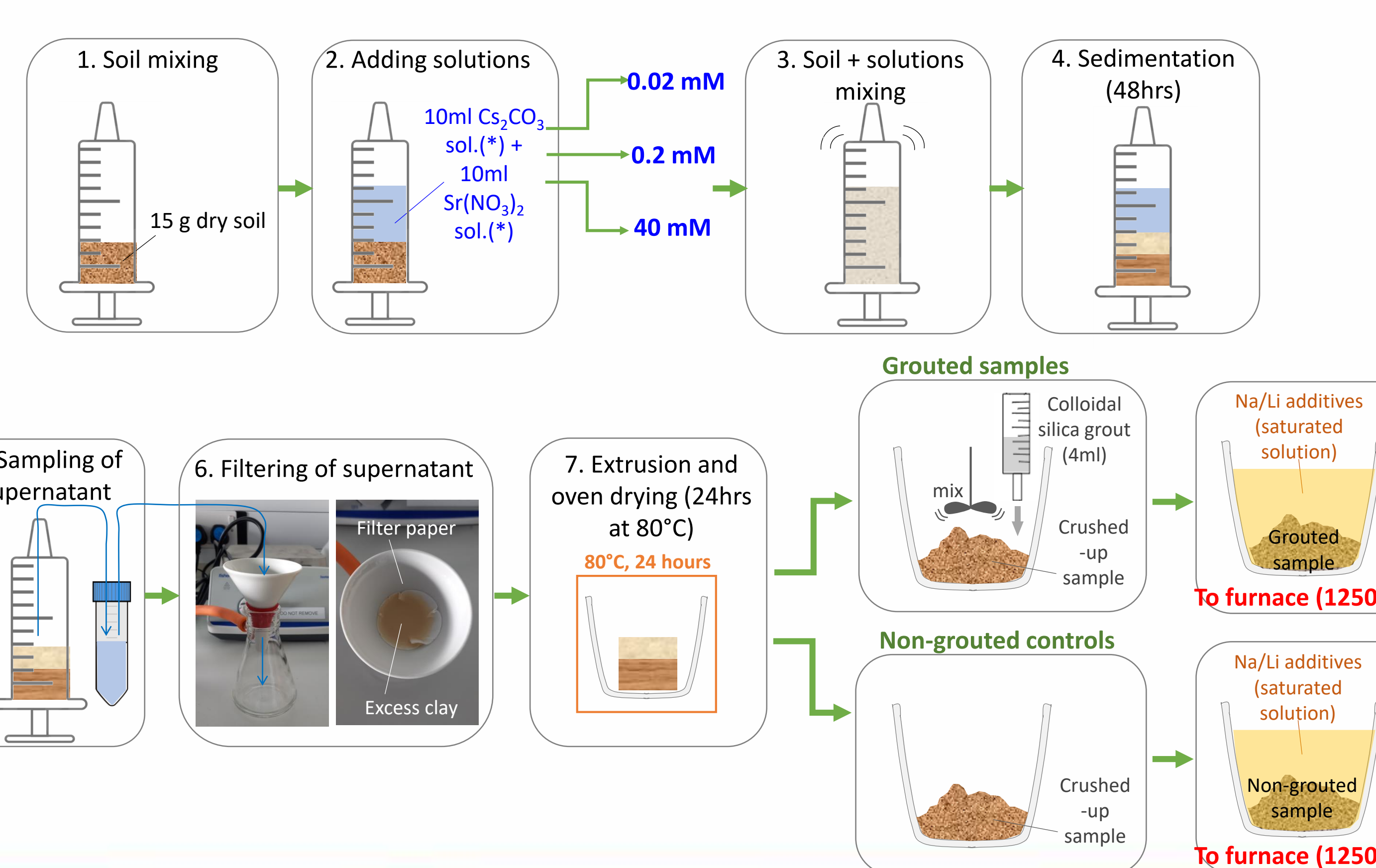


Dry clay/sand was mixed with either Cs_2CO_3 or $\text{Sr}(\text{NO}_3)_2$ in solution at high concentrations (1wt% Cs_2O or SrO of the dry soil mass). Upon melting:

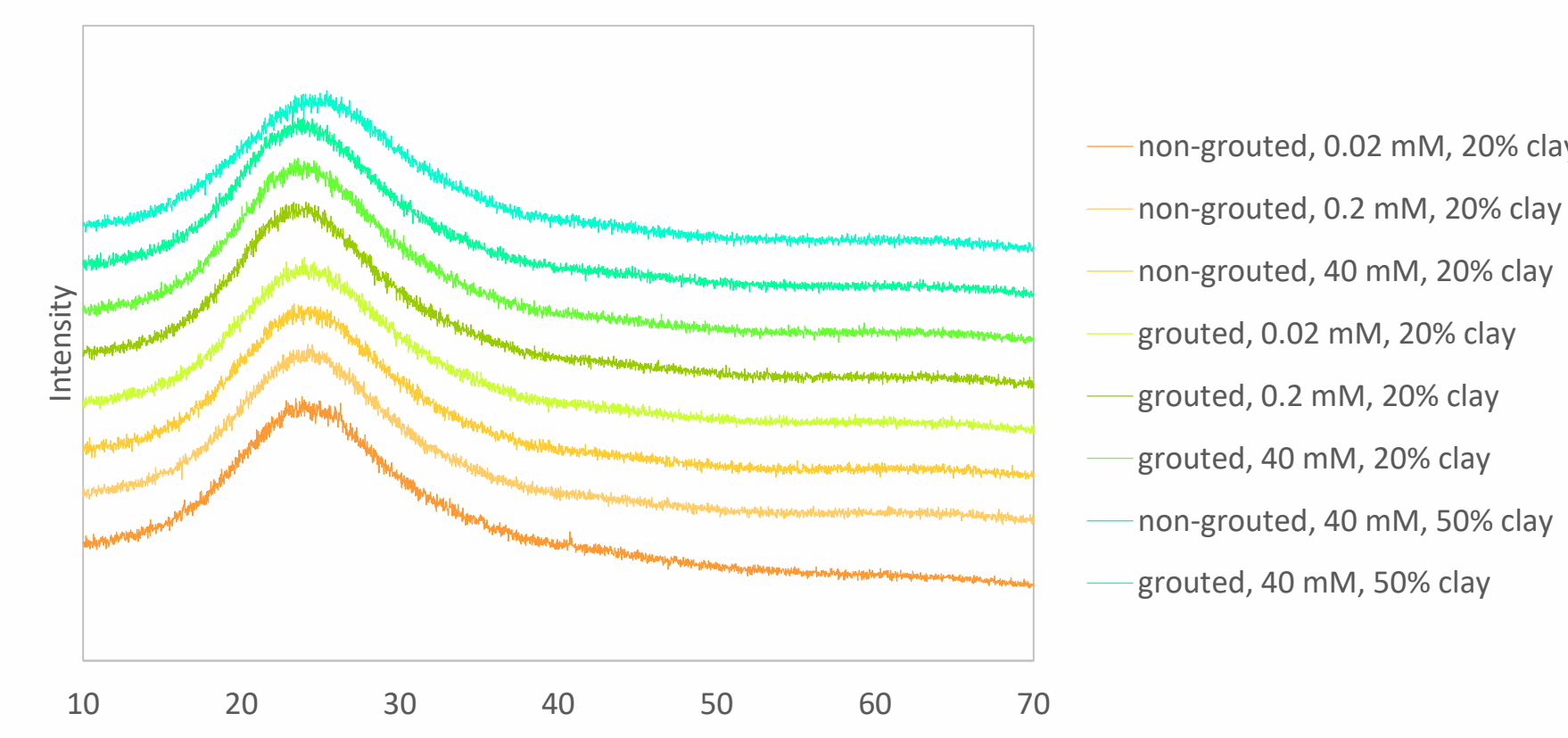
- o Cs-contaminated samples exhibited a higher radionuclide retention when grouted with colloidal silica, compared to non-grouted controls
- o Sr-contaminated samples exhibited lower radionuclide retention when grouted with colloidal silica, compared to non-grouted controls

Radionuclide retention rates (from XRF analyses):

3. Low Sr/Cs concentration (adsorption experiments)



XRD patterns of crushed-up and sieved glasses:

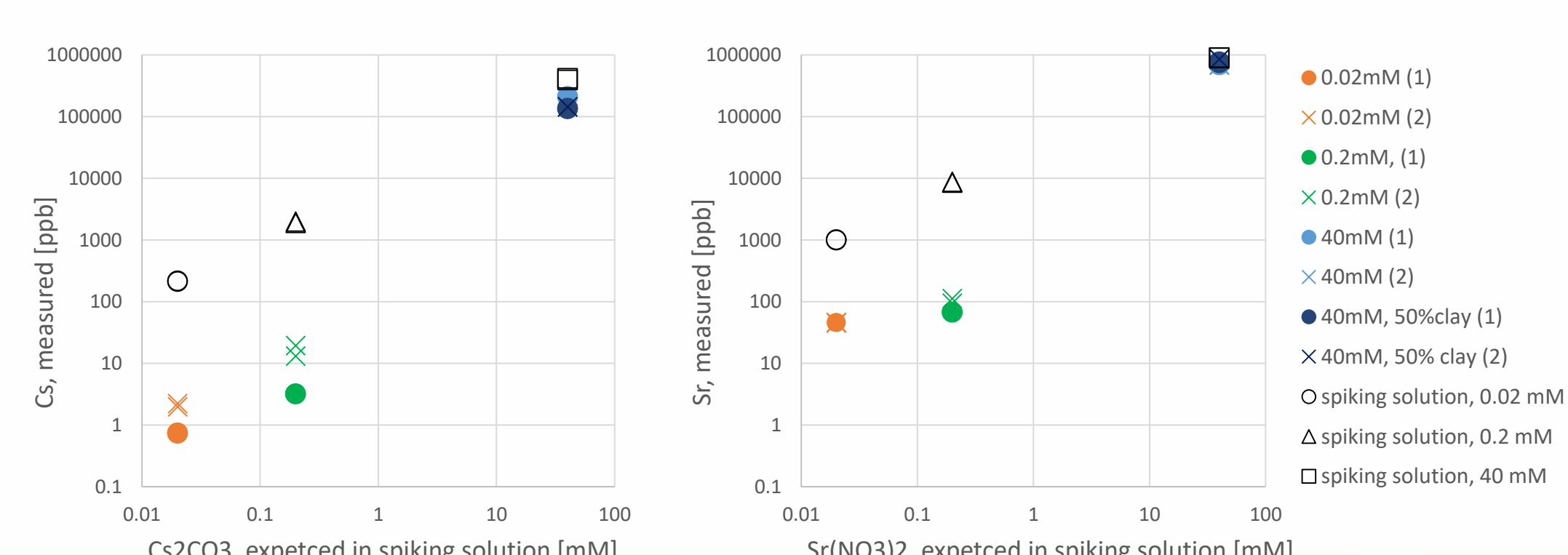


- o Clay/sand soil mixtures were spiked with Cs and Sr by performing adsorption experiments, using either Cs_2CO_3 or $\text{Sr}(\text{NO}_3)_2$ solutions at low concentrations (0.02 mM, 0.2 mM, 40 mM)

- o ICP-MS analyses were carried out to determine Cs and Sr uptake prior to melting

- o ICP-MS analyses of crushed-up and sieved glasses are currently being carried out to determine Cs and Sr retention rates upon melting (**work in progress!!**)

Cs and Sr uptake: ICP-MS analyses of supernatant





What is Electrokinetic Remediation (EKR)?

- Clean-up of the UK's nuclear legacy is estimated at ~ £200 billion over 100 years
- There is an urgent need to reduce decommissioning costs - could new approaches to remediation help?
- Technique must work in soils, sands, concretes, cements, groundwater, etc., AND be site-scalable, cheap, energy efficient and sustainable

EKR involves decontamination by electrocution, concentrating pollutants within cell or electrodes. It is an adaptable and low-energy waste minimisation technique

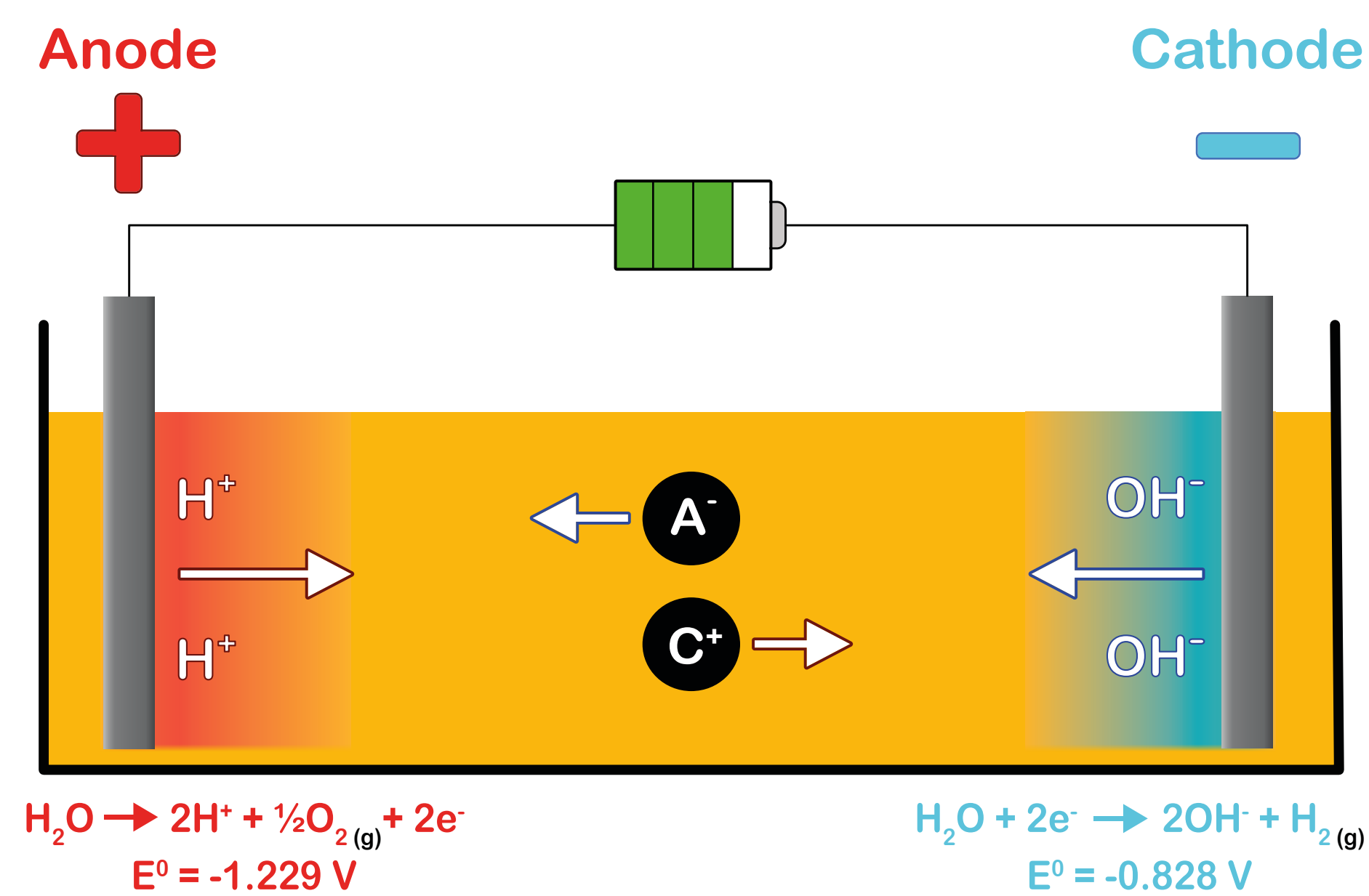


Figure 1: A typical electrokinetic cell. C⁺ are cations and A⁻ are anions

Groundwaters - Ongoing Work

- Investigation into the application of electrokinetics for 54 hour remediation of stable Sr, I and Re (as an analogue for Tc) in groundwater
- Sellafield groundwater simulant as well as real sediment obtained from close to the Sellafield site was used to maximise the trial's real-world validity

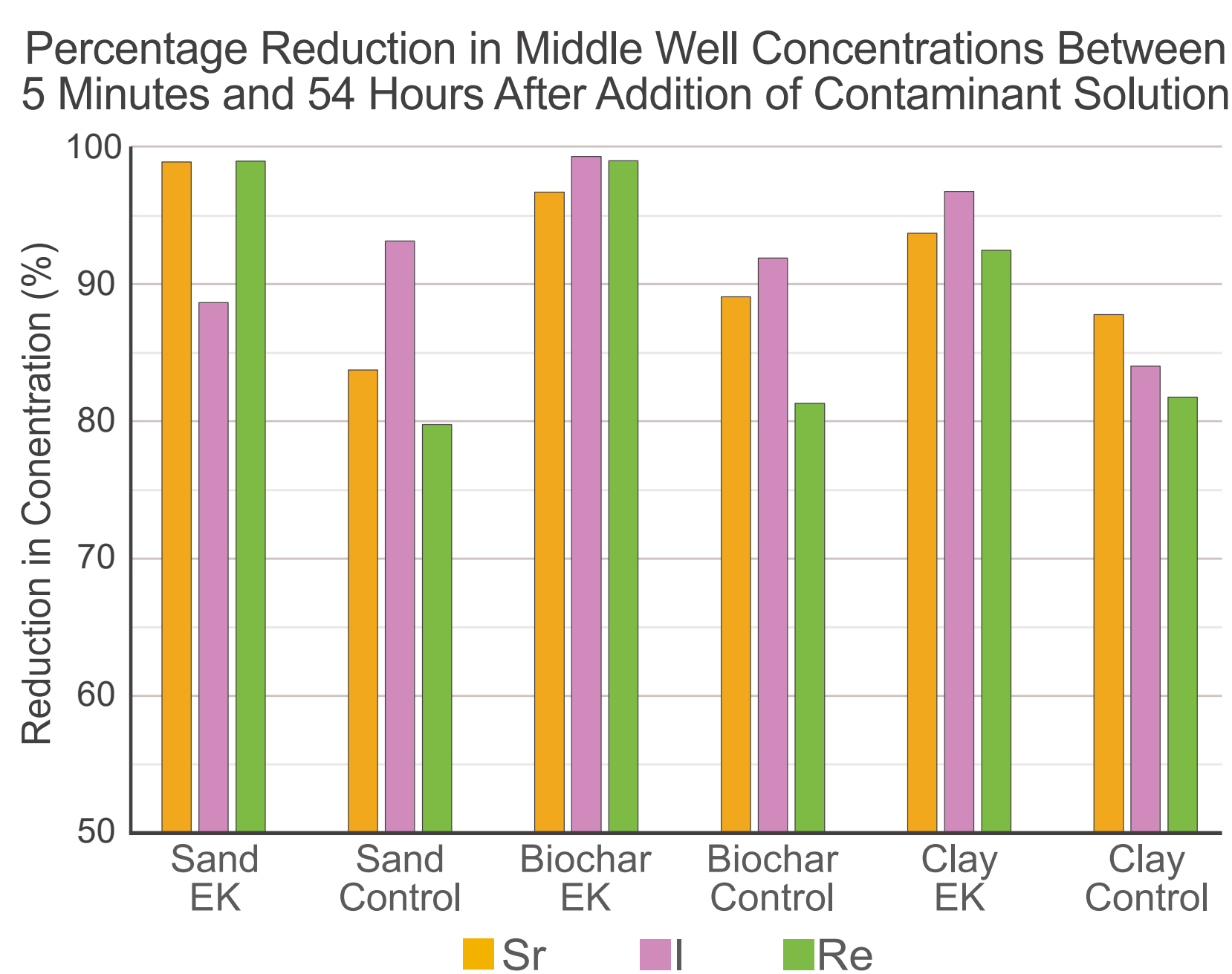


Figure 2: Top - electrokinetic cell with sand and a biochar barrier to mimic a PRB. Bottom - Graph to show concentration reductions of Sr, I and Re in the middle well of each cell

- 3 types of cell were created:
 - sand only (simplified setup)
 - 80% sand and 20% clay, homogeneously mixed (more representative of Sellafield subsurface)
 - sand with 2 biochar barriers (charcoal derived from sewage sludge; proof of concept for a system that utilises both EKR and permeable reactive barriers (PRBs))
- EKR impact is most notable in middle wells, where concentrations of Sr, I and Re decrease over time
- The percentage reduction of target nuclide concentrations is, on average, 10% higher in the EKR cells compared to the control cells. This implies EKR is migrating ions away from the centre quicker than by diffusion alone

Cements - Ongoing Work

Ongoing Work

- Collaborative work led by Ian Burke (University of Leeds) into whether electrokinetics can remediate cement containing ²³⁶U, ¹³⁷Cs, ¹²⁹I, ⁹⁰Sr and ³H
- Cement was chosen instead of concrete to simplify the system. Consequently, only cement and water were added, in a 2:1 ratio
- Cement cores were contaminated in 2 different ways:
 - Homogeneous Set - radionuclides were added as the cement and water were mixed (RNs are homogeneously distributed throughout core, simulating concrete biosheilding)
 - Soaked Set - cores harden (known as curing) and were placed in a bath containing radionuclides (RNs are bound to the surface or near-surface, simulating storage pond concretes)
- Cores are currently curing and will undergo EKR shortly

Sediment Core - Upcoming Work

- Evaluation of whether electrokinetics can migrate the radionuclides present in a 55 cm sediment core from the Ravenglass saltmarsh (~9 km south east of Sellafield)
- Sellafield discharges into the Irish Sea have accumulated in the saltmarsh
- Historical discharges are buried over time by new sediment, creating a discharge profile in the core
- Radionuclides may have been remobilised over time due to changes in conditions
- Itrax XRF scan shows stable element composition throughout the core. Key elements are:
 - S indicates whether the sulphidic zone of respiration has been reached
 - Mn and Fe mark sub-oxic zone of respiration
- Radionuclide analysis will follow soon

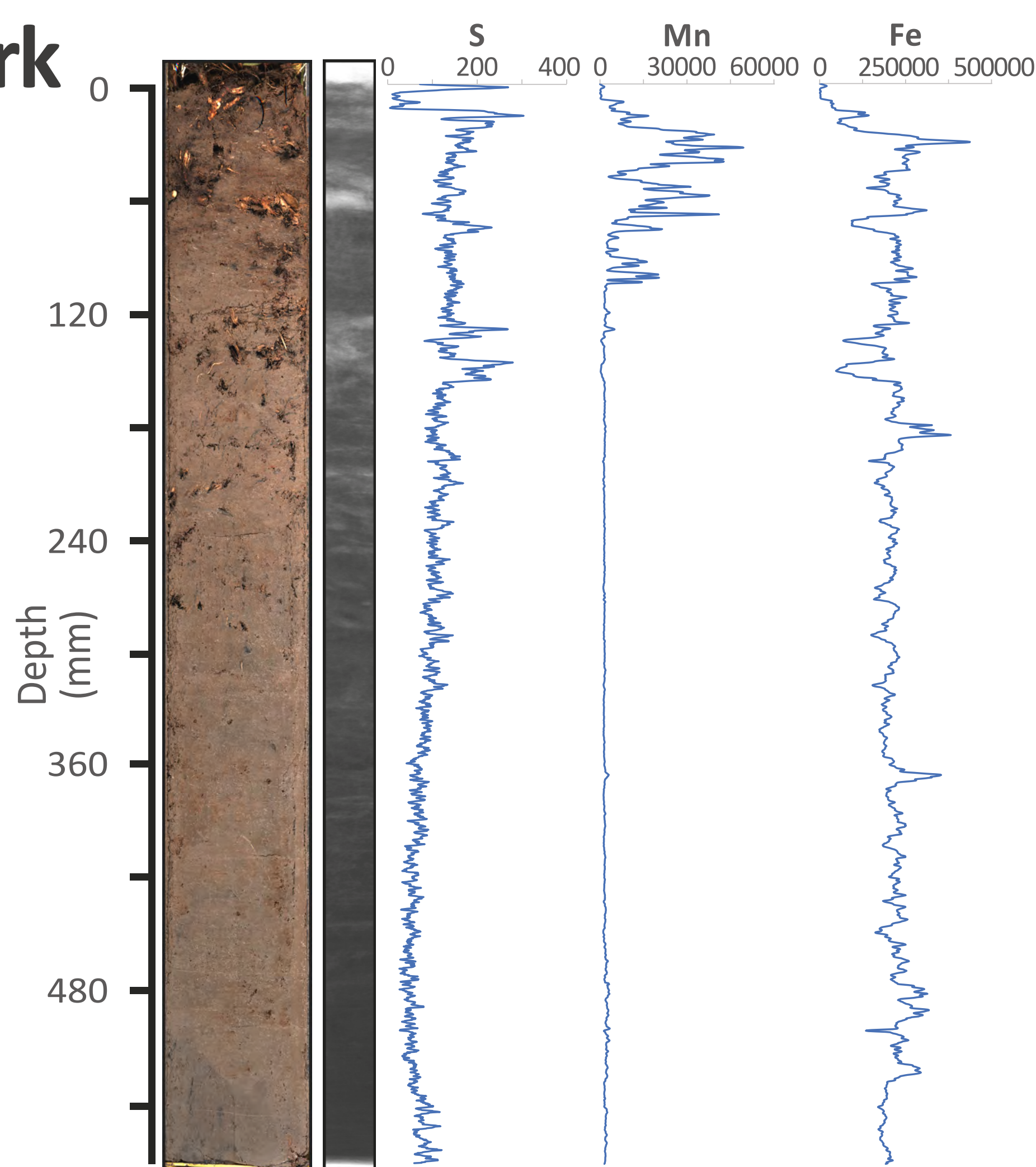


Figure 4: Optical image, radiograph and Itrax XRF scan of key stable elements in the Ravenglass sediment core before EKR treatment



Figure 3: Top - trial cement core undergoing electrokinetic treatment. Bottom - 8 cement cores in the initial stages of curing

Acknowledgements: Prof. Phil Warwick; GAU Radioanalytical; NERC, INSPIRE DTP and TRANSCEND consortium project (EPSRC grant number EP/S01019X/1) for funding; the British Ocean Sediment Core Research Facility (BOSCORF) for supporting XRF core scanning; the National Nuclear User Facility EXACT laboratory and team, via the UK EPSRC (grant EP/T011548/1), for support with cements work.

Problem Introduction

Nuclear Decommissioning

- Almost all of the UK's nuclear power stations were built from late 1970 to late 1980, with most of them closing by 2030.
- The harsh environment and conditions these assets are exposed to, leads to degradation and cracking of concrete.
- We have to guarantee the safety of the structures, until the decommissioning process is completed.



More attention should be given to effectively repairing and maintaining the existing structures and infrastructure.

New repair technique – MICP

Microbially Induced Carbonate Precipitation (MICP) is a novel concrete repair method that takes advantage of bacteria like *S. Pasteurii* where together with urea and a calcium source can form calcium carbonate (CaCO_3).

Calcium Carbonate is very durable in environmental conditions and binds well with concrete surfaces.

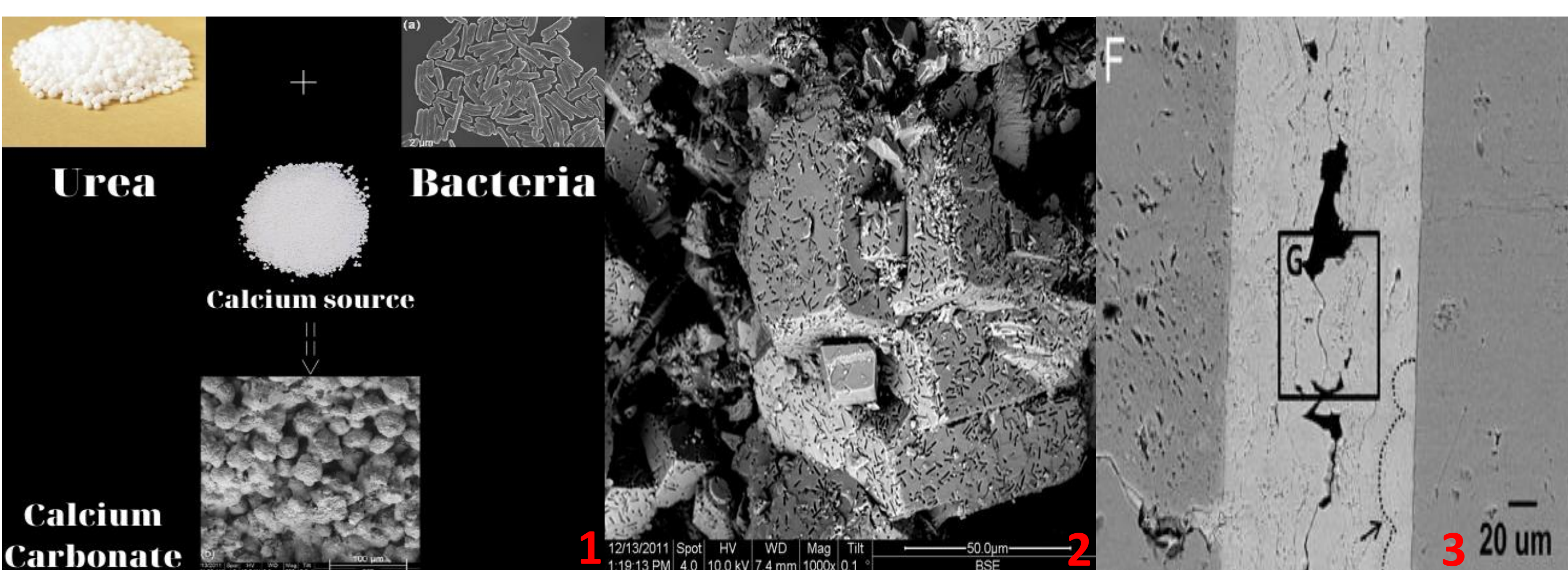


Figure 1: How to precipitate calcium carbonate crystals using the MICP method.

Figure 2: A SEM image presenting calcite crystals with encapsulated bacteria. [1]

Figure 3: A SEM image showing the growth of calcite crystals in layers. [2]

Acknowledgements

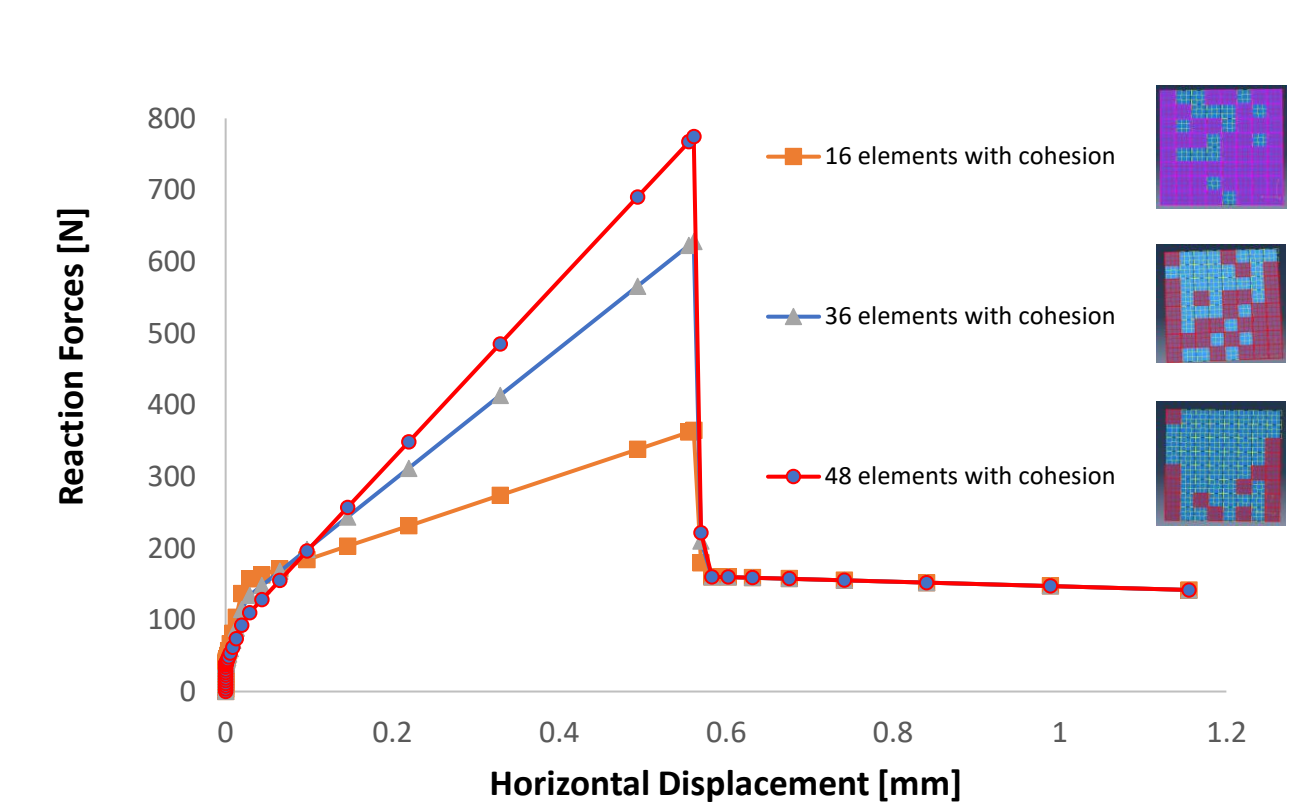
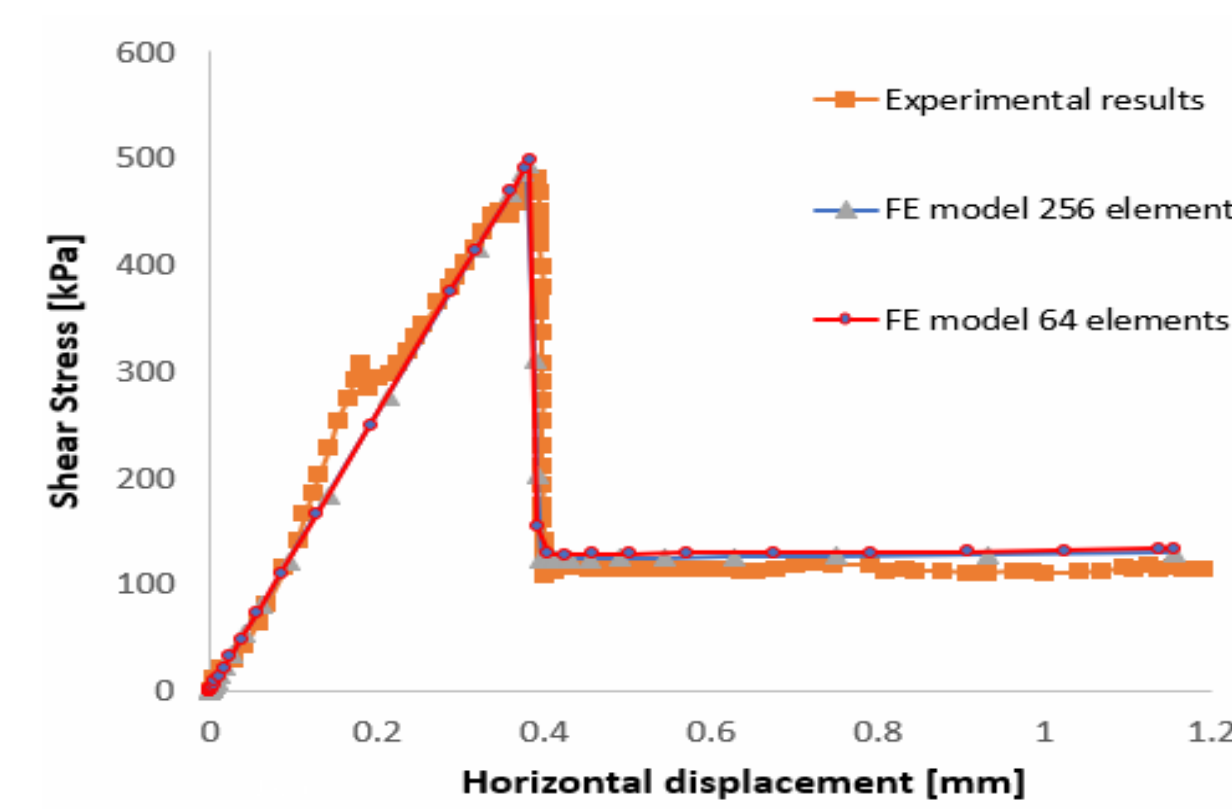
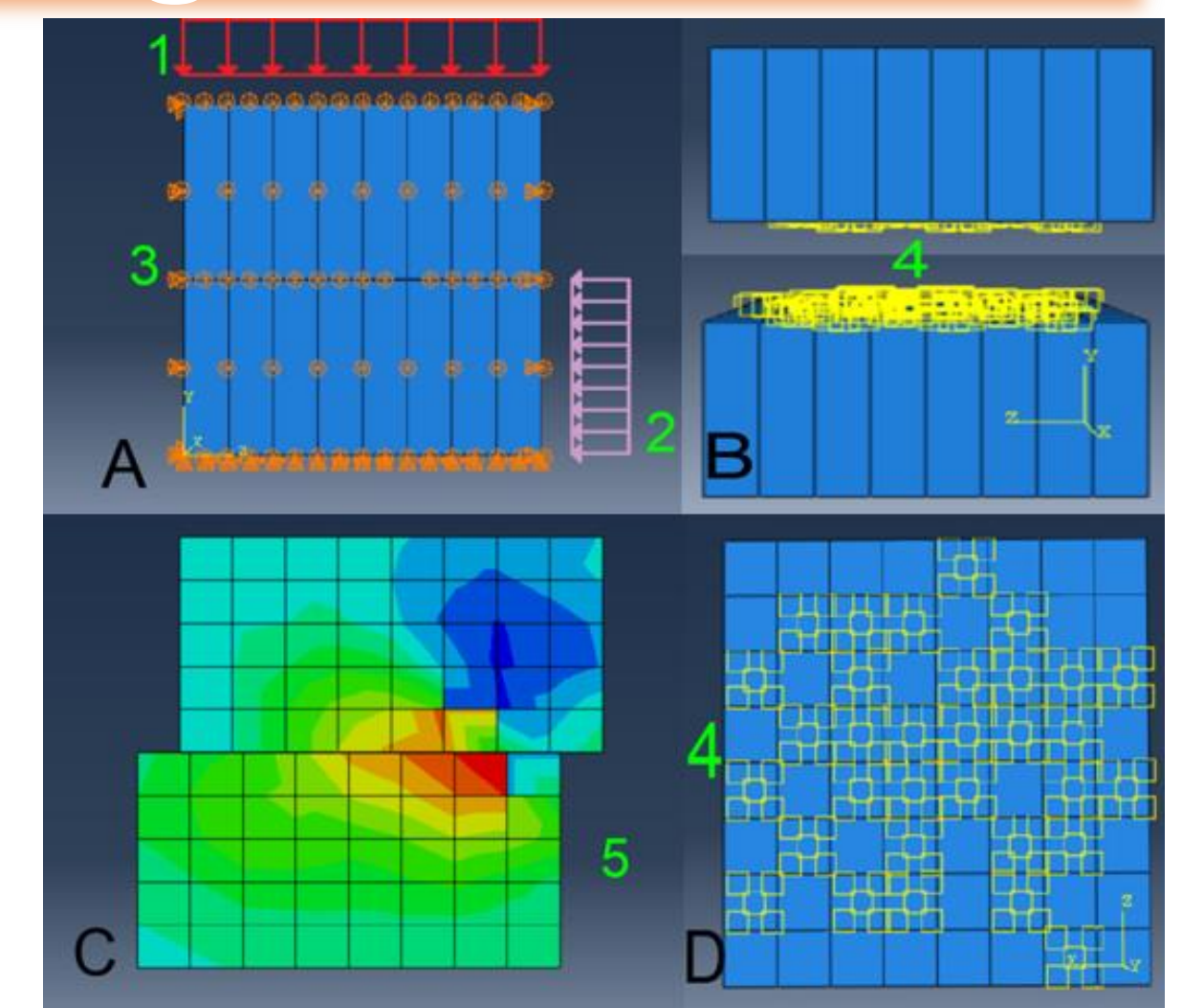
This PhD project is funded by Cavendish Nuclear



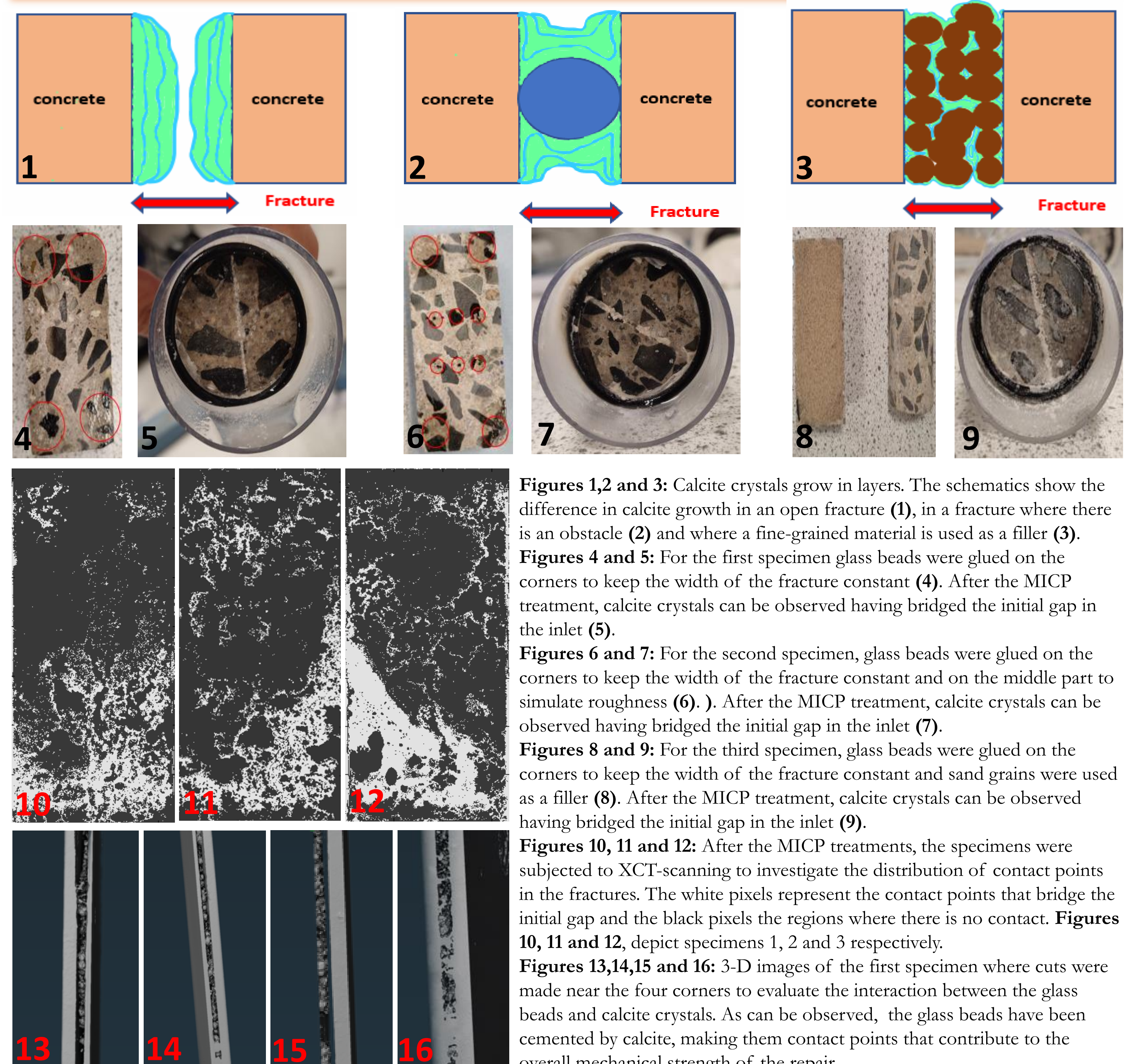
Transformative Science and Engineering for Nuclear Decommissioning

Mesoscale Modelling - FEM

- Mesoscale modelling of concrete is being performed by conceptualizing a fractured core as a composite material under various loading conditions.
- A Finite-Element model has been constructed, which gives a good representation of the MICP-repair under shear failure.



Experimental Results



Figures 1,2 and 3: Calcite crystals grow in layers. The schematics show the difference in calcite growth in an open fracture (1), in a fracture where there is an obstacle (2) and where a fine-grained material is used as a filler (3).
 Figures 4 and 5: For the first specimen glass beads were glued on the corners to keep the width of the fracture constant (4). After the MICP treatment, calcite crystals can be observed having bridged the initial gap in the inlet (5).
 Figures 6 and 7: For the second specimen, glass beads were glued on the corners to keep the width of the fracture constant and on the middle part to simulate roughness (6). After the MICP treatment, calcite crystals can be observed having bridged the initial gap in the inlet (7).
 Figures 8 and 9: For the third specimen, glass beads were glued on the corners to keep the width of the fracture constant and sand grains were used as a filler (8). After the MICP treatment, calcite crystals can be observed having bridged the initial gap in the inlet (9).
 Figures 10, 11 and 12: After the MICP treatments, the specimens were subjected to XCT-scanning to investigate the distribution of contact points in the fractures. The white pixels represent the contact points that bridge the initial gap and the black pixels the regions where there is no contact. Figures 10, 11 and 12, depict specimens 1, 2 and 3 respectively.
 Figures 13,14,15 and 16: 3-D images of the first specimen where cuts were made near the four corners to evaluate the interaction between the glass beads and calcite crystals. As can be observed, the glass beads have been cemented by calcite, making them contact points that contribute to the overall mechanical strength of the repair.

References

[1]: El Mountassir et al., 2018. Applications of Microbial Processes in Geotechnical Engineering, Advances in Applied Microbiology;104:39-91

[2]: Tobler et al., 2018. Microscale Analysis of Fractured Rock Sealed With Microbially Induced CaCO_3 Precipitation: Influence on Hydraulic and Mechanical Performance, Water Resources Research;54:8295-8308



Fig 1. AGR fuel assembly [2]

Research Background

What is the current strategy?:

The current strategy is to interim wet store the fuel pending a decision on final disposal. This is expected to be into a GDF in 2075, with dry storage being investigated as an alternative interim storage method. In addition drying will be a prerequisite for disposal. To reduce the risk of corrosion in storage the ponds are dosed to a pH of 11.4 [1].

Why do we need to dry the fuel?:

Drying will reduce the risk posed by radiolysis. If the cladding has failed then water could seep through any cracks during wet storage. If water is not removed then radiolysis can produce H₂ and H₂O₂. This poses a risk as H₂ is flammable and explosive while H₂O₂ is corrosive and will exacerbate the issue.

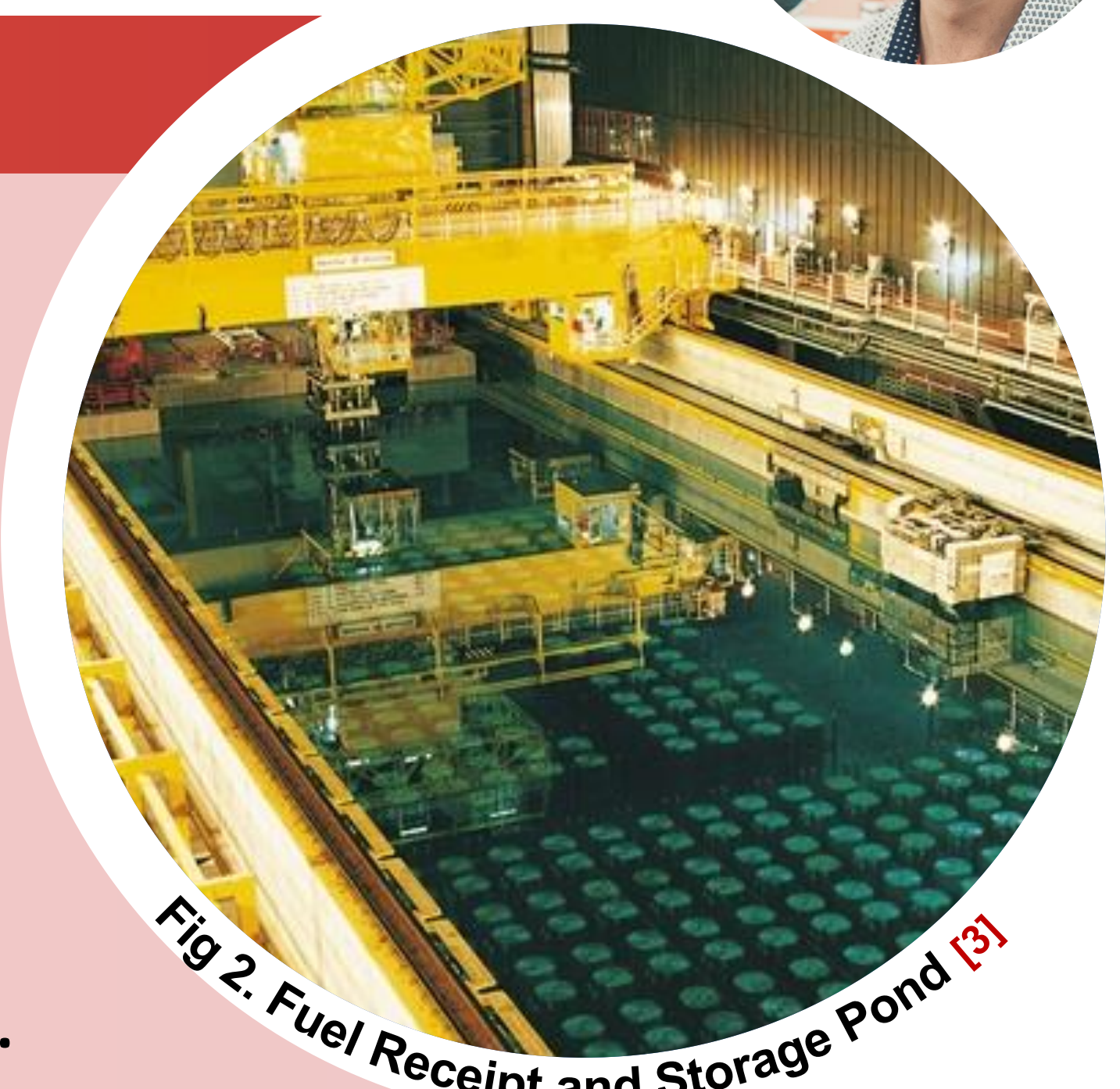


Fig 2. Fuel Receipt and Storage Pond [3]

Project Overview

Experimental:

1. Produce representative cracks in stainless steel.
2. Measure the leak rate through pinhole and crack defects.
3. Conduct drying trials with the pinhole and crack samples.
4. Validate the process model produced to model the drying trials.

Computational:

1. Model the flow of gasses through pinholes.
2. Model the flow through a crack network.
3. Characterise the representative cracks produced.
4. Validate this model using the drying trials.



Fig 3. Drop Evaporation (DE) rig in operation

Comparing Flow Rate Models

Bomelburg: [6]

$$Q = 54.8 \cdot m \cdot \frac{d^4}{\mu \cdot l} \cdot (p_u^2 - p_d^2)$$

Taggart & Budden: [7]

$$Q = C_D \cdot (P \cdot \rho)^{1/2} \cdot W_c \cdot L$$

Beck et al: [8]

$$0 = \frac{\rho \cdot u^2}{2} \left[N \left(1 - \left(\frac{d_{eff}}{d} \right)^2 \right) \right] + \frac{2 \cdot u}{\rho} \left[\frac{12 \cdot \mu \cdot l_{eff}}{d_{eff}^2} \right] - \Delta P$$

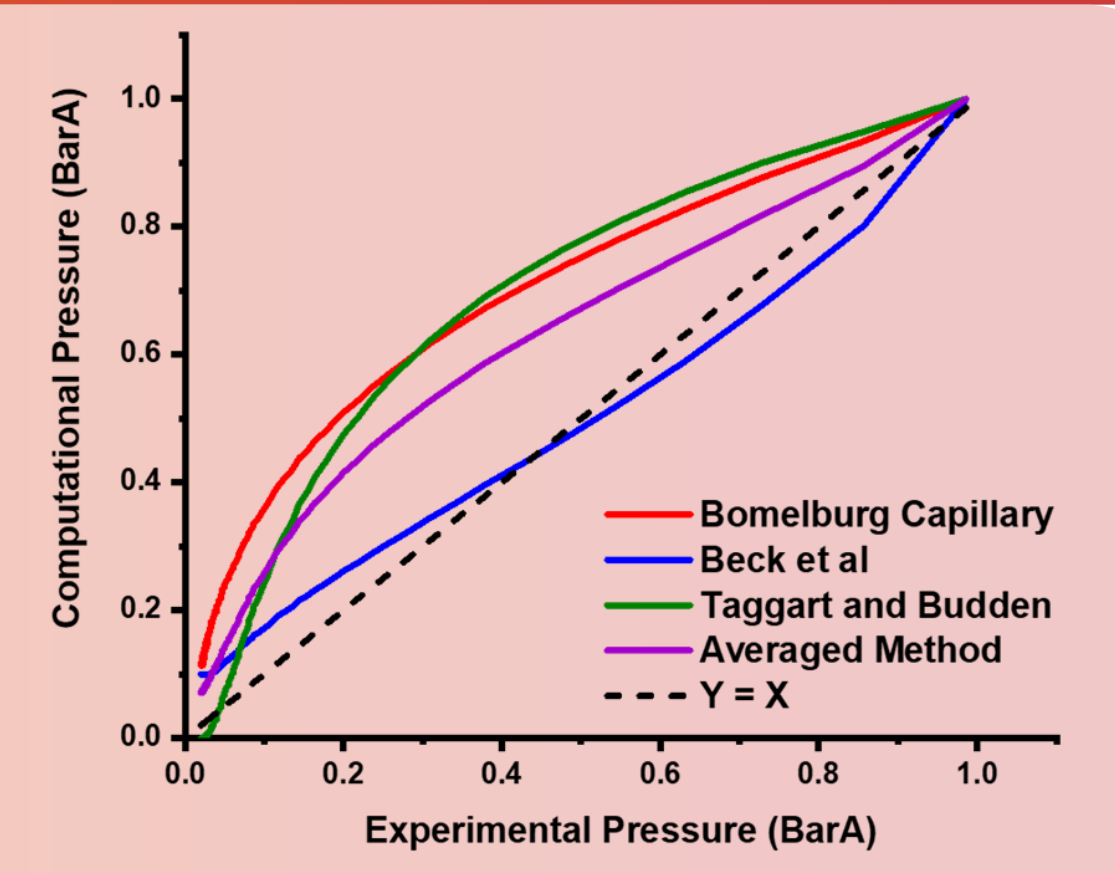


Fig 8. Comparison of the different methods

Corrosion – Producing Cracks in Stainless Steel

Stress Corrosion Cracking:

Thermal conditions and radiation can cause sensitisation of the cladding.

The chromium is depleted around the grain boundaries leaving them susceptible to attack and corrosion.

This leads to narrow tortuous cracks which follow grain boundaries.

Producing Representative Cracks – Drop Evaporation (DE):

A rig similar to that used for 4 point stress testing of materials and has been used to assess SCC in stainless steels used in offshore oil and gas [5].

The sample is stressed and heated to 180°C.

Then a 35g/L NaCl solution is dripped onto the centre of the sample allowing the previous drip to evaporate before the next droplet falls.

By letting each droplet evaporate the chloride is concentrated leading to a more aggressive environment.

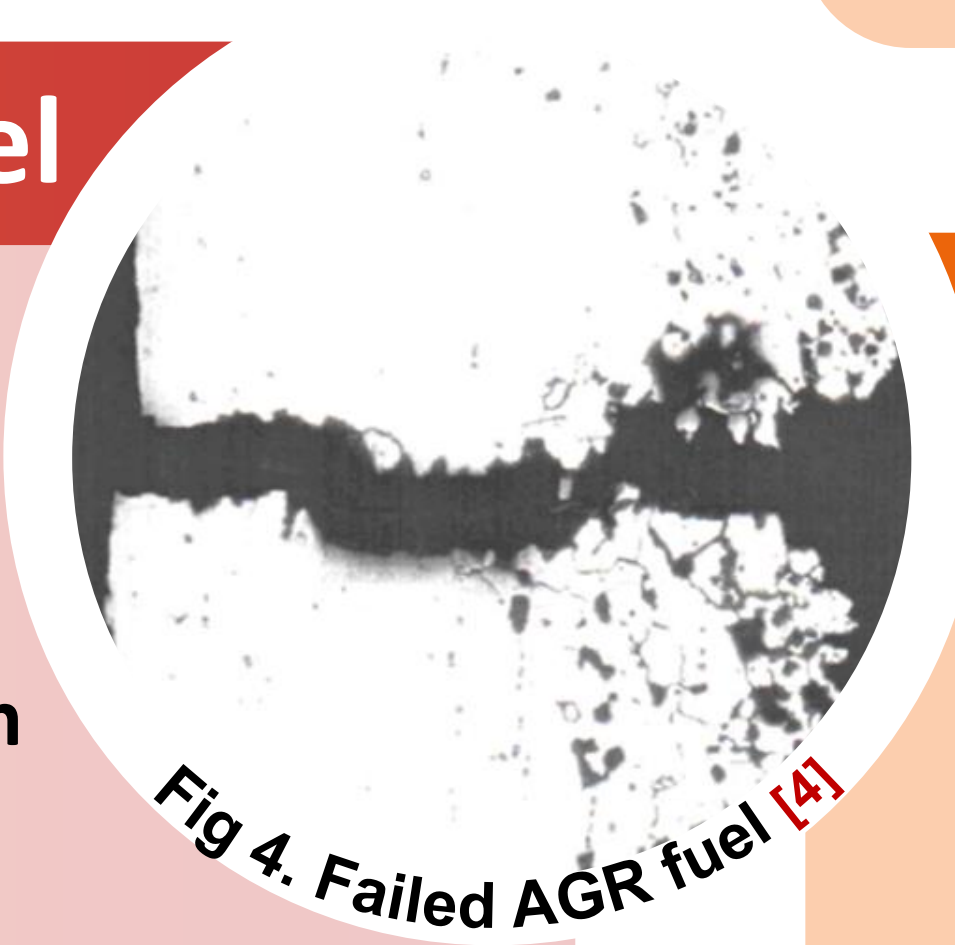


Fig 4. Failed AGR fuel [4]

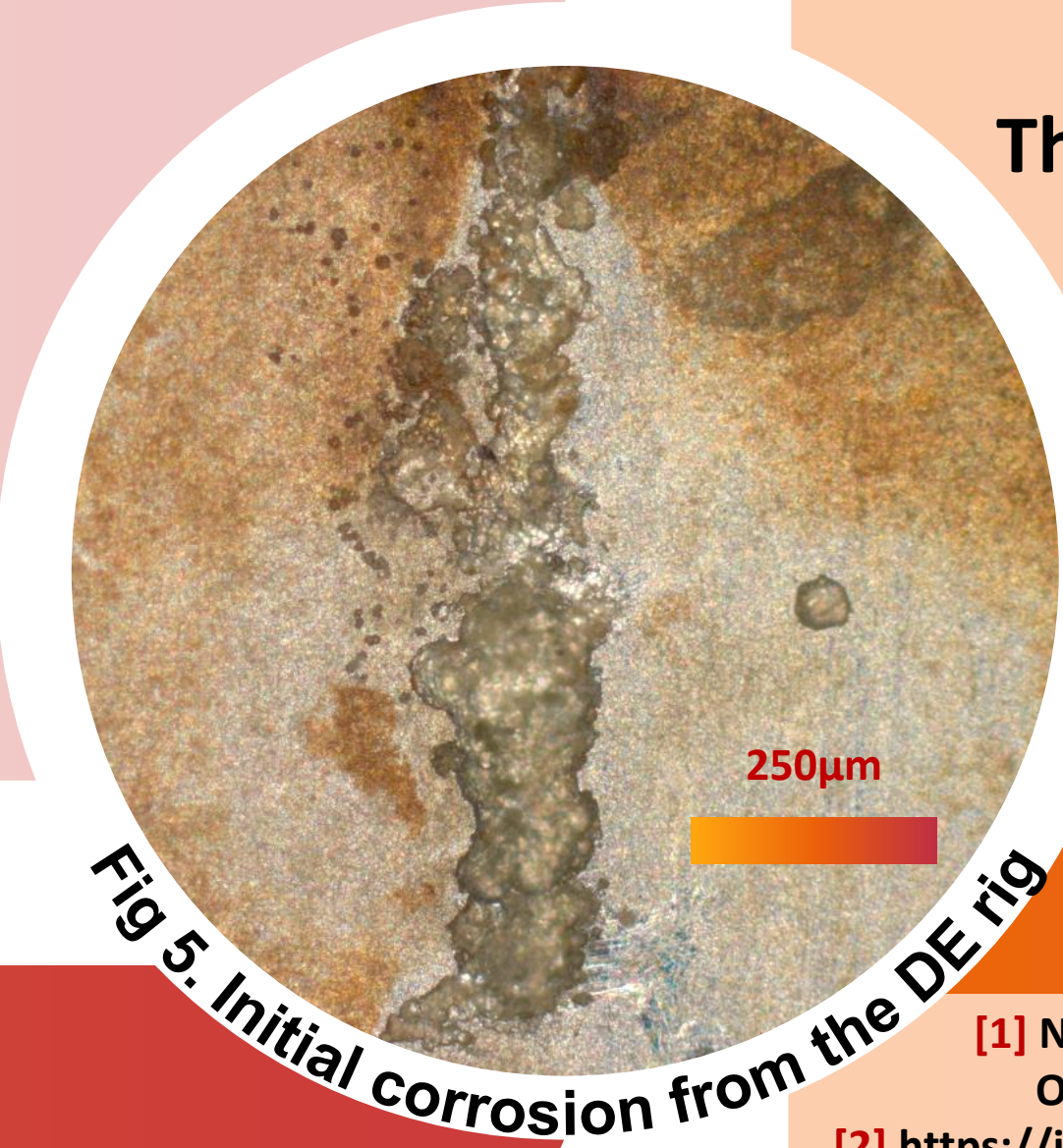


Fig 5. Initial corrosion from the DE rig

Flash Evaporation

Flash evaporation occurs here when the water is suddenly exposed to a reduced pressure.

We are treating it as an adiabatic process with the energy being required for the boiling coming from the water.

$$m_{evap} = \frac{\rho_{water} \cdot V_0 \cdot c_p}{h_{fg}} [T_1 - T_2] \quad [9]$$

$$T_2 = \frac{m_{water} \cdot c_{p_{water}} \cdot T_1 + Q}{(m_{water} - m_{evap}) \cdot c_{p_{water}} + m_{evap} \cdot c_{p_{vapour}}}$$

The aim of incorporating this is to account for some of the “bouncing” seen in the experimental data.

The working hypothesis is that the flash evaporation occurs, the vapour is evacuated and the next flash evaporation occurs.

Drying Experiments

A few grams of water is added to the sample and it is placed into the vessel.

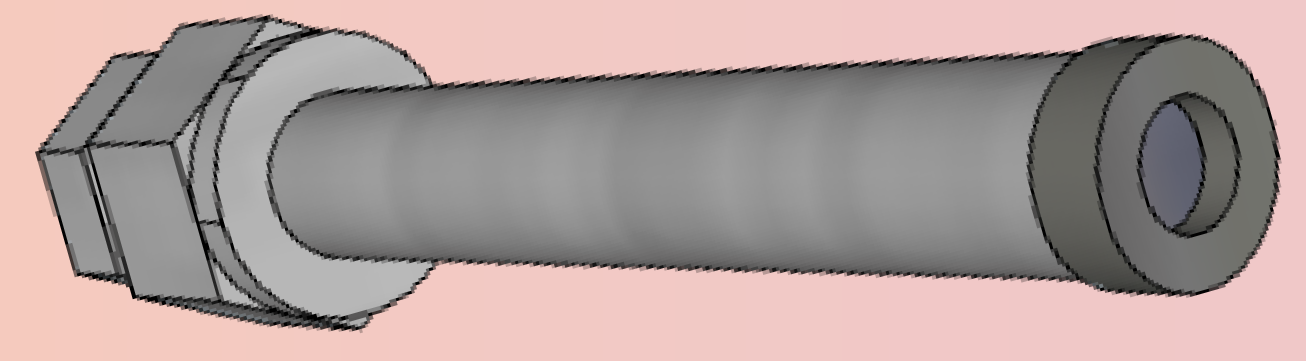


Fig 6. CAD model of the drying sample

The vessel and sample is heated to the test temperature.

Once at the test temperature the vessel is evacuated.

The temperature, pressure and dew point is recorded continuously with the mass recorded by pausing the experiment and weighing the sample periodically.

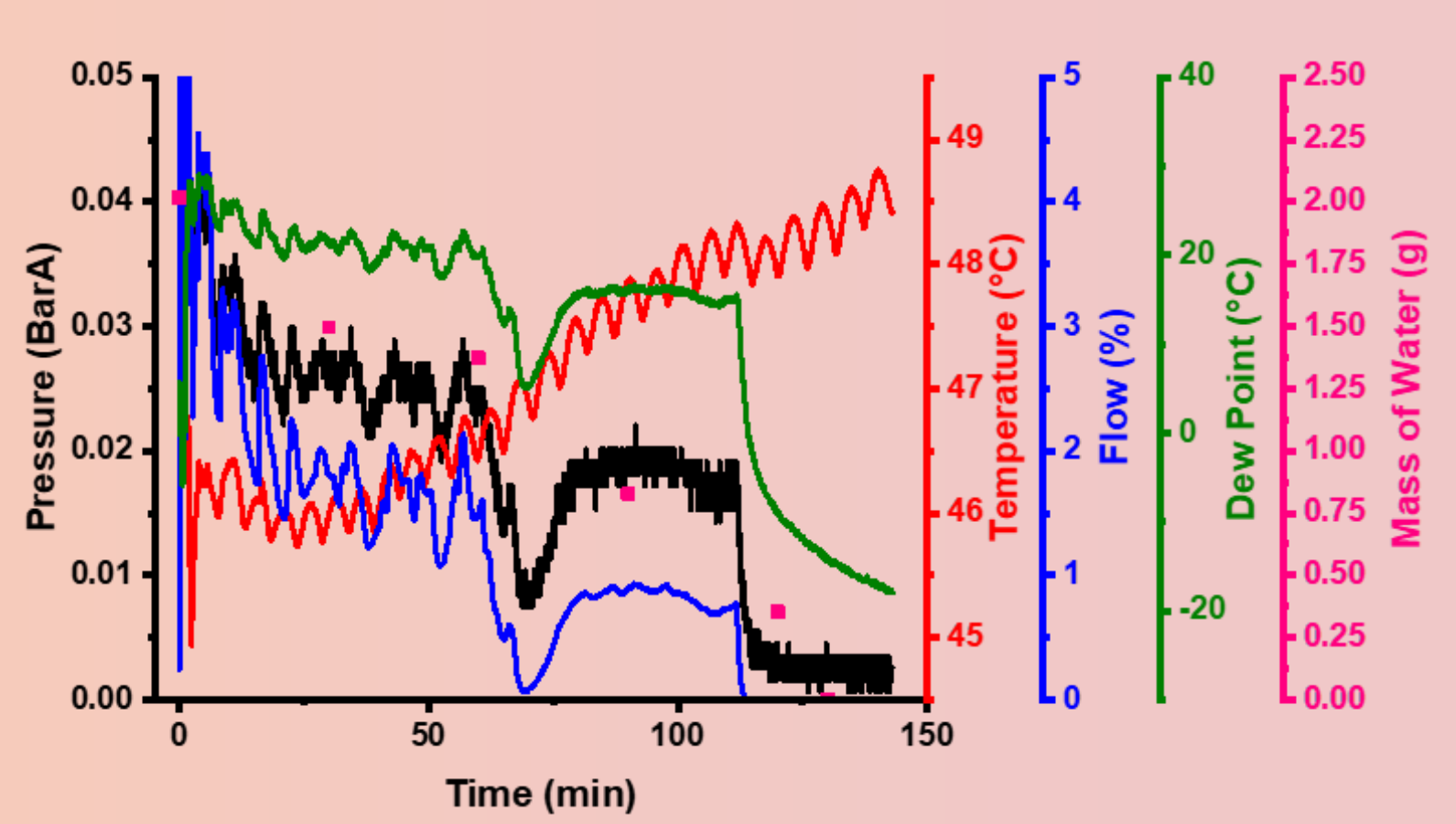


Fig 7. Experimental results from the 20µm sample at 50°C

References

[1] Nuclear Decommissioning Authority. Oxide Fuels - Preferred Option - Publications - GOV.UK. Technical Report SMS/TS/C2-OF/001/Preferred Option, June 2012. URL <https://www.gov.uk/government/publications/oxide-fuels-preferred-option>.
 [2] <https://info.westinghousenuclear.com/blog/the-art-of-innovation-westinghouse-agr-fuel>
 [3] <https://processengineering.co.uk/article/2012839/sellafield-nuclear-r>
 [4] J. Kyffin and A. Hillier (2015). "Technological Development to Support a Change in the United Kingdom's Strategy for a Management of Spent AGR Oxide Fuel." *International Conference on Management of Spent Fuel from Nuclear Power Reactors*.
 [5] Pereira, H. B., et al. (2019). "Investigation of stress corrosion cracking of austenitic, duplex and super duplex stainless steels under drop evaporation test using synthetic seawater." *Materials Research* 22(2).
 [6] Bomelburg, H. J. (1977) 'Estimation of Gas Leak Rates Through Very Small Orifices and Channels', (February), pp. 1–39. Available at: <https://www.osti.gov/servlets/purl/7318185>
 [7] Taggart, J. P. and Budden, P. J. (2008) 'Leak before break: Studies in support of new R6 guidance on leak rate evaluation', *Journal of Pressure Vessel Technology, Transactions of the ASME*, 130(1), pp. 0114021–0114026. doi: 10.1115/1.2826422.
 [8] Beck, S., et al. (2005). "Explicit equations for leak rates through narrow cracks." *International journal of pressure vessels and piping* 82(7): 565-570.
 [9] Saury, D., Harmand, S. and Siroux, M. (2005) 'Flash Evaporation from a Water Pool: Influence of the Liquid Height and of the Depressurization Rate', *International Journal of Thermal Sciences*, 44(10), pp. 953–965. doi: 10.1016/j.ijthermalsci.2005.03.005.

Acknowledgements

Academic Supervisors: Prof. Bruce Hanson
 Dr Nicole Hondow
 Industrial Supervisor: Dr Carlos de la Fontaine

Background

Research topic

The goal of the PhD research is to develop a micromechanical testing method for spent AGR cladding to study stress corrosion cracking (SCC), and this side project was proposed to investigate the relationship between thermal sensitisation and two different grain boundary properties.

Grain Boundary Misorientation or Boundary Plane Orientation

Traditionally, boundary misorientation was believed to be the main factor of sensitisation [1], where LAGBs and HAGBs with special CSL (coincidence site lattice, $CSL=\Sigma 3, \Sigma 9, \Sigma 27$ or $\Sigma \leq 29$) are more resistant to thermal sensitisation.

However, in a study using DCT (diffraction contrast tomography) on a thermally sensitised wire [2], the special boundaries, which located near low $\{hkl\}$ Miller index planes of both grains, were found resistant to thermal sensitisation.

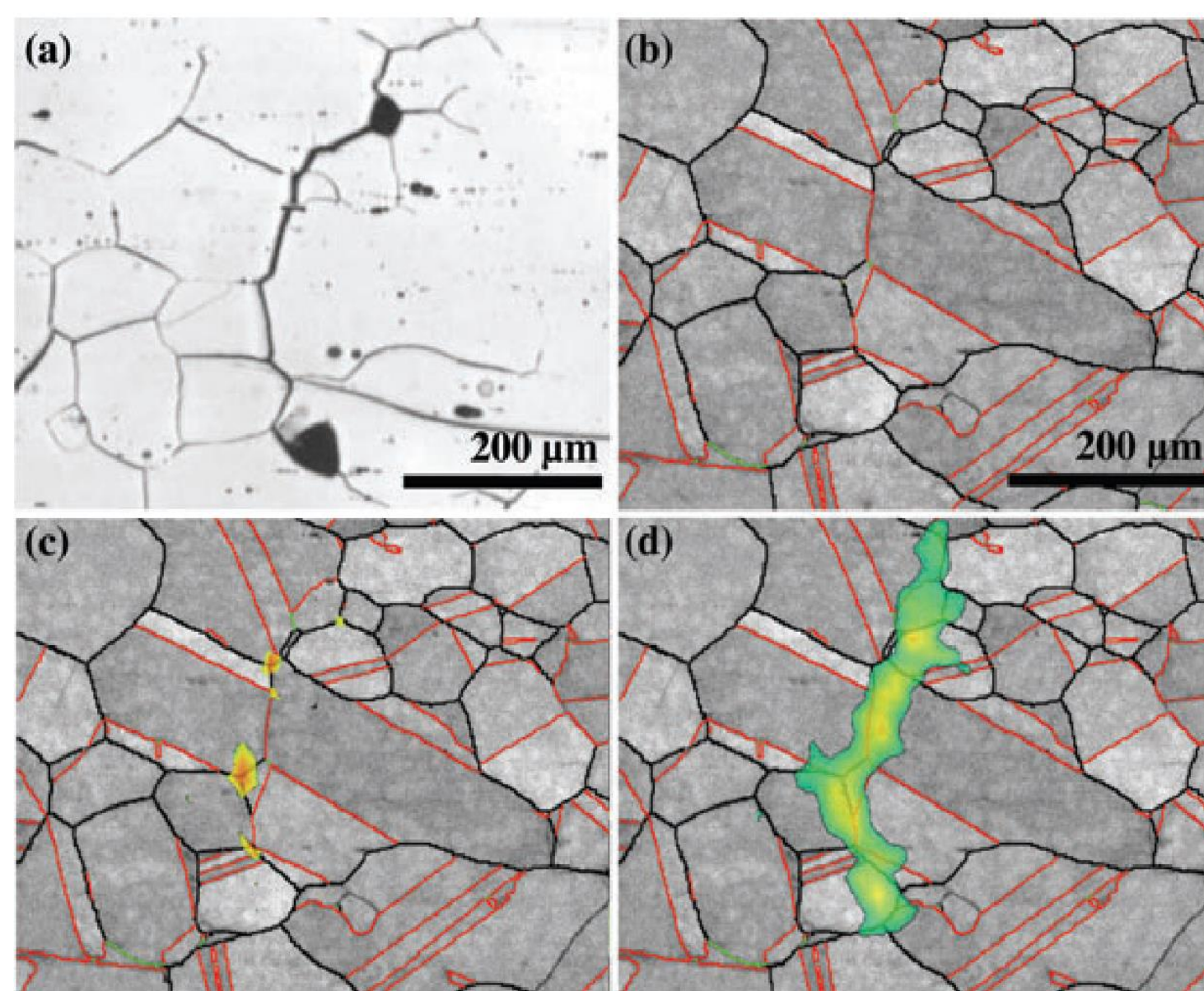


Fig. 1 Correlation between observations in the microstructure of 304 stainless steel: (a) optical image of an intergranular crack, (b) EBSD map of the same area of microstructure, (c) strain map obtained after 16 h, (d) strain map after 24 h. In (b), (c) and (d), the $\Sigma 3$ boundaries are represented in red lines, $\Sigma 9$ and $\Sigma 27$ boundaries are green lines, low-angle grain boundaries ($\Sigma 1$) are white lines and random boundaries are black lines [1]

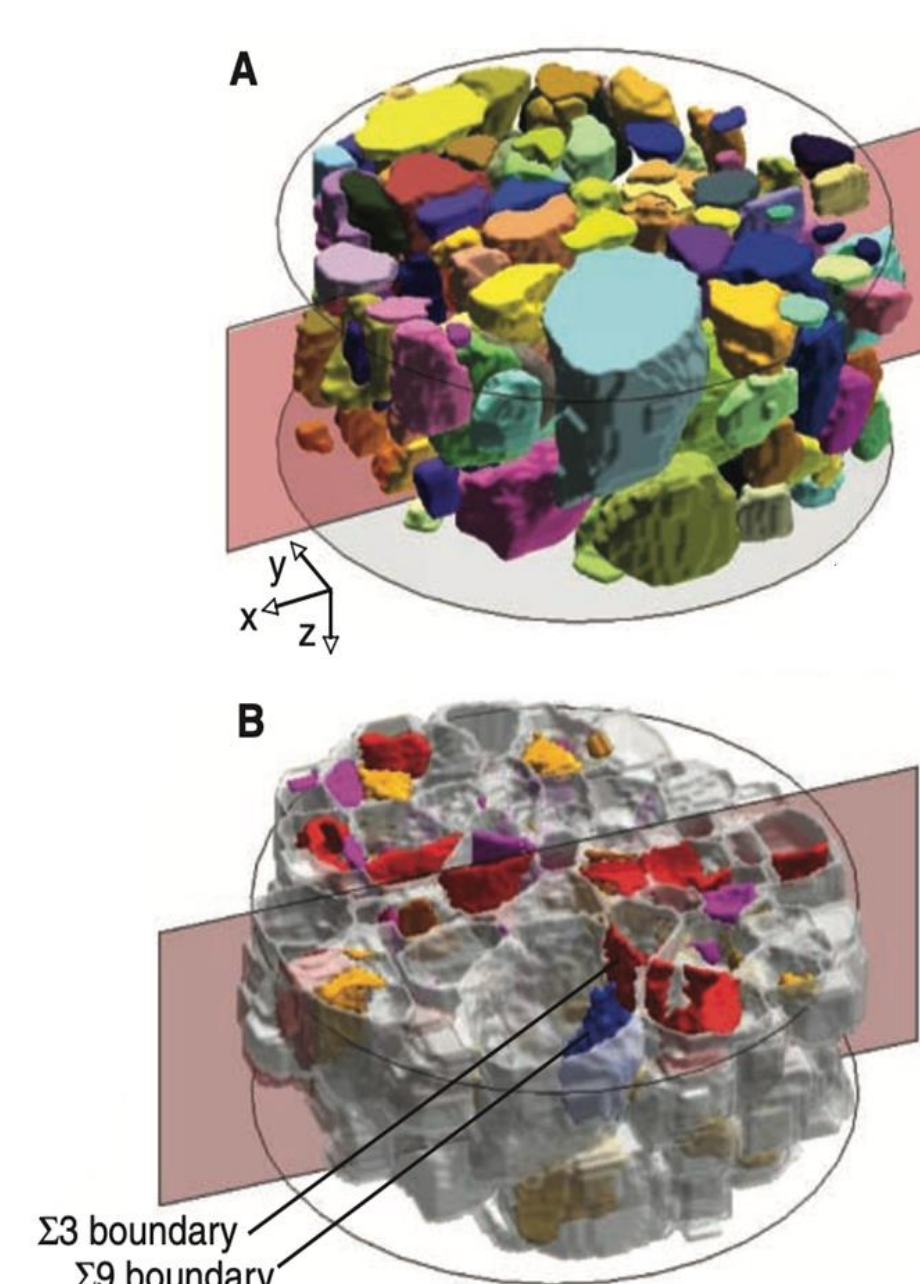


Fig. 2 3D DCT grain map of a section from a wire sample: (A) crystallographic orientation of grains, (B) low Σ CSL grain boundaries are shown in colour: LAGBs, orange; $\Sigma 3$, red; $\Sigma 9$, blue; other boundaries $\Sigma \leq 29$, purple [2]

Therefore, current study was proposed to compare the relationship between the level of sensitisation and these two grain boundary properties: misorientation and plane orientation.

Previous experiment

A piece of thermally sensitised (ageing at 600 °C for 50 hours) 304 stainless steel was serial sectioned by plasma FIB and the grains were reconstructed to reveal the boundary plane orientation.

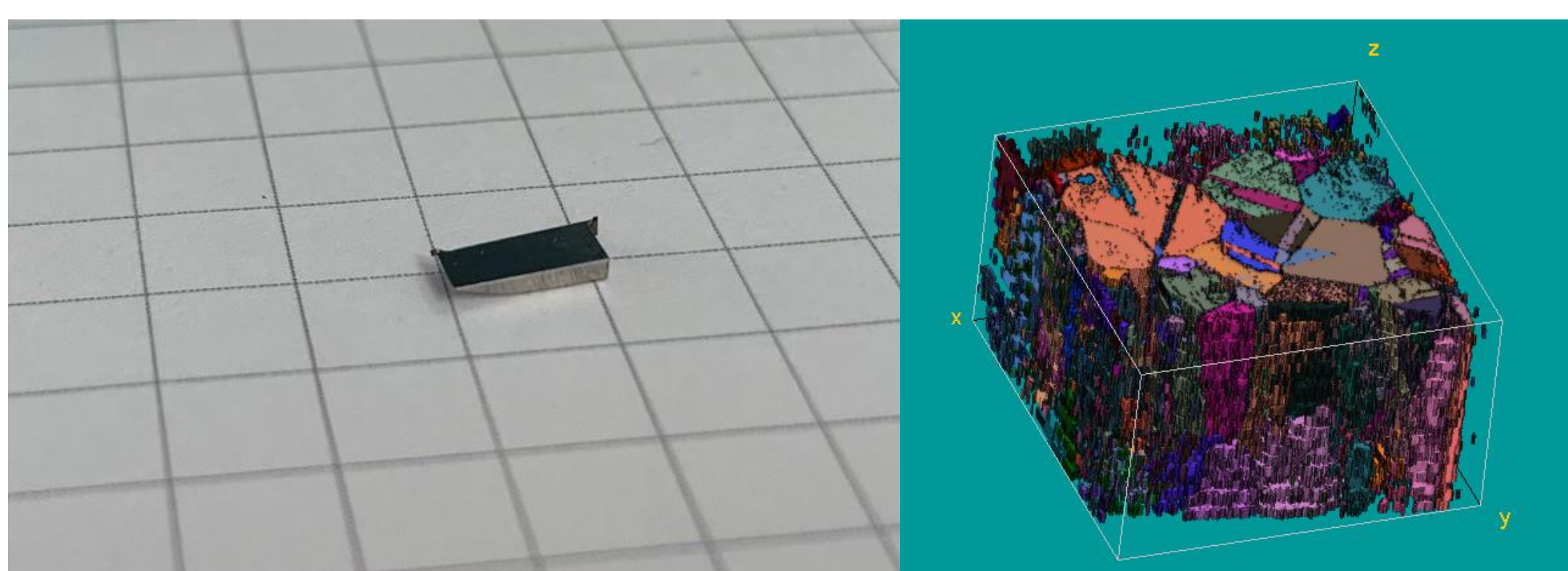


Fig. 3 Prepared specimen

Fig. 4 3D reconstruction of the FIB serial sectioning

Experimental Methods

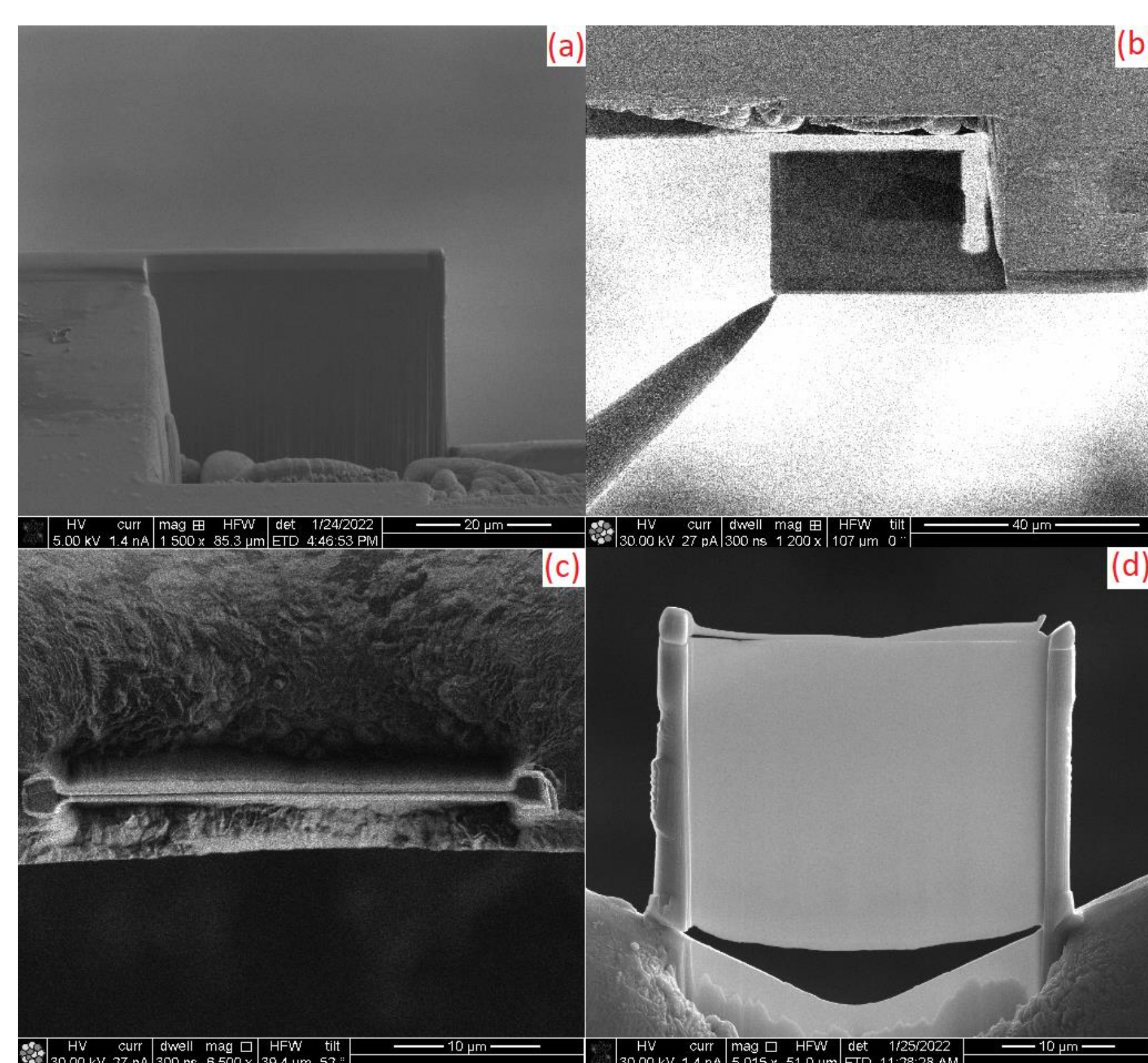


Fig. 5 FIB sample lifting out: (a) removing the material behind the lift-out sample, (b) welding the needle to the sample, (c) polishing the TEM sample and (d) polished sample

Two foil samples were extracted from the bulk sample and polished by using a gallium FIB:

- Platinum was deposited on the potential foil.
 - Trenches were milled to form the foil for extraction.
 - A needle was welded to the foil and the sample was placed on a sample holder.
 - The foil was polished on each side to ~ 200 nm.
- Several regions of interest on each foil sample were then mapped by TEM at Henry Royce Institute.

Results

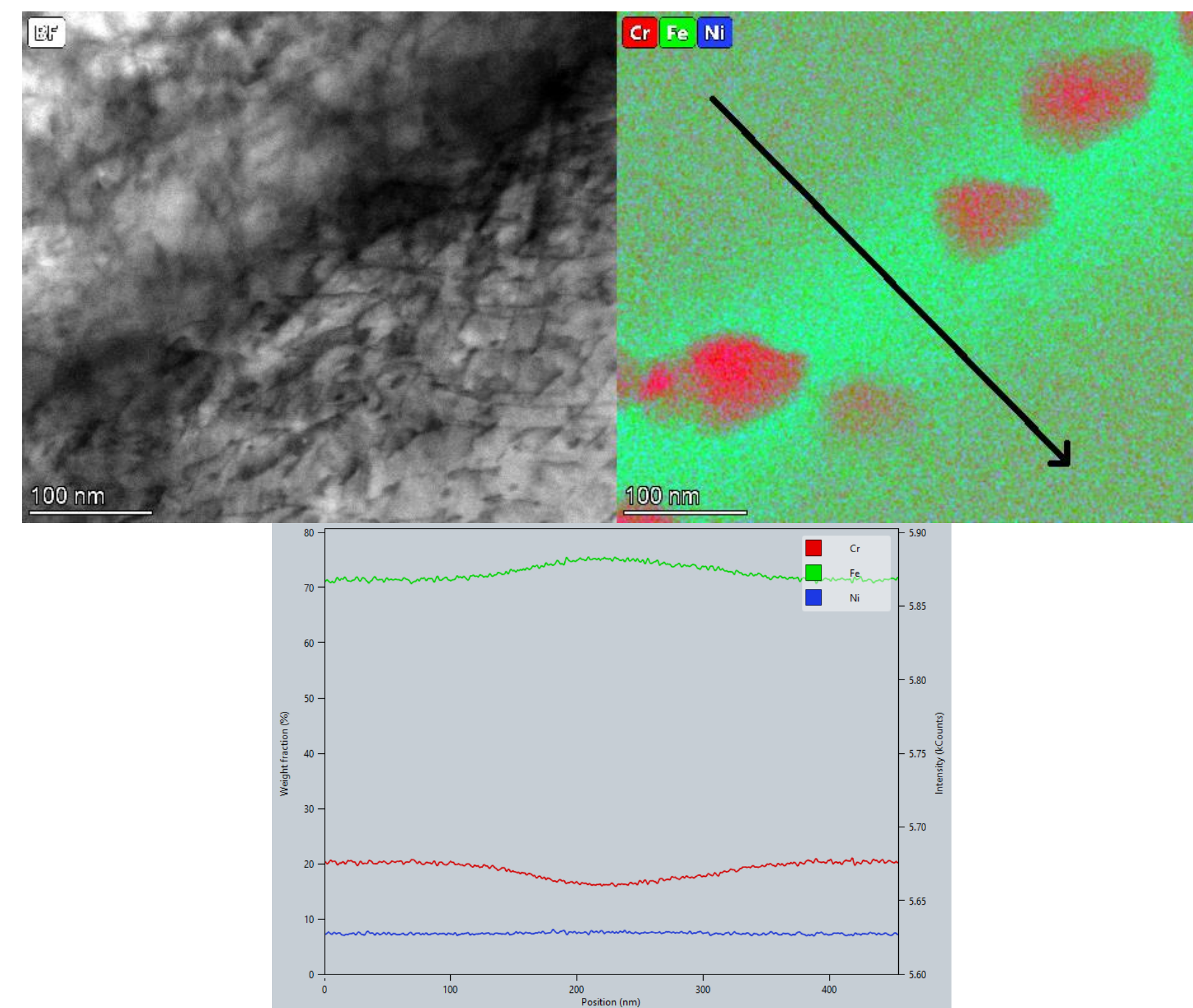


Fig. 6 Elemental map of ROI 1 with a line scan across depleted grain boundary

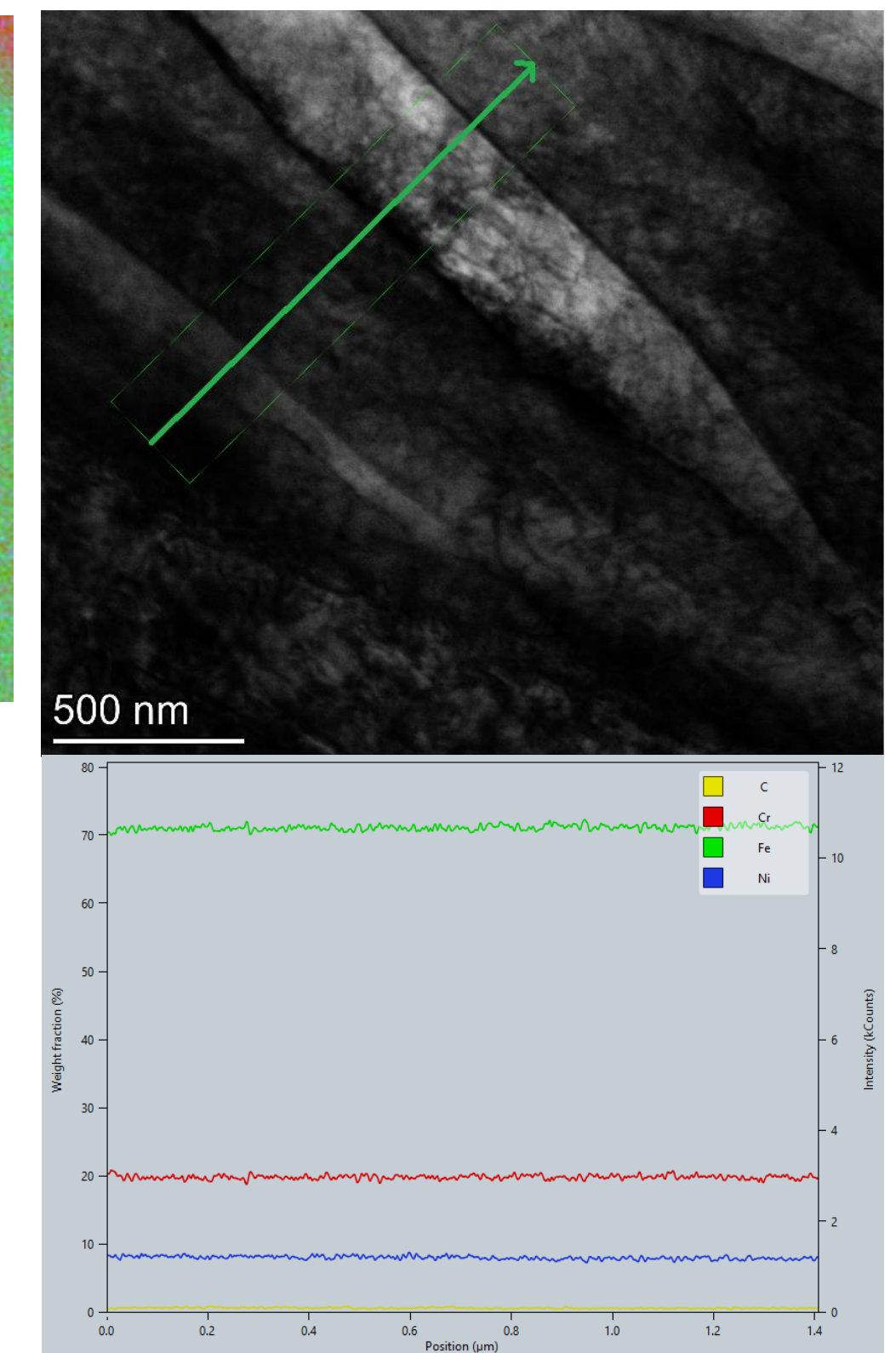


Fig. 7 Line scan of a the grain boundaries in ROI 2

ROI 1 shows the elemental mapping of a single sensitised grain boundary, where the chromium carbide precipitates along grain boundary causing the depletion of chromium that can allow the initiation of SCC and ROI 2 shows no sign of sensitisation.

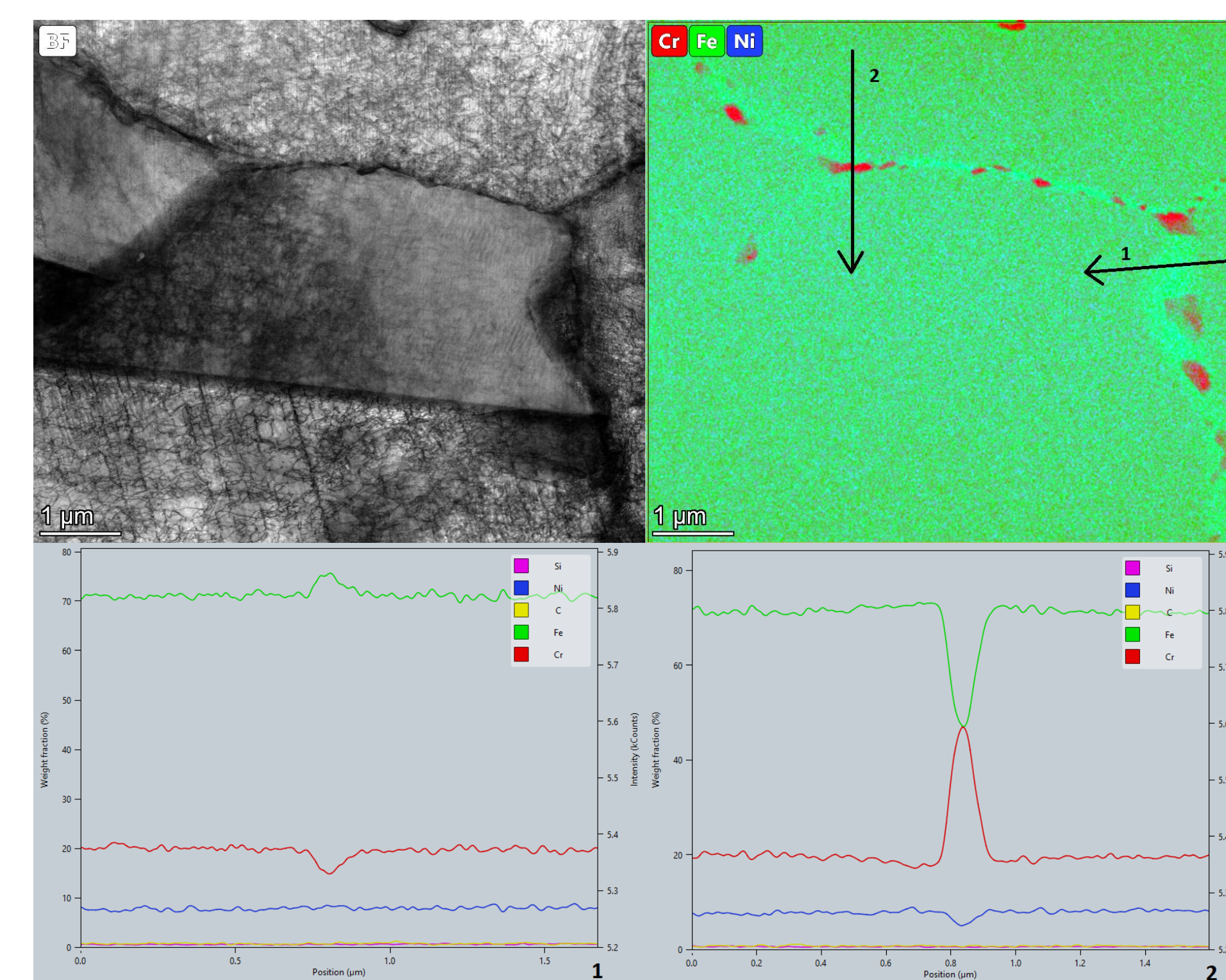


Fig. 8 Elemental map of ROI 3 with 2 line scans across depleted grain boundary and carbides

When there are multiple grain boundaries in this ROI, and not all of them are showing chromium depletion due to their boundary properties. Two line scans show the chemical concentration on the depleted and precipitated area of the grain boundary.

Some grain boundaries have unusual precipitation. In ROI 3, the grain boundary shows depletion of chromium but the chromium carbide precipitates around a small grain on the boundary.

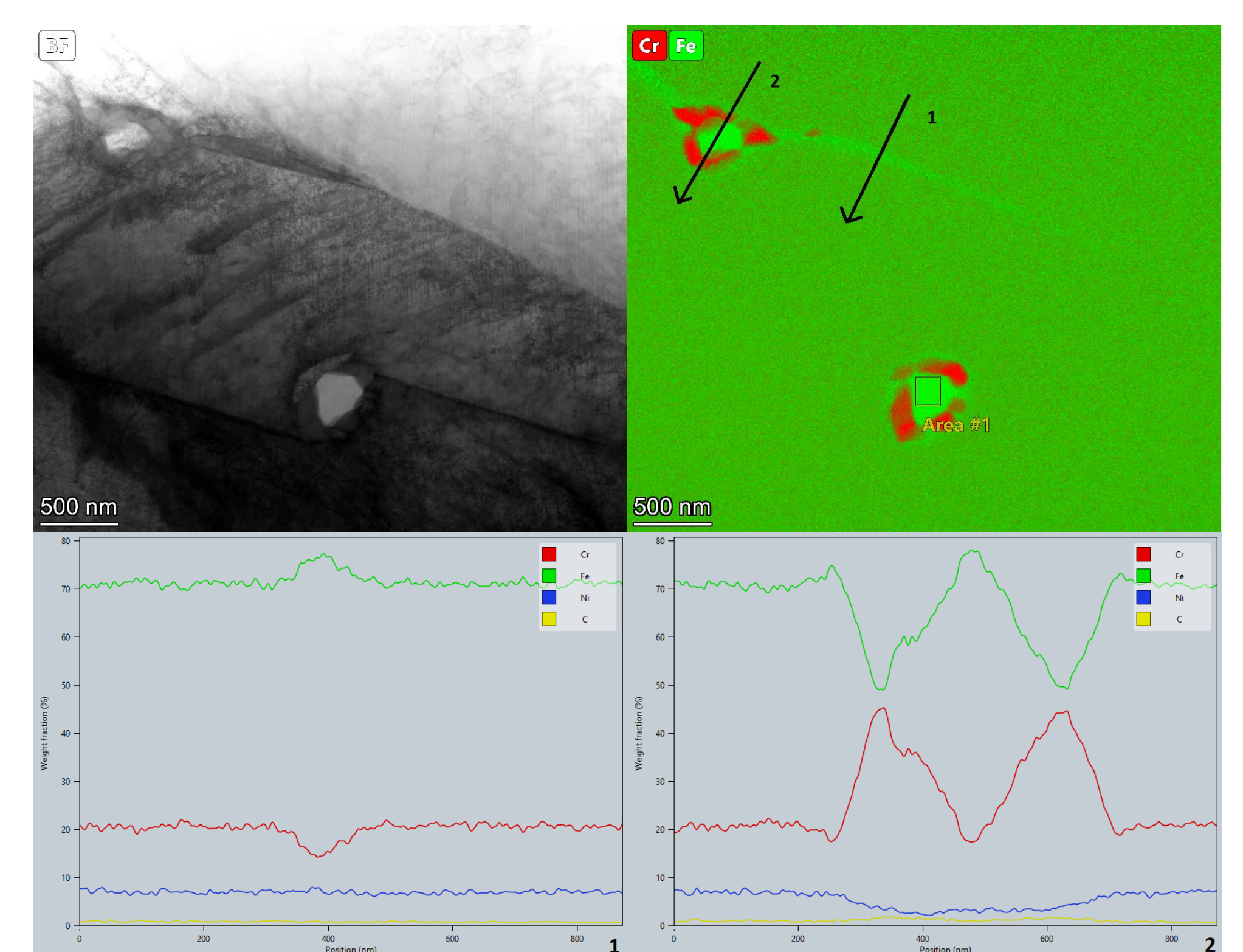


Fig. 9 Elemental map of ROI 4 with 2 line scans across depleted grain boundary and carbides

Conclusions

Two foil samples were extracted from the previously studied bulk sample and were polished by FIB. They were then scanned by elemental mapping using TEM at Henry Royce Institute.

Two foils will be finally scanned by EBSD to identify the CSL number of the grain boundaries, and the grain boundaries with special CSL numbers will be correlated to the chromium depletion level from the TEM mapping to find the boundaries that do not follow the misorientation rule. They will then be compared with the plane orientation from the 3D reconstruction.

References

- [1] S. Rahimi, D. L. Engelberg, J. A. Duff, and T. J. Marrow, "In situ observation of intergranular crack nucleation in a grain boundary controlled austenitic stainless steel," *J. Microsc.*, vol. 233, no. 3, pp. 423–431, 2009, doi: 10.1111/j.1365-2818.2009.03133.x. [2] A. King, G. Johnson, D. Engelberg, W. Ludwig, and J. Marrow, "Observations of intergranular stress corrosion cracking in a grain-mapped polycrystal," 2008.

Introduction

Radiogenic helium gas generation naturally occurs in the ageing of PuO₂ due to the spontaneous alpha decay of Pu isotopes, creating self-radiation damage to the lattice [1]. The accumulation of helium atoms into bubbles could lead to pressurisation of storage canisters. As such, it is crucial to develop understanding of helium diffusion in PuO₂. This study uses molecular dynamics to investigate the diffusion of helium in PuO₂ for the first time. The system sizes were 8x8x8 supercells, with simulation times of 5 ns over a 1000 – 3000 K temperature range.

Diffusion Regimes

A PuO₂ system with 0.5% He in interstitial sites was evolved using molecular dynamics at 100 K intervals; the diffusivity was calculated via the Einstein relation. Fig.1 plots the diffusivity of He, O and Pu calculated at each temperature. Three regions of interest (R1, R2 and R3) are highlighted:

- R1 (1000-1500 K): There is no diffusion. Here atoms only vibrate around their lattice sites over the simulation time scale.
- R2 (1500-2500 K): The diffusivity of He and O increases with increasing temperature, with their diffusion closely aligned. This suggests the main helium diffusion mechanism is oxygen vacancy assisted. Fig 2. displays an example of oxygen vacancy assisted diffusion at 2100 K.
- R3 (>2500 K): The oxygen diffusion levels off, which may be due to the oxygen sub lattice going through a Bredig phase transition and becoming amorphous [3]. Also in this region plutonium diffusivity increases. It is possible that the helium diffusivity plateau could be due to plutonium vacancies becoming available and trapping helium.

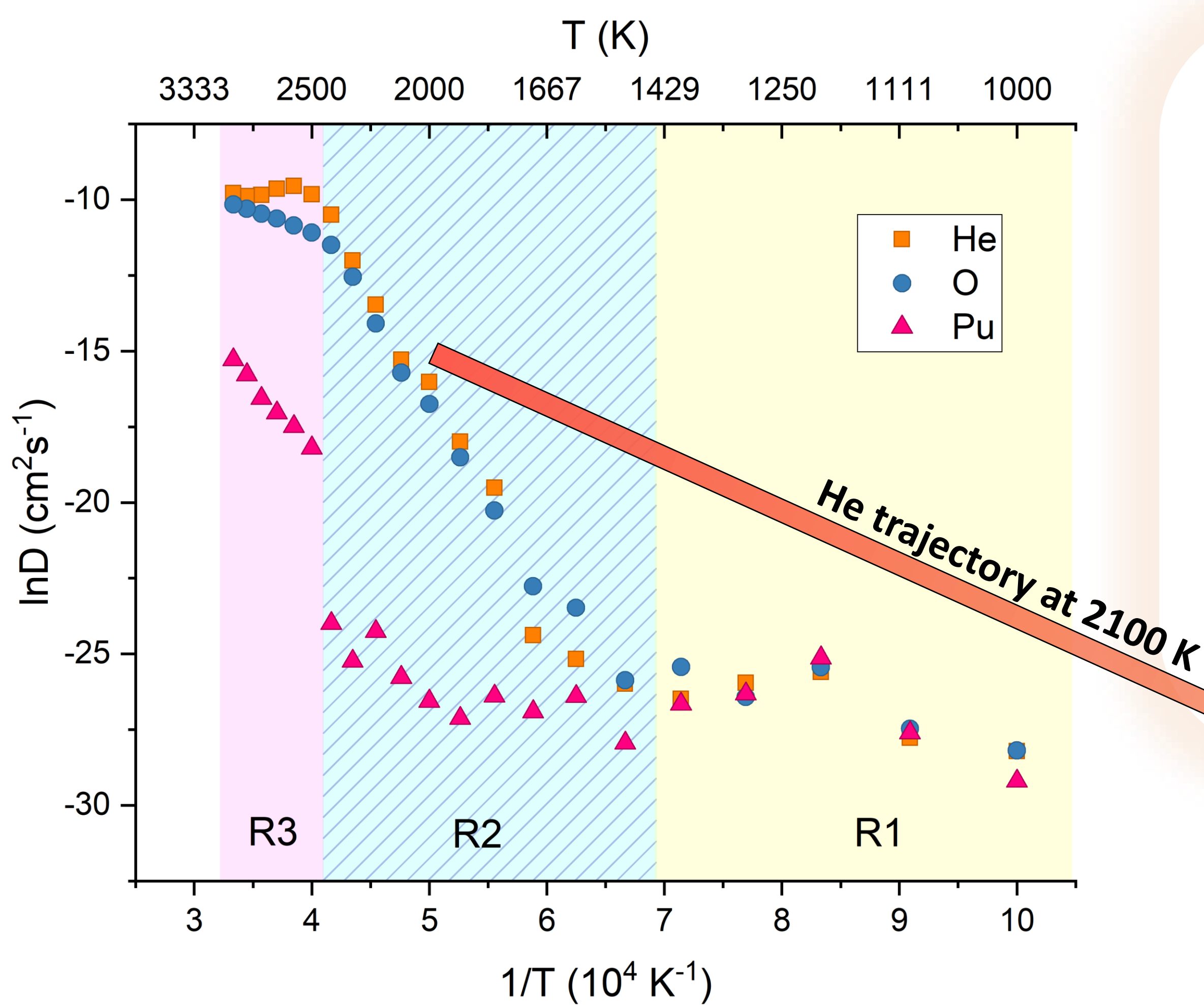


Fig 1: Diffusivity as a function of temperature for helium, oxygen and plutonium in PuO₂ with 0.5% He concentration.

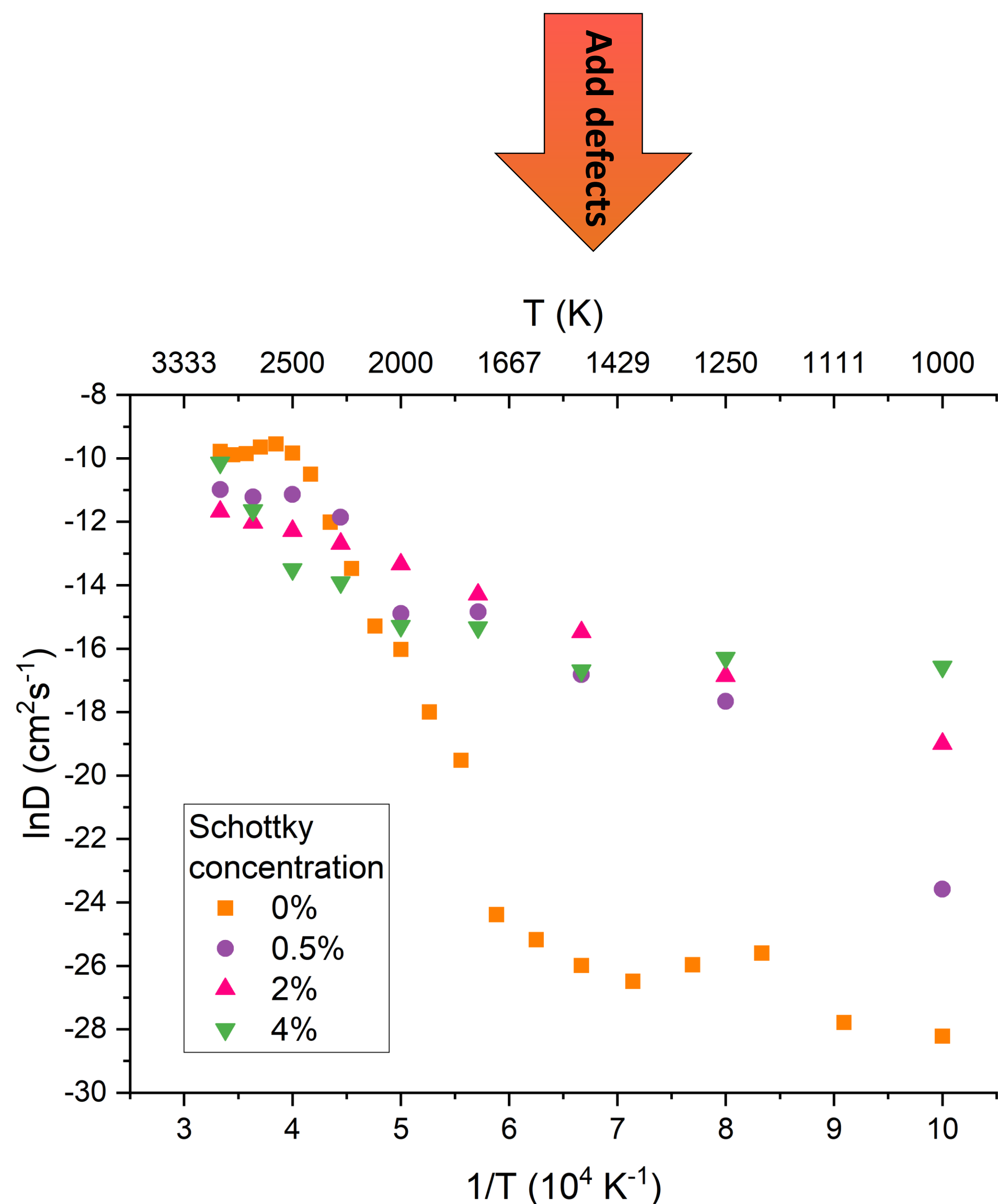


Fig 3: Helium diffusivity as a function of temperature for four different Schottky defect concentrations in PuO₂ with 2% helium concentration.

Defects

Structures with different concentrations of Schottky trios were generated, Fig. 3 displays the He diffusivity results. As the number of vacancies in the lattice increases, the diffusivity is greatly increased at lower temperatures. This is likely due to the reduction in energy barrier given by oxygen vacancy assisted migration, as O vacancies are already present in the system. Helium diffusion energy barriers were calculated from the Arrhenius behaviour exhibited in R2 in Fig. 3. The E_a values calculated were 5.3, 1.7, 1.1 and 1.0 eV for Schottky concentrations of 0, 0.5, 2 and 4% respectively. Although PuO₂ is stored in the lower temperature regime (R1), vacancies will be naturally be present due to irradiation events so that He diffusion will occur at a faster rate than in the vacancy-free system.

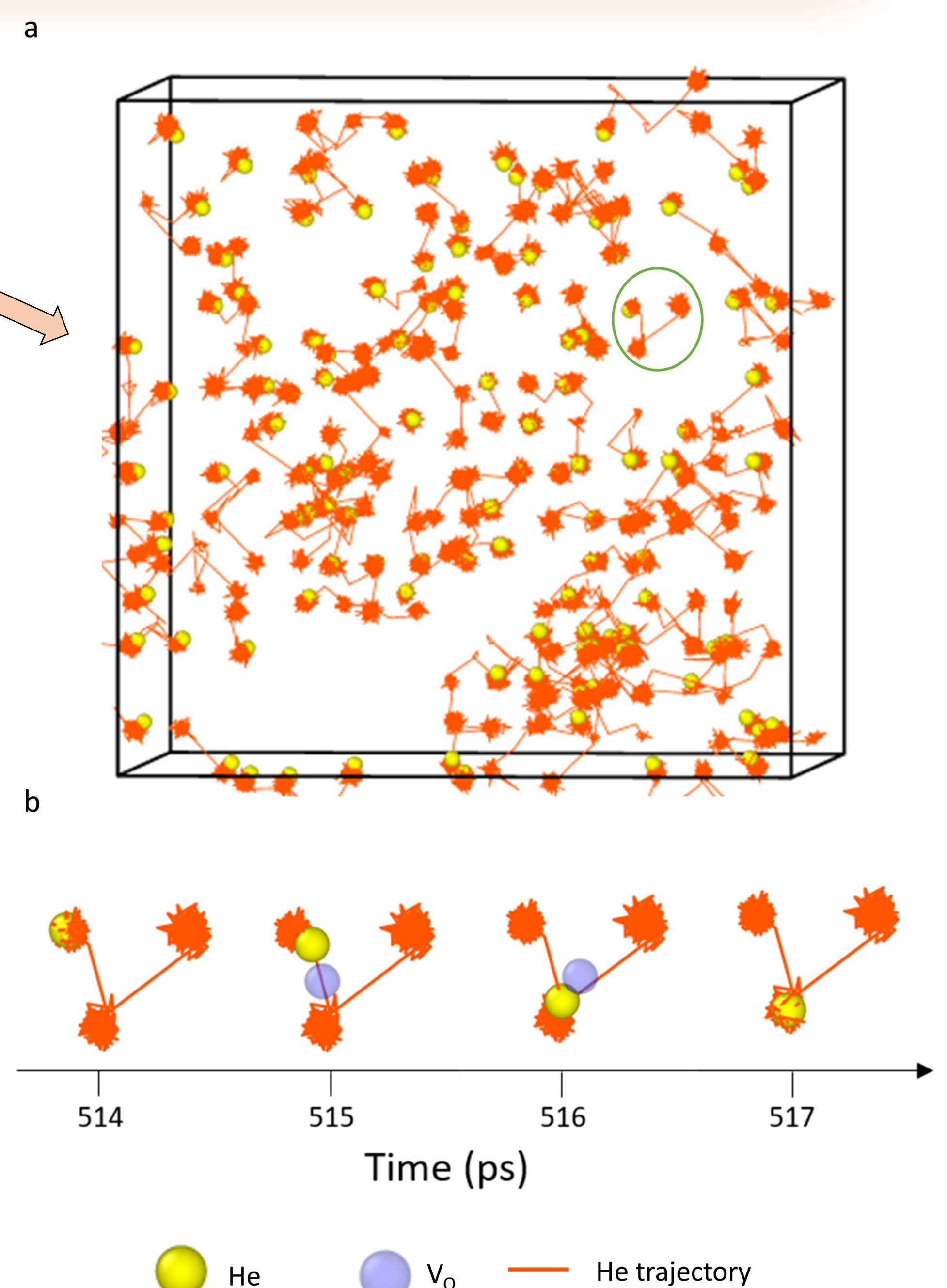


Fig 2: Trajectories of He atoms in initially defect-free PuO₂ at 2100 K. a) displays the trajectory of all He atoms over a period of 1ns. b) displays a snapshot of an inter-site hop by a He atom from the area circled in green in a). The time period in b) is 514-517 ps. It can be seen that at 515 ps an oxygen vacancy is generated in the vicinity of the helium and the helium uses this to migrate to a neighbouring OIS.

Conclusions

In defect free PuO₂, He exhibits limited diffusive behaviour until the temperature exceeds 1500 K. However, we have found that when vacancies are present within the lattice, the He diffusion energy barrier is significantly reduced and He atoms exhibit diffusive behaviour at lower temperatures. Therefore whilst the storage of PuO₂ will be at temperatures well below 1500 K, due to the presence of defects within the lattice we suggest that He will be mobile during storage. The main He diffusion mechanism proposed is oxygen vacancy assisted inter-site hops with helium and oxygen having comparable diffusion rates.

References: [1] W. G. Wolfer, Los Alamos Sci., 2000, 26, 274–285, [2] H Mehrer, Diffusion in Solids, Springer, 2007, [3] M. W. D. Cooper, S. T. Murphy, M. J. D. Rushton and R. W. Grimes, J. Nucl. Mater., 2015, 461, 206–214. *The computations described in this poster were performed using the University of Birmingham's BlueBEAR HPC service.*

Introduction

The UK has a large stockpile of plutonium (Pu) which is predominantly stored at the Sellafield site. This material is in a range of chemical forms dependent on its origins and must be stored accordingly in order to ensure its long term safety. The UK's Pu is mainly derived from spent fuel sources, these being MAGNOX Reactor Spent Fuel – referred to as MAGNOX Material - and Advanced Gas Reactor (AGR) Spent Fuel reprocessed in the Thermal Oxide Reprocessing Plant (THORP) – known as THORP Material. Both of these material groups are stored in a “Russian Doll” type arrangement with the material packaged inside a central canister which is itself contained within successive packages. Pu material is stored in a variety of waste forms though this project will focus on material in the PuO₂ powdered form.

A 1999 literature study by Lloyd of the Los Alamos National Laboratory (LANL) highlighted concerns with the storage methods employed for the MAGNOX and THORP Material. [1] The potential for can pressurisation caused by generation of hydrogen and oxygen was theorised by Lloyd. It was believed that this increase in internal pressure could lead to can rupturing over extended storage periods. In 2000 Bailey et al. [3] identified the two most likely causes of this pressurisation to be the Decomposition and Desorption of Adsorbed Species – each contributing 200-300 psi to the internal pressure increase.

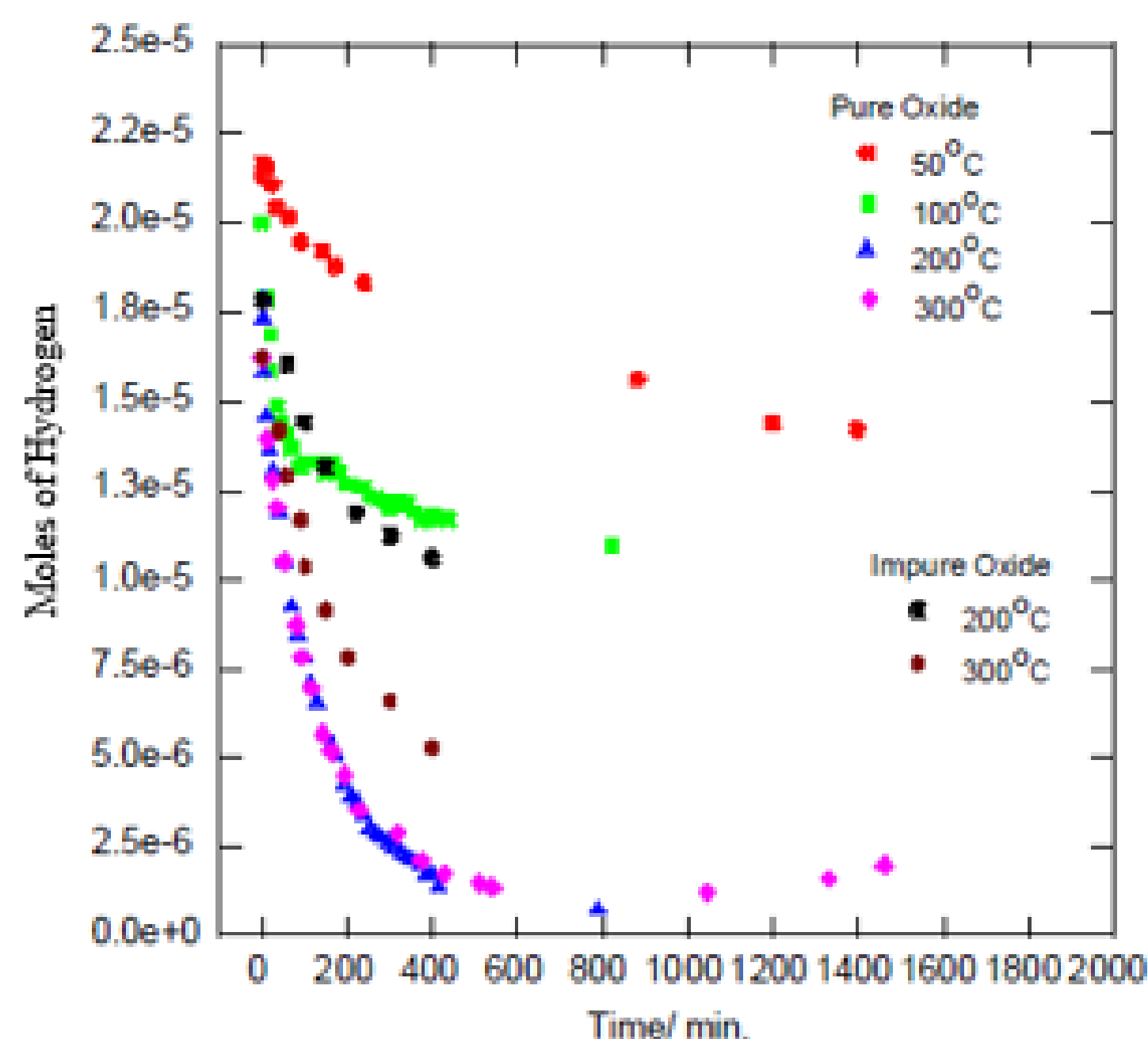


“Figure 1 – Russian Doll Type storage cans for THORP Material storage” [2]

Experimental Data in Literature

However, examination of canisters of a range of storage ages has revealed lower than expected levels of pressurisation across the range. This could suggest that the estimated impact of can pressurisation has simply been exaggerated, however, it is theorised that there is a counter process in effect to reduce the internal pressure of the canisters. A prime candidate for this counter process is the recombination of hydrogen and oxygen to form water. Morales (LANL) completed experimental work to examine the rate of this hydrogen-oxygen recombination process over plutonium oxide powders – he believed that this recombination process was likely to occur due to its thermodynamic favourability and as such would lead to the levels of reduced pressurisation shown in the case studies. [4]

Morales’ work made use of Pressure-Volume-Temperature (PVT) apparatus to enable the collection of rate determining data. He also compared the reaction rates for recombination over pure and impure PuO₂ powders to determine if the powder itself had an impact on recombination rate. He concluded that, firstly, the final gas mixture was approximately stoichiometric which is consistent with the reformation of water even though it isn't seen within the gas phase. Secondly, the reaction rate for pure PuO₂ was faster than that of the impure PuO₂ which implies that there is a surface interaction in the reformation mechanism. This second point is further supported by the plateau in the rate at longer reaction times which is indicative of the blocking of reaction sites – likely by adsorbed water. A surface chemical mechanism seemed to be the most likely process for recombination in Morales’ opinion though he noted that there are avenues through which a radiolytic process could also be involved.

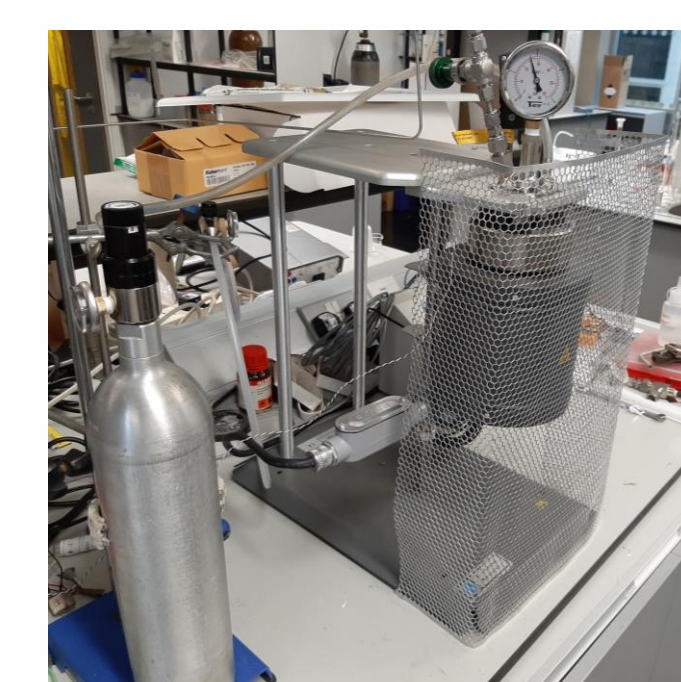


“Figure 2 – Plots of the pressure-time curves measured for both the pure and impure oxides as a function of moles of hydrogen consumed during the experiments” [4]

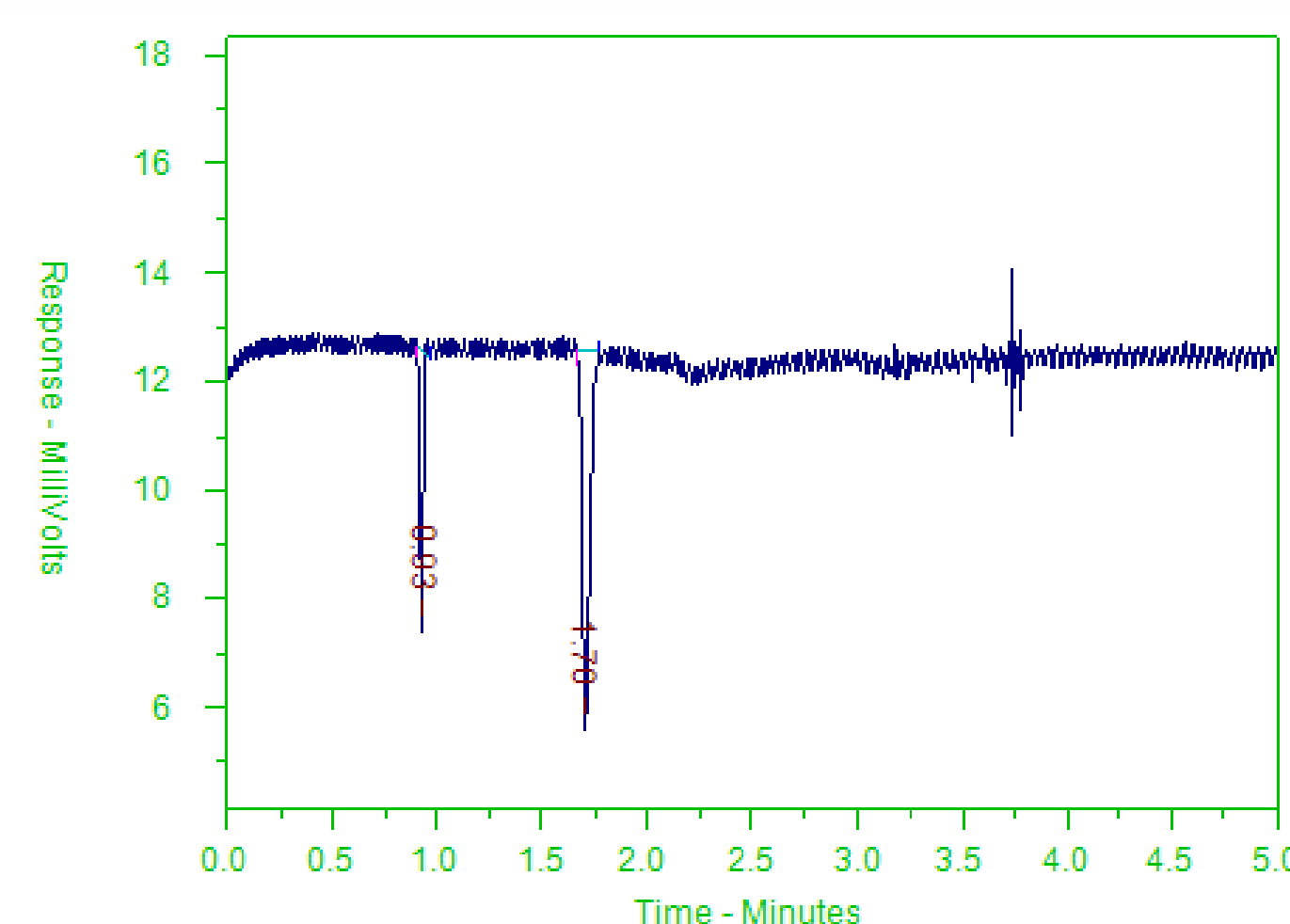
Experimental Work

Experimental work on this project employs an Agilent 5890 Series II Gas Chromatograph (GC) equipped with a Thermal Conductivity Detector (TCD). A custom valve sampling system is used to collect headspace samples from a heated pressure vessel containing bespoke gas mixtures of hydrogen, oxygen and argon over cerium oxide powder.

The vessel is heated through a ramping profile from room temperature to 350 °C. Samples are collected throughout in order to examine the impact of increasing temperature on reaction rate. These experiments are performed in a non-active environment initially, though there are plans to make use of active environments and/or active powders in the future to explore how the addition of initiating species could affect the reaction pathway. The system in question is highly complex so it is important in the initial stage to isolate as many factors as possible to see the individual impact each plays on the system as a whole.



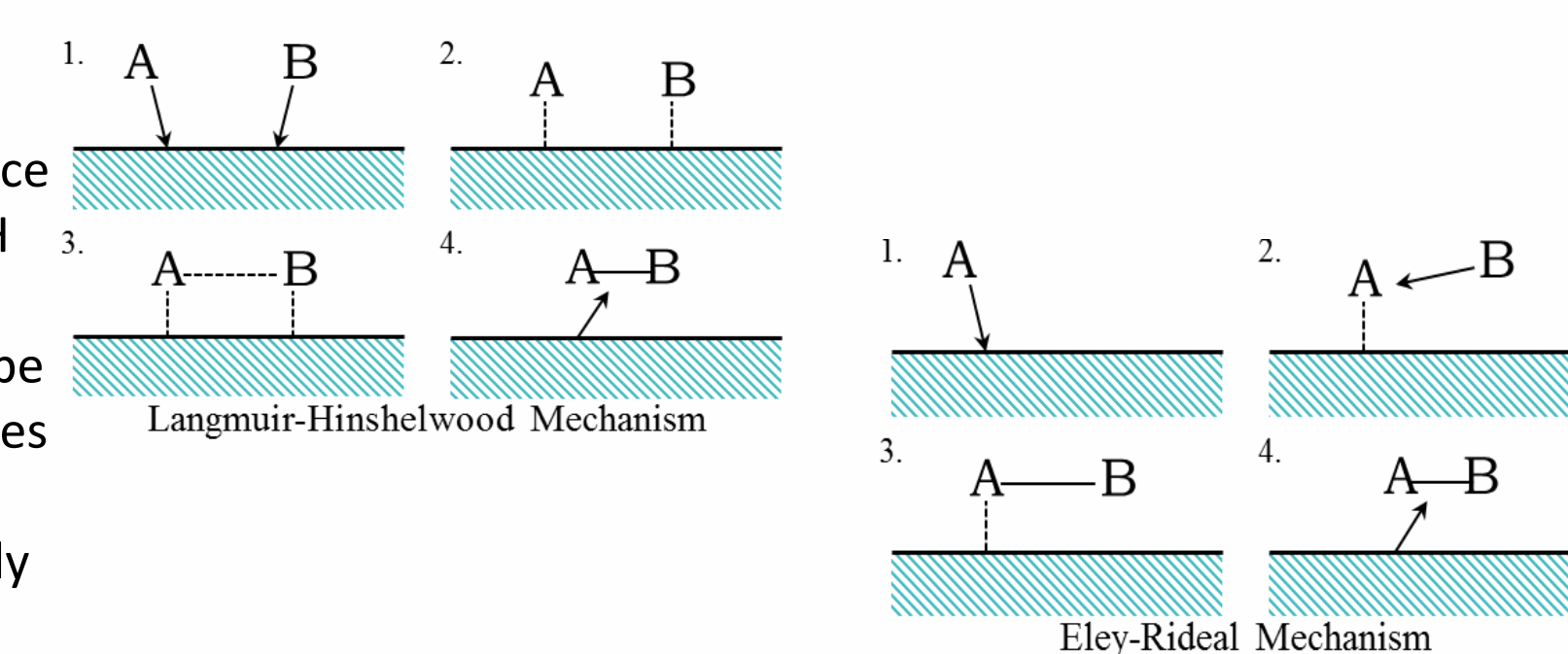
“Figure 3 – Heated pressure vessel with connected bespoke gas mixture cylinder (above) and Agilent 5890 Series II GC with custom gas sampling valve rig (below)”



“Figure 4 – Initial data showing system in operation - chromatogram showing 0.4 : 1 : 98.6 H₂ : O₂ : Ar gas system in the absence of metal oxide powder”

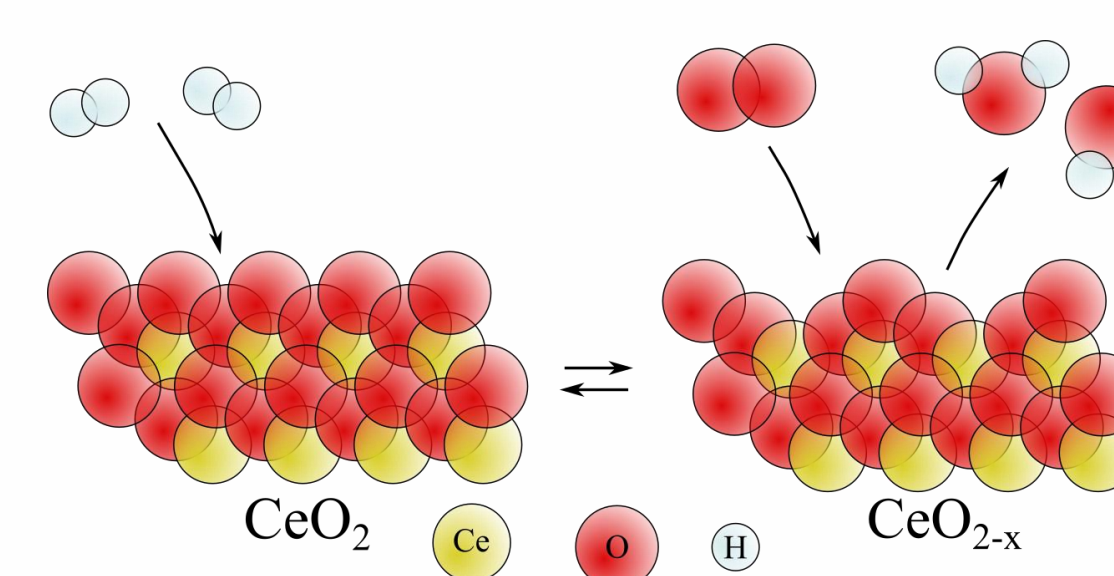
Mechanistic Analysis

Two surface mechanisms fitted Morales’ data closely, these were the Langmuir-Hinshelwood (L-H) and Eley-Rideal (E-R) mechanisms. Both mechanisms function similarly with initial surface binding of at least one of the reactants. The L-H mechanism involves binding of both species A and B and as such the rate of this reaction will be dependent on the concentrations of both species A and B whereas for the E-R mechanism only species A binds to the surface meaning that only the concentration of species A will be rate controlling. In the case of the hydrogen-oxygen recombination process species A represents hydrogen and species B represents oxygen. Concentration based experiments could be used to determine which of these mechanisms is in effect – the L-H would show an initial increase in rate until the stoichiometric point (2:1 hydrogen:oxygen) is passed after which the rate would decrease whereas a plateau would be observed beyond this point for the E-R mechanism. These experiments will form the initial phase of this project's experimental phase.



“Figure 5 – Langmuir-Hinshelwood and Eley-Rideal mechanism diagrams”

In addition to the work of Morales, Lloyd and Bailey the work of former PhD candidates has also been of great value in exploring the potential mechanisms for the recombination process. Whilst working at the Dalton Cumbria Facility (DCF) Thomas Donocliift examined a third potential mechanism for recombination which involved an interaction with the surface. [5] This mechanism was the Mars van Krevelen (MvK) mechanism which Donocliift believed was in effect for his experiments using CeO₂ as a simulant in place of PuO₂ powder.



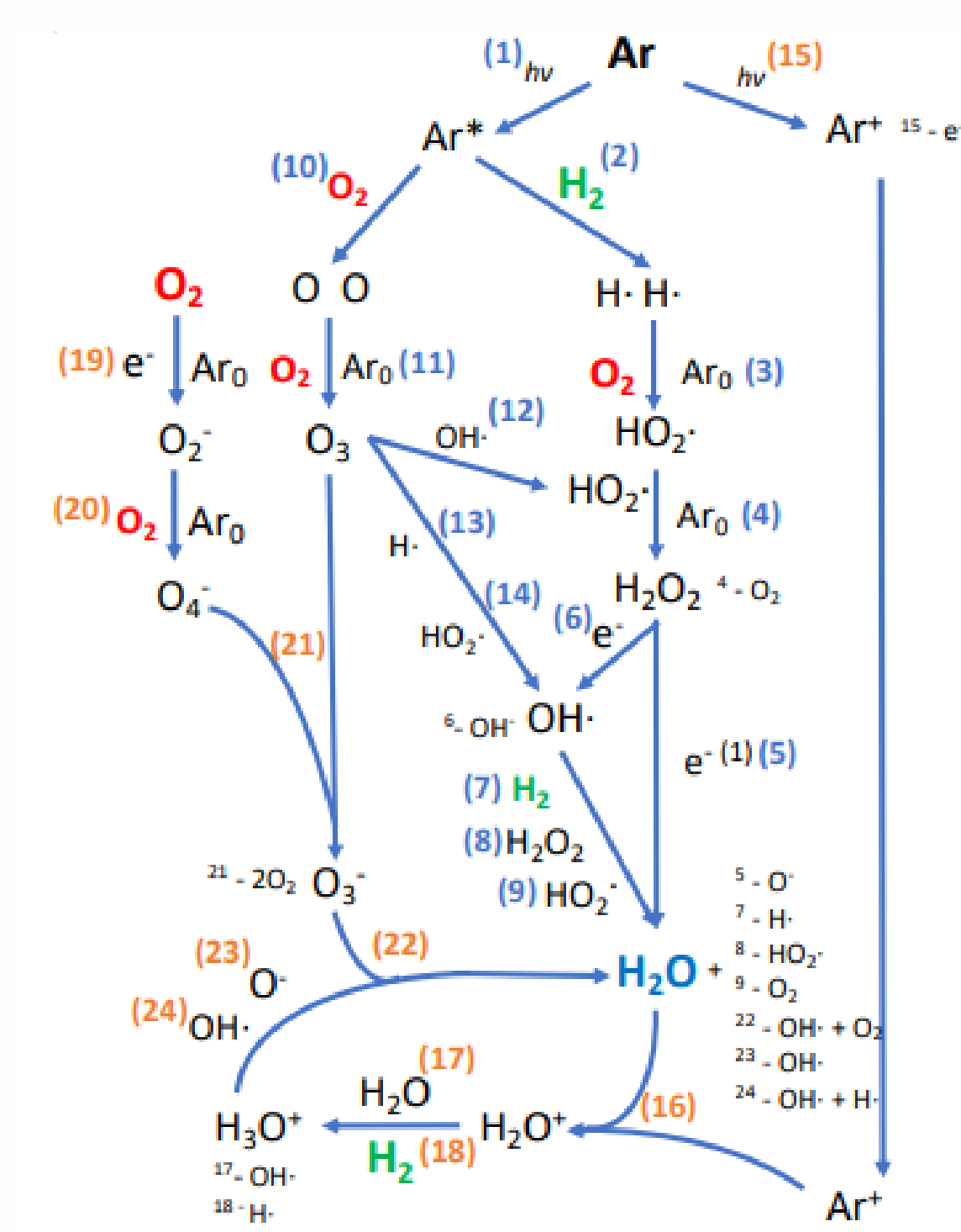
“Figure 6 – Mars van Krevelen mechanism diagram” [5]

As opposed to the L-H and E-R mechanisms where hydrogen and oxygen from the gas phase interact directly using the powder as a platform, the MvK mechanism utilises these components in isolation. The CeO₂ donates oxygen from the surface to hydrogen from the gas phase forming water – this leaves the CeO₂ surface in a temporarily reduced state (CeO_{2-x}) – oxygen from the gas phase is then taken into the powder to oxidise it back to its stoichiometric form.

Donocliift conducted experiments using a continuous flow type reactor to examine how changes in the concentration of either hydrogen or oxygen could impact the rate of hydrogen consumption. In these experiments the concentration of the varied component was moved through an approximate range of 5x10⁻⁵ mol dm⁻³ to 4.5x10⁻⁴ mol dm⁻³ whilst the other component was held at a fixed concentration of 4.3x10⁻⁴ mol dm⁻³. This data was then plotted as shown in the graphs to the left. It can be seen that when hydrogen concentration is fixed and oxygen is varied that the rate of hydrogen consumption increases initially before plateauing at around 2.1x10⁻⁴ mol dm⁻³. However, when hydrogen concentration is varied against a static oxygen concentration the graph is linear across the full range.

Donocliift used this data as evidence in support of the MvK mechanism as it shows dependence on the concentration of hydrogen, however, this could also be used as support for an E-R mechanism where hydrogen was the species bound to the surface (as would be the most logical arrangement).

Further examination of the data however highlighted that the point of plateau in the varied oxygen graph is approximately 2.1x10⁻⁴ mol dm⁻³ which is half of the concentration of hydrogen in the vessel, or put alternatively, the concentration of hydrogen to oxygen is 2:1 – the same as the stoichiometry of water. The same point in the other experiment would therefore occur at 8.6x10⁻⁴ mol dm⁻³, however, this point is beyond the experimental range used. It is therefore plausible that the plateau in this scenario would appear and that the observed linear range is simply the same linear range observed at the beginning of the varied oxygen experiments. Extending the experimental range over in order to observe if this plateau occurs will be the first priority of the experimental phase.



“Figure 7 – Reaction mechanism proposed by Messer (reaction numbers in blue represent phase one reactions and reaction numbers in orange represent phase two reactions)” [6]

In addition to Donocliift’s work, another PhD candidate – Darryl Messer’s research has also provided valuable insight into the experimental aspects of this project. [6] Messer also utilised a GC with TCD to examine fixed concentration atmospheres of hydrogen, oxygen and argon gases. Unfortunately due to the ongoing COVID-19 Pandemic Messer was unable to complete the volume of experimental work he had initially intended and as such there are some avenues of further testing that have been left unexplored which this project intends to examine in more detail.

Within the thesis Messer proposes a large multi-step mechanism for the reformation of water within the system which consists of two phases which transition according to the experimental rate data acquired earlier in the project. The data presented makes a strong argument for a mechanistic change during the process as is highlighted, however, the data also supports the presence of an E-R type mechanism as suggested previously by Morales which is not explored – again this is an area which this project intends to examine in more detail.

References

- [1] - J. A. Lloyd, Literature Search on hydrogen/oxygen Recombination and Generation in plutonium Storage Environments, 1999
- [2] - L. Jones, The Radiation Chemistry of Gases at the Interface with Ceramic oxides, The University of Manchester, 2015
- [3] - G. Bailey, E. Blumh, J. Lyman, R. Mason, M. Paffett, G. Polansky, G. D. Roberson, M. Sherman, K. Veirs and L. Worl, Gas Generation From Actinide oxide Materials, 2000.
- [4] - L. Morales, Preliminary Report on the Recombination Rates of hydrogen and oxygen over Pure and Impure plutonium oxides, Los Alamos Tech. Rep., 1999
- [5] - T. A. Donocliift, A Catalytic Approach to H₂ and O₂ Recombination over PuO₂ and PuO₂ Surrogates - PluteFutures Presentation.
- [6] - D. Messer, Radiolytic Recombination of H₂, O₂ and N₂ over PuO₂ Surrogate Materials, The University of Manchester, 2021

Acknowledgements

I'd like to take this opportunity to thank the Nuclear Decommissioning Authority for providing the funding to make this research possible.

The Characterisation of Nanopowders for use as Plutonium Dioxide Surrogates

Daniel L Mabon

Supervisors: Prof Colin Boxall, Dr Robin Orr (NNL), Dr Helen Steele (Sellafield)

Introduction and Proposed Methodology

- The UK has the world's largest civil storage of Separated Plutonium in the world at ~140 tons
 - It is stored as Plutonium Dioxide powder in stainless steel cans, which can pressurize over time. The least studied route of pressurisation is Helium accumulation due to α decay
- A cheap & accessible method of manufacturing helium infused plutonium dioxide surrogate was required
- Methodology based of Maugeri et al. (2009) involves Cerium Dioxide Nanopowder in a high-pressure autoclave. Autoclave conditions: 550 °C and 150 bar helium atmosphere
- Before infusion sample will undergo Characterization techniques at a range of temperatures to provide baseline:
 - Raman Spectroscopy (Figure 1)
 - Scanning Electron Microscopy (Figure 2)
 - Thermogravimetric Analysis with Mass Spectrometry (Figure 3)
 - X-Ray Diffraction Analysis (Figure 4)
- Infused Sample will undergo same techniques to allow comparisons to be made, and a conclusion on the success of the infusion methodology to be made
 - Other surrogates, such as Yttria-Stabilised Zirconia and Urania, will be tested

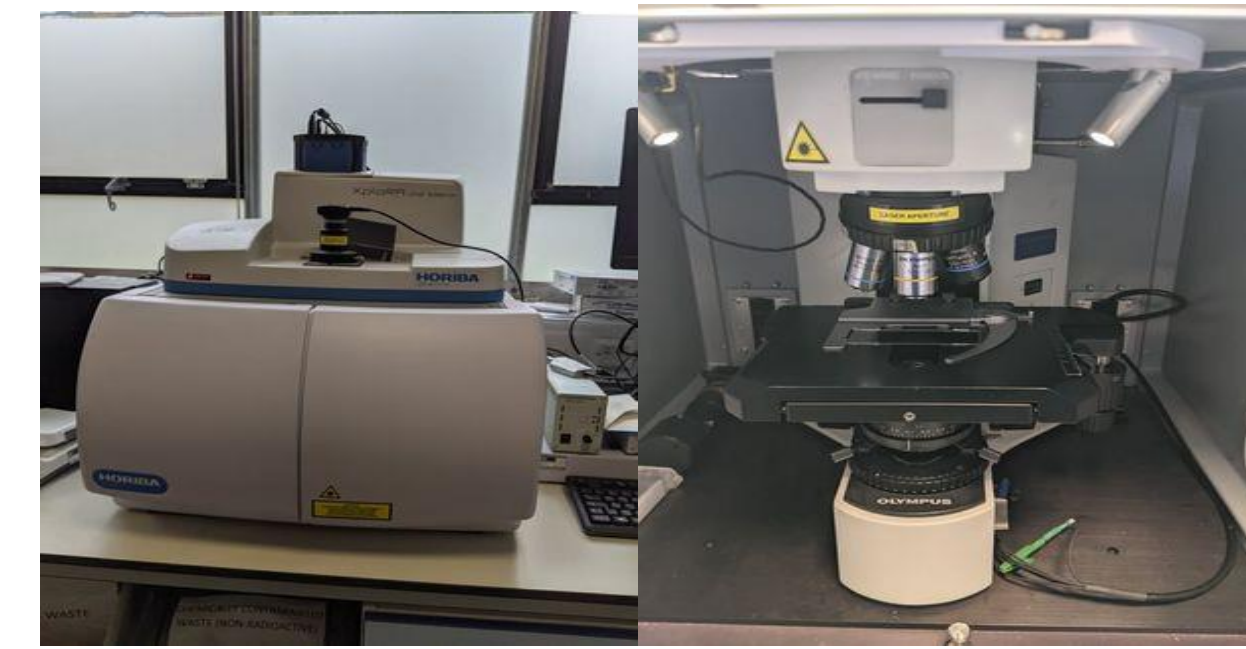


Figure 1: Raman Spectrometer in the UTGARD Lab at Lancaster University



Figure 2: Scanning Electron Microscope (SEM) in the UTGARD Lab at Lancaster University

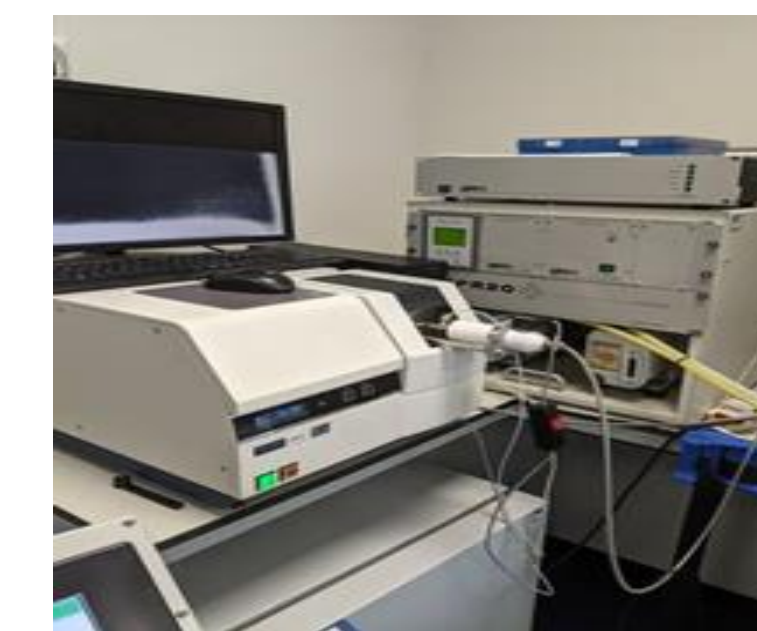


Figure 3: Thermogravimetric Analyzer (Left) and Mass Spectrometer (Right)



Figure 4: X-ray Diffractometer in the Chemistry Department at Lancaster University

Analysis of the Cerium Dioxide Sample

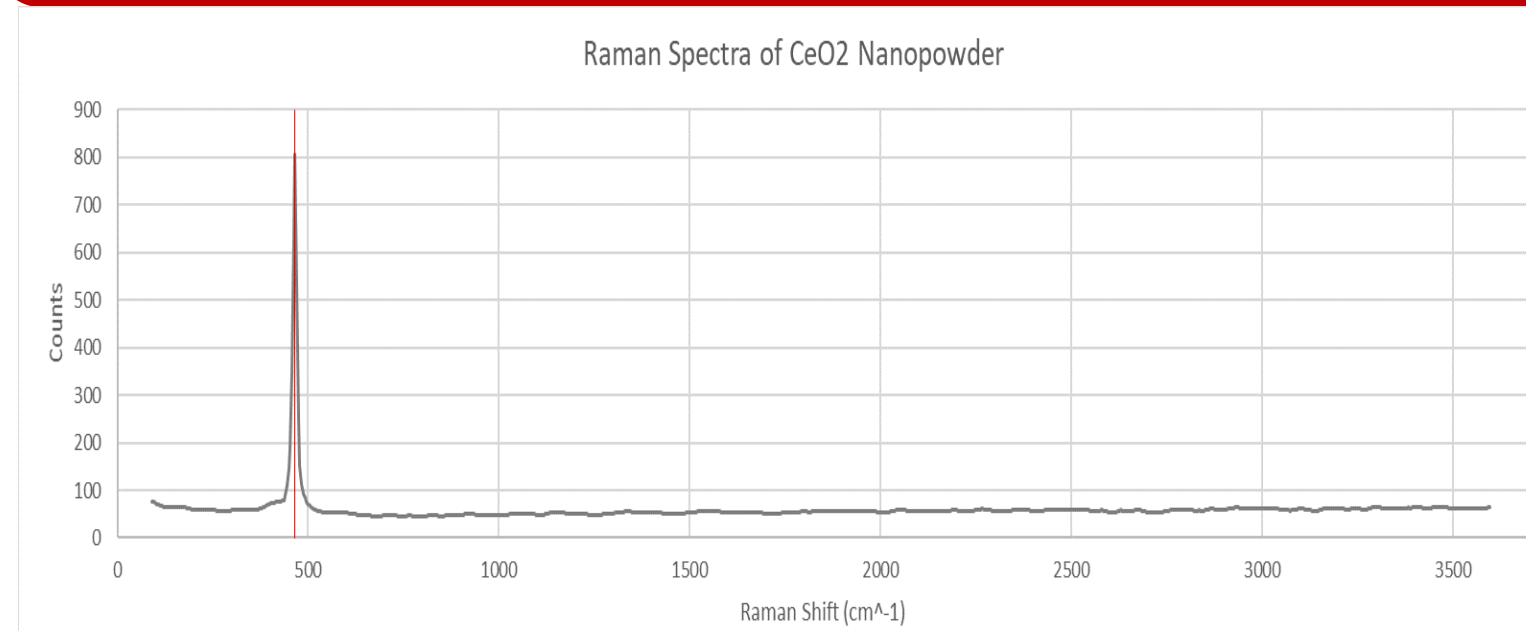


Figure 5: Raman Spectra of the Cerium Dioxide nano-Powder sourced from Sigma-Aldrich

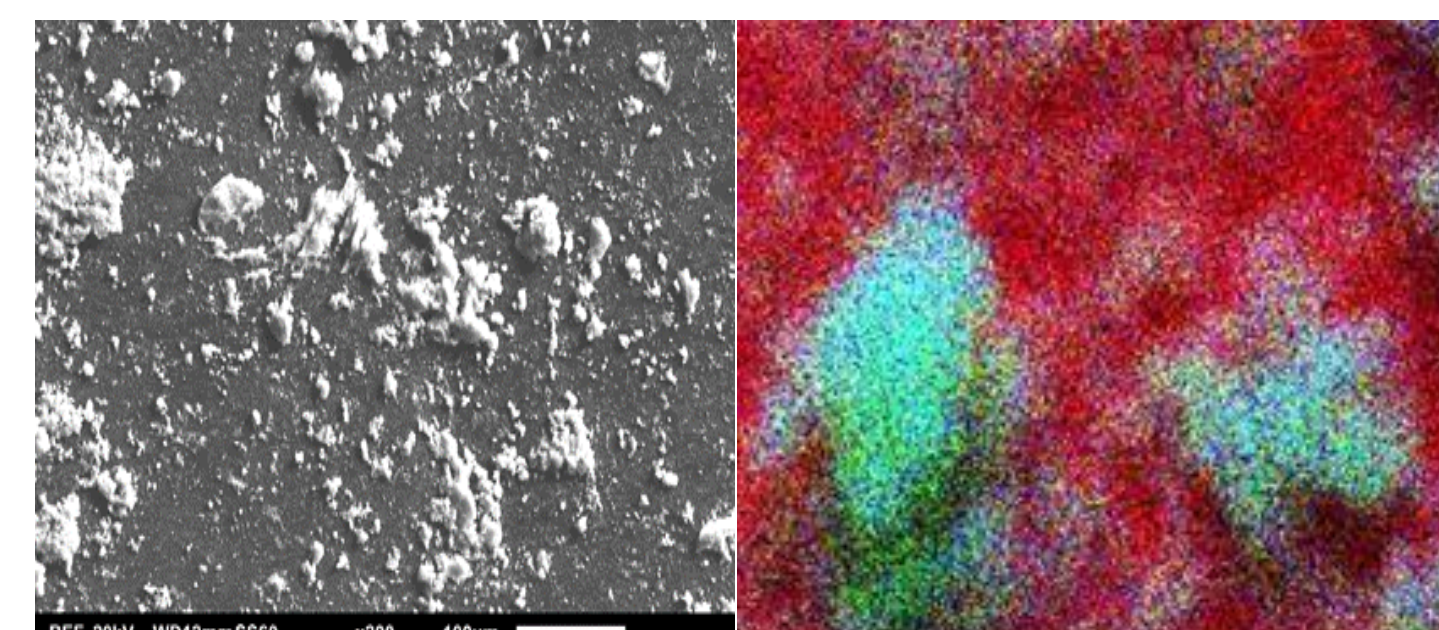


Figure 6: SEM Image of the CeO₂ Nano-Powder (X200 Magnification) (Left), Composition image (Right, carbon - red, cerium - green, oxygen - blue)

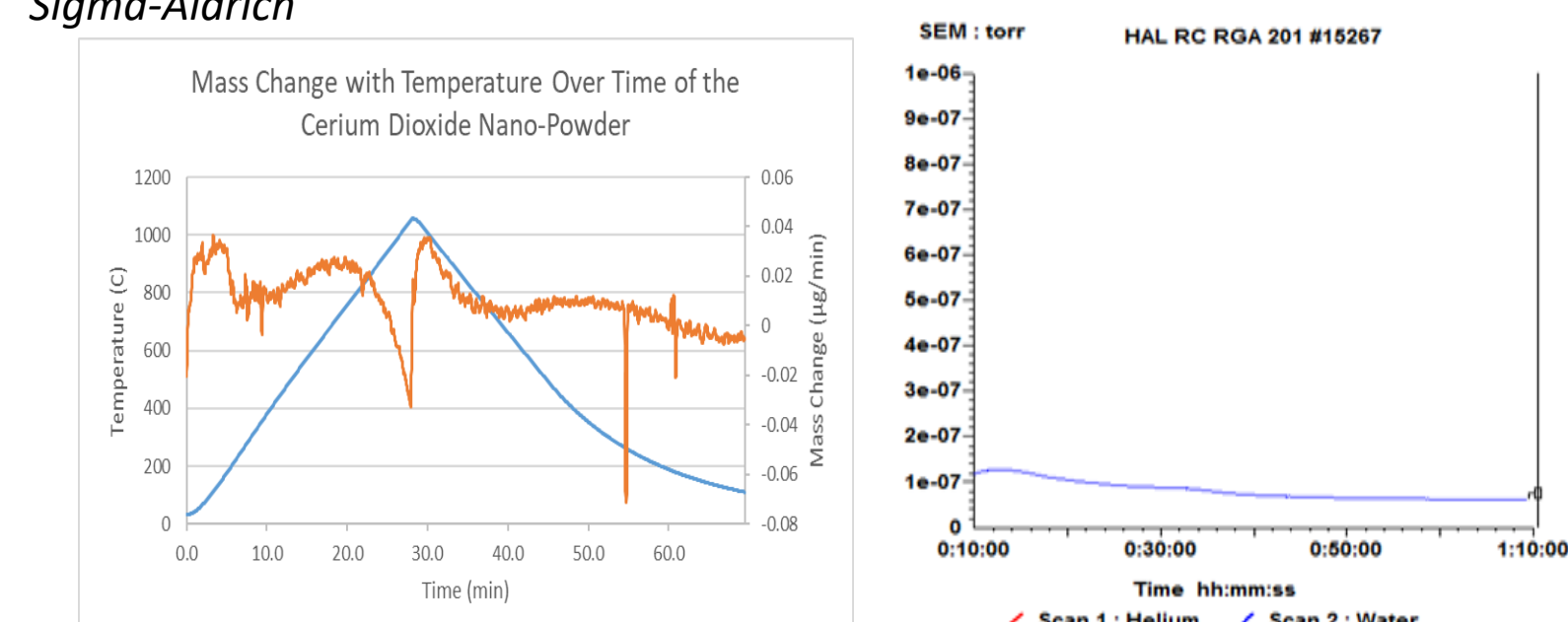


Figure 7: Mass Change with change in temperature over time of the Cerium Dioxide sample (Left), Detected Pressure of Water and Helium using an air gasflow into the Mass Spectrometer

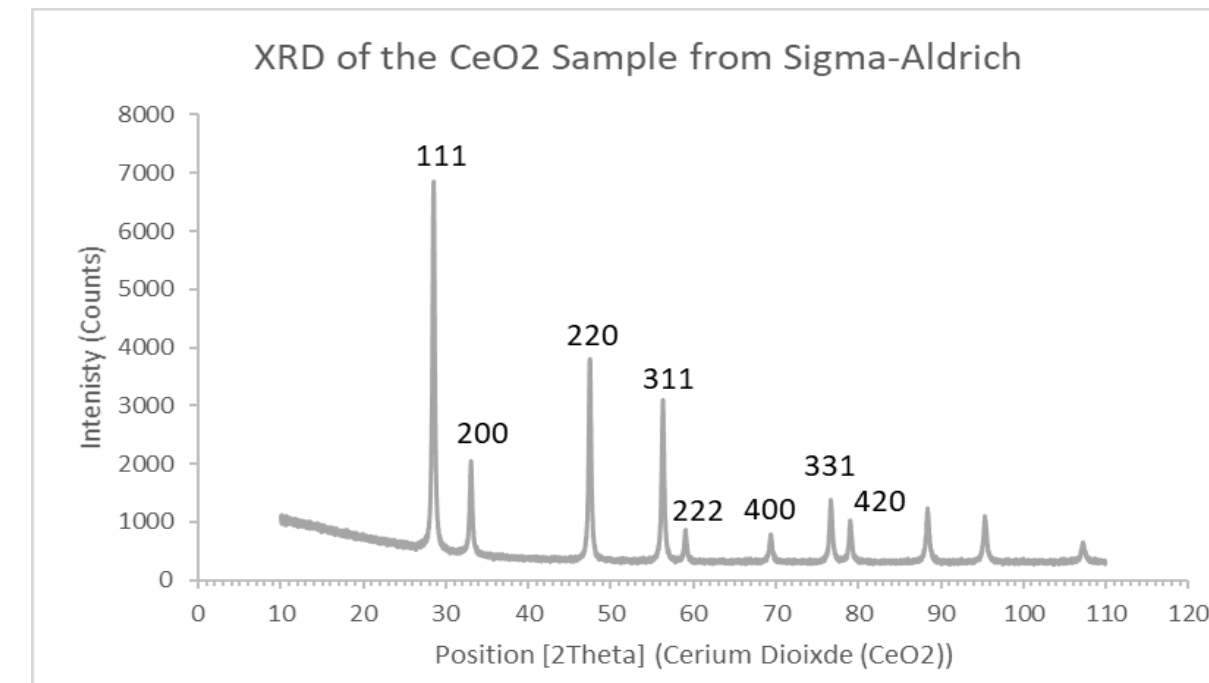


Figure 8: X-Ray Diffraction Pattern of the Cerium Dioxide Sample.

- Samples sourced from Sigma-Aldrich
- Cerium Dioxide Nano-Powder of <25 μm particle size
- Characterization Techniques confirmed this
- Raman Spectroscopy (Figure 5) has one peak at 465 cm^{-1} which is the characteristic peak of the Ce-O-Ce symmetric vibration (Cui and Hope., 2015)
- SEM/EDX (Figure 6) confirms particle size as under 25 μm , and composition of Cerium and Oxygen
- TGA-MS (Figure 7) displays two mass changes with temperature:
 - First at 100 °C – MS suggest it is most likely water
 - Second at 800 °C – possible ejection of O to form CeO_{2-x}
- XRD (Figure 8) consistent with reflection from CeO₂ cubic fluorite structure:
 - (111), (200), (220), (311), (222), (400), (331) and (420)

Thermal Annealing of Ceria and Yttria-Stabilised Zirconia

- Ceria Nanopowder were thermally annealed at a range of temperature for a period of 2 hours
 - Temperature ranged from 500 °C to 1100 °C in 100 °C increments
- Methodology was also carried out with Yttria-Stabilised Zirconia (YSZ) nanopowder
- Characterisation Techniques were then carried out on the resultant samples
 - Due to equipment constraints, only SEM & Raman results obtained
- SEM results (Figure 9) indicate pre-sintering occurs between 1000 °C and 1100 °C in Ceria, but does not with YSZ (Figure 11)
- Limits the temperature that Ceria can be thermally infused with Helium
- Proposed Thermal Infusion of Helium will be carried out using the pressure vessel shown in Figure 10

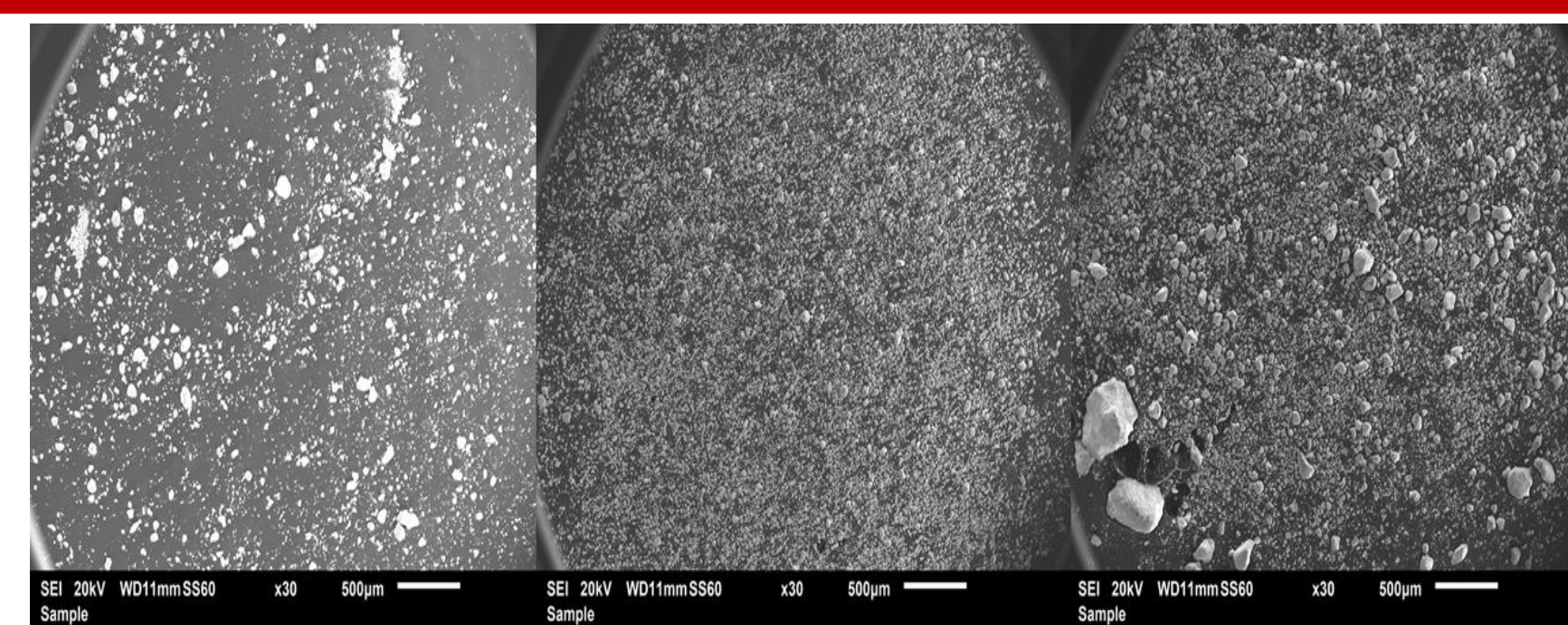


Figure 9: SEM of Ceria thermally annealed at different temperatures



Figure 10: High Temperature High Pressure Reactor Vessel Exterior (Left) and Interior (Right).

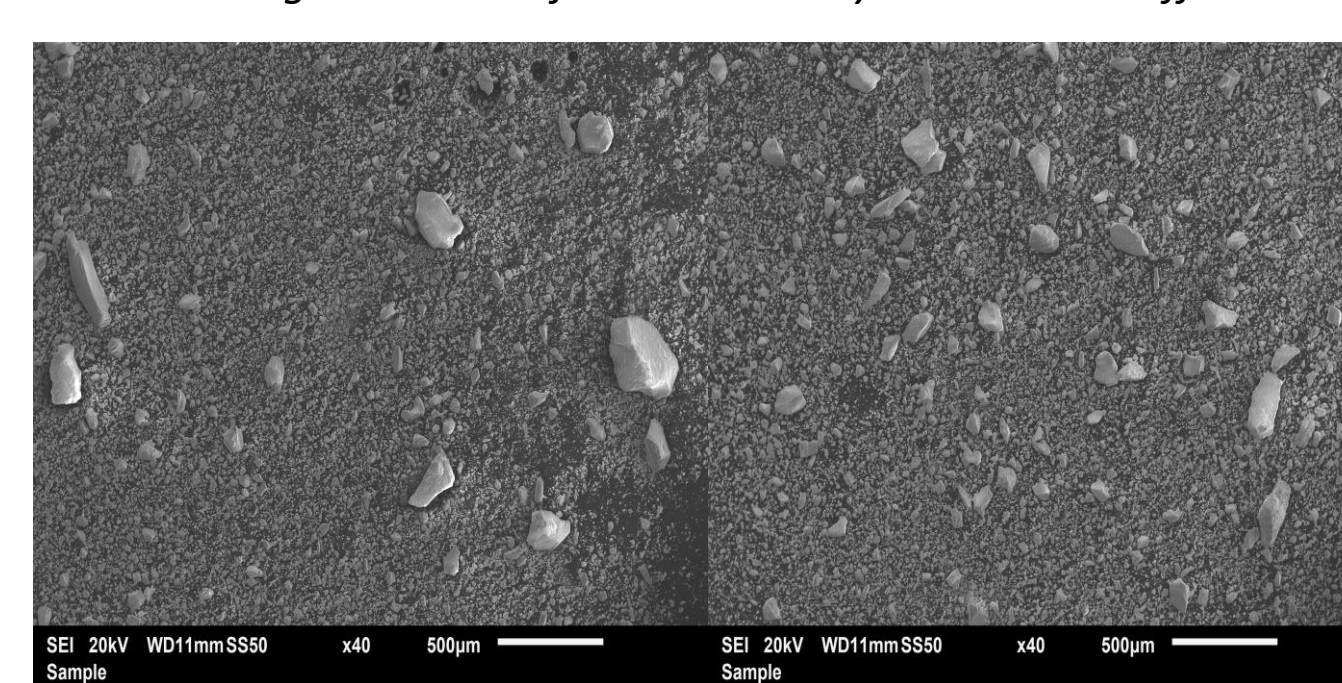


Figure 11: SEM of YSZ thermally annealed at different temperatures

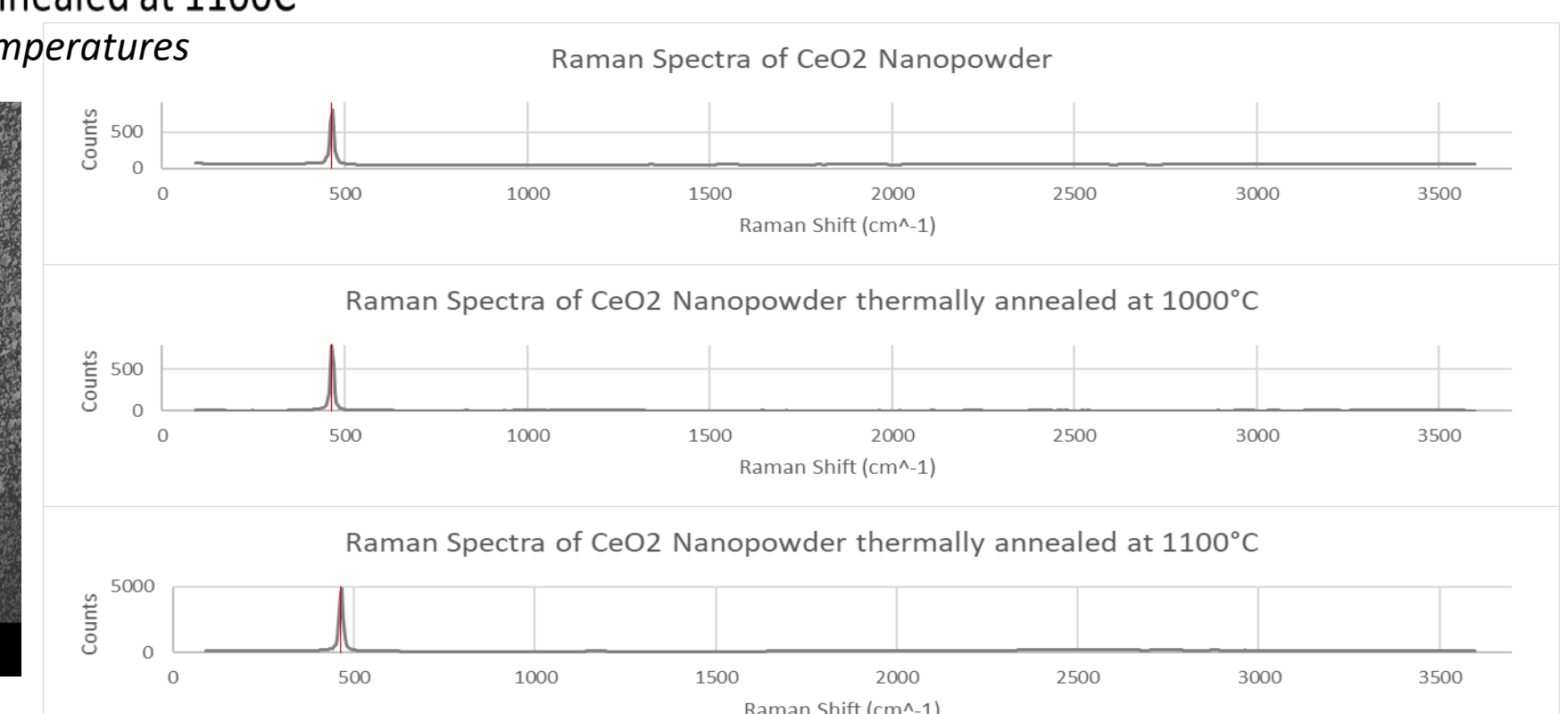


Figure 12: Raman Spectra of Ceria thermally annealed at different temperatures

Conclusions and Future Work

- Overall, the temperature range at which the thermal infusion of helium can be conducted without morphological change to the powders has been identified
- The results of the characterization techniques also provide a reasonable baseline comparison, so that the success of the infusion can be evaluated
 - Further Nanopowders, such as Thoria and Urania should be obtained for testing as well

References

Cui, J. and Hope, G., 2015. Raman and Fluorescence Spectroscopy of CeO₂, Er₂O₃, Nd₂O₃, Tm₂O₃, Yb₂O₃, La₂O₃, and Tb₄O₇. *Journal of Spectroscopy*, 2015, pp.1-8.
 Maugeri, E., Wiss, T., Hiernaut, J., Desai, K., Thiriet, C., Rondinella, V., Colle, J. and Konings, R., 2009. Helium solubility and behaviour in uranium dioxide. *Journal of Nuclear Materials*, 385(2), pp.461-466.



What is Colloidal Silica (CS)?

- Novel grouting material used in nuclear decommissioning as an **injectable hydraulic barrier**

- Prevents release of contaminants in soil to the environment via groundwater flow

- Starts as a **water-like liquid: 5 mPa·s**
- Mixed with salt solution (usually **NaCl**) and injected
- Stays water-like for a desired time
- Transition to rigid gel

How does it work?

Why is it so exciting?

Very low hydraulic conductivity
 10^{-9} m/s for grouted sand

Precisely controllable gel time

Non-toxic & eco-friendly



Uses minimal injection pressures

- No risk of ground disruption

Sorption of radionuclides,

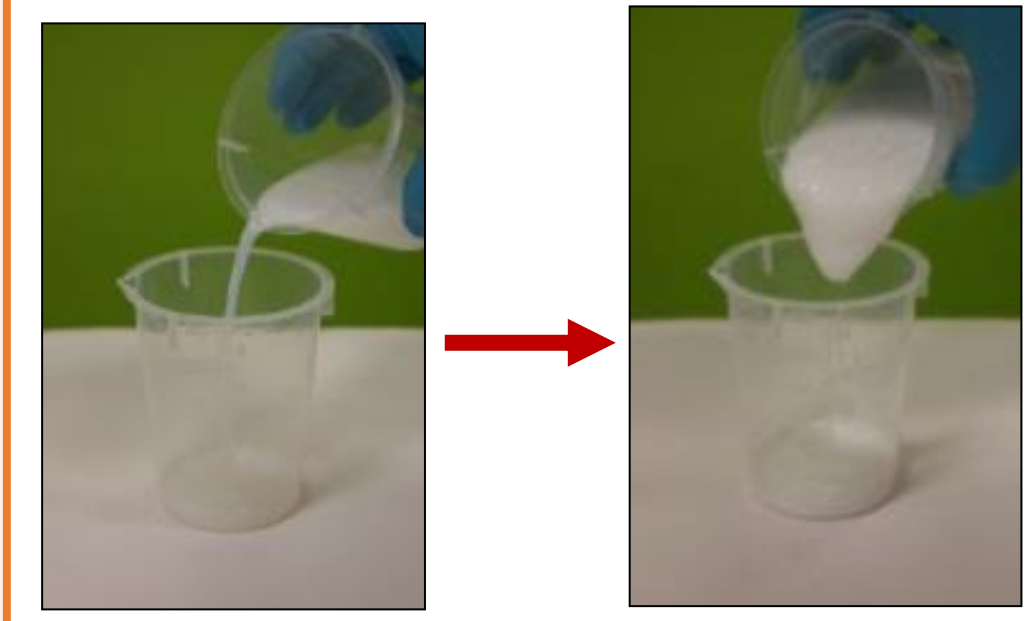
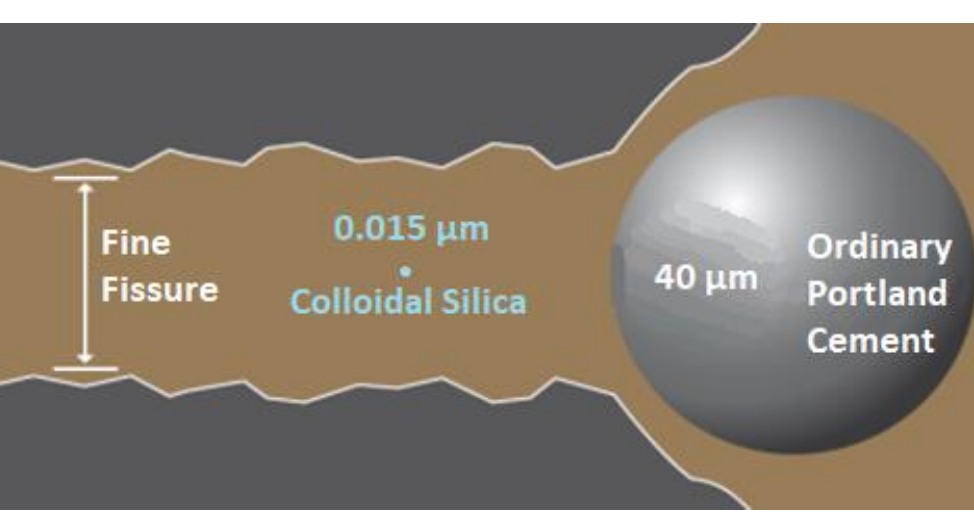
- E.g. **Cs-137, Sr-90**



Inexpensive

- Comparable to concretes

nm particle size allows permeation of finest fissures



My Project

CS already an excellent hydraulic barrier... **but can it do more?**

Can easily modify CS in various ways to potentially...

- Specialise properties for particular grouting applications:
 - Chemical barrier
 - Hydraulic barrier
 - Mechanical strength

- Specialise for **specific soil environments**

- Open CS up to **new nuclear applications**

Recent Experiments

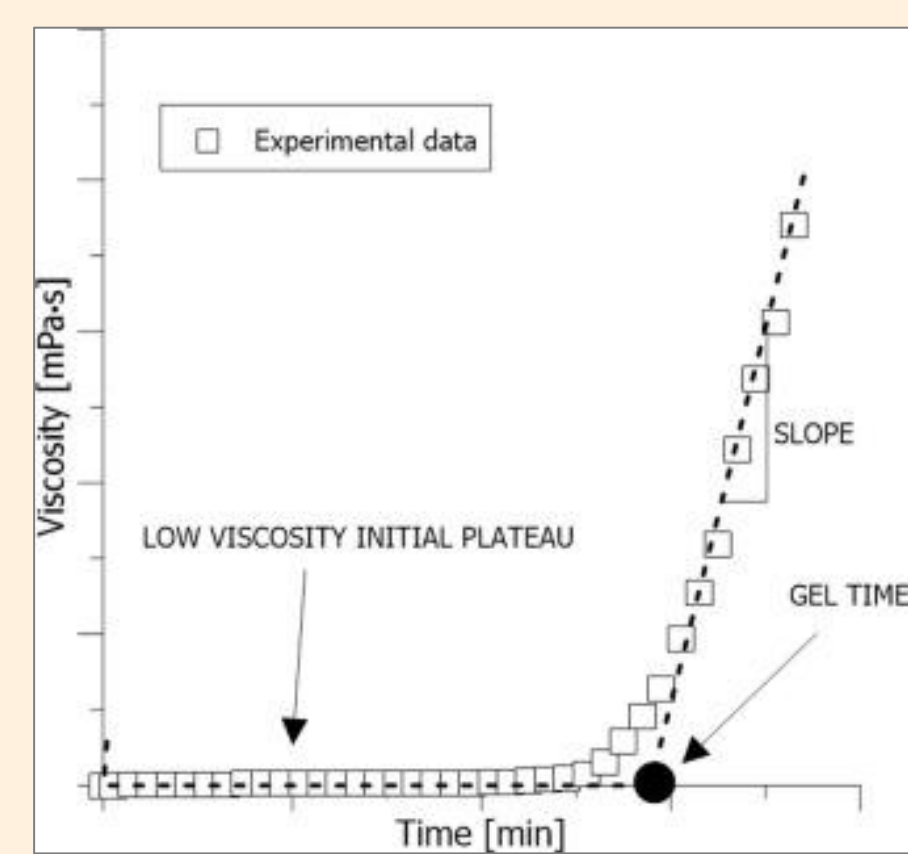
- Compression tests on sand grouted with Colloidal silica variants

AIM:

- Improve strength and/or flexibility using different factors and additives

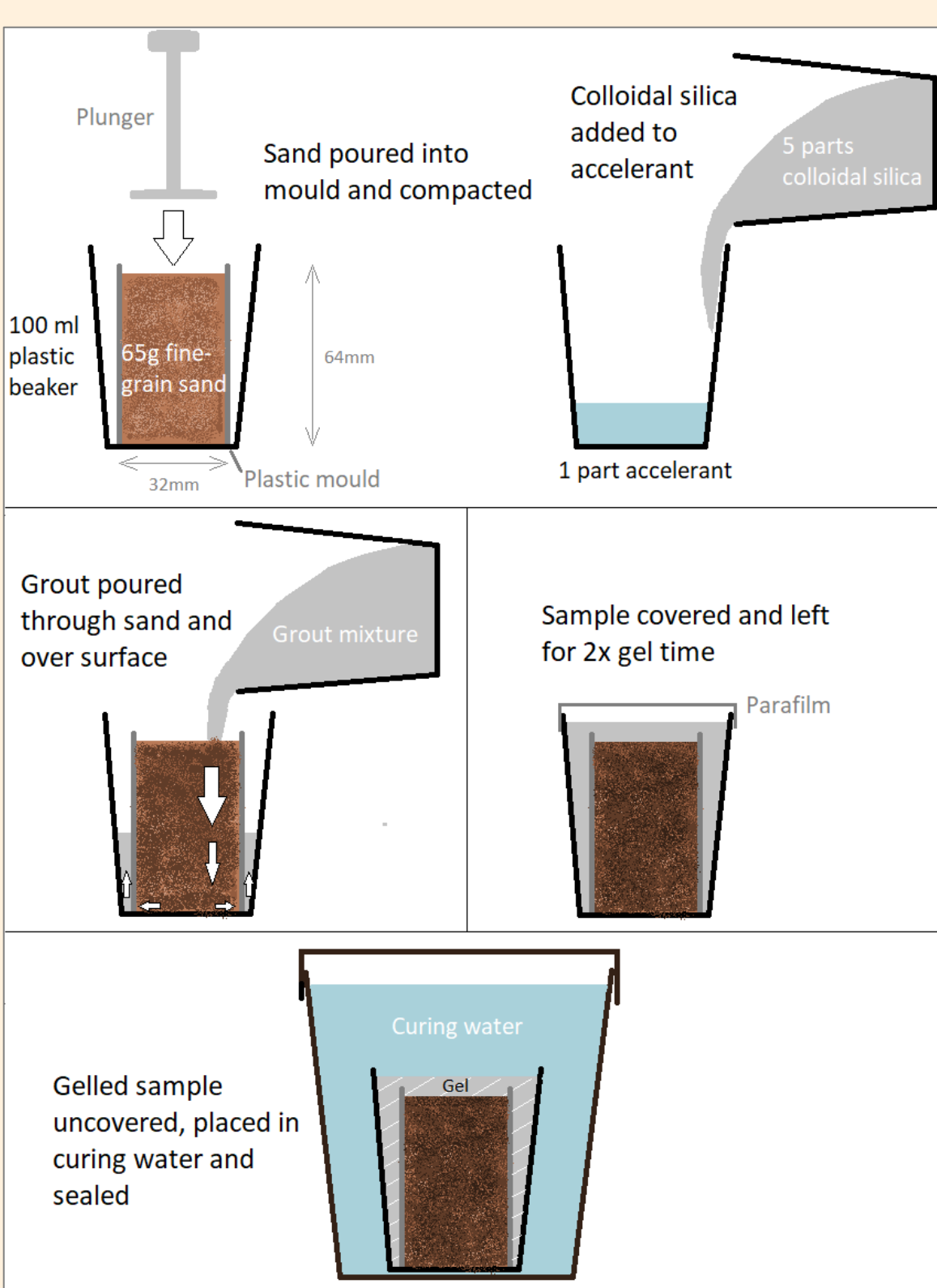
Experimental Method

Viscometer to measure gel-time:

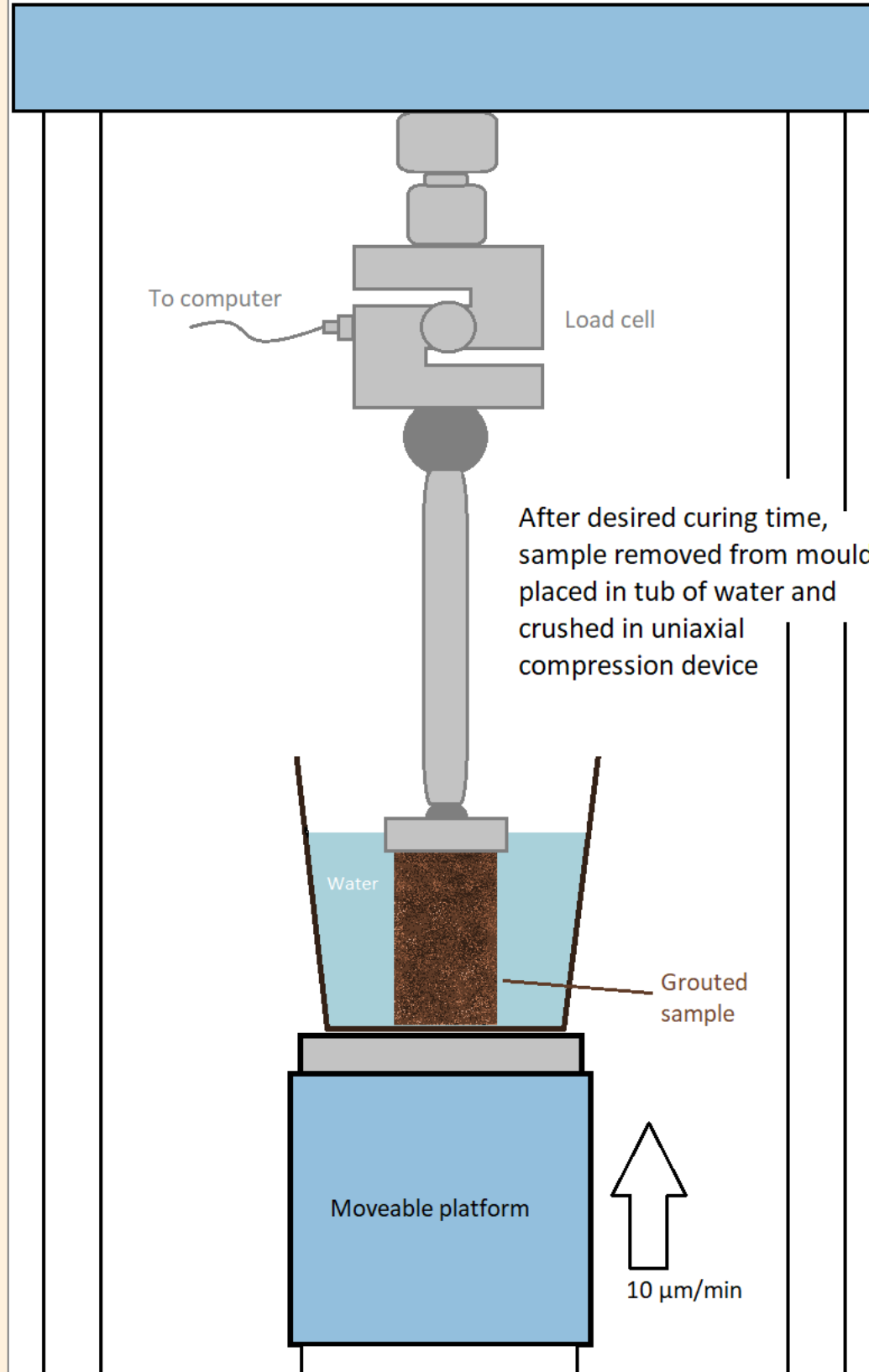


- Unconfined
- Saturated
- Uni-axial

Sample prep:



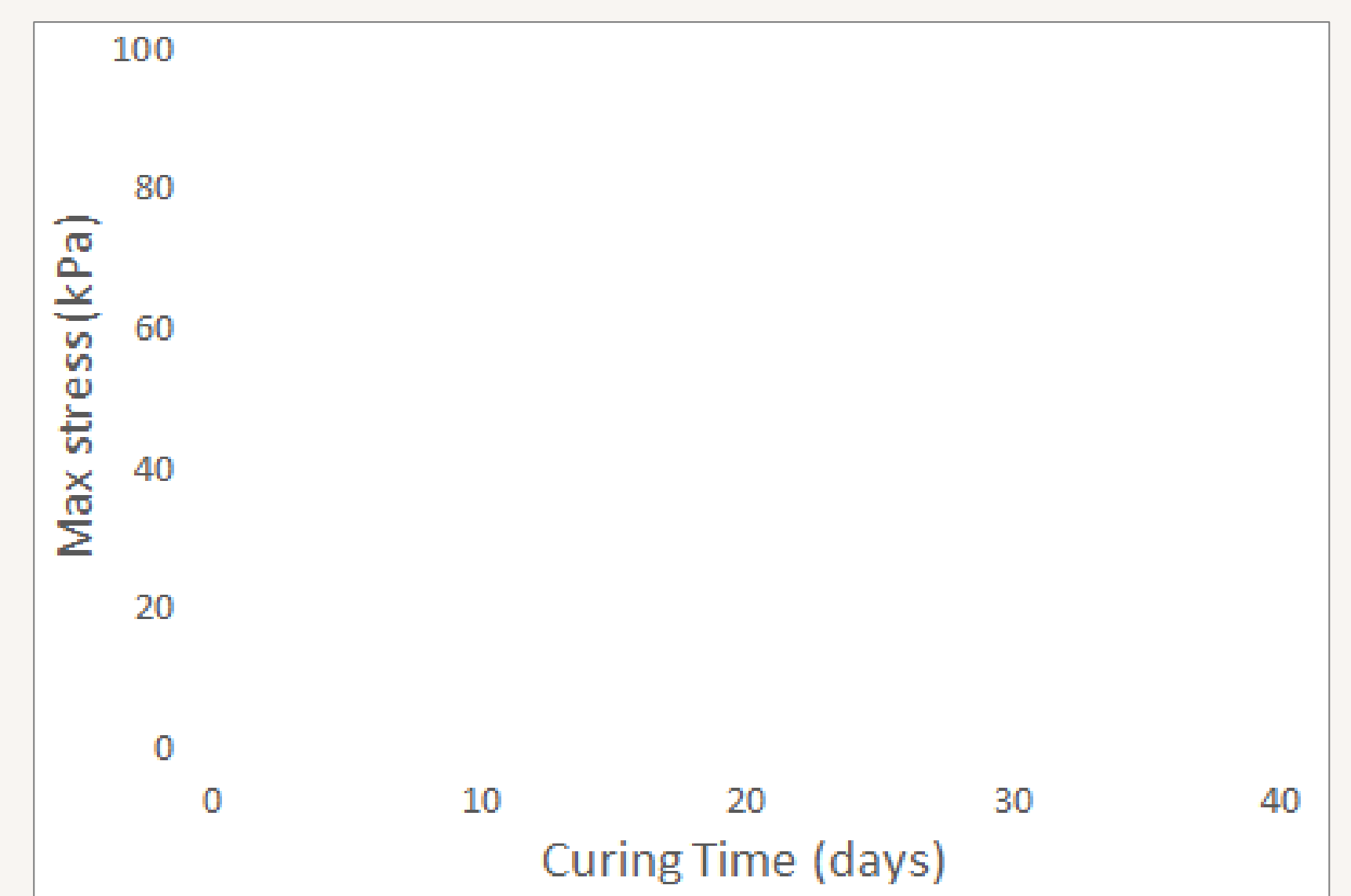
Compression test:



Key Results

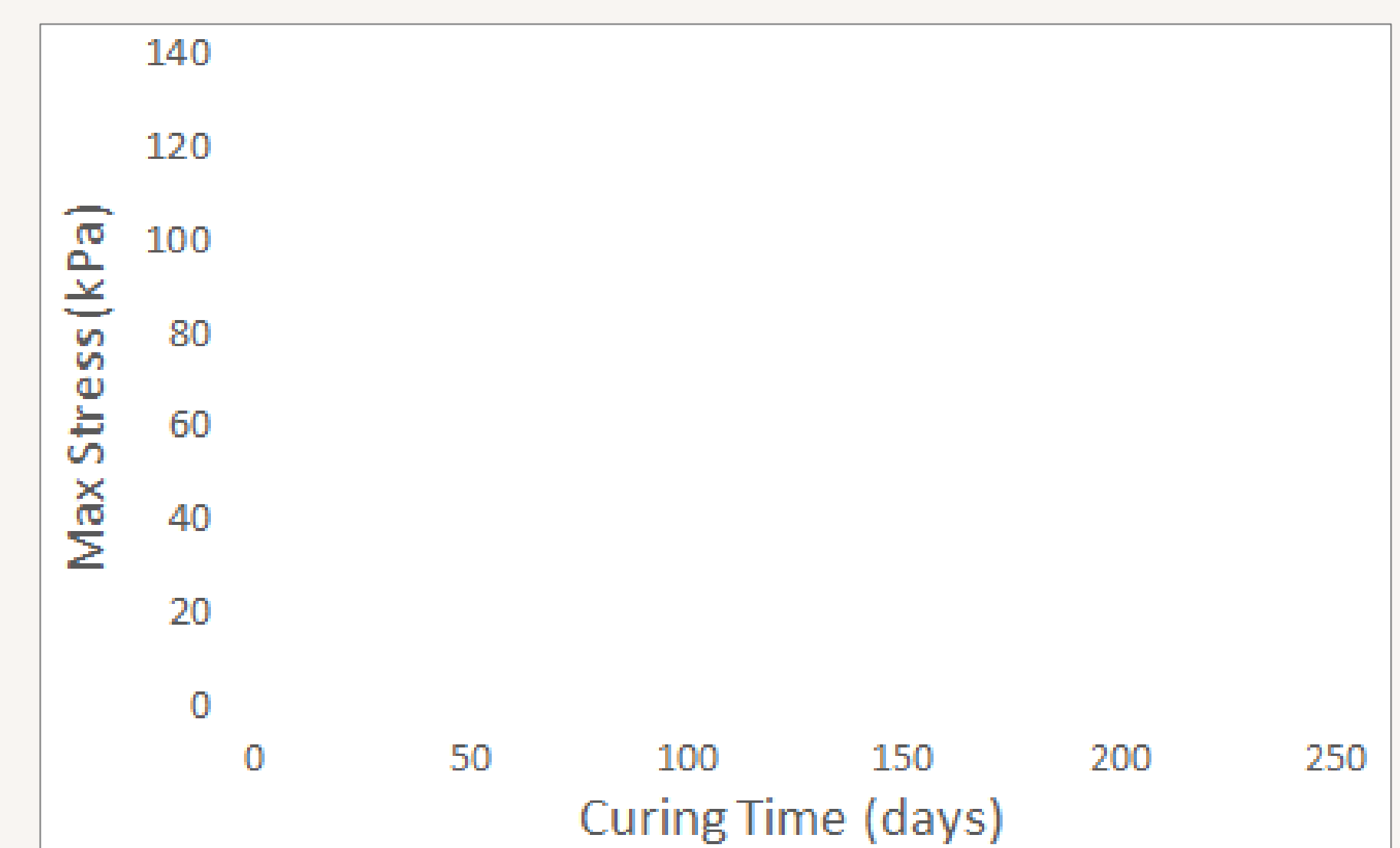
Gelation Rate:

- Faster gelling samples **cure faster** and have **higher compressive strength**



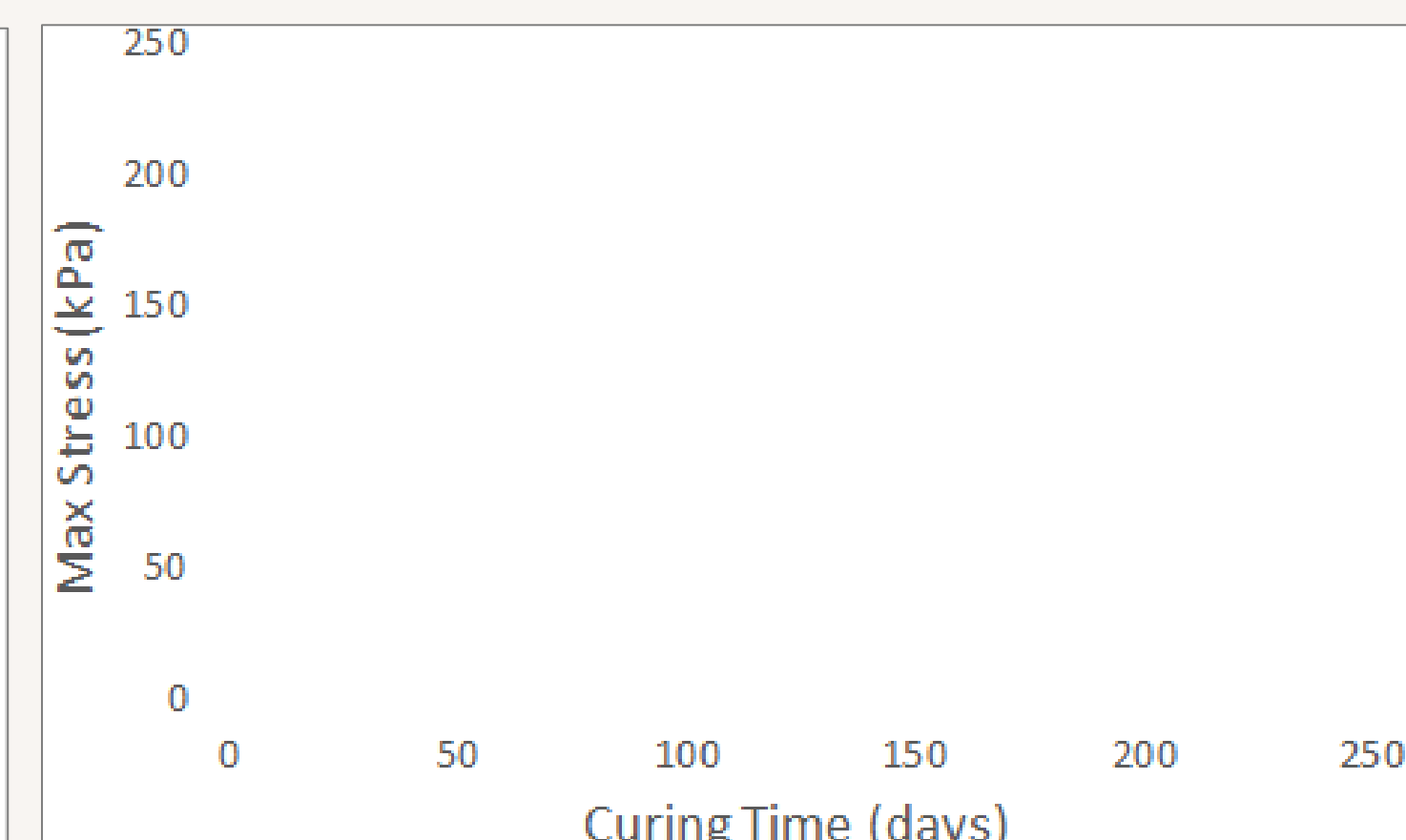
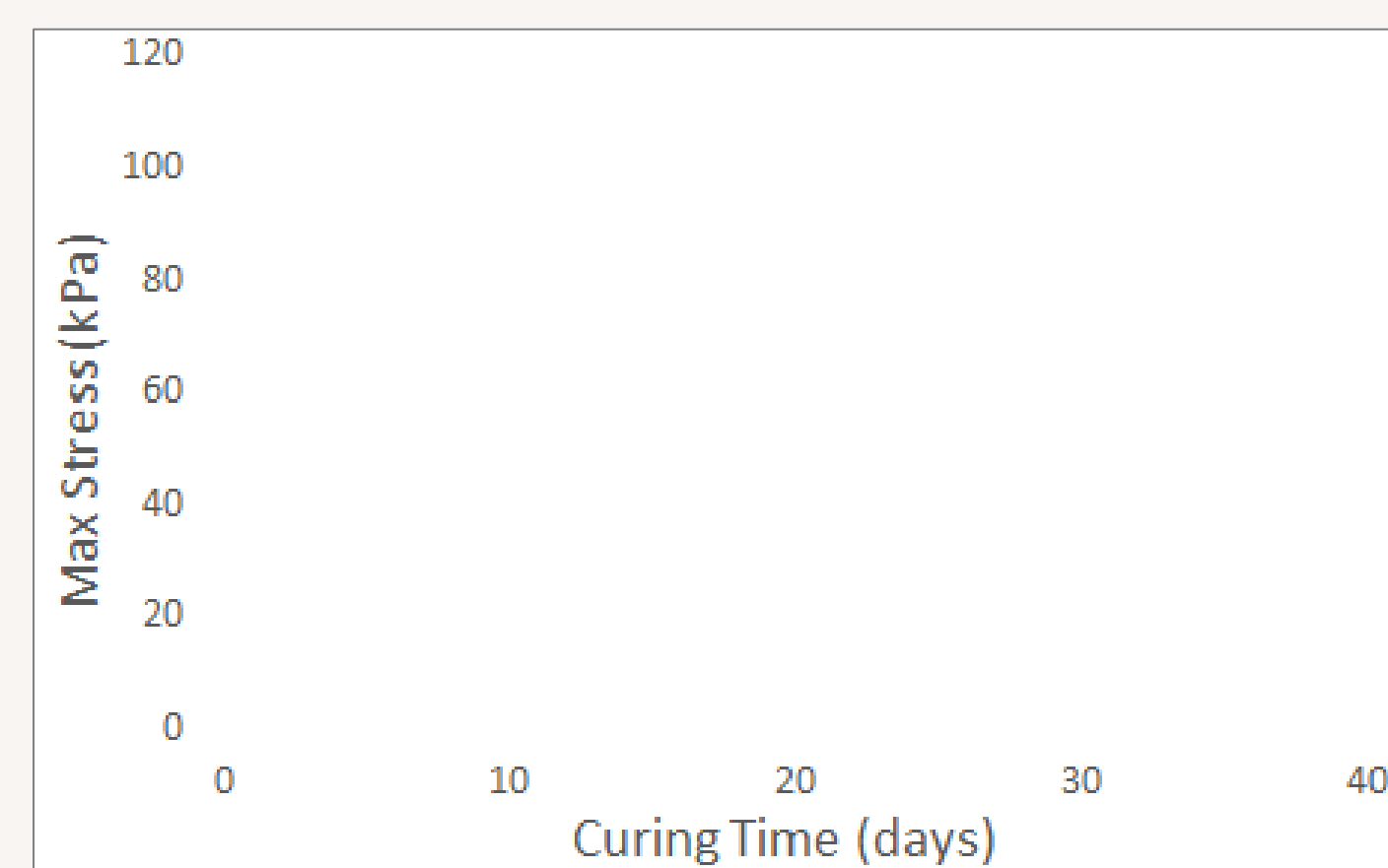
Curing time:

- Longer curing times give **higher compressive strength**



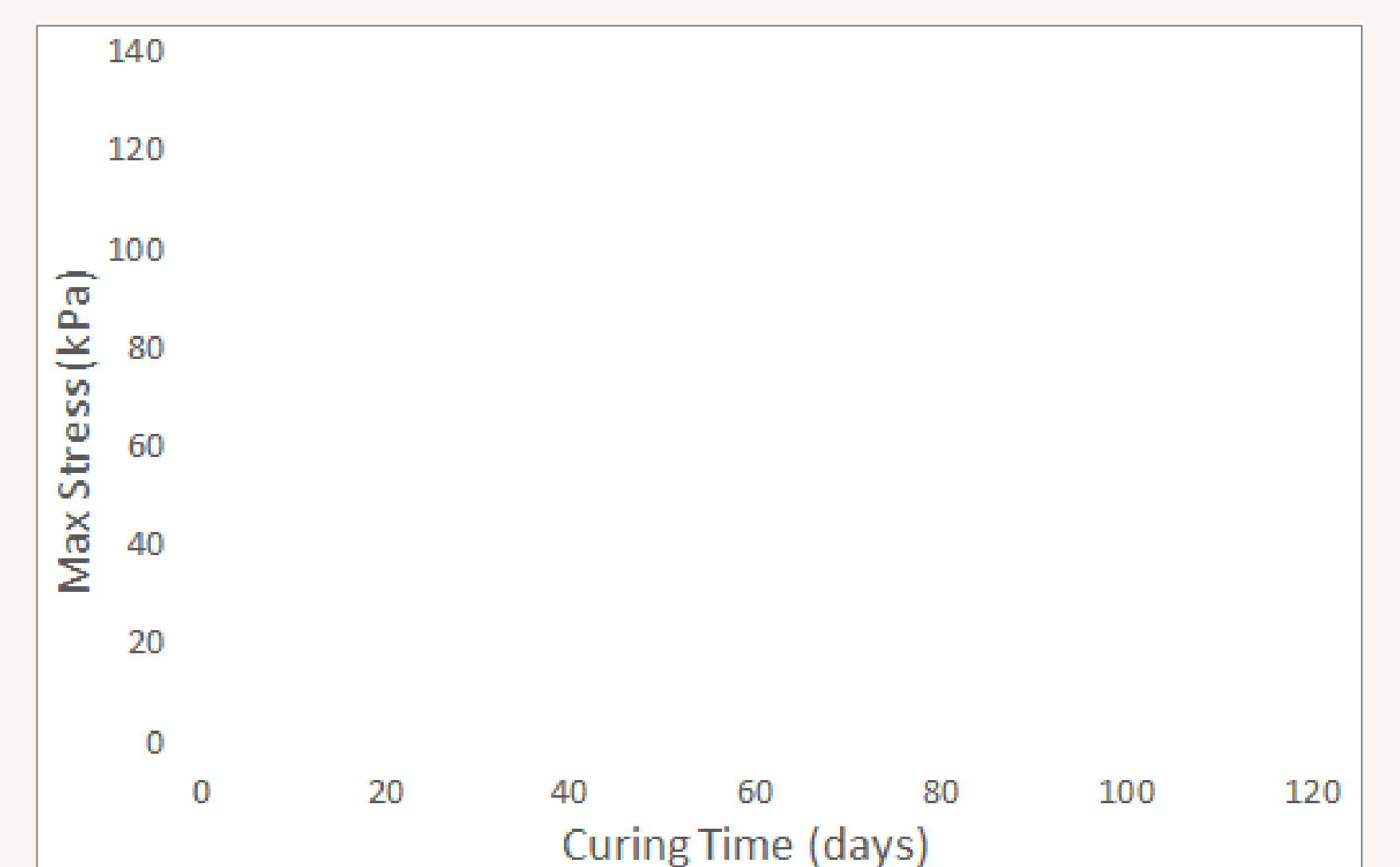
Curing conditions:

- Samples cured in **salt water** stronger than those in **fresh water**
- Effect increases with salt **valency** and **concentration**



Additives:

- Adding **kaolin clay** increases compressive strength



Summary & Conclusion

- Increased compressive strength** of CS grouted soil in various ways
- Can therefore use less material while maintaining mech. performance -> **Decreasing cost**
- Stronger CS gives grouted soil additional **resistance to settling, protection from seismic activity**, etc.
- Can open CS up to new applications where strength is important

Further work

- Use **clay** and **hydrophilic polymer** additives to...
 - Increase strength & flexibility
 - Increase **sorption capacity** for radioactive ions in soil (**Cs⁺**, **Sr²⁺**, **I⁻**, etc.)
 - Further reduce **hydraulic conductivity**
- Shear tests: **study re-healing capacity**
- Improve water retention** -> Resistance to drying
- Investigate structure of CS variants with **fluorescence microscopy**, **cryo-SEM**



Spent Fuel

Nuclear fuel is inherently complex. Probing fundamental mechanisms, like oxidation and dissolution, on bulk materials is difficult due to the radioactivity of nuclear fuel compounds.

Thin films provide a solution by reducing the complexity, and allowing idealised surfaces to be produced, upon which single parameter studies can be conducted. Furthermore, by building predictive models for the corrosion behaviour of spent fuel exposed to aqueous environments, we can simulate corrosion scenarios. The results can be used to assess risk and support decisions within the nuclear industry.

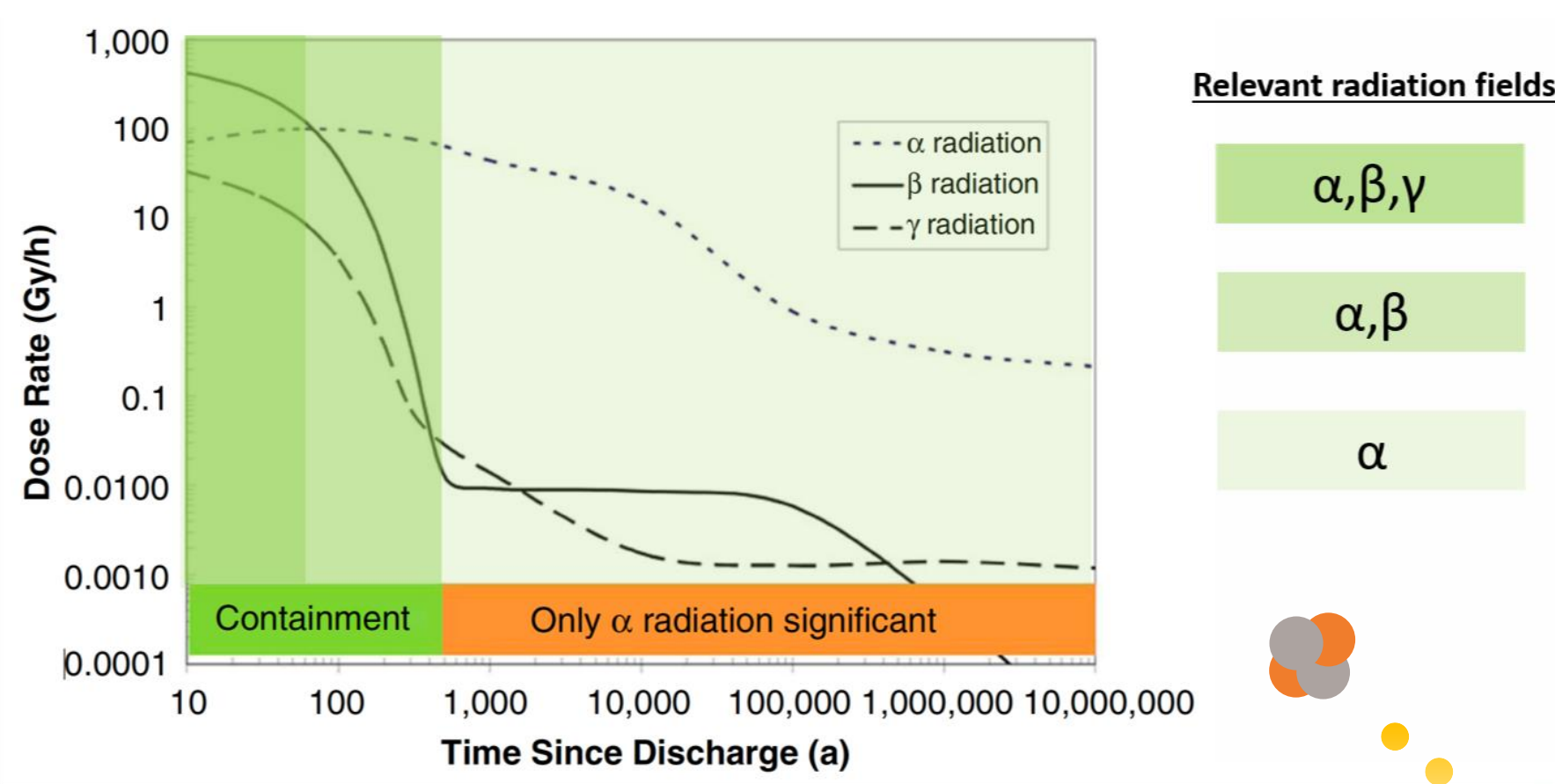


Fig 1: Radiation field lifetimes [1].

Interaction with water

When building a safety case for fuel/water interactions, radiolysis rates and localised concentration of oxidising species are key in understanding the dissolution of the fuel surface. To do this, predictive tools are needed to produce dose rates and dose rate distributions in multiple geometries, as a function of fuel type and age.

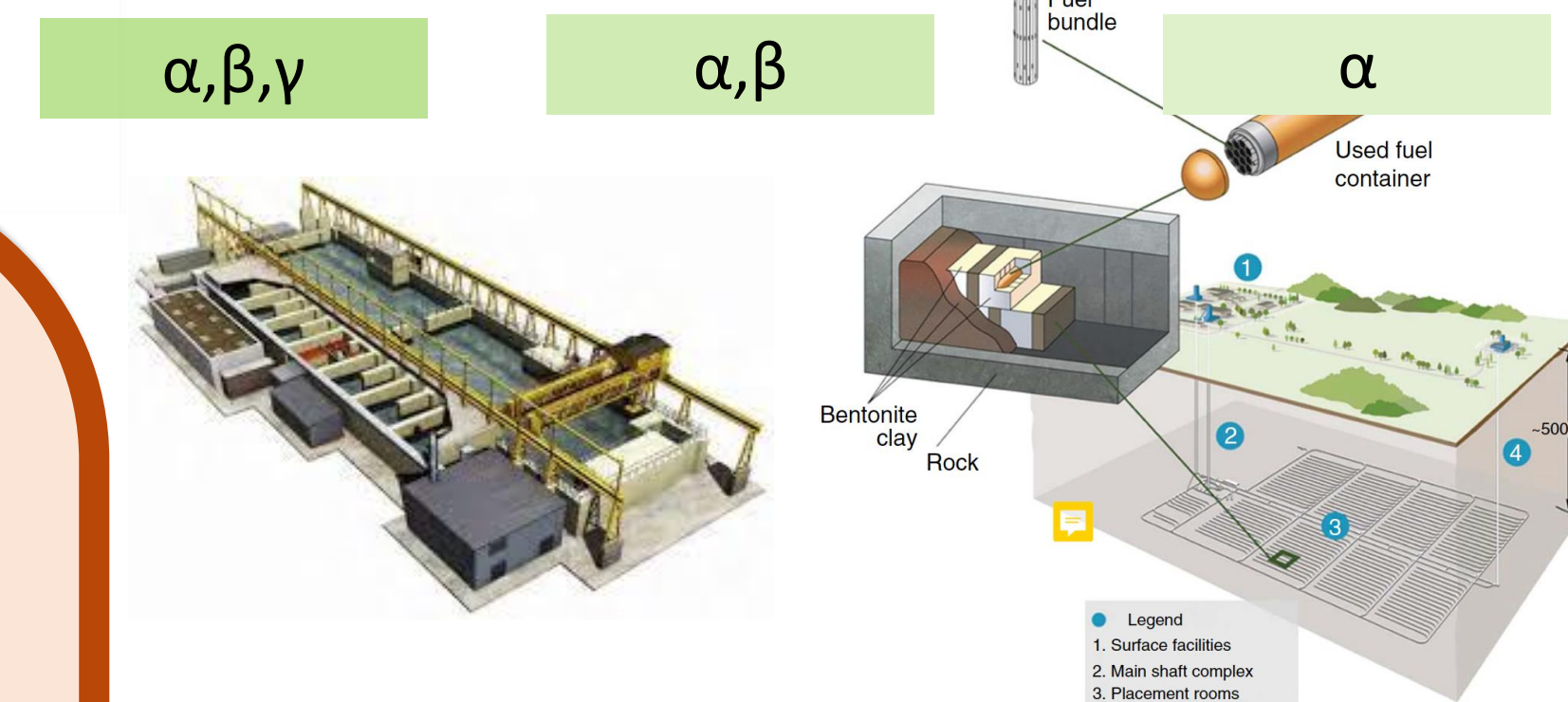
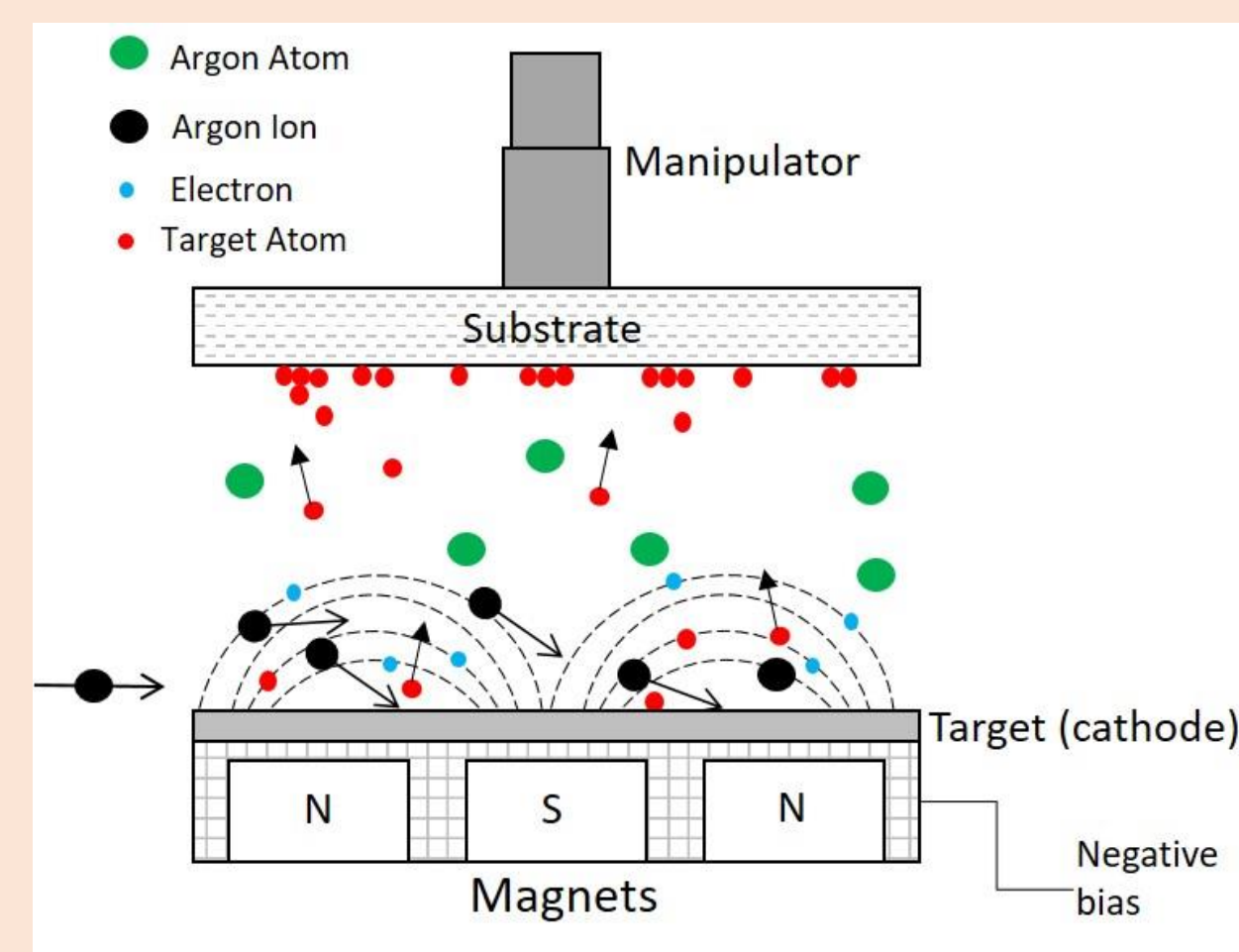
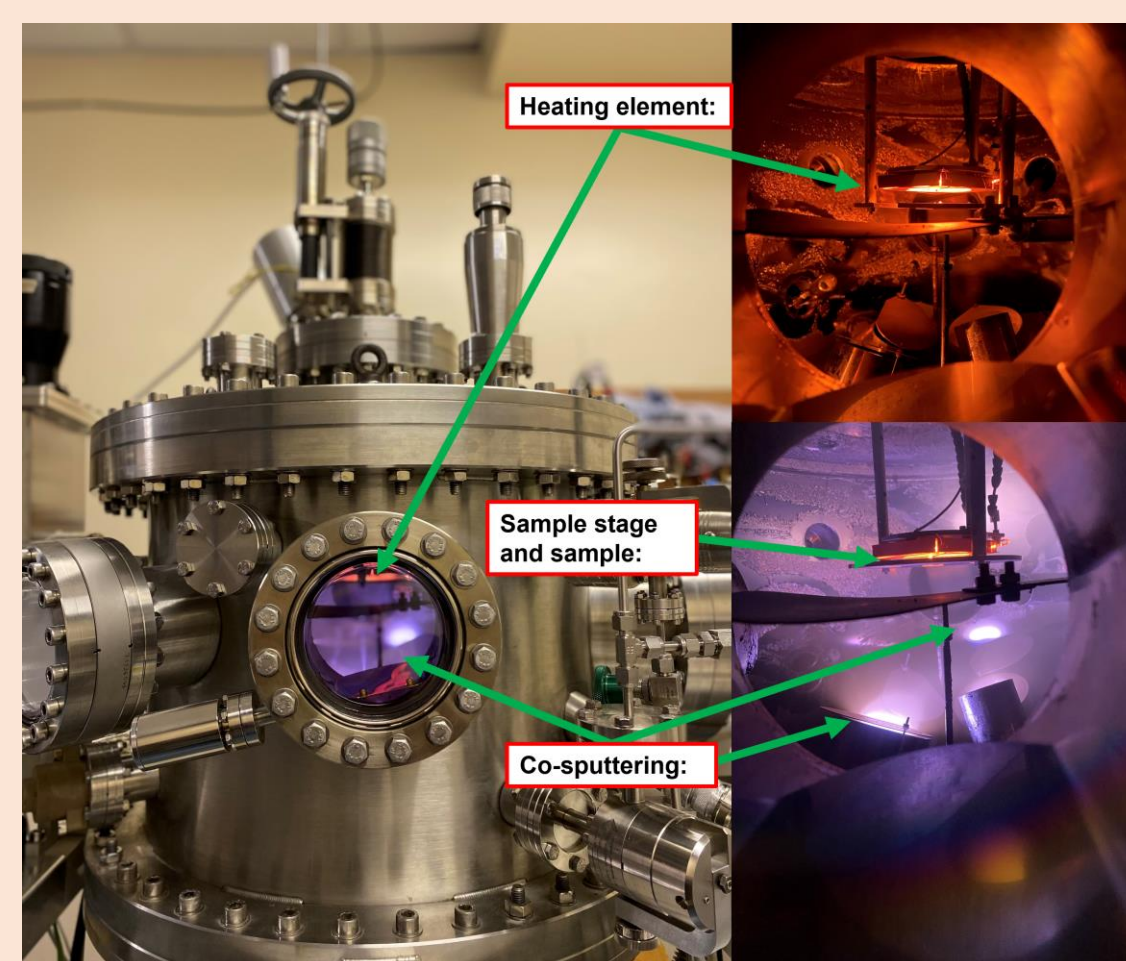


Fig 6: Graphic of Interim Wet storage (left) and a Geological Disposal Facility (GDF) (right).

Thin Film Fabrication

We utilise the PVD method of DC magnetron sputtering to engineer idealised surfaces. Through conducting reactive and co-sputtering techniques, we are able to synthesise actinide compounds including: **uranium oxides, nitrides, and silicides**, allowing for the surfaces of nuclear fuel candidates to be probed.



Aqueous Dissolution

A series of single- and poly-crystalline uranium oxide, nitride, and silicide surfaces have been exposed to aqueous media in order to probe the dissolution properties of each candidate fuel type. All samples were synthesised at the University of Bristol using FaRMS.

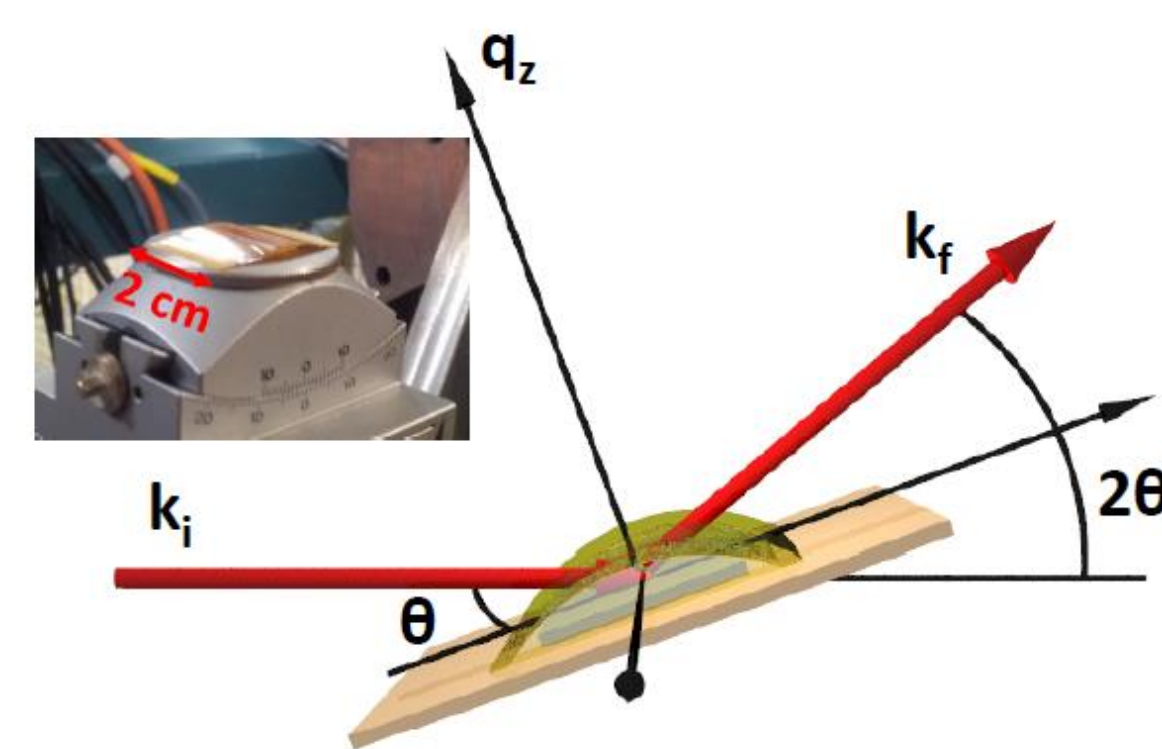


Fig 2: Sample geometry for synchrotron dissolution experiments. Taken from [2].

The Experiment

The surface of each film was exposed to oxidising environments. The media used to explore the dissolution of the **Silicide** and **Nitride** compounds was 0.1 mol. H₂O₂. The work conducted on **UO₂** single crystals induced the radiolysis of MilliQ H₂O using a synchrotron source.

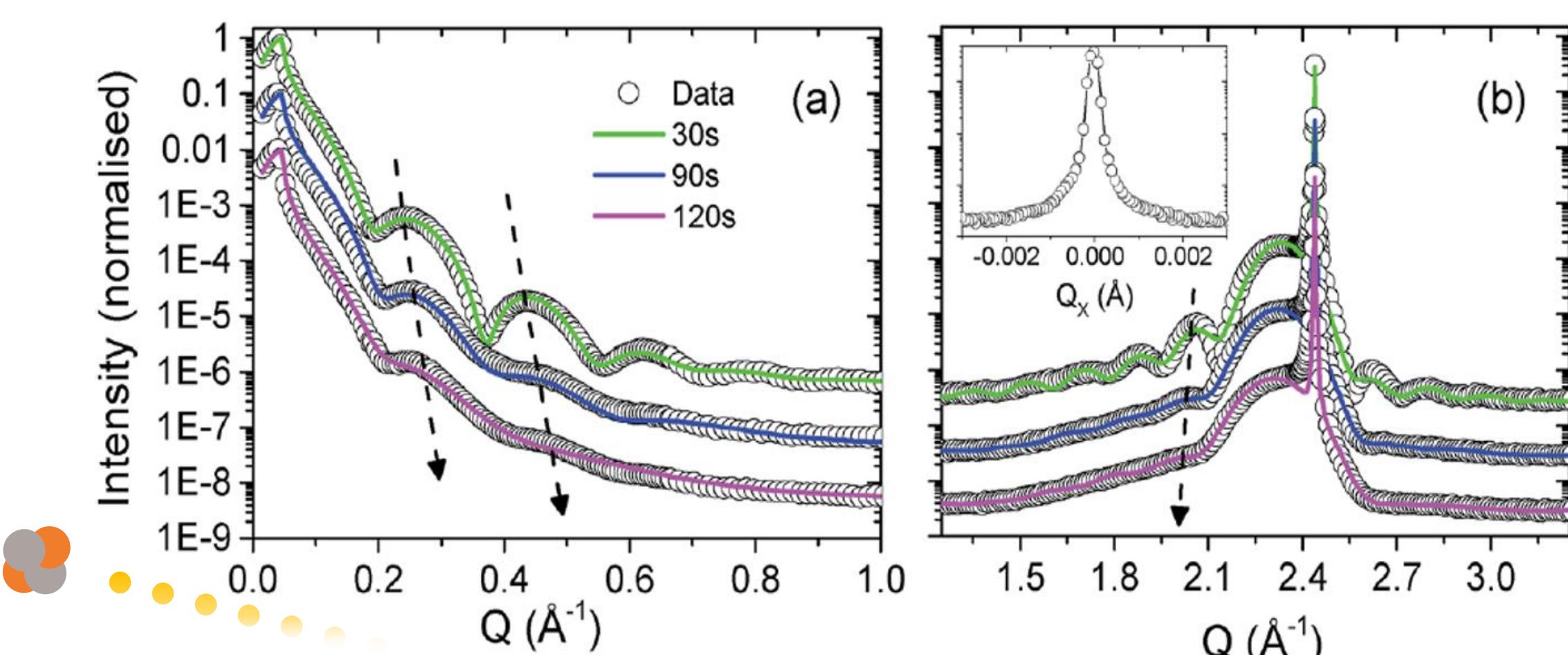


Fig 3: X-ray reflectivity and specular x-ray diffraction spectra collected from [001] oriented UO₂ [2].

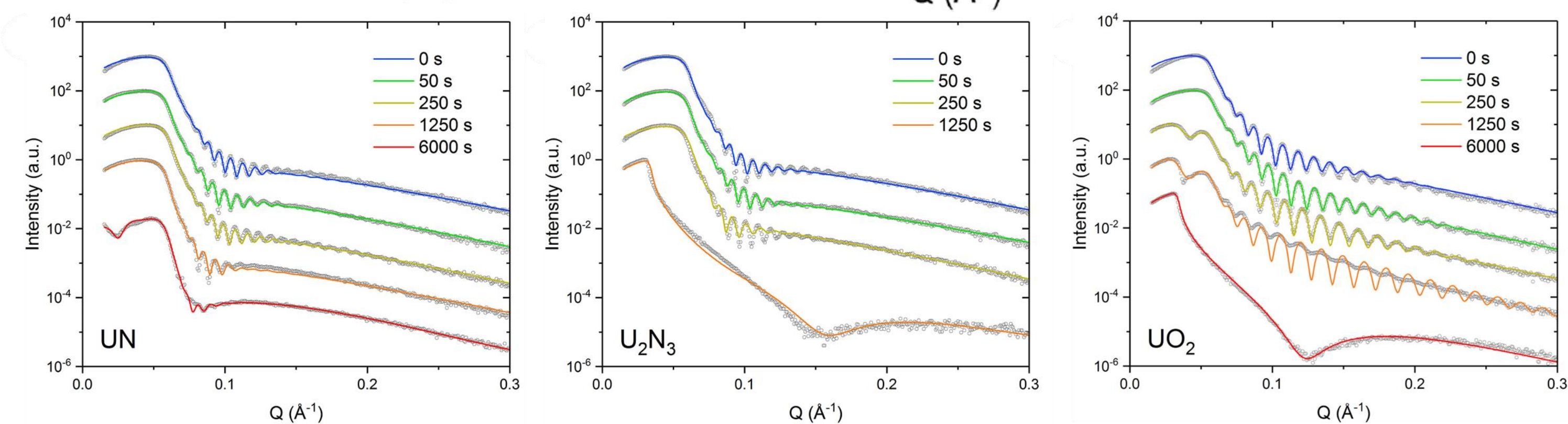


Fig 4: X-ray reflectivity spectra collected from poly-crystalline UN, U₂N₃, and UO₂ thin films. Figure from [3].

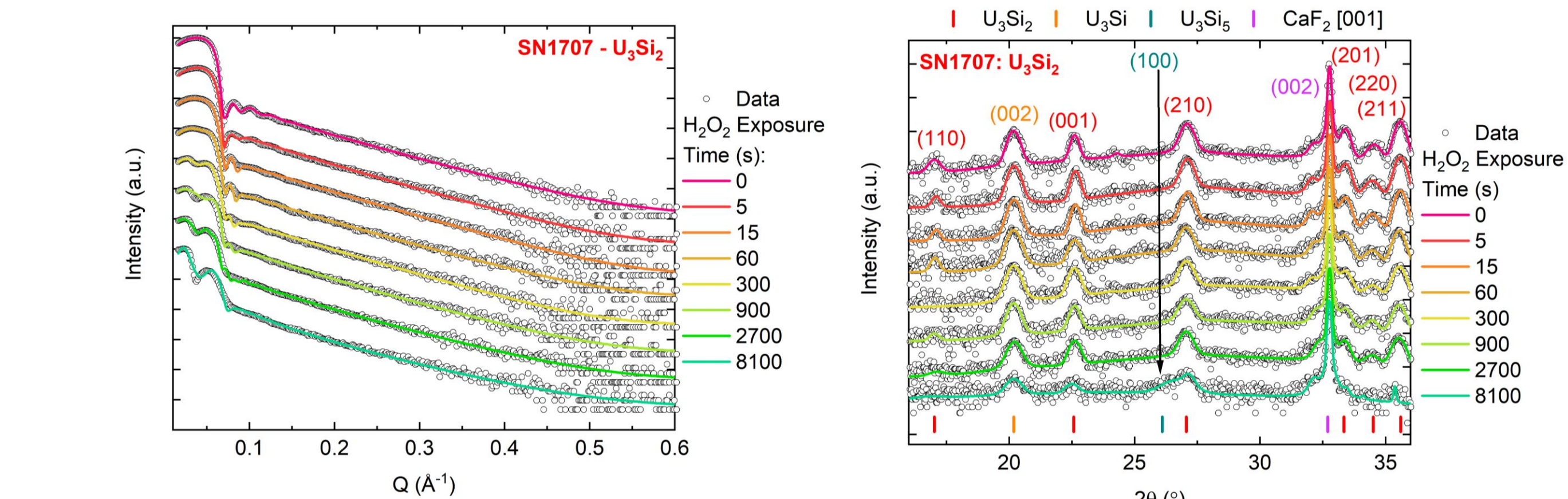
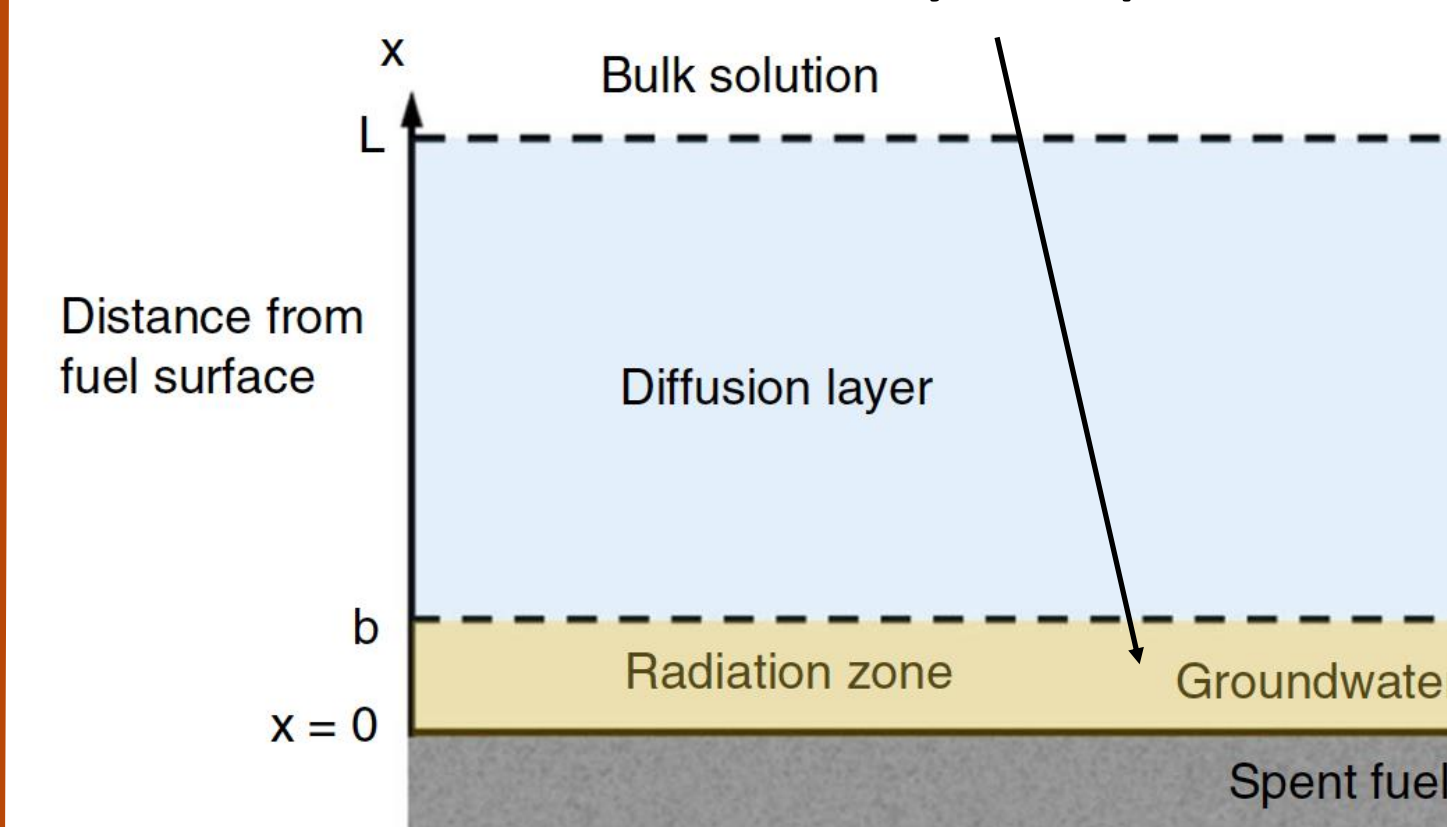
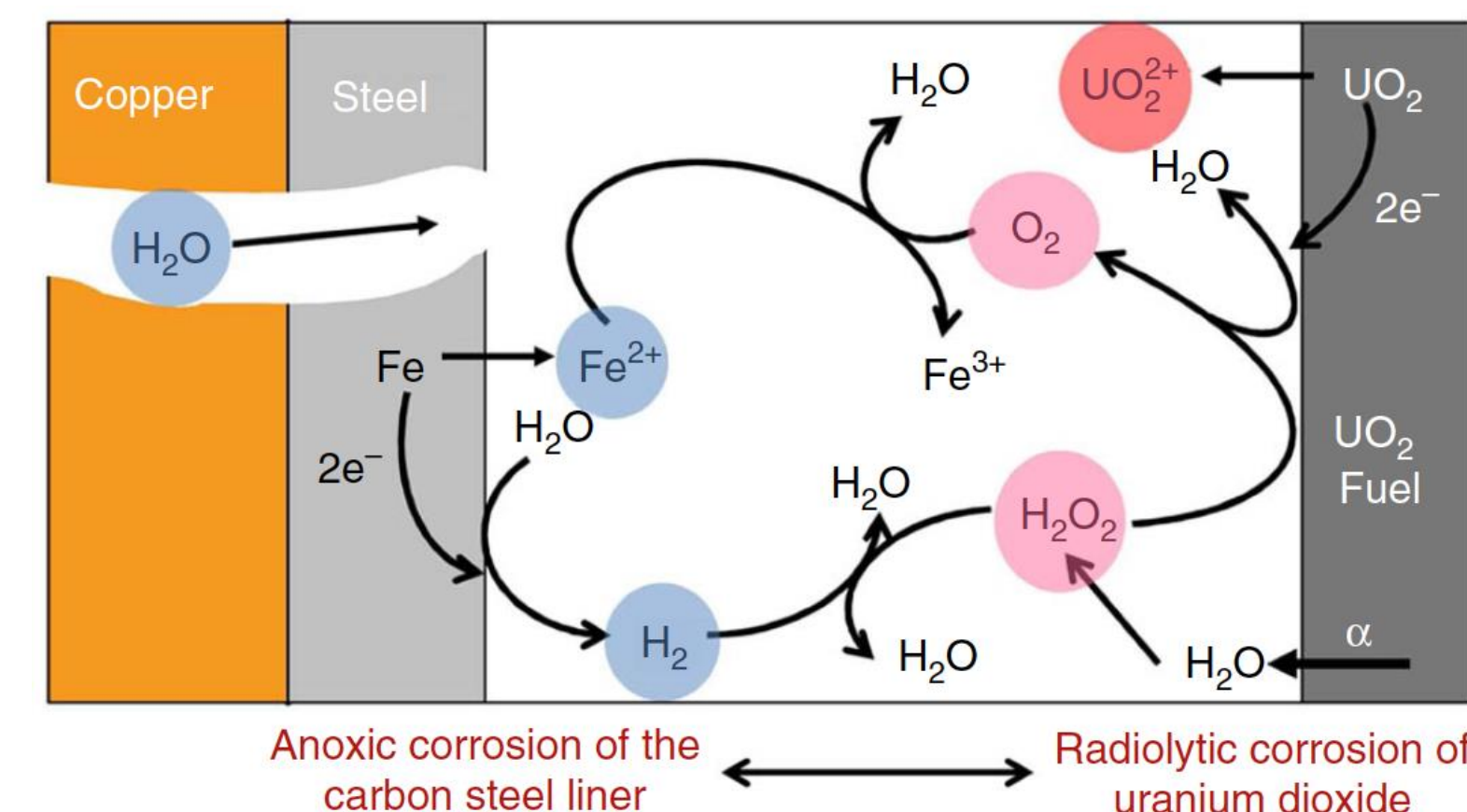


Fig 5: X-ray reflectivity spectra collected from a poly-crystalline U₃Si₂ thin film. Figure from [4].

Source term for radiolytic species



Incorporate into 1D Chemical reaction and diffusion models



Key Results

Through the combination of surface experiments and modelling spent fuel dissolution, the understanding of how these nuclear fuel candidates behave in aqueous media has been furthered.

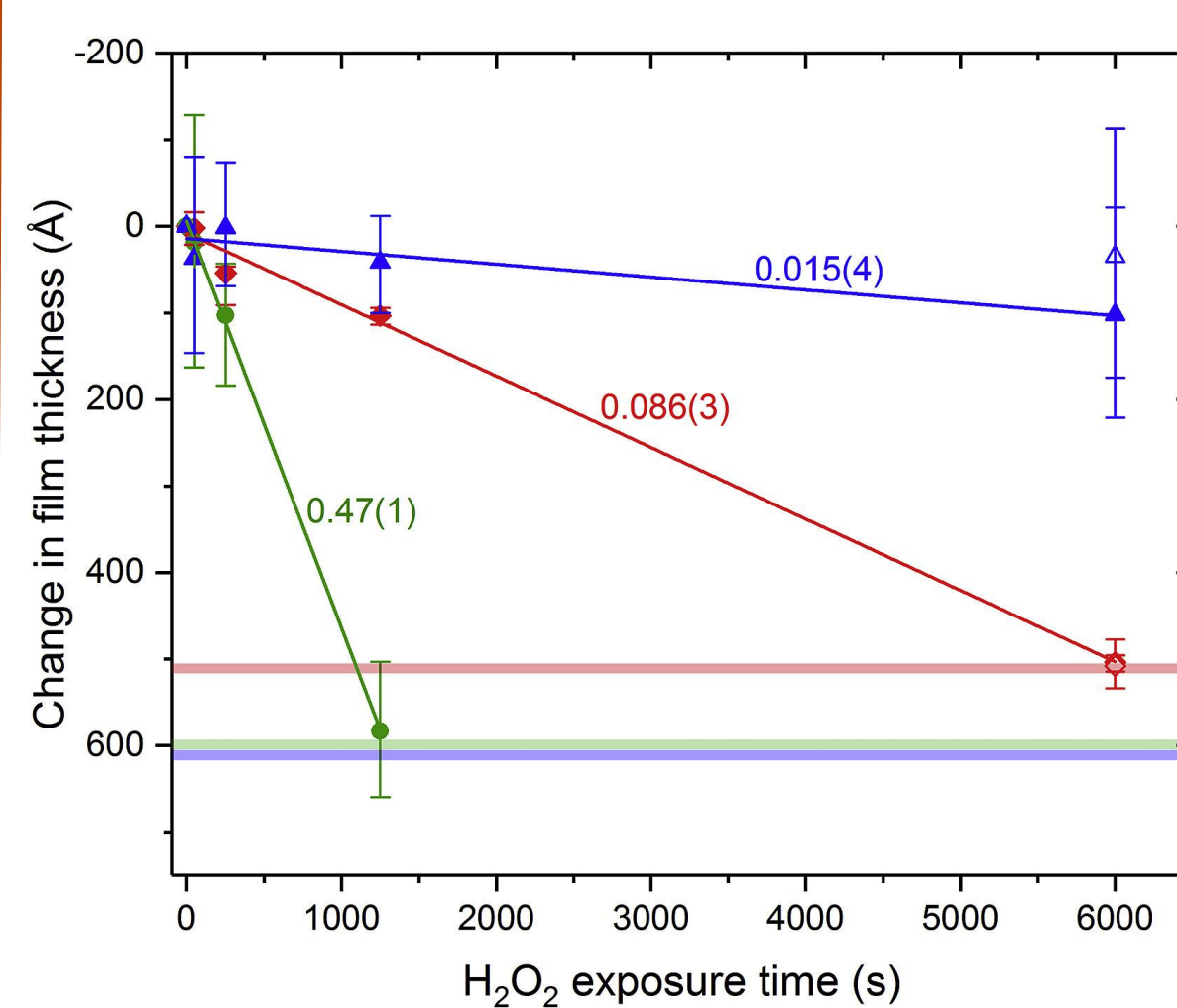


Fig 7: Change in film thickness for UN (blue), UO₂ (red), and U₂N₃ (green) when exposed to H₂O₂. Taken from [3].

Dissolution rates for each candidate fuel, UO₂, UN, and U₃Si₂, were measured and modelled using x-ray reflectivity. This surface sensitive technique has allowed the interface thickness, roughness, and electron density to be probed for each fuel type. Modelled dissolution rates presented below.

Phase	Dissolution Rate (Ås ⁻¹)
UO ₂	(4.9 ± 0.2) × 10 ⁻²
UN	(1.5 ± 0.2) × 10 ⁻²
U ₃ Si ₂	-(8.5 ± 5.7) × 10 ⁻³

This work [5,6] has led to the development of the radiation dosimetry software, **ADRC**, and web application, **Rad-dose**.



<- Scan here for **ADRC** and the top right corner for **Rad dose**

For more information on the sample synthesis, characterisation techniques, and expertise available at FaRMS, please get in contact via: <https://www.nnuf.ac.uk/farms>

Summary

Epitaxial thin films of ThO_2 , UO_2 and $(\text{Th,U})\text{O}_2$ MOX have been synthesized using DC magnetron sputtering. These engineered surfaces can be used to analyse certain corrosion properties in spent fuel, specifically under interim storage conditions.

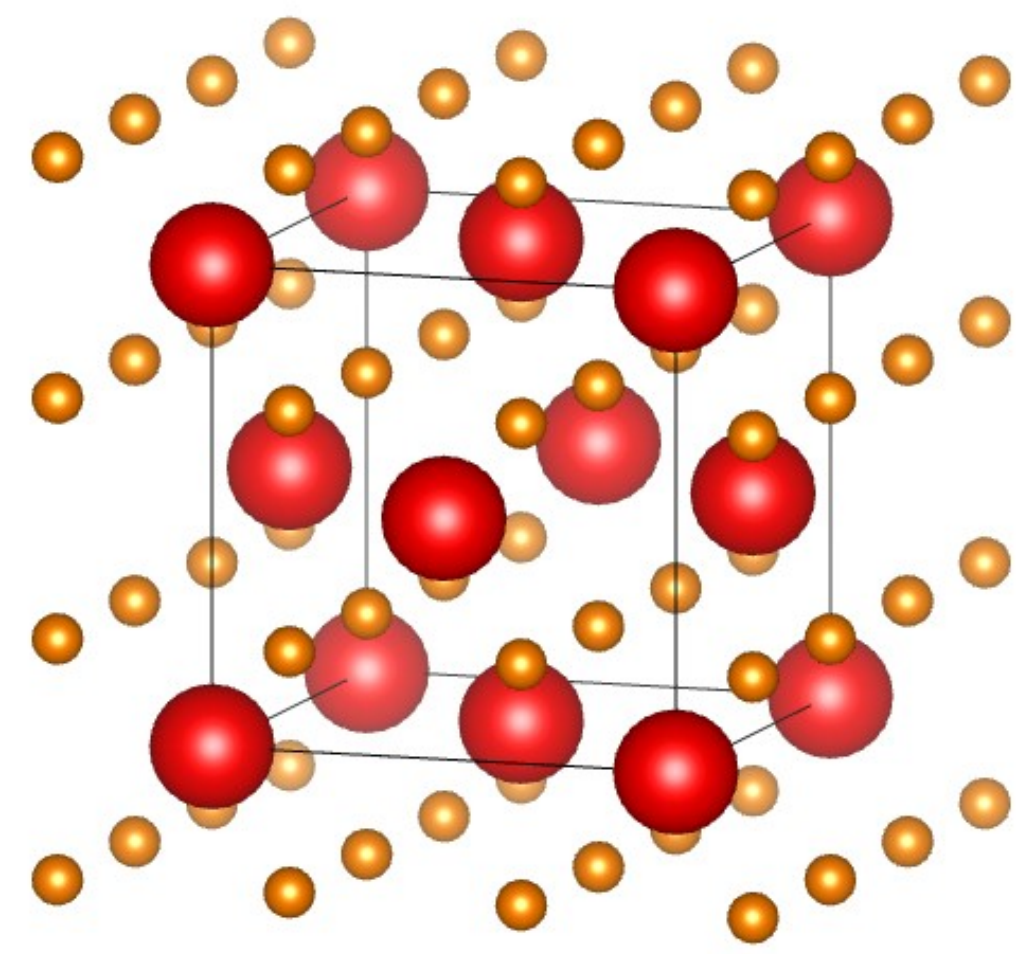


Figure 1 (above) - FCC structure of ThO_2 and UO_2 , lattice parameters 5.603 Å and 5.468 Å respectively.

Figure 2 (left) - PuO_2 storage facility at Sellafield site [1].

Experimental Methods

The samples were synthesized using DC Magnetron Sputtering. This is a physical vapour deposition process involving using a closed magnetic field parallel to the target surface, confining electrons in the plasma near the surface of the target.

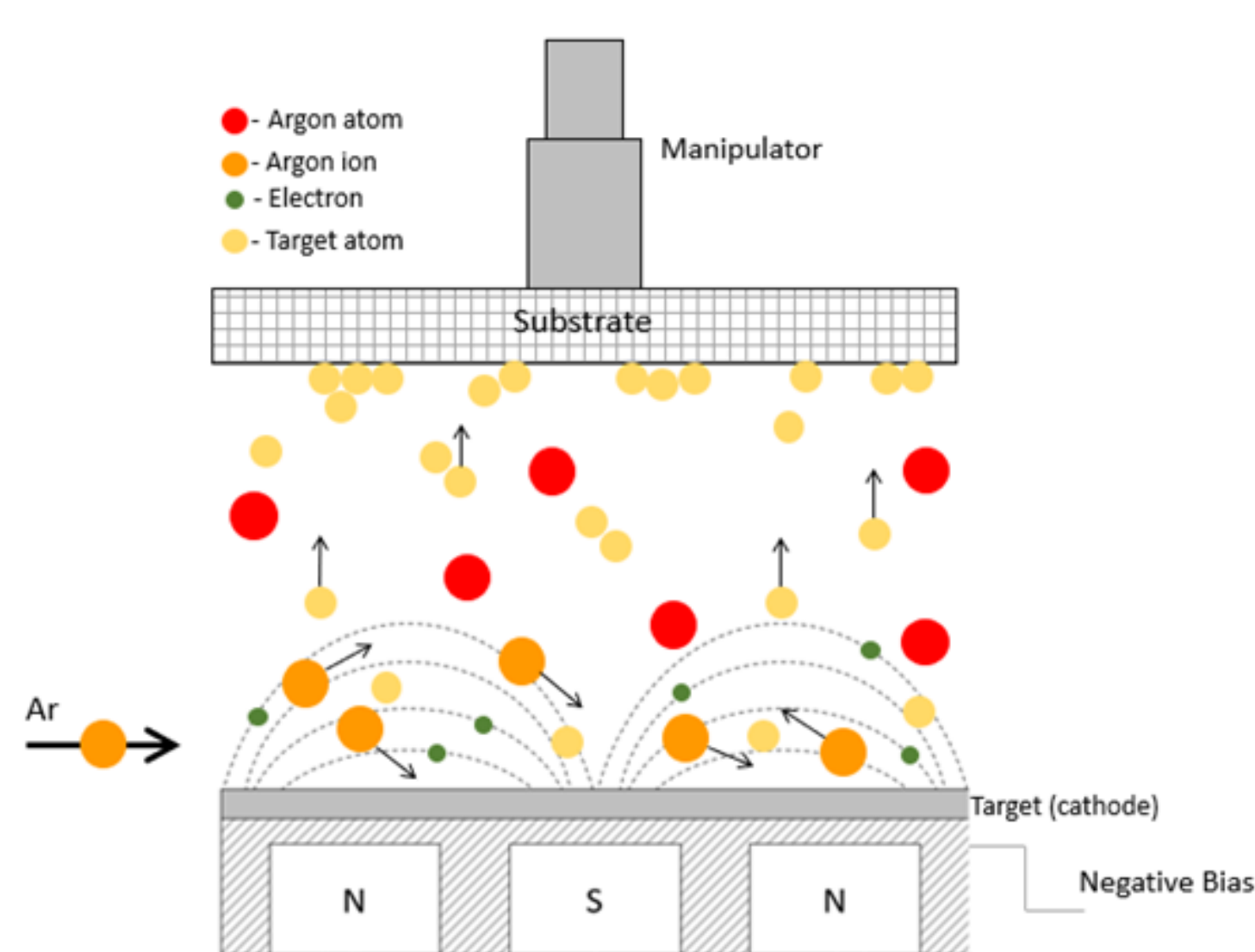


Figure 3 - Diagram showing the DC Magnetron Sputtering process.



Figure 4 - Image of the sputtering kit at the University of Bristol.

Samples are characterized XRR. This technique provides a non-destructive method for determining the thickness, roughness and density of thin films.

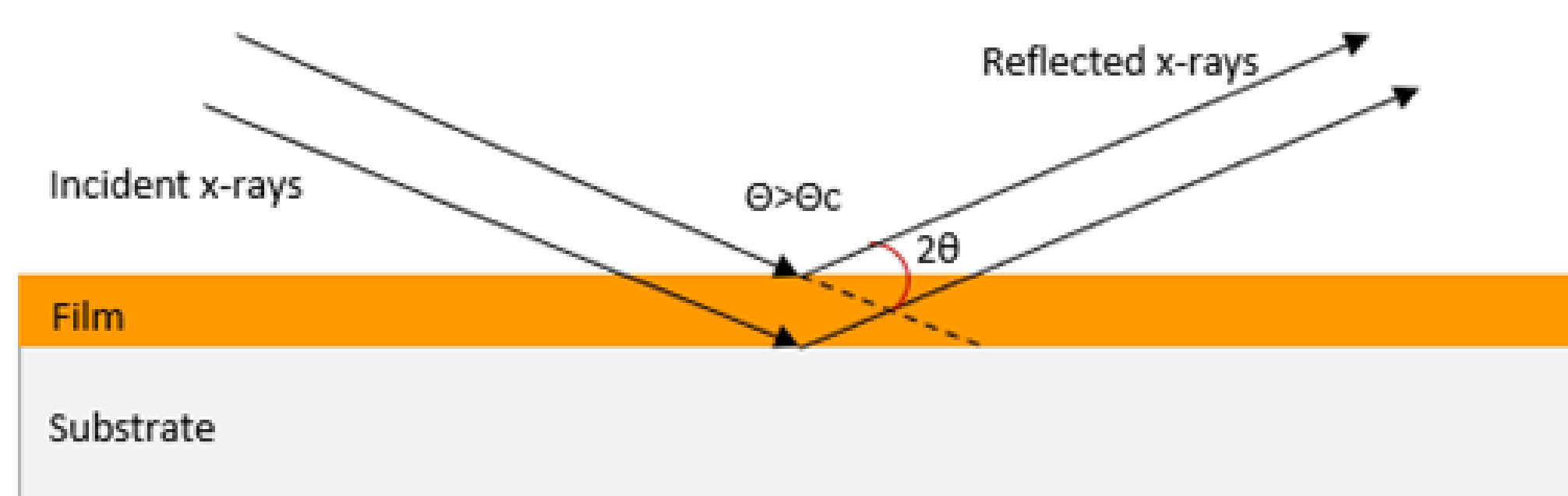


Figure 5 - Diagram illustrating X-ray reflectivity.

An example of a XRR scan is shown in Figure 8. Surface properties can be determined based off periodicity of oscillation and oscillation patterns amplitude.

Results

Figure 6 shows specular 2θ - ω XRD scan of epitaxial ThO_2 , UO_2 and $(\text{Th,U})\text{O}_2$ MOX samples. This figure suggests that solid samples of $(\text{Th,U})\text{O}_2$ MOX has been achieved, and that the change in lattice parameter is proportional to amount of ThO_2 in the sample.

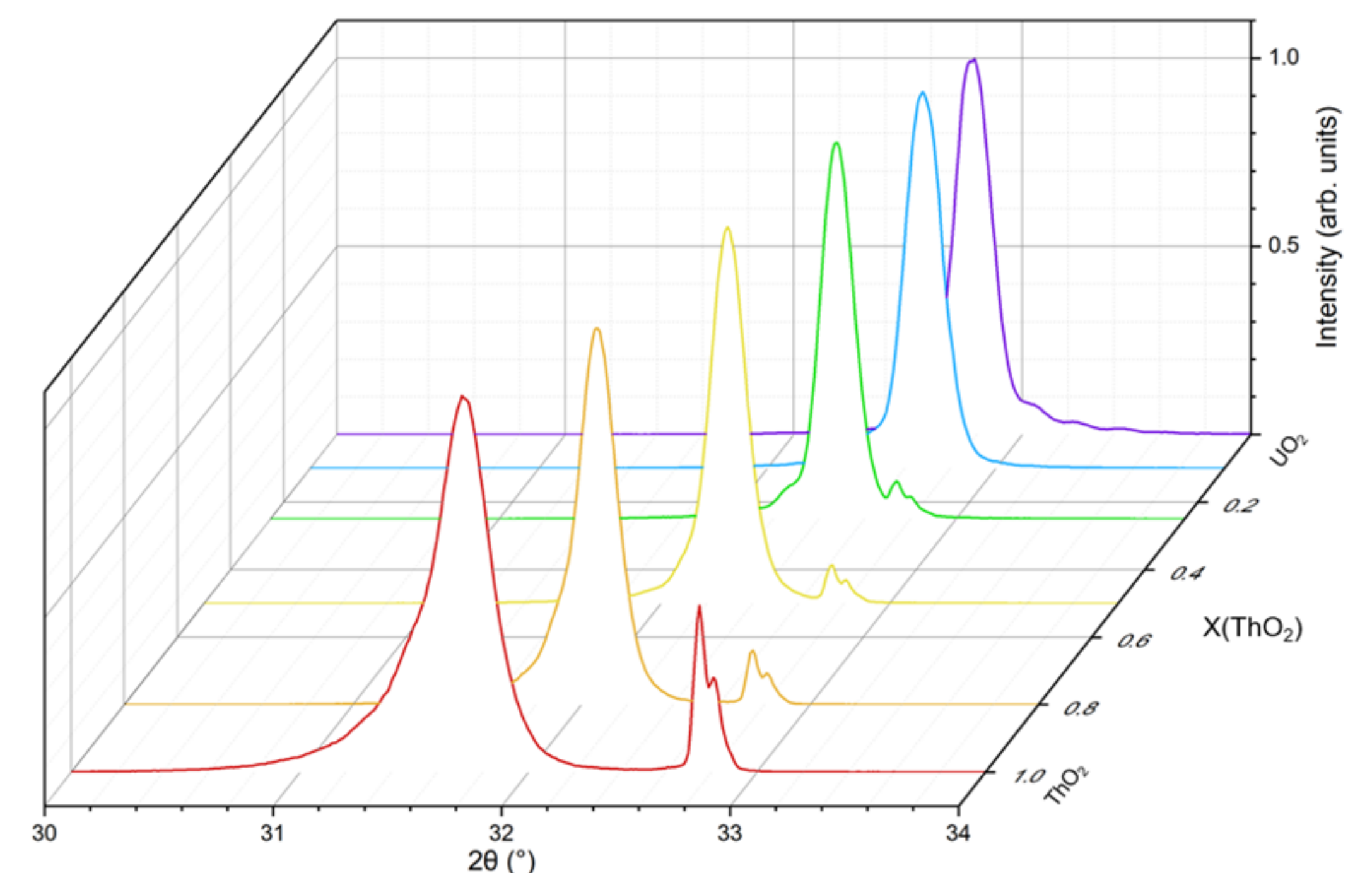


Figure 6 - Specular 2θ - ω XRD scan of epitaxial ThO_2 , UO_2 and $(\text{Th,U})\text{O}_2$ [2 0 0] thin films. The substrate (CaF_2 [2 0 0]) peak is shown at 32.76° .

Sample	Lattice Parameter (Å)	CaF_2 Mismatch
ThO_2	5.637 ± 0.002	3.1%
80% ThO_2	5.578 ± 0.002	2.1%
50% ThO_2	5.540 ± 0.002	1.4%
25% ThO_2	5.508 ± 0.002	0.8%
10% ThO_2	5.476 ± 0.002	0.2%
UO_2	5.461 ± 0.002	0.04%

Table 1 - Lattice constants determined from the 2θ - ω specular scans shown in Figure 6. The percentage mismatch with CaF_2 (lattice parameter = 5.463 Å) is also shown.

Figure 7 indicates that the ThO_2 sample is single domain, and therefore single crystal. Figure 8 indicates that the ThO_2 sample has a thickness of 511 Å and a surface roughness of 24 Å.

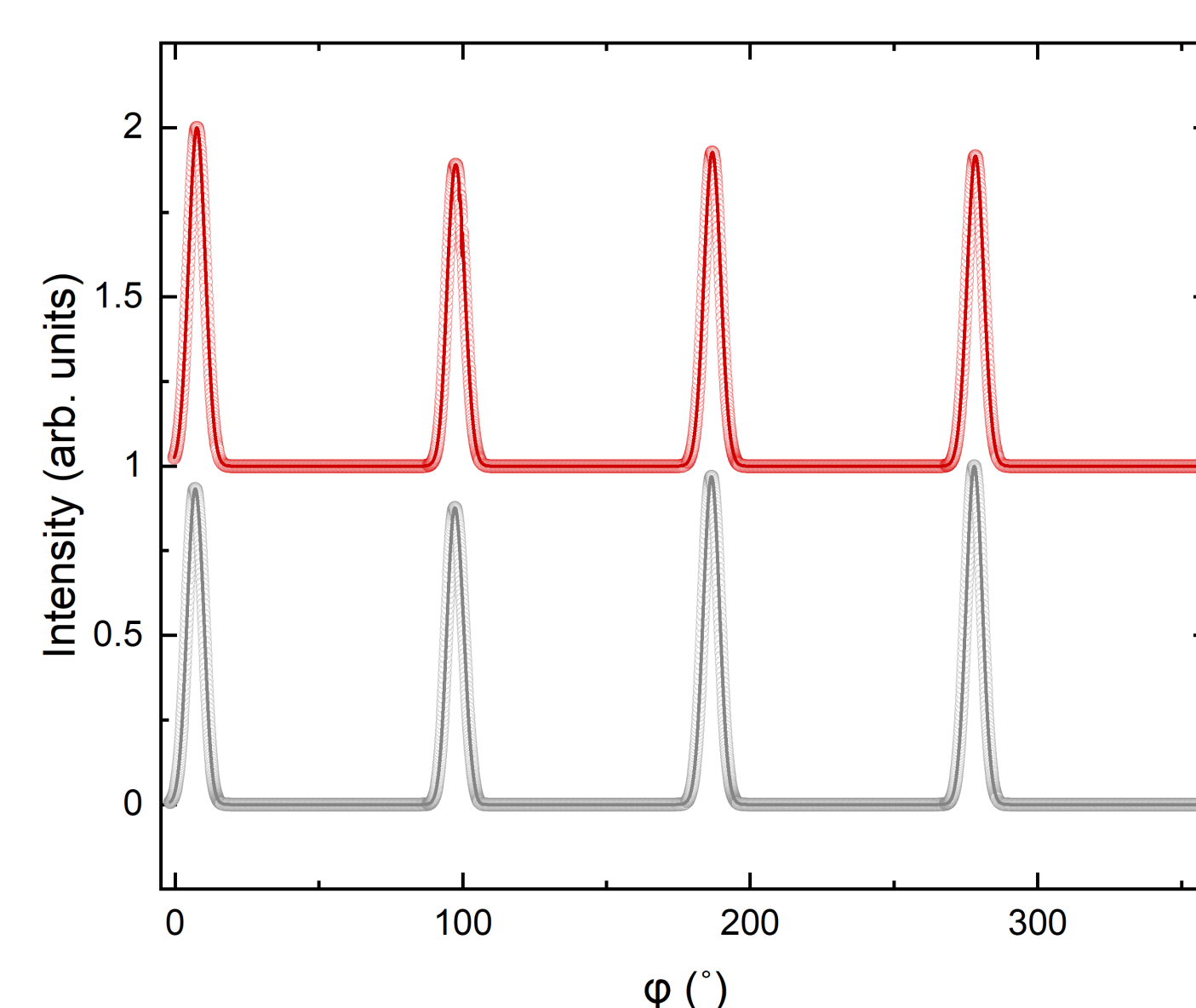


Figure 7 - ϕ scans of the off-specular CaF_2 and ThO_2 (4 2 0) Bragg peaks, shown in grey and blue respectively.

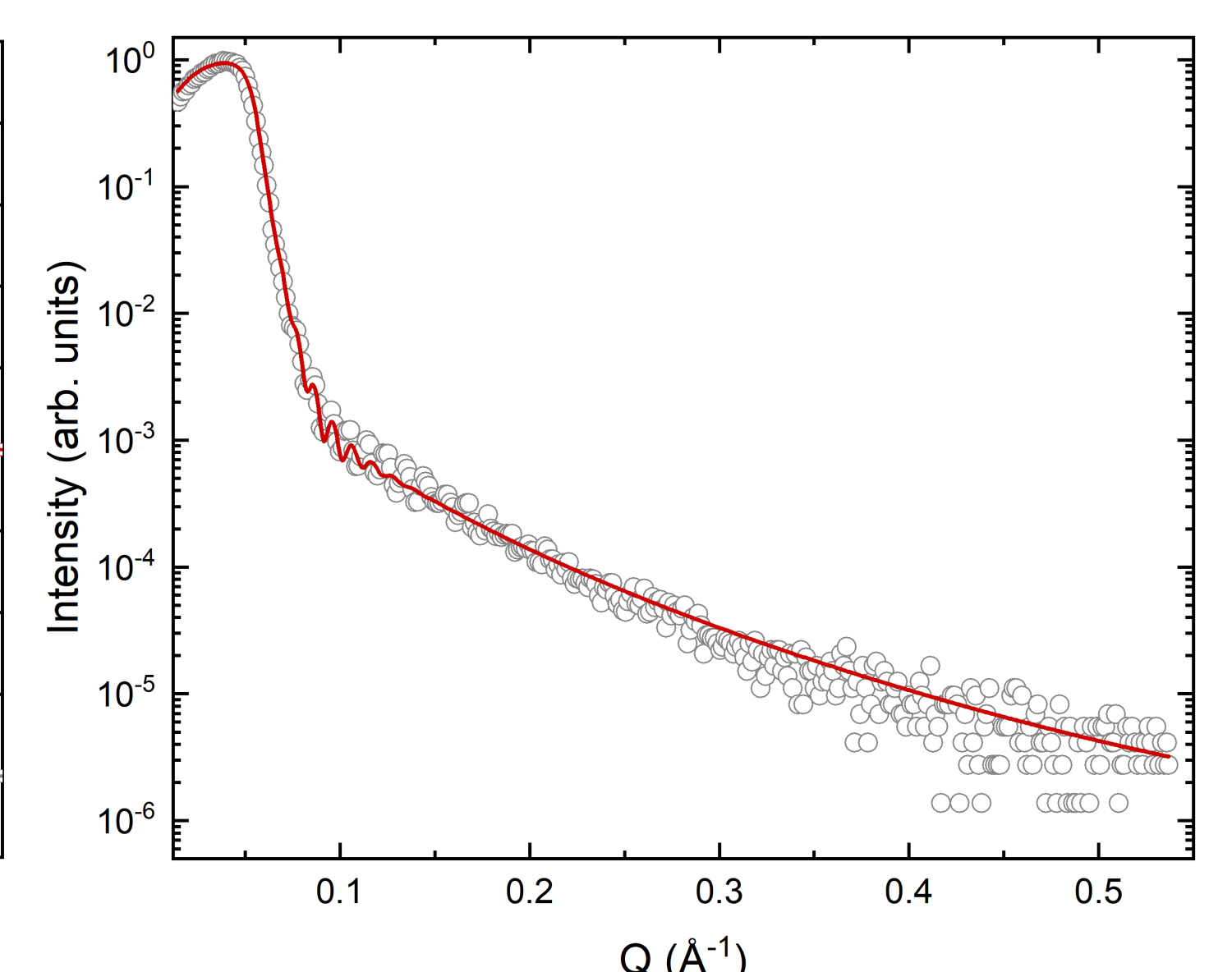


Figure 8 - ThO_2 XRR scan and fit as a function of Q . The momentum transfer wave vector is shown in red.

Future Work

- These samples will be used in several corrosion experiments, including an investigation into the photocatalytic properties.
- Further characterization of these samples will be undertaken, including XPS and Ellipsometry.

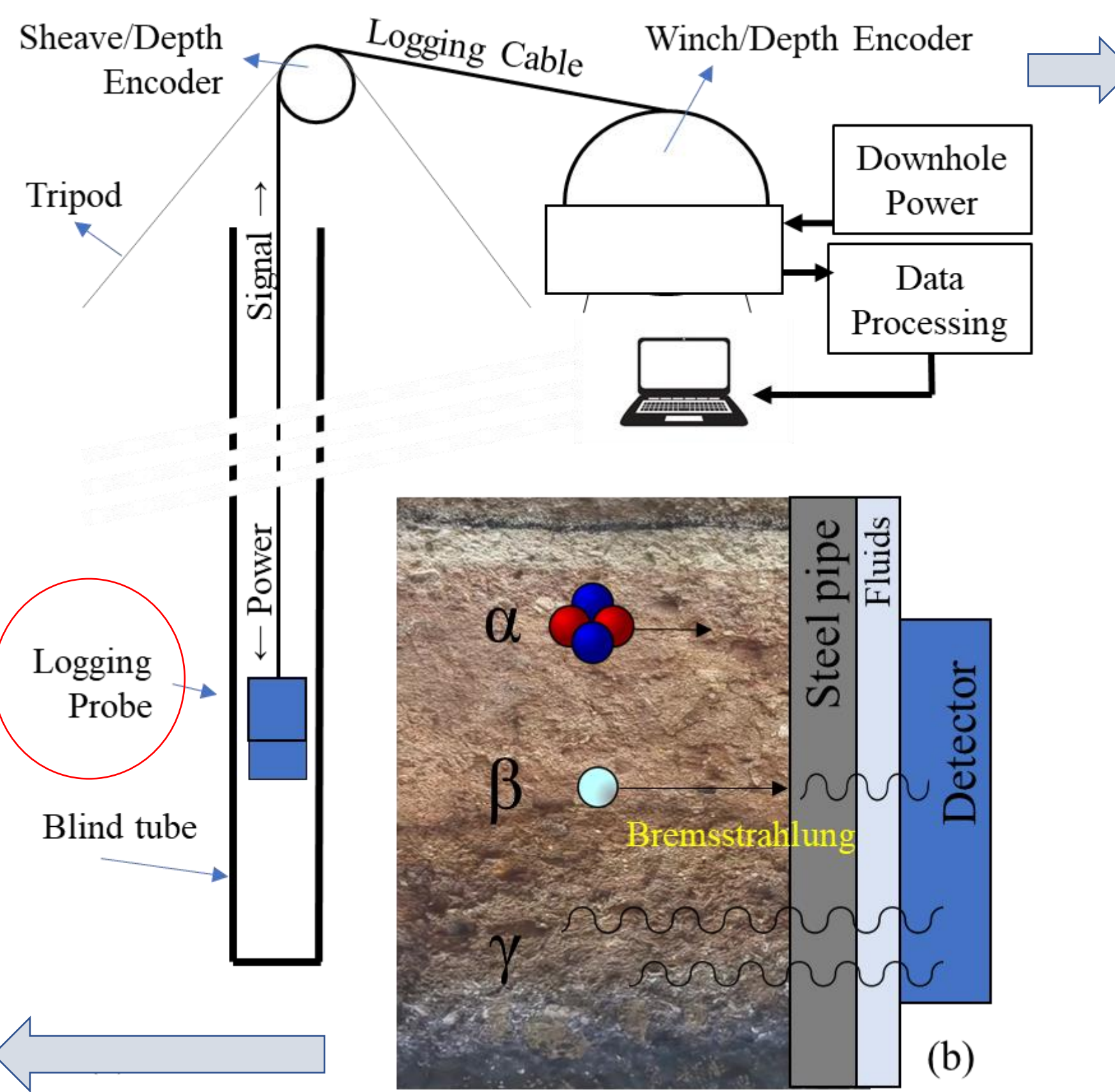
Abstract – Measurements made with a prototype radiometric logging probe for underground monitoring of long-lived radioactivity in blind-tubes are described. The probe comprises a $\varnothing 10$ mm \times 9.5 mm cerium bromide detector coupled to a full-featured MCA Topaz-SiPM digitizer. γ rays from radioactive decay and interactions in the surrounding materials are detected. A shape-fitting algorithm for peaks in vertical γ -ray spectral logs is validated successfully to localize a single, point source γ -ray emitter to 1% relative error.

Motivation:

- Whilst interim storage of spent fuel and associated solid wastes in ponds and wet silos is widespread, some facilities used for this purpose were not designed to modern standards and have **leaked**.
- The resulting migratory radioactivity in the ground could **pose a risk** to groundwater, surface water receptors and subsequently **public health**.
- This project is focused on this requirement concerning the Magnox Swarf Storage Silos (MSSS) at Sellafield (UK).

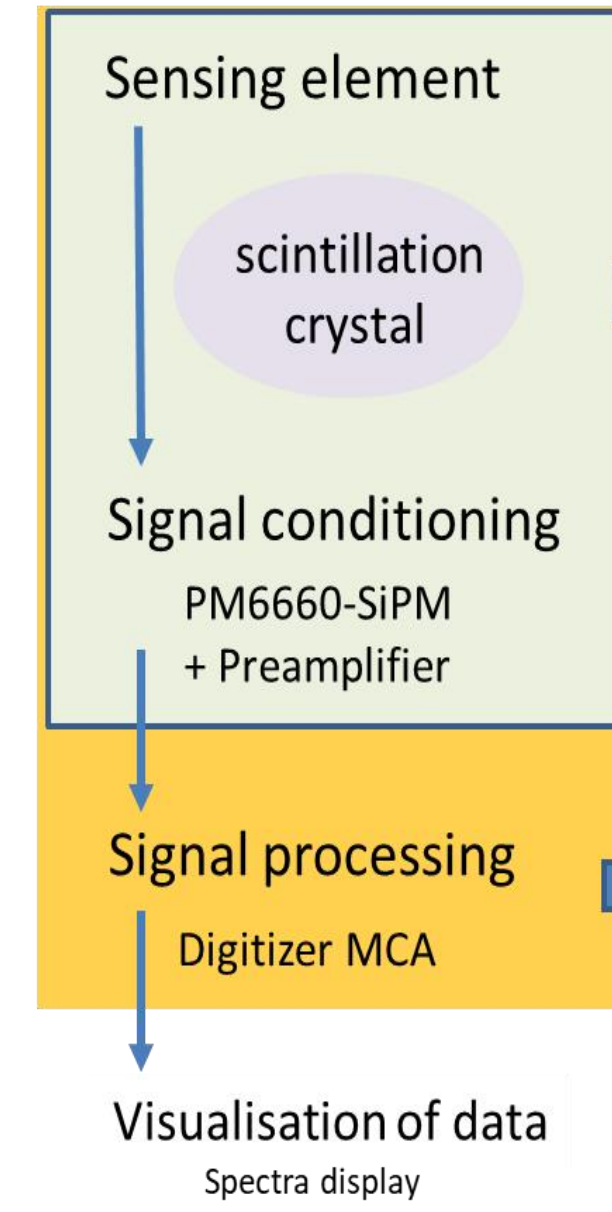
- Radioactive ground contamination migrating with water is likely to be dominated by ¹³⁷Cs and ⁹⁰Sr.
- Detection can be achieved by detecting the γ -rays from radioactive decay and **bremstrahlung photons** arising from the deceleration of energetic beta particles in the steel of the blind-tube lining, respectively.

The concept: Blind-tube logging probe prototype



- Measurements logs can be obtained with (1) the probe lowered in a borehole to obtain γ -ray spectra at a **number of depths**, or (2) as a **time series** with the detector fixed at a specific position and γ -ray spectra obtained at **different times**.

Logging probe



Ø10 mm x 9 mm CeBr₃ detector

- ✓ Good γ -ray detection efficiency
- ✓ Good energy resolution: 4 % @ 662 keV
- ✓ High count-rate capability: $\tau = 17$ ns
- ✓ High radiation hardness: < 100 kGy

Size $\varnothing 1.5 \times 6.5$ cm

Commercialized by Scionix (Netherlands)



TOPAZ-SiPM digital MCA

- ✓ Compact full-featured MCA
- ✓ Compatible with dimensions of typical blind-tubes
- ✓ Designed specially for SiPM detectors
- ✓ 5V low-ripple, low-noise supply
- ✓ Powered from the PC via the USB cable

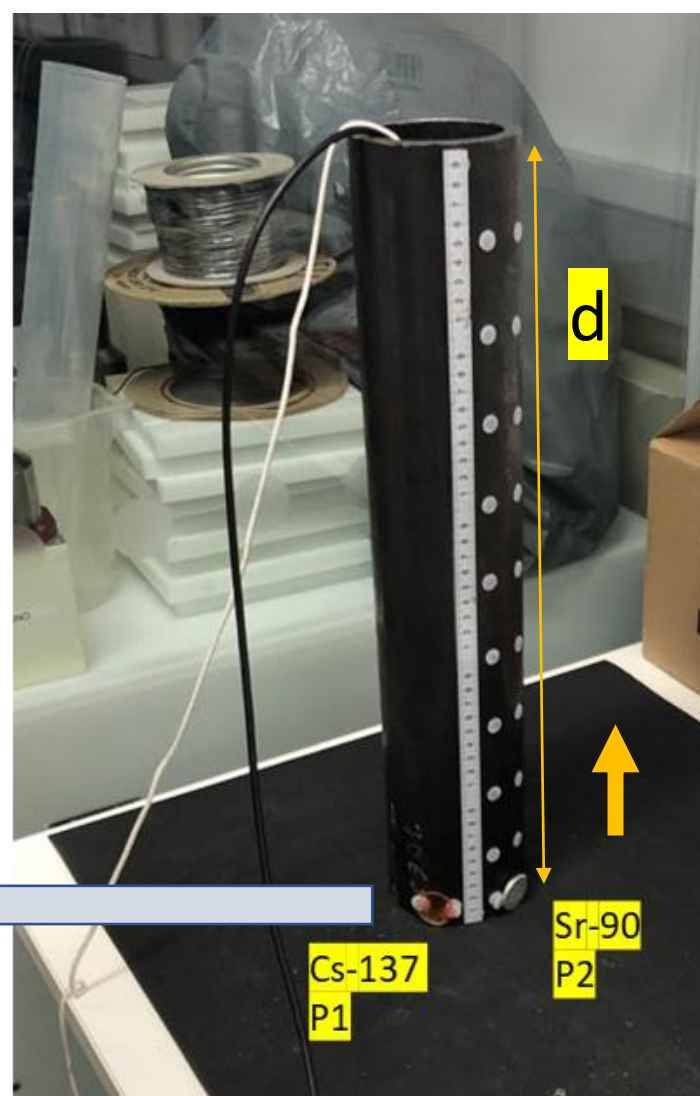
Size 7x4.5x2.6 cm

Detection of ¹³⁷Cs and /or ⁹⁰Sr:

Spatial source distribution is point sources surrounding the blind-tube and are close to the wall.

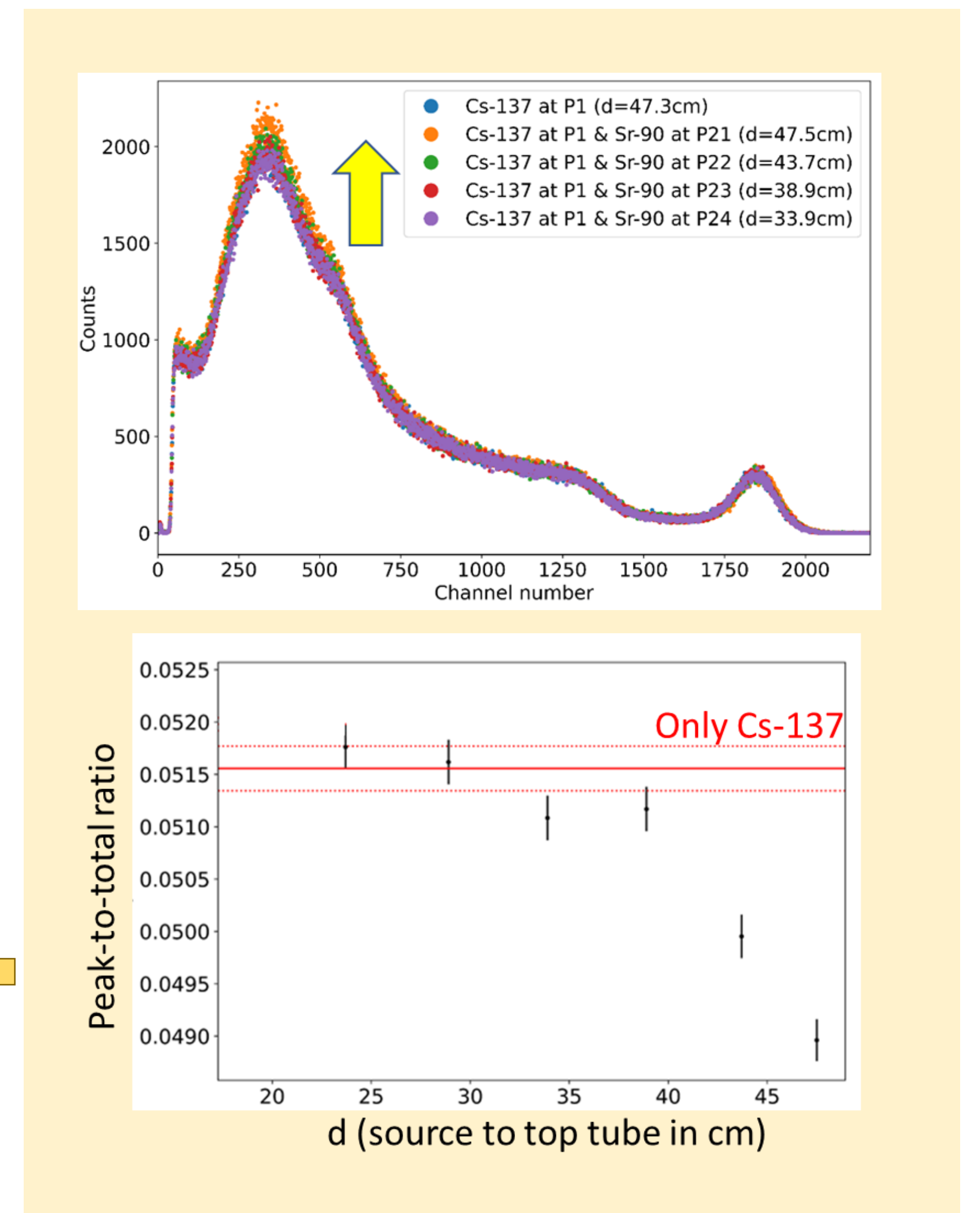
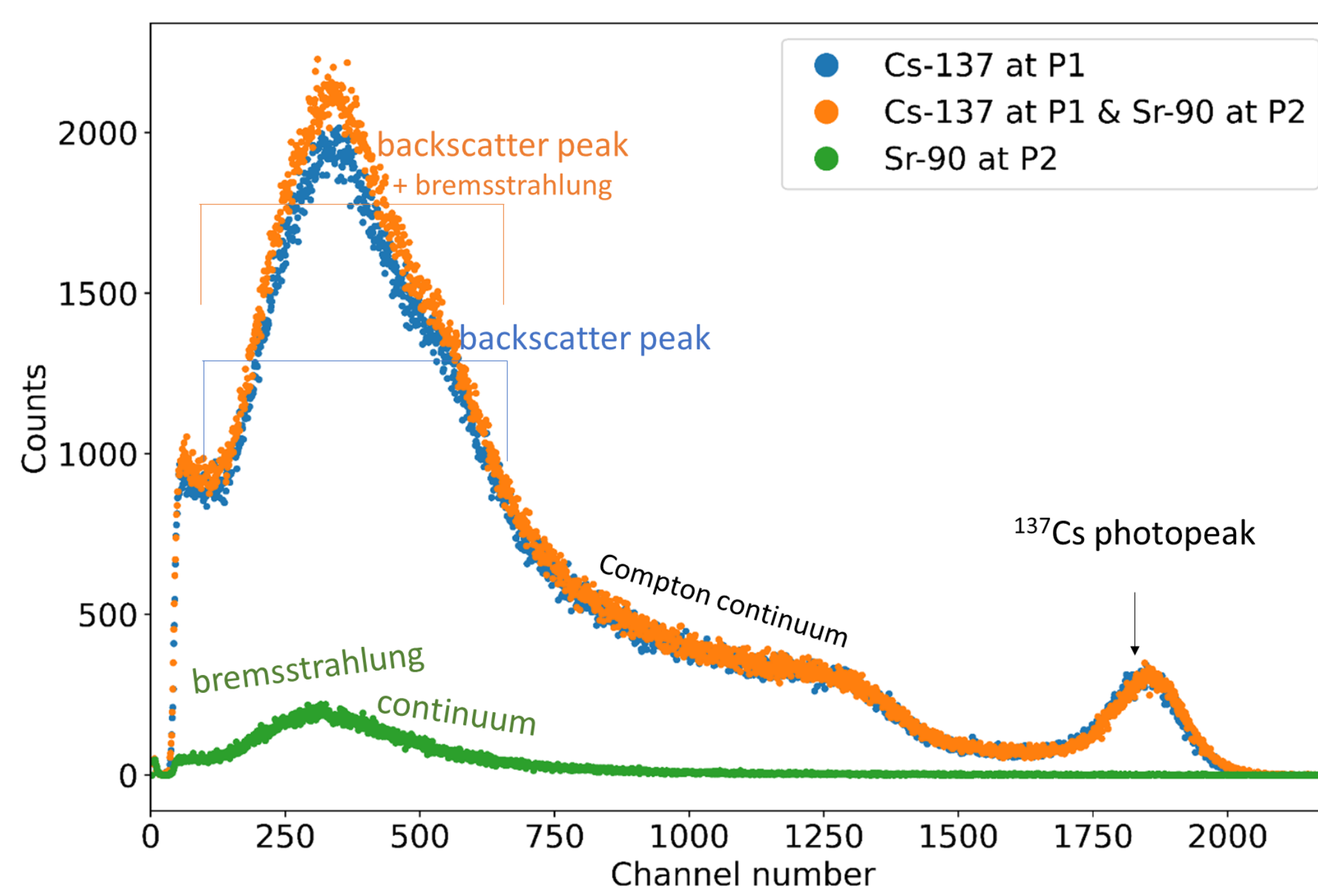
Contamination Simplified scenario

Experimental set-up



Cs-137 (304 kBq) Sr-90 (370 kBq)

Typical spectra expected for these situation and representative of these two types of contamination:

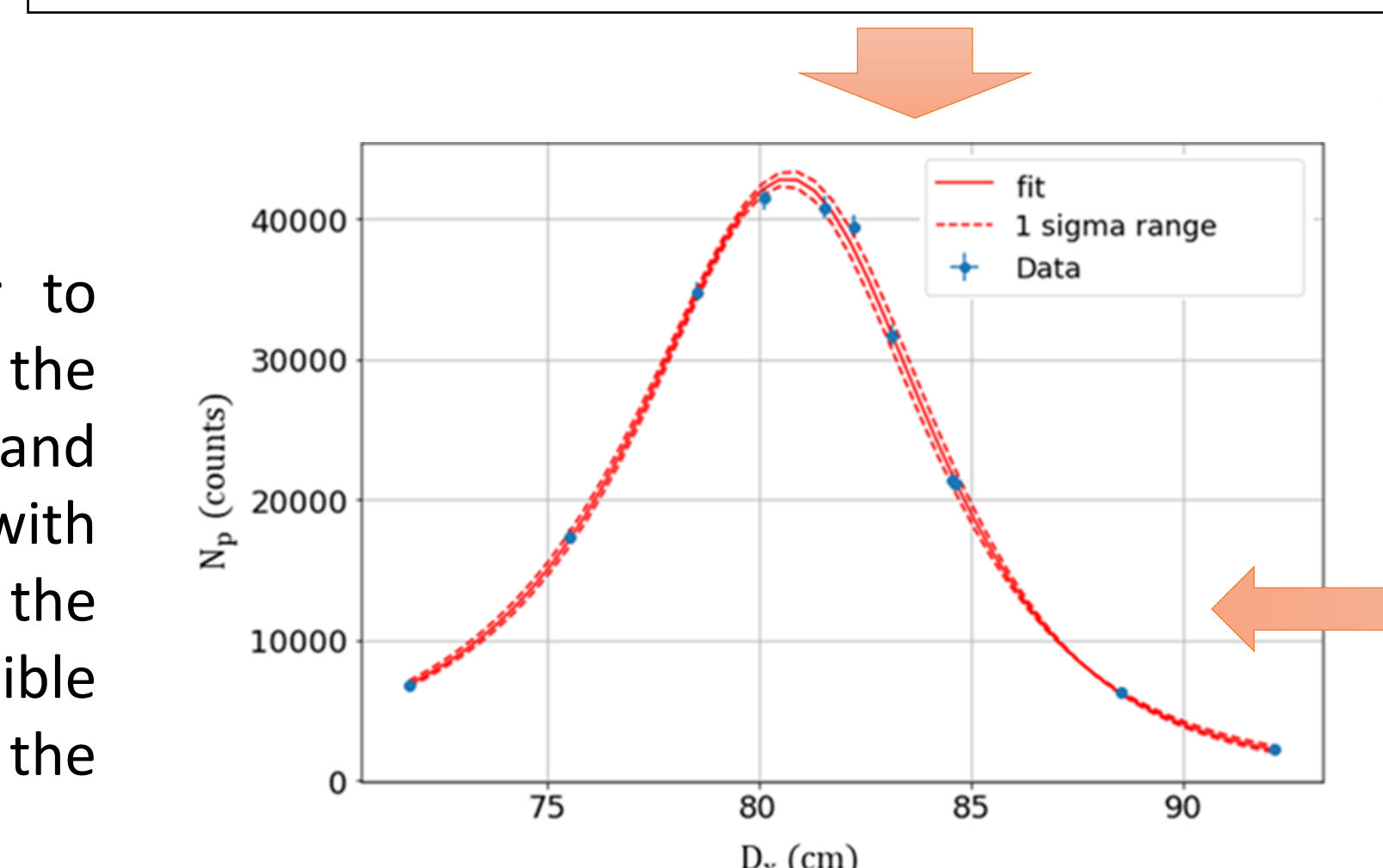
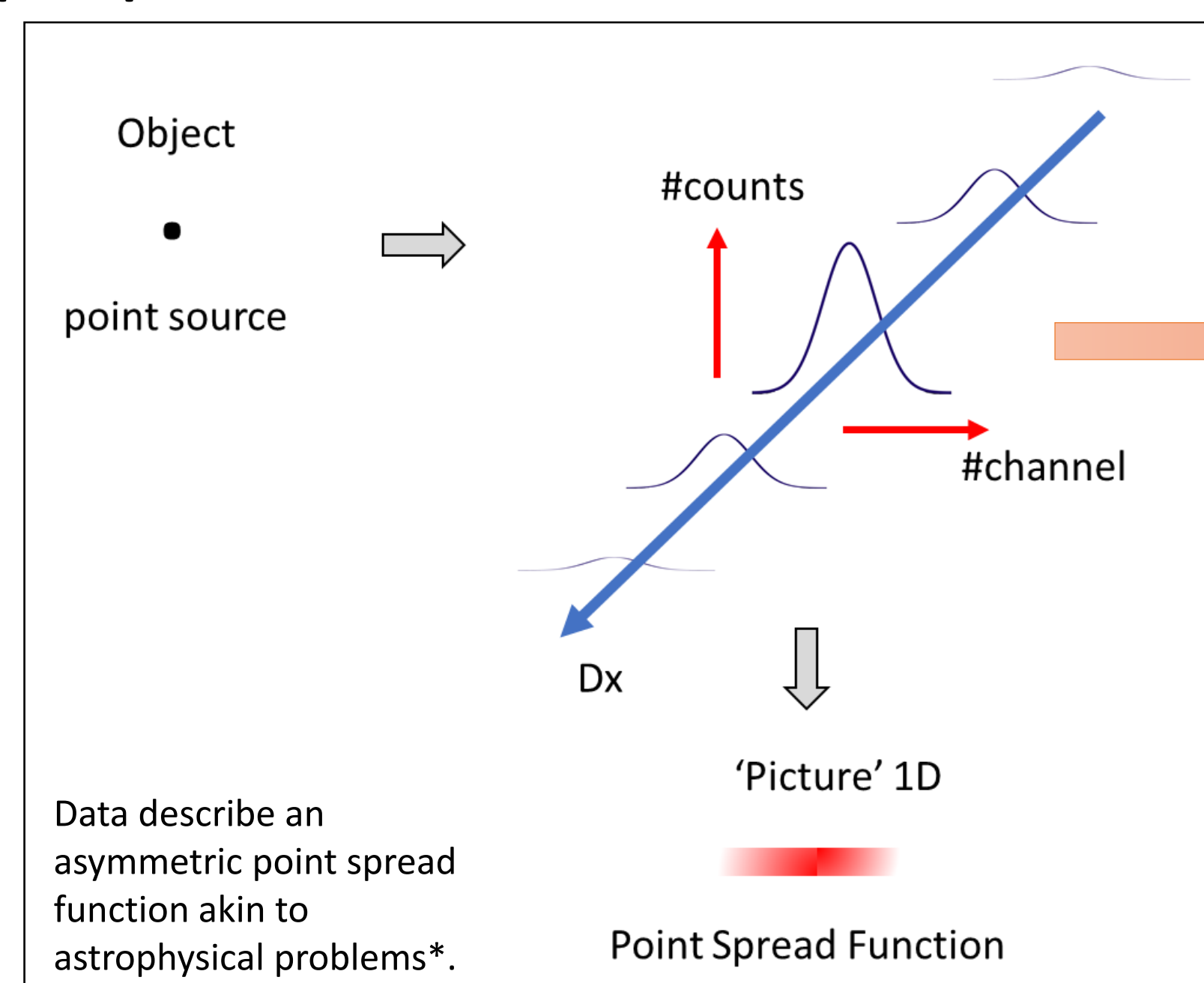
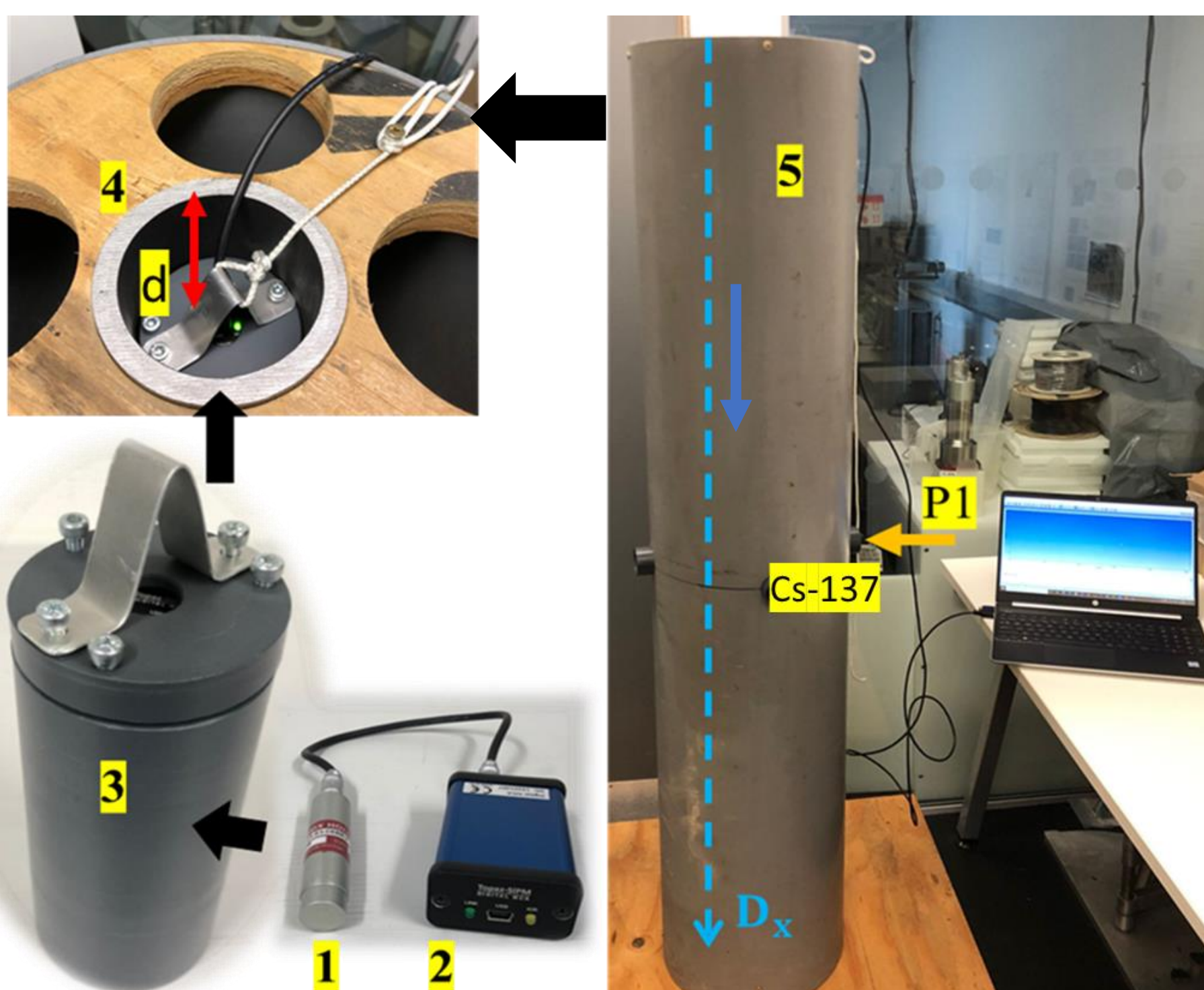


- Significant quantities of ⁹⁰Sr contamination might be sufficient to yield measurable levels bremstrahlung radiation which act to degrade the spectrum from ¹³⁷Cs.

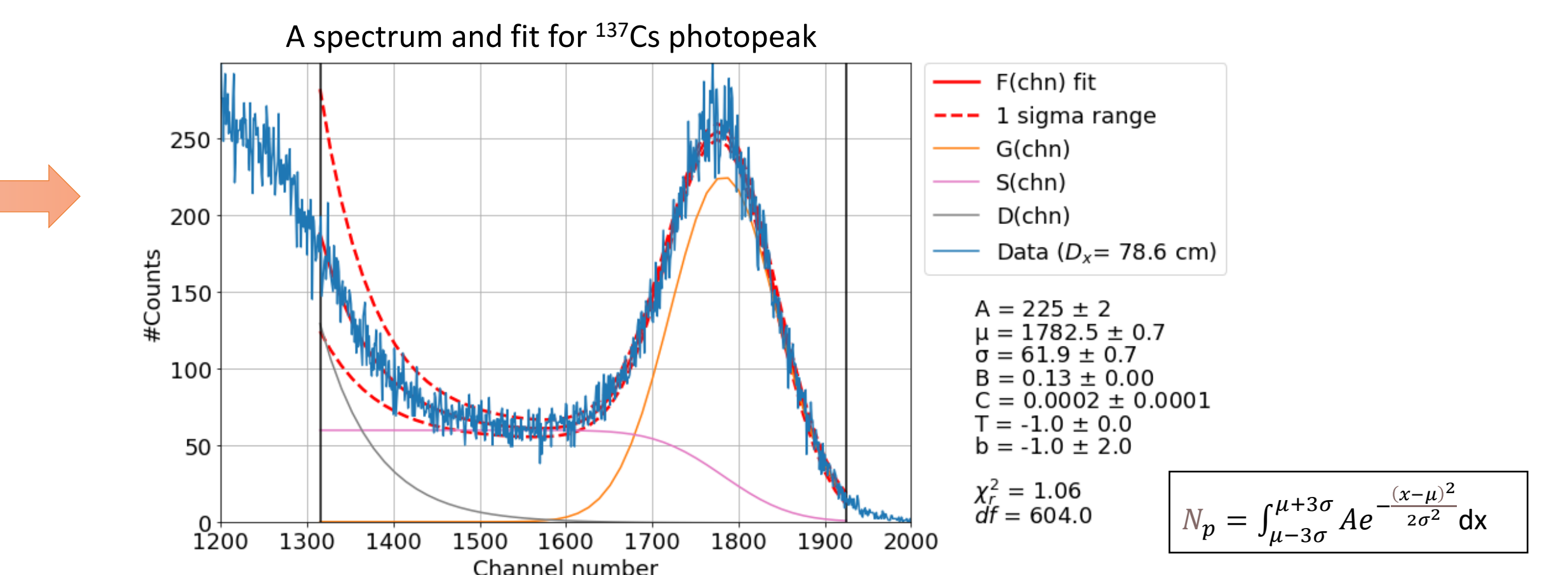
- **Focus:** We are interested in changes in the shape and intensity of spectra recorded successively as well as specific sections of spectrum when the source distribution changes from one measurement to the next.

Detection of ¹³⁷Cs and Point-spread analysis of photon-depth spectra:

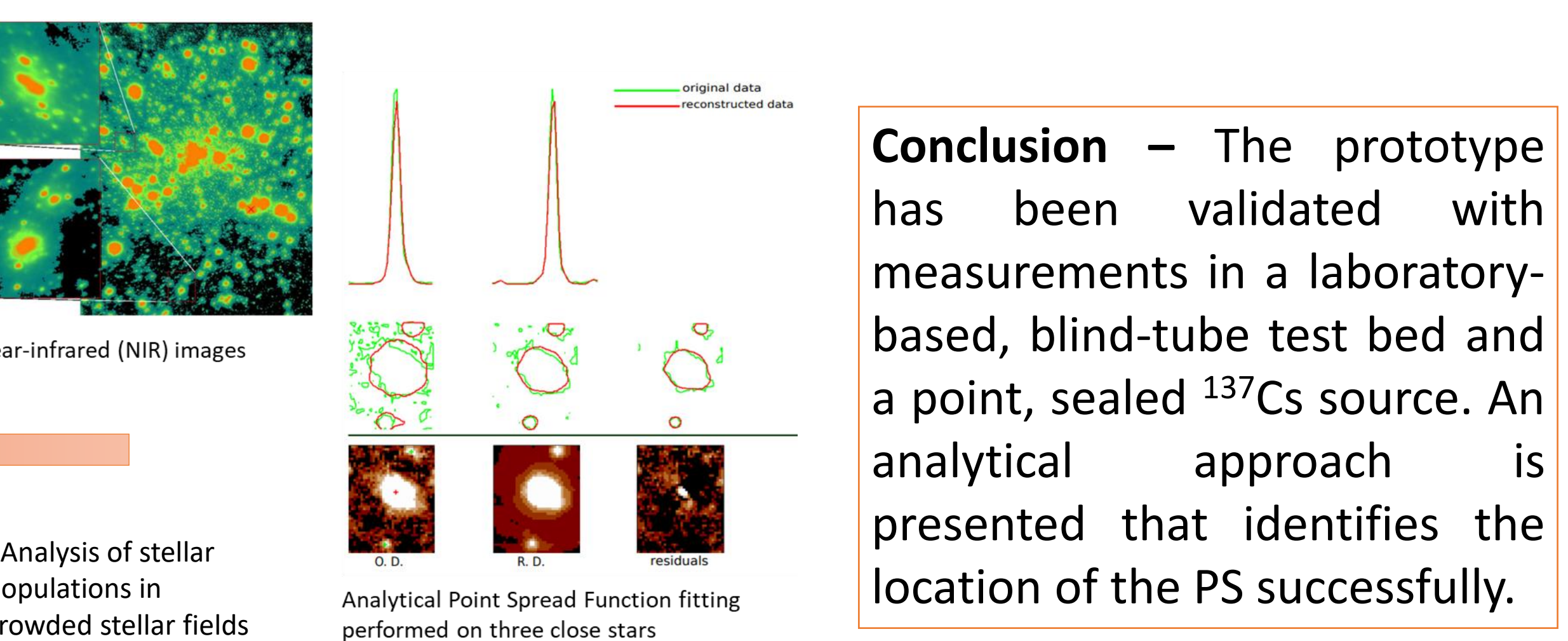
Experimental set-up – The blind-tube test bed



- Full-energy peaks above a continuum background, and quantification of the variation in the number of events in this selected region:



$$f(x; A, \mu, \sigma, B, C, T, b) = Ae^{-\frac{(x-\mu)^2}{2\sigma^2}} + AB \operatorname{erf}\left(\frac{x-\mu}{\sigma\sqrt{2}}\right) + ACe^{\frac{x-\mu}{T\sigma}} \operatorname{erf}\left(\frac{x-\mu}{\sigma\sqrt{2}}\right) + \frac{1}{T\sqrt{2}} + b$$

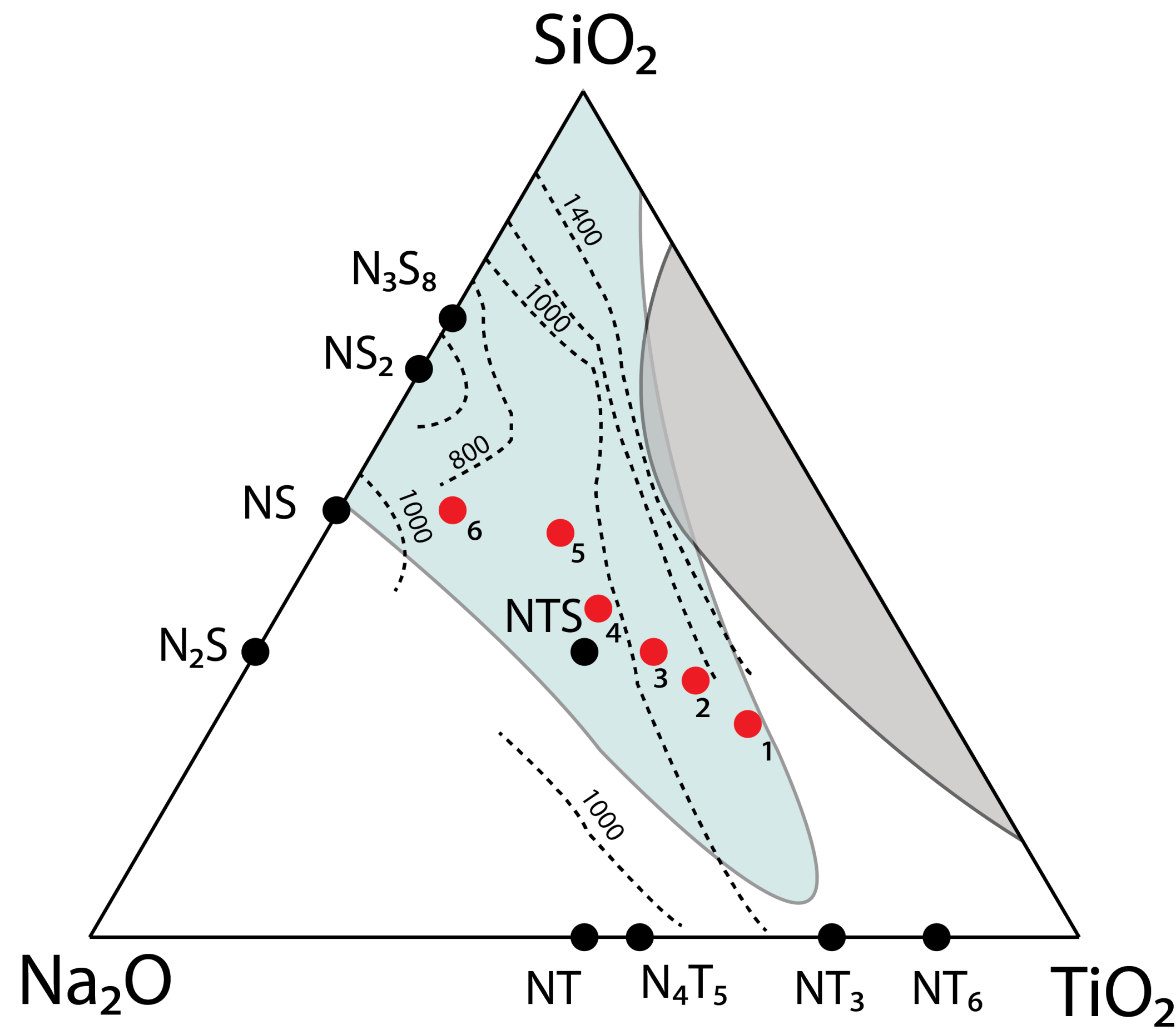


Conclusion – The prototype has been validated with measurements in a laboratory-based, blind-tube test bed and a point, sealed ¹³⁷Cs source. An analytical approach is presented that identifies the location of the PS successfully.

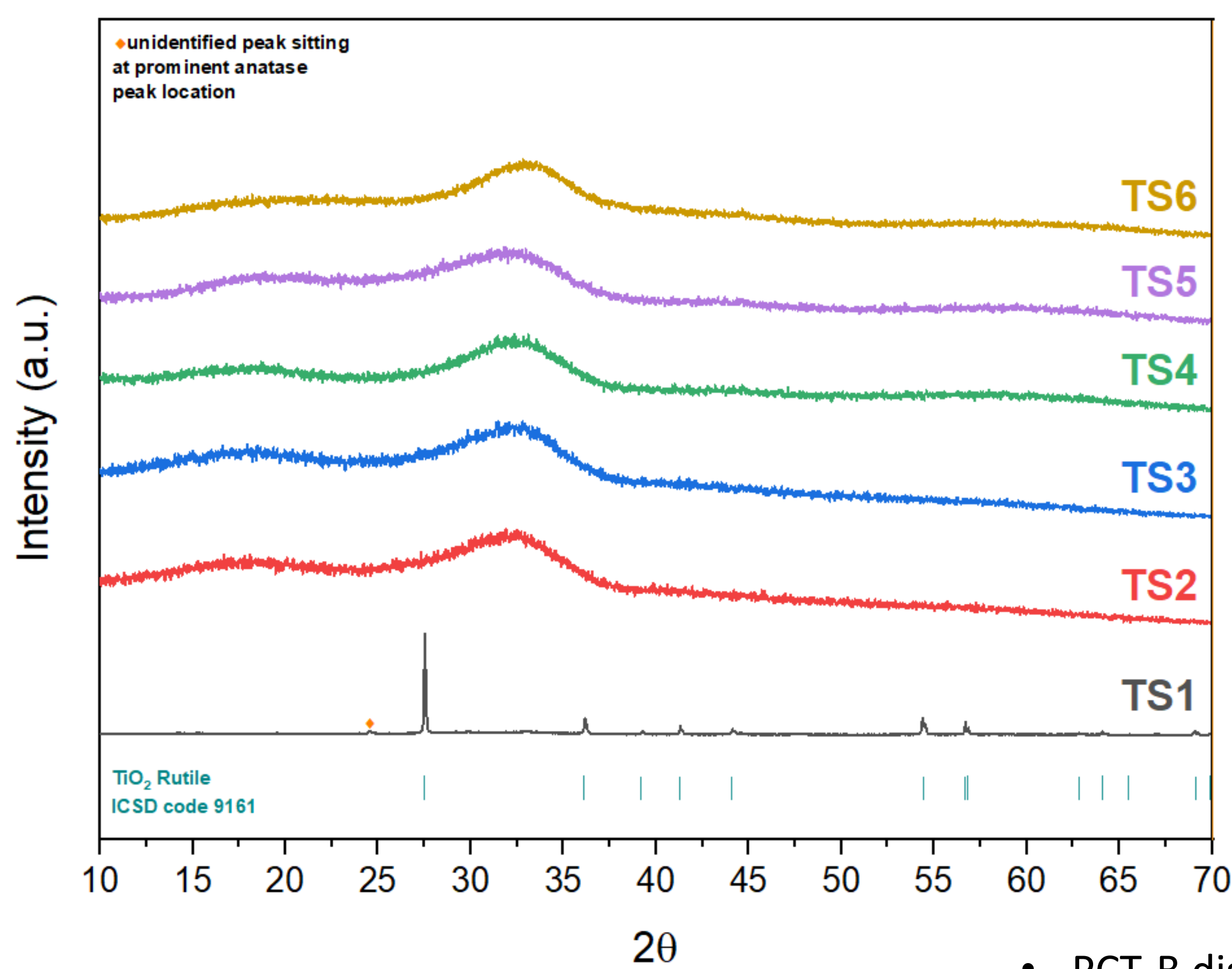
- With the detector closer to the source, the intensity of the photopeak increases, and decreases further away, with the highest intensity at the shortest distance possible between the source and the detector.

Acknowledgment – This research is supported by NNL and Sellafield Ltd. (UK) via the EPSRC programme TRANSCEND (TRANSformative Science & Engineering for Nuclear Decommissioning), code EP/S01019X/1. M. J. J. acknowledges the support of the Royal Society via a Wolfson Research Merit Award.

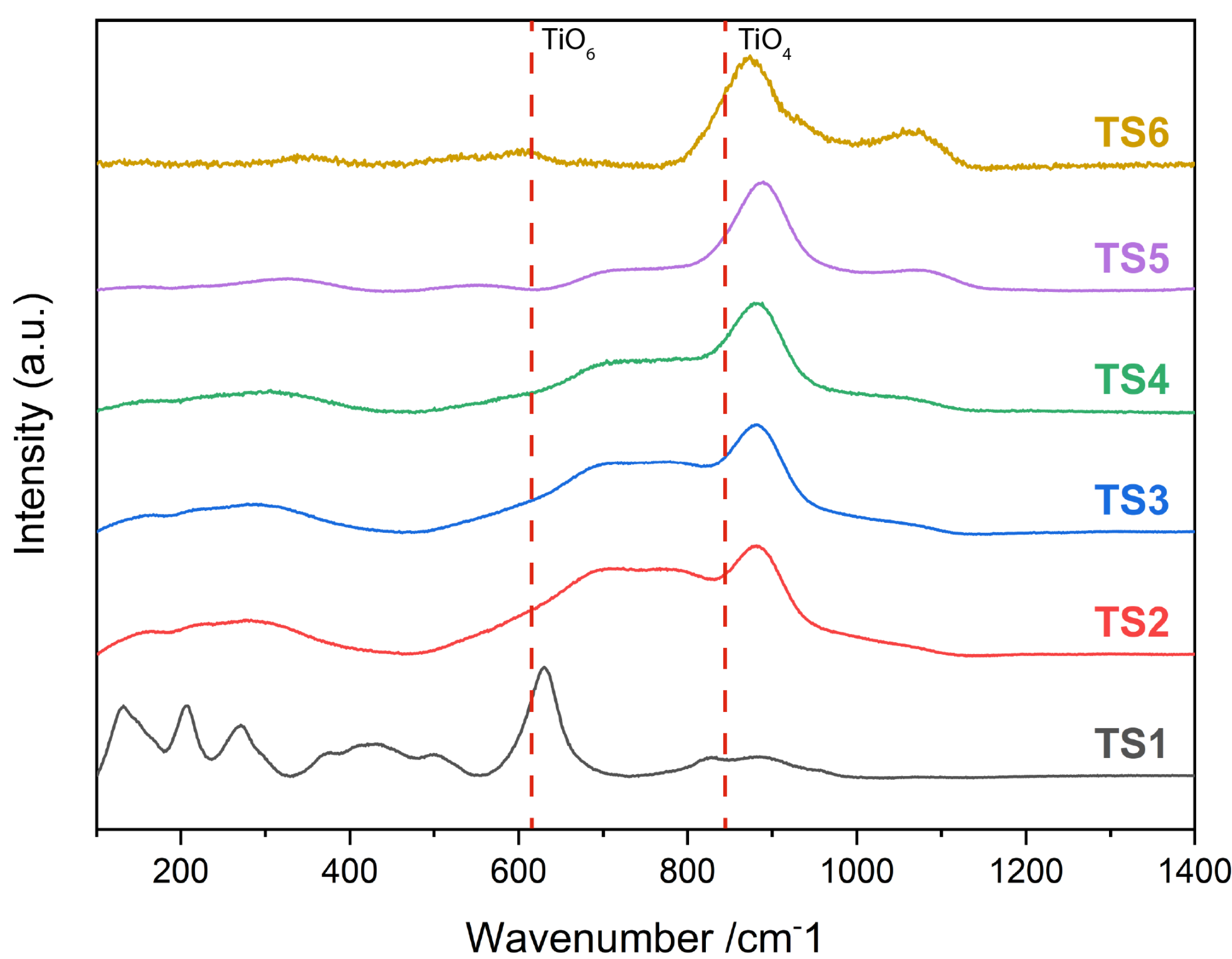
- Interest in the system stems from the knowledge that a glass forming region exists in the $TiO_2-Na_2O-SiO_2$ phase diagram (Richet et al 2006) and this also forms the basis for the framework titanates which are known ion exchangers
- As a result, a glass series was created in the glass forming region (1-6).



- The XRD showed that TS2-6 were amorphous and that TS1 was likely recrystallised rutile with a slight amount of potential anatase



- Raman analysis displays a shift in regime from a TiO_4 dominated system to further influence of TiO_5 and TiO_6 before TS1 shows a TiO_6 dominant system with some evidence of framework titanate formation



- The glass series saw limited success with TS1 crystallising, TS2 & 3 looking phase separated, with TS2 having macro-crysts, but TS3-6 looked like homogenous glasses (all observations on pouring)



- Batches were made to add 0.125 Mol%, 0.5 Mol% and 1 Mol% caesium from caesium carbonate. Then glasses TS4 and TS5 were selected (due to issues with the other glasses) and Ionsiv was loaded with caesium from caesium nitrate solution and then batch was added to target these stoichiometries. The retention from these samples are shown below.

Sample ID	retention %	Sample ID	retention %
TS5_0.125	42	TS5_ION	80
TS5_0.5	44		
TS5_1	44		
TS4_0.125	44		
TS4_0.5	42		
TS4_1	43		
TS3_0.125	48		
TS3_0.5	42		
TS3_1	43		
TS2_0.125	47		
TS2_0.5	43		
TS2_1	43		

- TS5_ION is quoted alone as when the samples were made only the TS4 target sample made a homogenous glass as the TS3 version crystallised.

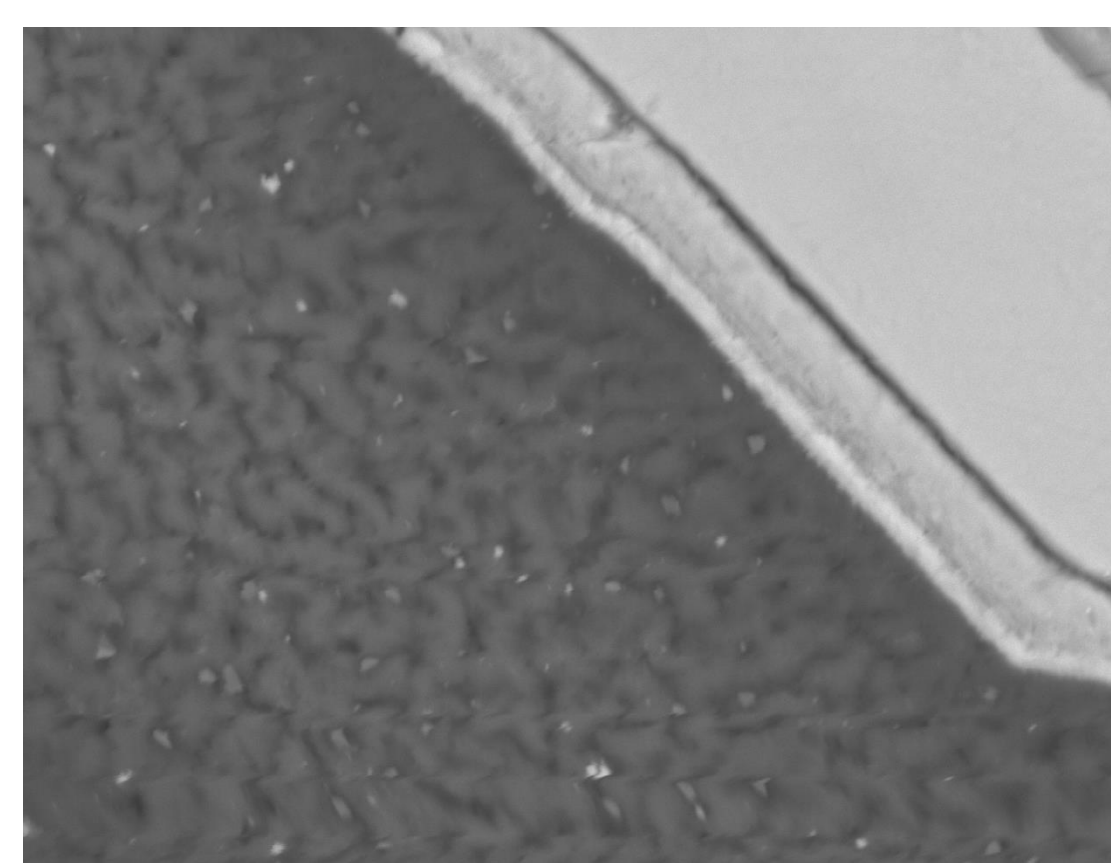


TS4_ION sample

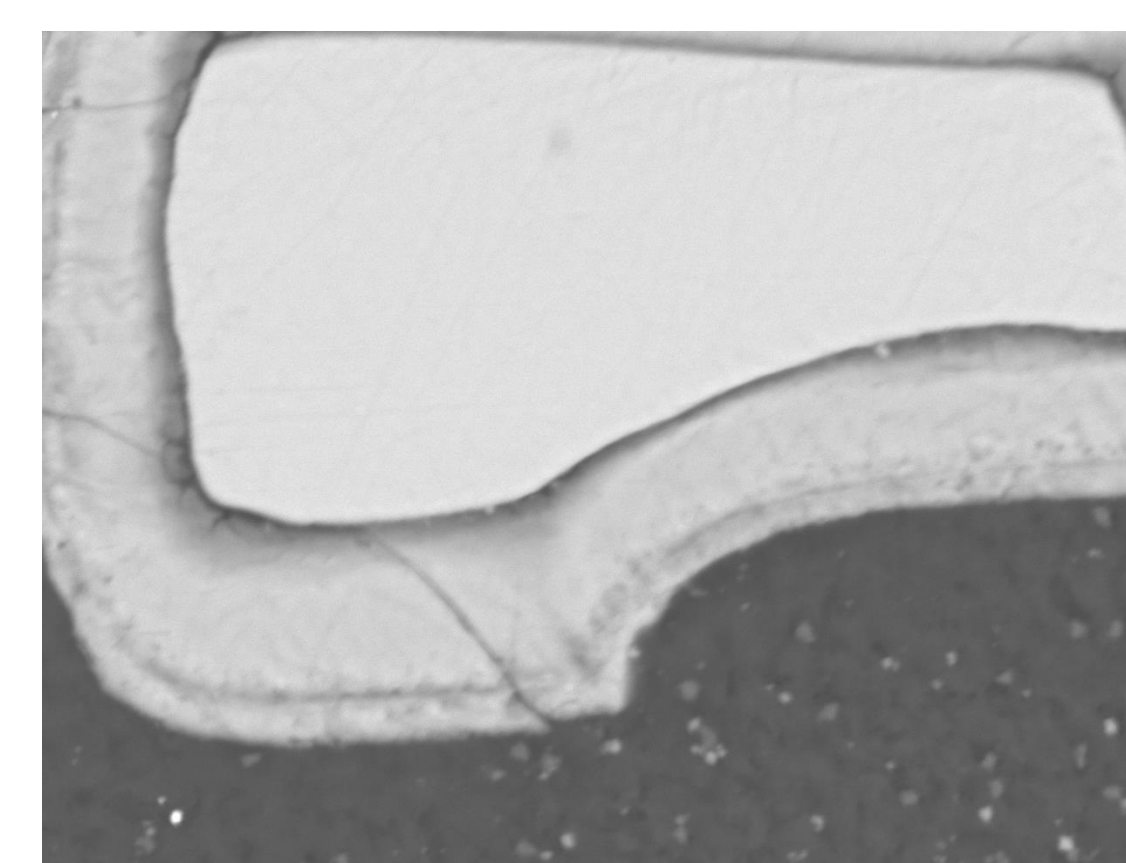


TS5_ION sample

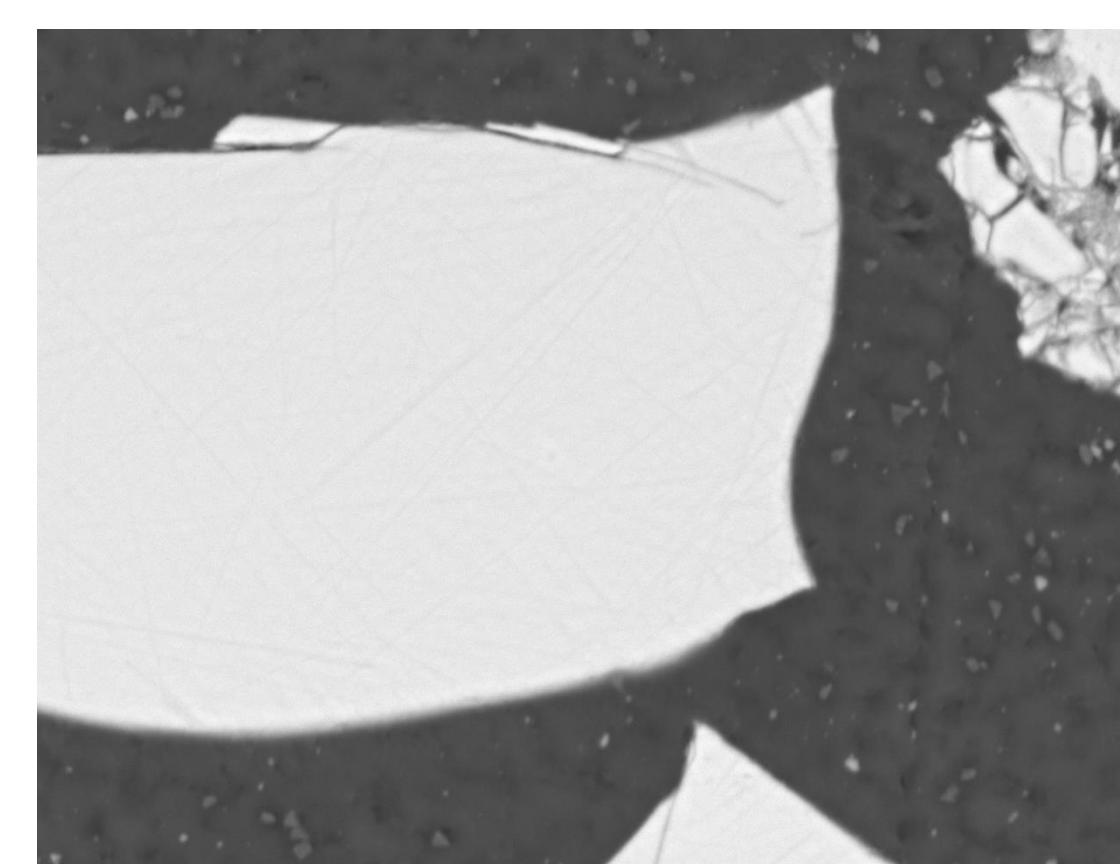
- PCT-B dissolution studies were conducted on the samples TS5, TS5_1 and TS5_ION for 28 days at 90°C in UHQW, SEM images of the post dissolution samples are shown below



TS5 sample



TS5_1 sample



TS5_ION sample



Project supervisors are:
Russell J. Hand
Industry – Stephen Hepworth

Background & Introduction

Use of acoustic backscatter to characterise high concentration sediments in the near-field, and characterisation of bi-disperse systems is not yet fully understood. Application of these techniques is being introduced to monitor the PSDs of legacy nuclear waste sludge which are currently undergoing processing and disposal. The processing utilises polymeric behaviour modifiers which aid settling, but are shear dependent.

As such Machine Learning (ML) will help to automate and improve the analysis of the backscatter data so the concentration and PSD can be characterised relatively easily, and the changes of these measurements can be tracked through time with varying shear.

Materials & Methods

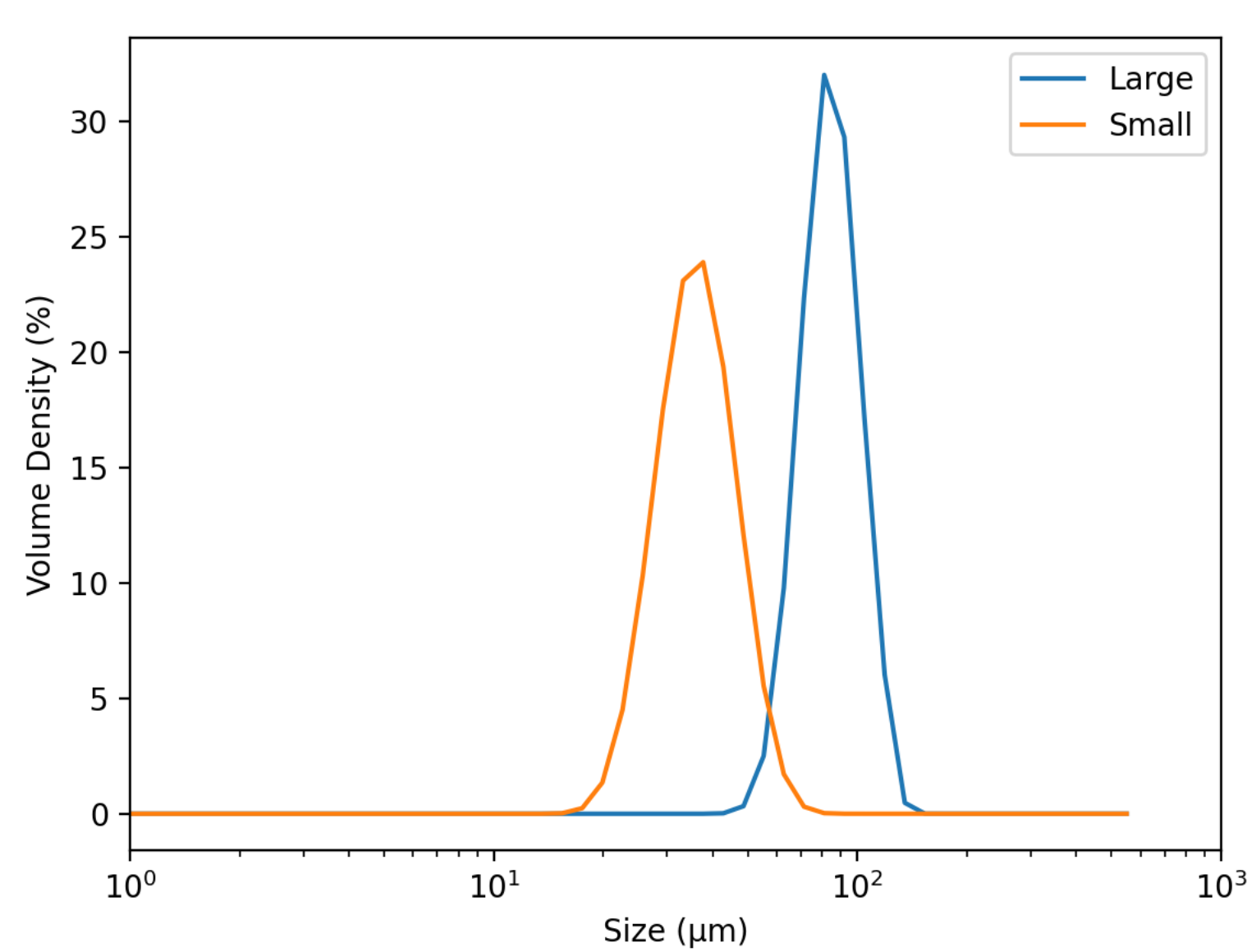


Fig 1 – PSDs of two sizes of silica glass beads used, data gathered using a Malvern Mastersizer 3000.

Spherical silica glass beads of different sizes, $d_{50} = 41\mu\text{m}$ and $d_{50} = 81\mu\text{m}$, were investigated at concentration range 14 to 68 g/L.

Acoustic data was collected using in situ probes with the UVP-DUO on homogenised sediment suspensions.

Research Aims

- ❖ Size Characterisation of virgin vs. sieved size fractions and bimodal size fraction mixtures of spherical glass particles.
- ❖ Development of Machine Learning code to characterise size and concentration of spherical glass particles.
- ❖ Application of aforementioned research to flocculated systems.

Fig 2 – Python Logo (Wikipedia, 2021).



Data were analysed in Python scripts and the concentration independent sediment attenuation coefficients (SAC) for both glass sizes at 2MHz and 4MHz were calculated using the G-function method outlined in Bux et al. (2019).

Comparison of these measured SACs against values calculated from the acoustic models in literature, which incorporate attenuation losses from both viscous elastic and scattering mechanisms, are plotted below.

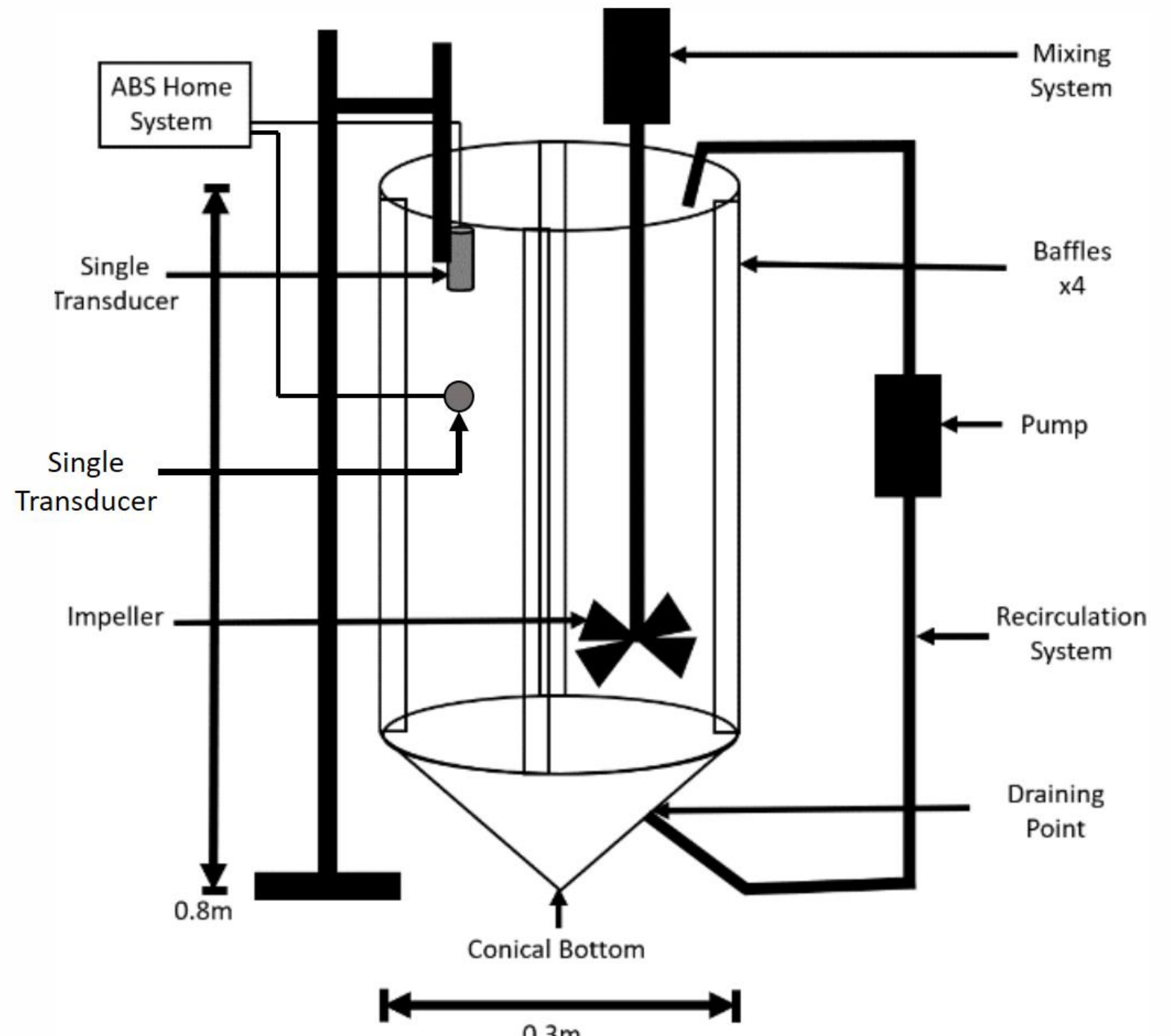


Fig 3 - Schematic of the calibration rig used in this project, modified from Hussain et al. (2020).

Results & Discussion

Fig 4 – Backscatter G function vs. distance from transducer, at 4MHz; (left) large glass, (right) small glass. Vertical black lines show where the gradient of each plot was taken.

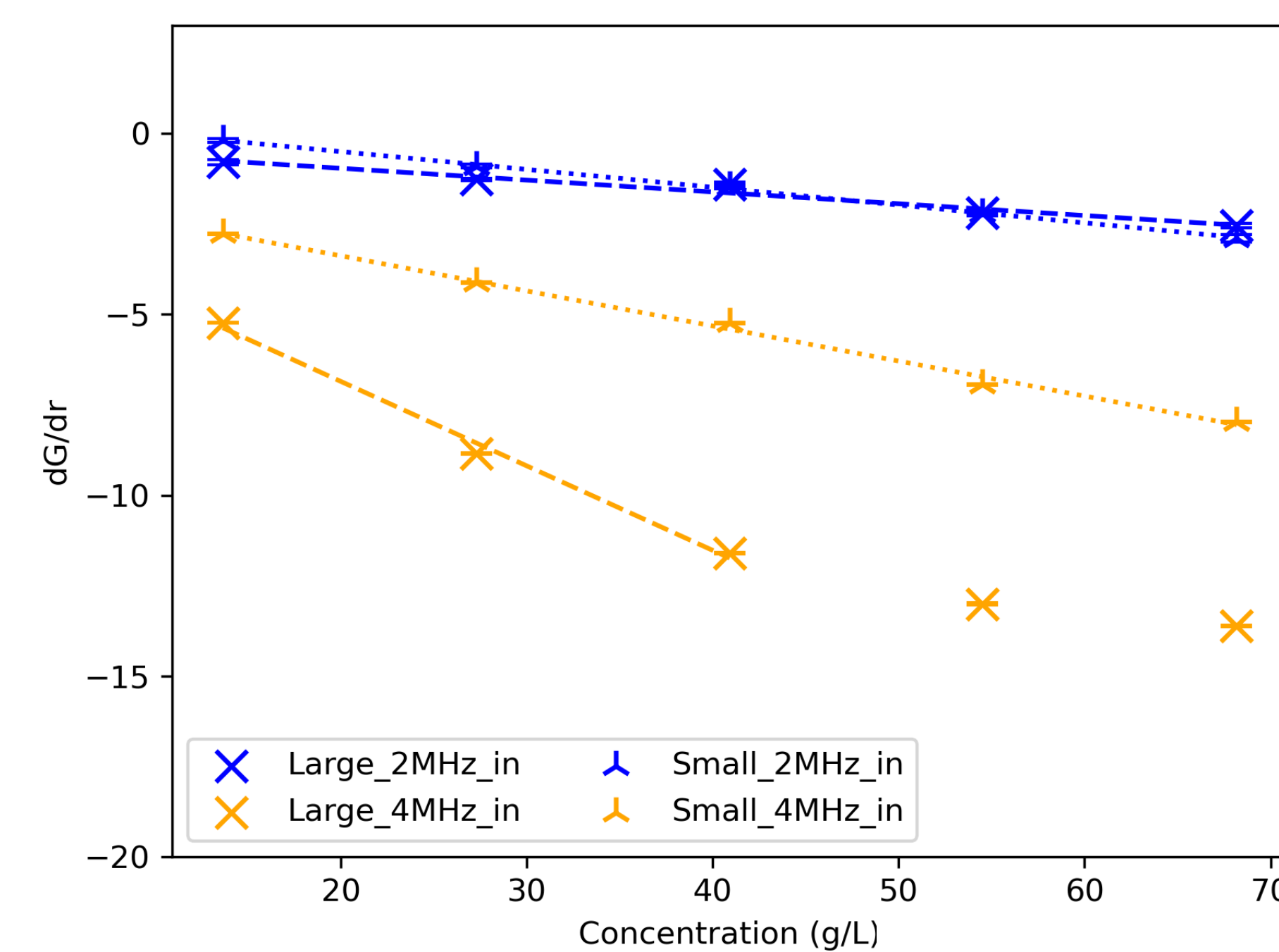
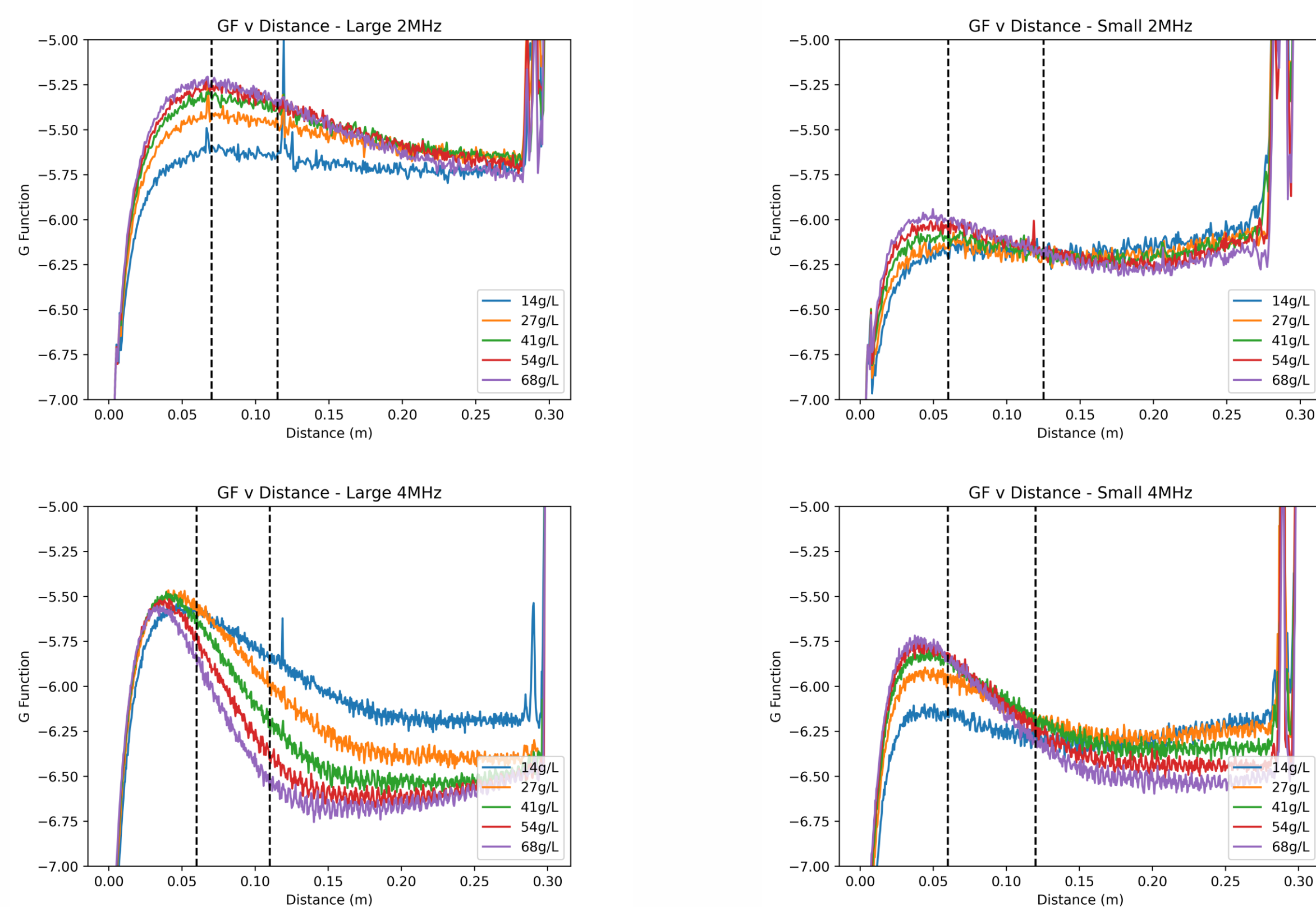
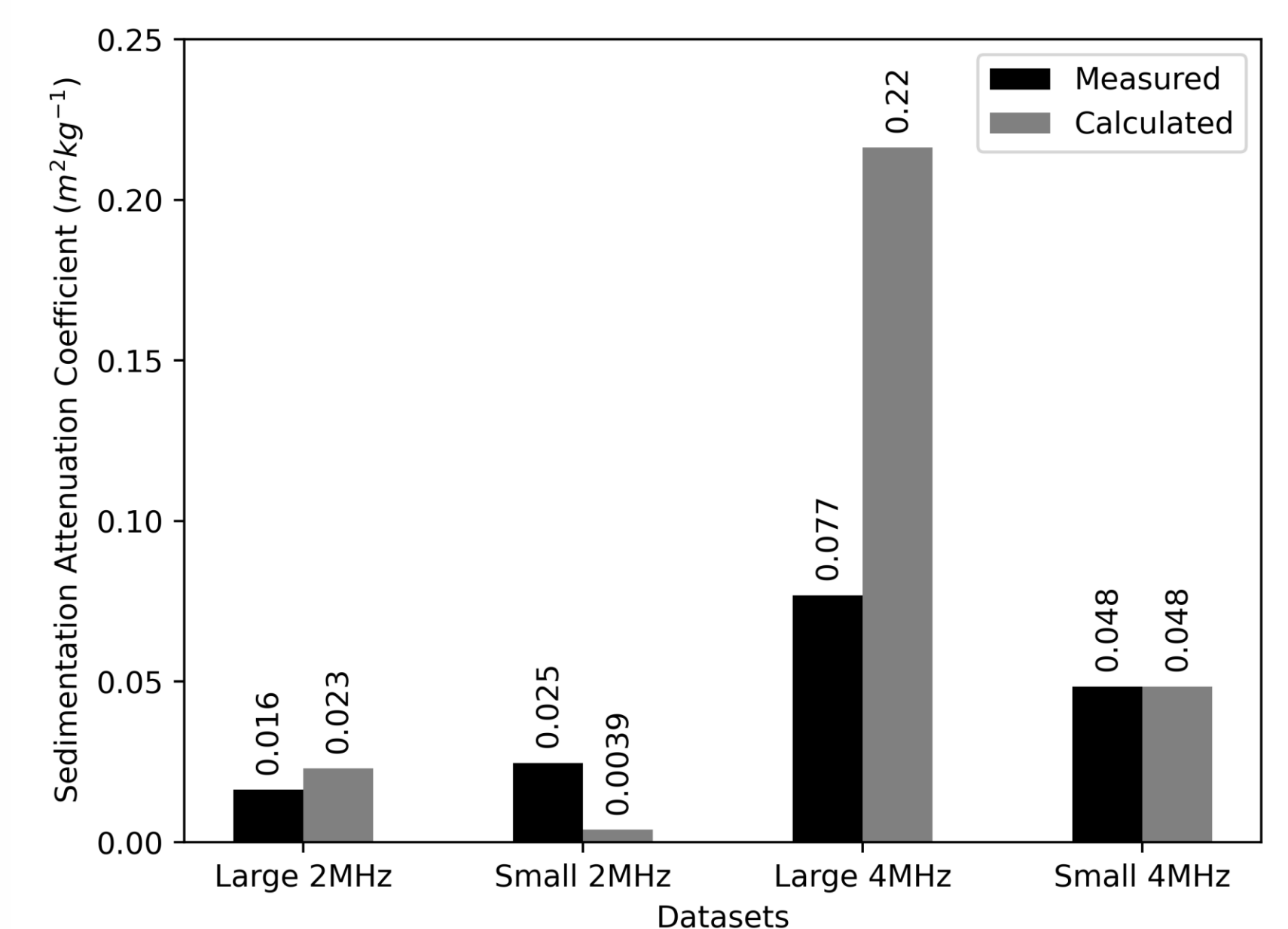


Fig 5 – dG/dr (gradient from G-function vs. distance from transducer in Fig 4) vs. concentration for all data collected.

The 4MHz signal for the large glass highlights the limits of the UVP transducer as the points bottom out, thus a gradient is only taken from the first three points.

Fig 6 – Measured concentration independent SAC for all systems in comparison to calculated values from the model including both scattering and viscous elastic losses (Urick 1948).

Fig 6 highlights that the SAC is larger for the 4MHz compared the 2MHz signal and the large glass attenuates the signal of both frequencies more than the small glass.



Conclusions & Further Work

- Broad agreement between measured and calculated SACs.
- SACs larger for 4MHz than 2MHz, and larger for the large glass than small glass.
- Measured SAC of large glass at 4MHz significantly below calculated values because of multiple scatterings artificial increasing strength of backscatter signal received.
- Investigate the effect of sieved size mixes on backscatter data, and comparison of UVP and Aquascat ABS acoustic backscatter measuring equipment.
- Understand the effect of bi-disperse size mixes on backscatter data, when looking to characterise a PSD.
- Development of ML code package for determination of PSD, from acoustic backscatter data.

References

- Hussain, S.T., Hunter, T.N., Peakall, J. and Barnes, M. 2020. Utilisation of underwater acoustic backscatter systems to characterise nuclear waste suspensions remotely. In: *International Conference on Underwater Acoustics*.
- Bux, J., Peakall, J., Rice, H.P., Manga, M.S., Biggs, S. and Hunter, T.N. 2019. Measurement and density normalisation of acoustic attenuation and backscattering constants of arbitrary suspensions within the Rayleigh scattering regime. *Applied Acoustics*. **146**, pp.9-22.
- Urick, R.J. 1948. The absorption of sound in suspensions of irregular particles. *The Journal of the Acoustical Society of America*. **20**(3), pp.283-289.
- Wikipedia. 2021. *Python (programming language)*. [Online]. [Accessed 07/11/21]. Available from: [https://en.wikipedia.org/wiki/Python_\(programming_language\)](https://en.wikipedia.org/wiki/Python_(programming_language))